Spectroscopy of Single Rare Earth Solid-State Qubits

Von der Fakultät 8 Mathematik und Physik der Universität Stuttgart zur Erlangung der Würde eines Doktors der Naturwissenschaften (Dr. rer. nat.) genehmigte Abhandlung

Vorgelegt von

Kangwei Xia

aus Shanghai, V. R. China

Hauptberichter:	Prof. Dr. Jörg Wrachtrup
Mitberichter:	Prof. Dr. Peter Michler

Tag der mündlichen Prüfung: 05.08.2016

3.Physikalisches Institut
Universität Stuttgart

2016

List of abbreviations

AOM	acousto-optic modulator
APD	avalanche diode
Ce	cerium
CPMG	Car-Purcell-Meiboom-Gill
CPT	coherent population trapping
CW	continuous wave
DD	dynamical decoupling
ESA	excited state absorption
eV	electronvolt
FIB	focus ion beam
FWHM	full width at half maximum
LuAG	lutetium aluminum garnet
MW	microwave
N. A.	numerical aperture
NV	nitrogen-vacancy
ODMR	optically detected magnetic resonance
PBS	polarizing beamsplitter
PDD	period dynamical decoupling
PLE	photoluminescence excitation
PMT	photomultiplier tube
ppb	parts per billion
ppm	parts per million
ppt	parts per trillion
Pr	praseodymium
SEM	scanning electron microscopy
SET	single electron transistor
SIL	solid immersion lens
TCSPC	time-correlated single photon counting
UV	ultraviolet
YAG	yttrium aluminum garnet
YSO	yttrium orthosillicate
ZPL	zero phonon line

Summary

Light-matter interaction at single quantum object level is a long-lived challenge and dream of physicists. From the 1970s, the development of single ion spectroscopy and the observation of single photon states pave a way to a new era of detecting, and coherently manipulating quantum objects with electromagnetic field at single-ion levels. Later on, the invention of single molecular spectroscopy offers a new approach to investigate single quantum objects in condensed matter, where the sophisticated trapping systems like in ions and cold atoms are not needed, resulting in the discovery of various of single photon emitters embedded in solids. Among all, single quantum dots and single negatively charged nitrogen-vacancy centers in diamond attract most attentions, since their single spins can be coherently manipulated and entangled by the light field giving rise to numerous applications from nanoscale sensing to quantum computing. They are intensively studied as the most promising candidates for the realization of solid-state quantum bits. However, these systems coupled to a complex environment which can result in rapid loss of spin coherence or optical instability. Finding an alternative solid-state single system with remarkable optical and spin properties is the motivation of this dissertation.

Rare earth ions doped in inorganic crystal hosts provide promises not only by the high quality factor $4f \leftrightarrow 4f$ optical transitions but also by the well preserved and long-lived spin states, with the applications from solid-state laser spectroscopy to quantum information processing. However, for almost three decades, not being able to identify single rare earth elements in solids is the obstacle to achieve their full potential functionality.

We demonstrated the first direct optical detection of single rare earth ions (praseodymium) in solids in 2012. This research was covered in my Master Degree Thesis. This dissertation presents experimental progress in optically detecting other single rare earth species in crystals, understanding their fundamental spectroscopy properties and coherently controlling them, which is mainly focused on single trivalent cerium ions in different host materials. Following the optical detection of single cerium ions in yttrium

aluminum garnet (YAG), the optical and spin properties of single Ce ions are investigated.

Single Ce ions show good photostability under the pulsed laser excitation. Still, like in other solid emitters, photo-induced dynamics of single Ce ions is observed, however, in a counterintuitive way under the continuous laser irradiation. To understand this behavior, we proposed a charge dynamics model, and developed a novel method to suppress this undesired charge dynamics. With this approach, we obtain the photoluminescence excitation spectrum of single Ce ions in YAG under a CW laser excitation. Narrow ($\sim$ 80 MHz) and spectrally stable optical transitions between the lowest Kramers doublets of the ground and the excited states are observed. In comparison with the large inhomogeneous broadening ($\sim$500 GHz), narrow resonant transitions provide the good selectivity in the spectral domain. Moreover, the single Ce ground spin state presents a spin 1/2 system with anisotropy g factor. It results in the optical selection rules dependent on the directions of the external magnetic field. Under parallel external magnetic field with respect to the quantization axis, only the spin-flip transitions are allowed with high transition contrast. It gives the opportunity to optically initialize the ground spin state of single Ce ions with 97.5% fidelity.

The coherent spin properties of single Ce ions can be investigated, after the successful optical initialization. By scanning the microwave frequency, we obtain the electron spin resonance of single Ce spin transitions. We show the spin state has a coherence time of 290 ns, which is dominated by the surrounding aluminum nuclear spin bath and impurities induced electron spin bath. The coherence time can be extended to 2 ms through dynamical decoupling method, which approaches closely to the upper limit 4.5 ms due to spin-lattice relaxation. This result indicates single Ce electron spin can be a good solid-state qubit.

With the combination of optical and spin manipulations of single Ce ions, a quantum interface between a single spin and a single photon is observed by monitoring the temporal behavior of circularly polarized emission photons from the ion. We obtain the Larmor precession of the excited spin state, indicating the direct mapping of the excited spin states of single Ce ions onto the polarization states of the fluorescence photons. Furthermore, with both optical and spin access, we all-optically demonstrate coherent population trapping of a single Ce spin qubit.

To scale up the system for further applications, we present the nano-scale engineering of

rare earth species in YAG crystal, with the acquirement of the production yield of Ce and Pr implantation (53 and 91% respectively). The optical and spin properties of single implanted Ce ions show fairly good performance, which paves the way towards coherent coupling of single rare earth qubits in a small volume.

Besides the study of single Ce ions, the spectroscopy properties of single praseodymium ions in YAG crystal are investigated. We obtain the photoluminescence excitation spectrum and the hyperfine splitting of a single praseodymium ion. All-optical control of a single praseodymium ion is achieved.

In this dissertation, we solve the key problem of optically detecting, spectrally studying and coherently manipulating single rare earth ions in solids. The developed methods including optical detection, initialization, readout, coherent control and nanoscale production of single rare earth elements in crystals offer novel and powerful tools for understanding and exploring the fundamental spectroscopy properties of single rare earth elements in solids. It paves a way towards constructing scalable quantum network based on single rare earth solid-state qubits.

Zusammenfassung

Die Wechselwirkung von Licht mit Materie auf Ebene einzelner Quantenobjekten ist seit langem eine Herausforderung und zugleich ein Traum vieler Physiker. Seit 1970 ebnete die Entwicklung der Spektroskopie einzelner Ionen und die Möglichkeit einzelnen Photonenzuständen zu untersuchen den Weg für ein neues Zeitalter der Detektion und Manipulation von Quantenobjekten mit elektromagnetischen Feldern auf einzel Ionen-Niveau. Später führte die Erfindung der Einzel-Molekül-Spektroskopie zu einem neuen Ansatz um auch einzelne Quanten-Systeme in Feststoffen zu untersuchen. Neben einer Vielzahl solcher Systeme sind insbesondere Quantenpunkte und die negativ geladenen Stickstoff-Fehlstellen im Diamant interessant, da deren Spinsystem sowohl kohärent manipuliert als auch mit anderen Quantensystemen verschränkt werden kann, was ein breites Spektrum an Möglichkeiten im Bereich der Nanosensorik und des Quantencomputings eröffnet. Solche Quantensysteme gelten als die aussichtsreichsten Kandidaten für die Realisierung von Festkörper Quantenbits und werden intensiv erforscht. Allerdings sind diese Systeme oft in einer komplexen Umgebung eingebunden und können zu einem rapiden Verlust von Spinkohärenz, oder zu einer optischen Instabilität führen. Die Entdeckung eines alternativen Festkörper-Einzelsystems mit ausgeprägten optischen und Spin-Eigenschaften bildet die Motivation dieser Dissertation.

Elemente der Seltenen Erden- dotiert in anorganischen Kristallen zeigen nicht nur hohen Qualitätsfaktor des optischen $4f \leftrightarrow 4f$ Überganges, sondern auch die gut erhaltenen und langlebigen Spinzustände versprechen Anwendungen in der Festkörper Laserspektroskopie zur Quanteninformationsverarbeitung. Doch seit fast drei Jahrzehnten wurden keine einzelnen Elemente der seltenen Erde in Feststoffen mehr detektiert, sodass das Funktionspotential nicht voll untersucht werden konnte.

Die erste direkte optische Detektion einzelner Ionen der seltenen Erden (Praseodym) in Feststoffen wurde von uns im Jahr 2012 gezeigt, was Gegenstand meiner Masterabschlussarbeit war. Diese Dissertation befasst sich mit den experimentellen Fortschritt zur optischen Detektion anderen Elemente der Klasse der seltener Erden in Kristallen, sowie

das Verständnis ihrer fundamentalen Spektroskopie-Eigenschaften und die zugehörige Manipulation deren Spin-Subsystems dar. Dabei liegt der Fokus dieser Arbeit auf die Untersuchung einzelne dreiwertige Ceriumionen in unterschiedlichen Einbettungsmaterialien wie zum Beispiel Yttrium-Aluminium-Granat (YAG). Nach der optischen Detektion einzelner Ceriumionen werden die Spin- und optischen Eigenschaften der Ce-Ionen untersucht.

Einzelne Ce-Ionen zeigen dabei eine gute Photostabilität bei gepulster Laseranregung. Wie in anderen Festkörperemittern wird auch bei einem einzelnen Ce-Ion photoinduzierte Dynamik beobachtet, jedoch entgegen der vorherigen Erwartung unter kontinuierlicher Laserbestrahlung. Um dieses Verhalten zu verstehen, entwickelten wir ein Model für die zugrundeliegende Ladungsdynamik und realisierten ein neues Verfahren zur Unterdrückung unerwünschter Dynamiken. Mit diesem Ansatz sind wir nun in der Lage das Photolumineszenz-Anregungsspektrum eines einzelnen Ce-Ions in YAG unter CW Laseranregung zu untersuchen: Schmalrandige (∼80 MHz) und spektral stabile optische Übergänge zwischen den niedrigsten Kramers Dubletten des Grund- und der Angeregten Zustände werden beobachtet. Im Vergleich zu der großen inhomogenen Verbreiterung (∼500 GHz) bieten schmale Resonanzübergänge eine gute Selektivität im Spektralbereich. Darüber hinaus besitzt der Grundzustand von Ce eine Spin $\frac{1}{2}$ System mit anisotropen g-Faktor. Daraus ergeben sich optische Auswahlregeln abhängig von der Richtung des äußeren Magnetfeldes. Wenn ein externes Magnetfeld parallel zur Quantisierungsachse des Ce-Ions angelegt wird sind nur Spin-flip-Übergänge mit hohem Übergangskontrast erlaubt. Es ergibt sich daraus die Möglichkeit den Spin Zustand eines einzelnen Ce-Ions optisch mit einer Güte von 97,5% zu initialisieren.

Die kohärenten Spineigenschaften einzelner Ce-Ionen werden nach einer erfolgreichen optischen Initialisierung untersucht. Durch variieren der Mikrowellenfrequenz wird die Elektronen Spin-Resonanz einzelner Ce-Spinübergänge identifiziert. Wir zeigen, dass der Spinzustand eine Kohärenzzeit von 209 ns besitzt, die durch die umliegenden Aluminiumkerne und von Verunreinigungen induziertem Spin-Bad dominiert wird. Unter Verwendung von Entkopplungssequenzen konnte die Kohärenzzeit auf 2 ms verlängert werden. Diese ist nahe der durch andere Spin-Gitter-Relaxationen vorgegebenen Obergrenze von 4,5 ms. Dieses Resultat zeigt, dass einzelne Ce-Eletronenspins ein gute Solid-State-Qubits darstellen.

Durch die Kombination von optischer und Spin-Manipulation einzelner Ce-Ionen ergibt sich eine Quantenschnittstelle zwischen einem einzelnen Spin und einzelnen Photon.

Abhängig vom Spin Zustand emittiert ein Ce-Ion entweder rechts oder links zirkular polarisierte Photonen. Darüber hinaus demonstrieren wir mit einem rein optischen Spinzugang gänzlich die kohärente Population Trapping eines einzelnen Ce-Spin Qubits.

Um das System für weitere Anwendungen zu skalieren, präsentieren wir das Engineering von seltenen Erdspezies im YAG-Kristall mit der Gewinnung der Produktionsausbeute von Ce- uns Pr-Implantationen (53% bzw. 91%). Die optischen und Spineigenschaften von einzelnen implantierten Ce-Ionen weisen recht gute Leistung auf, die den Weg zur kohärenten Kopplung von einzelnen seltenen Qubits in einem kleinen Volumen ebnen.

Neben der Studie von einzelnen Ce-Ionen werden die spektrosopischen Eigenschaften einzelner Praseodymionen im YAG-Kristall untersucht. Wir erhalten das Photolumineszenz-Anregungsspektrum und die Hyperfeinaufspaltung eines einzelnen Praseodymions. Eine ganzheitliche optische Steuerung eines einzelnen Praseodymion wird erreicht.

In dieser Dissertation lösen wir das Schlüsselproblem der optischen Detektion, bestimmen die spektralen Eigenschaften und zeigen kohärente Manipulation von einzelnen seltenen Erden in Festkörpern. Die entwickelten Methoden einschließlich der optischen Detektion, der Initialisierung, des Auslesens, der kohärenten Kontrolle und der Produktion einzelner Elemente der seltenen Erden in Kristallen auf Nanoebenen bieten neuartige und leistungsfähige Werkzeuge für das Verständnis und die Erforschung von grundlegenden spektroskopischen Eigenschaften von einzelnen seltenen Erdelementen in Feststoffen. Sie ebnen den Weg in Richtung eines skalierbaren Quantennetzwerkes, welches auf einzelnen Seltenerden-Qubits in Festkörpern basiert.

Contents

Chapter 1

Introduction

The observation and manipulation of quantum objects at single particle level is a long-felt challenge and aspiration for physicists since it reveals light-matter interaction in a most fundamental and microscopic point of view. It also opens a door to a new era of exploring novel physics phenomena such as quantum electrodynamics with extreme precision, single ion spectroscopy and the investigation of quantum mechanics at the most fundamental level. In 1977, Jeff Kimble and coworkers observed the photon antibunching behavior in diluted sodium atoms [1]. It indicates the detection at single photon level, which is regarded as the building block of modern quantum optics [2–4]. In 1980, Toschek's group reported the first observation of single Ba^+ ions in a Paul trap [5, 6]. The isolation, detection, and manipulation of single ions give a new platform for observing and coherently controlling individual quantum objects without destroying their quantum nature [7].

Instead of using restricted and sophisticated trapping systems like in cold atoms and trapped ions, the exploration of light interaction with stable single quantum objects in condensed matter is more desired by physicists. William Moerner and Michel Orrit, first demonstrated the detection of single pentacene molecules in a *p*-terphenyl crystal [8, 9]. The development of single molecular spectroscopy offers a novel and powerful tool for studying and exploring new physical effects [10].

The discovery and exploration of different types of single photon emitters embedded in solids attracted the curiosity and interests from a wide range of scientists. Single dye molecules [11–14], quantum dots [15–17] and point defects in crystals [18–23] have been investigated, while their quantum properties are explored for many applications from quantum physics [24–26], to super-resolution microscopy [27–33]. Among solid-state single emitters, atomic-like quantum dots present fascinating optical properties [15, 34–36] and negatively charged nitrogen-vacancy (NV) centers in diamond display great coherence properties [37–40] which provoke considerable attentions. Their individual spins can be coherently manipulated, measured and entangled by electromagnetic fields [41–46]. They are intensively studied as one of the most promising candidates for the realization of quantum bits [47–52]. However, these systems coupled to a complex environment which often results in rapid loss of spin coherence or optical instability [53–58]. Finding other species detectable at single-quantum-object level with distinct spin and optical properties

would attract broad interests in academia. It would also unleash new applications based on quantum effects and result in deeper insights into fundamentals of physics. Rare earth ions doped crystals showing distinguished optical and spin properties are potential candidates for this purpose.

One of the remarkable features of rare earth elements doped into crystals is that the unpaired electron in the $4f$ level is efficiently screened by the filled $5s$ and $5p$ states [59], resulting in sufficient decoupling from the local electrical noise [60]. It yields long coherence times of both optical and spin transitions [61–63]. The shielded $4f$ states show robustness against environmental fluctuations, and therefore present negligible spectral jump and diffusion. The $4f \leftrightarrow 4f$ transitions display high-quality factors with narrow resonant linewidths [64–66]. The exploration of rare earth doped crystals led to many applications in optics such as solid-state laser spectroscopy [67–69], electric field sensing [70], biological label [71, 72], and super-resolution microscopy [73, 74]. In addition, rare earth doped crystals are one of ideal hosts for solid-state quantum information processing [61, 62]. Examples include the quantum storage of the single photon state in Nd^{3+}:YVO_4 [75], preservation of entanglement after photon storage and readout in Nd^{3+}:Y_2SiO_5 [76], storage of quantum information in Pr^{3+}:Y_2SiO_5 [77–80], *etc.* Last year six hours coherence time of Eu^{3+}:YSO nuclear spin transition has been demonstrated [63]. Ideas of constructing scalable quantum computer based on rare earth qubits have been proposed [81, 82].

All the applications mentioned above were performed with ensembles of rare earth elements. With the detection of single rare earth ions, however, exploiting their full potential in the field of solid-state quantum optics can be attempted. Not only the macroscopic picture, but also the microscopic picture of rare earth ions can be acquired and studied. The detection of single rare earth ions provides a new and novel approach for investigating the fundamental spectroscopic properties of solid-state rare earth dopants. In addition, their long-lived spin states can be explored as single qubits, which could be the building block for constructing universal quantum computers based on single rare earth solid-state qubits. However, the detection and manipulation of single rare earth color centers at single-ion level are remaining challenging. In 2012, our group reported the first solid proof of single rare earth ion detection [83]. Followed by this pioneering work, this dissertation is mainly focused on the spectroscopy of single rare earth solid-state qubits. It is organized in the following way:

In Chapter II, a comprehensive overview of detecting single rare earth ions in solids is given. Since this dissertation is mainly focused on single praseodymium and cerium ions in crystals, the basic physical and optical properties of trivalent praseodymium and cerium doped crystal are introduced.

Chapter III presents the optical detection of single trivalent cerium ions in ultra-pure YAG bulk crystal under ambient conditions. The single Ce emitters are detected and confirmed by the second order correlation measurements, emission spectrum and excited states lifetime. We show that the excited spin state of single Ce:YAG can be optically initialized due to the special optical selection rule. With the observation of the Larmor precession of single Ce excited state spin transitions, we also obtain the coherent

properties of excited state spin transition in single Ce doped YAG crystal.

In Chapter IV, the ground spin states of single Ce in both YAG and LuAG crystal are optically initialized and readout with high fidelity. The coherent properties of single Ce ground spin states are investigated. Furthermore, with dynamic decoupling technique, the decoherence time of single Ce:YAG spin transition is extended to 2 ms. We also acquire the noise spectrum of single Ce electron spins. The results in this chapter offer a new opportunity of exploring single Ce spin qubits for quantum devices.

Chapter V gives the counterintuitive charge state dynamics of single Ce ions under CW laser excitation. A method is developed to suppress the CW laser induced photo-ionization, which removes the obstacle of addressing single Ce spin states all-optically. A proposed model is raised to understand this underlying progress.

In Chapter VI, high resolution spectroscopy of single Ce ions in YAG is performed. The optical transitions between the ground and excited states show narrow and spectrally stable lines. By using these optical transitions, all-optical preparation of coherent dark states in single Ce electron spin sublevels has been demonstrated. It is an essential step towards all-optical control of single rare earth qubits.

Chapter VII shows the optical detection and resonant excitation of single trivalent praseodymium ions in bulk YAG crystal in cryogenic temperature. The optical transitions of single Pr ions present stable and narrow lines. The ground state hyperfine splitting of a single Pr ion has been resolved. We also demonstrate the coherent driving of a single Pr ion all-optically.

Chapter VIII presents the nano-scale engineering of rare earth species in YAG crystal by means of ion implantation. The production yields of Pr^{3+} and Ce^{3+} are estimated to be 91% and 53%. The optical and spin properties of single implanted Ce ions have been investigated showing fairly good performance, which paves the way towards coherent coupling of single rare earth qubits in a small volume.

Chapter IX introduces the outlook of this dissertation, with the preliminary results of reading out single Pr nuclear spin state by coupled single Ce ions. We also show the evidence of resolving individual trivalent Ce ions in low-spin bath X2-Y_2SiO_5 crystal. At the end, cavity quantum electrodynamics in single rare earth ions has been proposed, which is an essential step towards constructing scalable quantum network based on rare earth solid-state qubits.

Chapter 2

General background

Rare earths are elements of the Lanthanide series. As dopants in solids, they have captured the attention of scientists for more than half a century, since their parity forbidden $4f \leftrightarrow 4f$ transitions give rise to narrow transition linewidths with high quality factors [61]. Meanwhile their partially filled $4f$ electrons are efficiently screened by the filled $5s$ and $5p$ orbitals [59] (see Fig. 2.1) where the $5s$ and $5p$ shells are acting as a Faraday cage and protect the inner $4f$ states from local environmental perturbations. This is the reason why unpaired $4f$ electrons of rare-earth impurities present weak coupling to surroundings, which results in well preserved optical and spin transitions [60, 84]. Owing to these fascinating properties, rare earth color centers embedded in solid state hosts have been widely investigated , with applications ranging from laser spectroscopy [67–69], biotechnological sensing [71, 72] to quantum information processing [62, 75, 78, 85]. Detection of single rare earth ions in solids will offer a microscopic method to study the rare earth ions and enrich more potential. It especially opens a new way of studying and exploring single rare earth ions as single solid-state qubits.

In this chapter, a comprehensive overview of solid-state based single rare earth ion detection will be introduced. Two different approaches to resolve single ions in solids are given. Since this dissertation is mainly focused on single praseodymium and cerium ions in crystals, the basic physical and optical properties of trivalent Pr and Ce ions doped in YAG crystal are presented. Meanwhile, the optical properties of Ce doped LuAG and YSO crystal are also introduced.

2.1 Detection of single rare earth ions in solids

Optical detection of single rare earth ions in solids is an arduous challenge in the field. In 1988, R. Lange *et. al.*, claimed for the first time the observation of single Sm^{2+} ions in CaF_2 crystal [86], however, the presented data could not proof the detection of impurities at single-ion level. Followed by this work, a couple of groups reported the indirect and non-persuasive evidence of finding single rare earth ions in solids in the last two decades [87–89]. None of the methods are suitable for detecting and exploring single rare earth ions as single qubits. So far, single rare earth ions in solids can be detected by two distinct approaches,

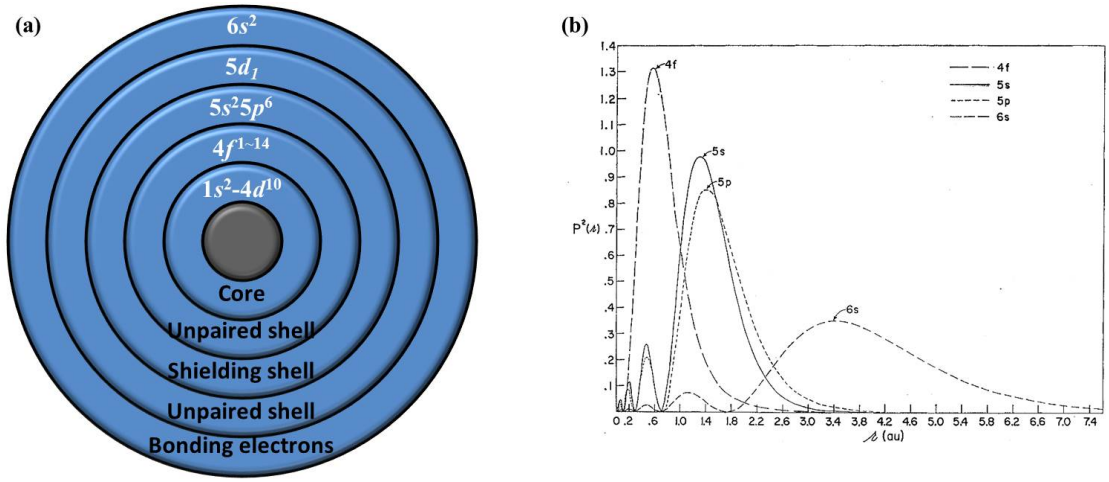

Figure 2.1: (a) Electronic ground state of rare earth ions. (b) A theoretical calculation of the radial distribution of the orbitals of Gd ions. The $4f$ electron state is screened by $5s$ and $5p$ levels. The figure is reproduced from [59].

namely optical microscopy approach and single electron transistor (SET) approach.

2.1.1 Resolving single rare earth ions under optical microscopy

Optical spectroscopy of single molecules in condensed phase usually suffers from low fluorescence yield. High excitation laser intensity, high collection efficiency and high signal-to-noise ratio are essential requirements to measure the weak fluorescence from the single photon emitters. Laser scanning optical microscopy can provide high laser intensity with high sensitivity which satisfies all demands. It also offers exceptional resolution in both spatial and spectral domain. Laser scanning optical microscopy is developed as one of the standard tools to detect and manipulate single quantum objects in solids [9, 18].

In the past decades, people are keen on studying and exploring the $4f \leftrightarrow 4f$ transitions for single rare earth ions detection, since these transitions present high quality factor. However, the $4f \leftrightarrow 4f$ transitions are parity forbidden transitions [65], and hence have rather weak oscillator strength. Moreover, the optical lifetime of the excited states is usually in the time scale from microseconds to milliseconds [90]. These parity forbidden transitions yield low excitation-emission-reexcitation cycling efficiency. Normally, the cycling efficiency is within 100$\sim$100,000 Hz. If the collection and detection efficiency of the optical microscope further is considered, typically low efficiencies unavoidably prevent single rare-earth ions in solid state hosts to be detected.

This intrinsic brightness obstacle of weak fluorescing rare earth ions can be overcome by promoting the $4f^n$ electrons onto the higher lying $4f^{n-1}5d$ states. The parity allowed $4f^{n-1}5d \rightarrow 4f^n$ transitions present strong oscillator strength [91]. The lifetime of the $4f^{n-1}5d$ excited states is much shorter (10-100 ns range). Thus a couple of orders stronger emitted photon flux can in principle be obtained. It offers the possibility to identify rare earth ions at single-ion level with optical microscopy.

Based on this perspective, in 2012 for the first time, we directly detected single rare earth ions in solids, namely a single trivalent praseodymium ion in a YAG crystal [83].

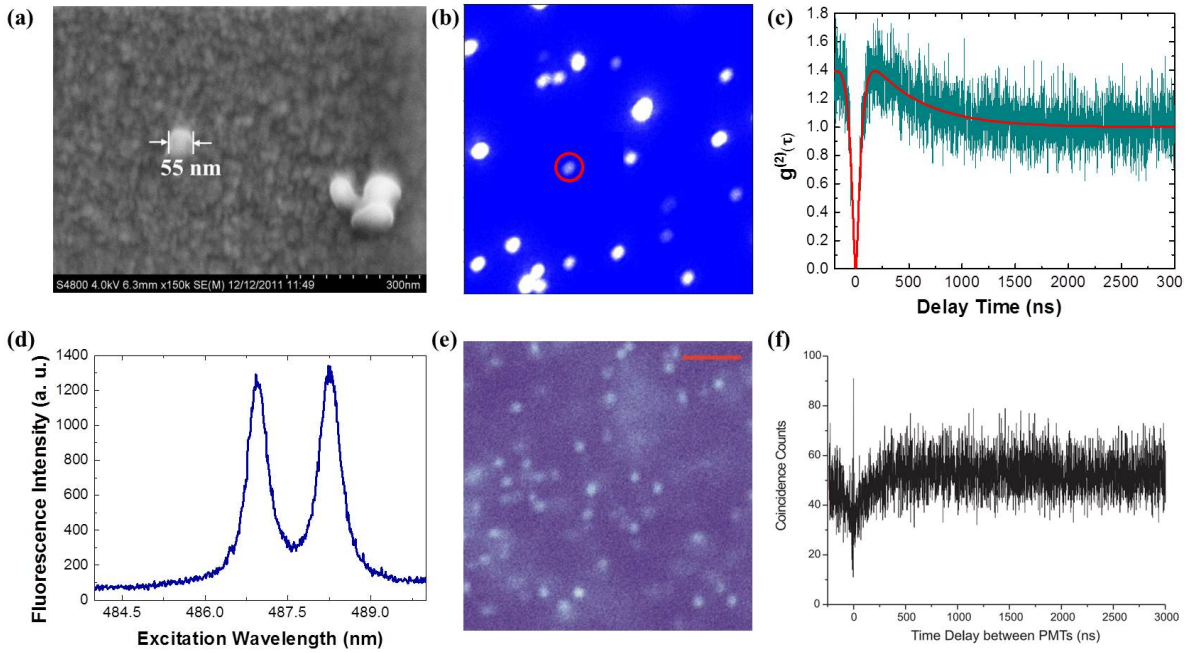

Figure 2.2: Optical detection of a single Pr ion in YAG crystals. (a) SEM image of an individual 2 ppm concentration Pr:YAG nanoparticle. (b) Upconversion fluorescence scanning image of Pr:YAG nanoparticles. (c) The second order correlation function measurement of a single Pr:YAG nanoparticle, marked with a circle in (b), presenting photon-antibunching behavior. (d) The excitation spectrum of a single Pr:YAG nanoparticle. (e) Upconversion fluorescence scanning image of an ultra-pure YAG crystal, displaying individual bright spots. (f) The second order correlation function measurement of an individual Pr ion in YAG crystal, showing photon-antibunching behavior.

In the experiment, the $4f^2 \rightarrow 4f5d$ transition of Pr:YAG was accomplished by excited state absorption, where Pr ions were excited through $^3\mathrm{H}_4$ $(4f) \rightarrow^3 \mathrm{P}_0$ $(4f) \rightarrow 4f5d$ states [92]. Due to 18 ns optical lifetime of the $4f5d$ state [93], this upconversion process hence results in at least 400 times stronger photon flux in comparison with $^3\mathrm{P}_0$ $(4f) \rightarrow^3 \mathrm{H}_4$ $(4f)$ transitions. With this enhancement, we found a nanoparticle showing photon anti-bunching behavior, marked with a red circle as shown in Fig. 2.2(b). The second order correlation function measurement (Fig. 2.2(c)) and excitation spectrum (Fig. 2.2(d)) [94] of the nanoparticle provide the unambiguous confirmation that the marked spot is a single praseodymium ion in a YAG nanoparticle. Furthermore,in one of the ultra-pure YAG crystal (the purest YAG crystal we found so far), single Pr ions can be optically resolved (see Fig. 2.2(e)). The second order correlation function measurement (Fig. 2.2(f)) proofed that the individual spots correspond to single Pr ions in YAG bulk crystal. The detection of single rare earth ions in solids provides the opportunity of exploring single Pr ions as a building block for quantum computers [95].

Two years later, V. Sandoghdar's group from Max Planck Institute for the Science of Light and Matsushita's group from Tokyo Institute of Technology resolved individual praseodymium ions in the spectral domain by single molecular microscopy technique [74, 96]. Sandoghdar's group introduced the combination of a solid-immersion lens

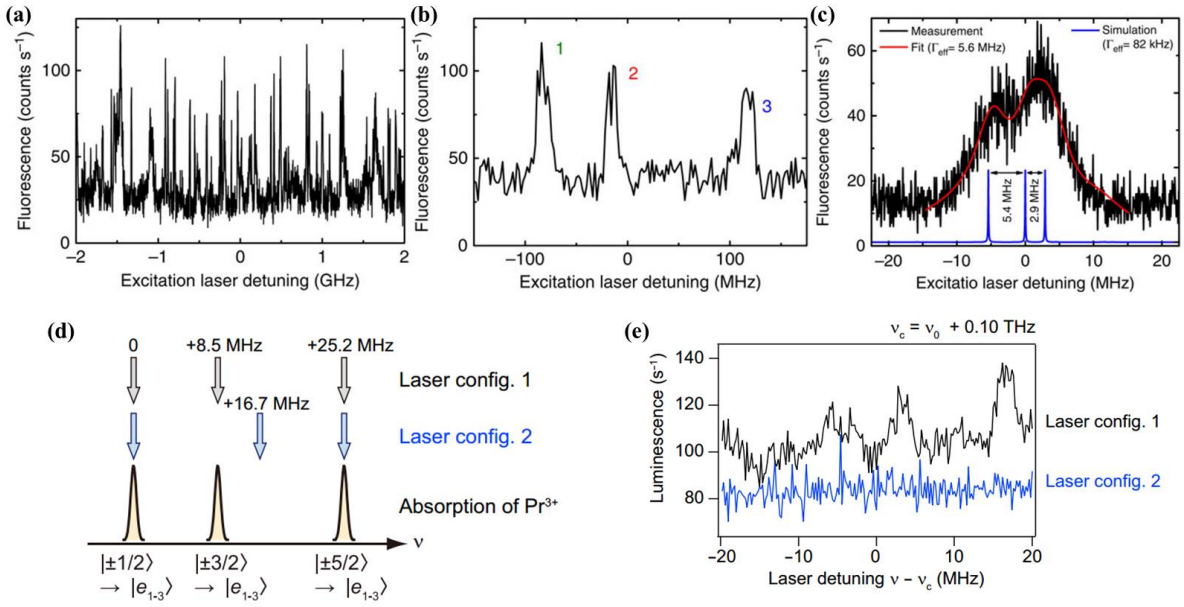

Figure 2.3: Detection of single praseodymium ions by single molecular spectroscopy. (a)-(c) PLE spectrum of praseodymium ions in an YSO nanoparticle. (d)-(e) PLE spectrum of single praseodymium ions in LaF_3 crystal. Figures are reproduced from [74] [96].

with nanoparticles to enhance the collection efficiency of the optical microscopy. While Matsushita's group utilized the high collection efficiency reflecting objective. Both groups took advantage of high spectral selectivity due to the narrow linewidth $4f \rightarrow 4f$ transitions of Pr ions in crystals (see Fig. 2.3). At cryogenic temperature, with the help of narrow linewidth laser, single praseodymium ions were identified in the frequency domain. However, even with the help of modern optical technology, the $4f \rightarrow 4f$ transitions result in extremely weak fluorescence yield with only 100 Hz count rate and low signal-to-noise ratio, which blocks the further applications, like exploring individual rare earth ions as single rare earth qubits.

2.1.2 Resolving single rare earth ions by SETs

Single electron transistor (SET) as an electronic device, is able to monitor electron tunneling by an amplified current, which has a sensitivity on the single electron level [97]. It was invented for more than two decades ago. Recently, SETs are applied to readout charge dynamics of single quantum objects in solids [98–100]. It offers a way to electronically drive and readout single electron spins. SETs can be used to detect the photo-ionization of a single rare earth ion in solids.

In 2013, S. Rogge's group from University of New South Wales reported the detection of single Er^{3+} in silicon by a SET [101]. It is the second species of rare earth ions resolved at single-ion level. In the experiment, a SET is fabricated on an Er doped Si crystal (see Fig. 2.4(a)). When an individual Er ion is excited, it has a chance to be photo-ionized. In this case, the Er ion losses an electron. It results in the transient shift of the current and gate voltage in the single electron transistor (Fig. 2.4(b) - (d)). The excitation spectrum of a single Er ion is also obtained (Fig. 2.4(e)), presenting 50 neV full

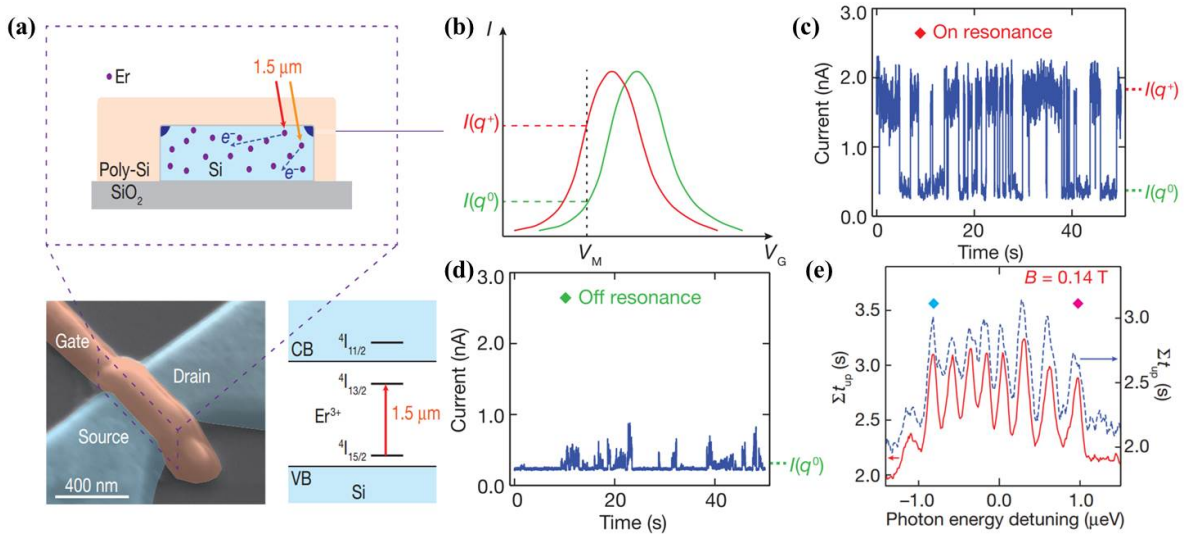

Figure 2.4: Detection of an individual erbium ion in silicon. (a) A single electron transistor fabricated on top of the Er doped Si. (b) The charge sensing scheme. When an individual Er ion is excited, it has a chance to be photo-ionized. The Er ion losses an electron. It results in the transient shift of the current with gate voltage. (c) The current-time trace when the Er is excited. (d) The current-time trace when the Er is excited. (f) The excitation spectrum of an individual Er ion in Si, presenting 50 neV FWHM. Figures are reproduced from [101].

width at half maximum (FWHM). However, this technique is based on a single electron transistor which readout the photo-ionized individual Er ions electrically. A SET has to be implanted in small band gap host, for example, Si based SET has only 1.1 eV band gap, which is not suitable to implant other species of rare earth impurities at single-ion level. On the other hand, the SET requires complex fabrication method, with manufacture at nanoscale. It is technically challenging to integrate several SETs in a small volume.

Another approach of single rare earth ion detection has been proposed. If a single rare earth ion is coupled to a high finesse photonic cavities, the optical lifetime of the excited state will be shortened due to the Purcell effect [63]. The excitation-emission-reexcitation cycling efficiency will be enhanced by the optical cavity, which make the detection of single rare earth ions possible. It has also the potential of demonstrating cavity quantum electrodynamics effect including the interfacing of single rare earth ions with single photons. However, the observation of cavity coupled single rare earth ion has not yet been demonstrated.

In comparison with different techniques of single rare earth ion detection, utilizing the parity allowed $4f^n \rightarrow 4f^{n-1}5d$ transitions result in the high fluorescence yield with high signal-to-noise ratio, which is the major technique used passive instead of active in this dissertation to detect, coherently manipulate and readout single rare earth ions.

2.2 Potential candidates on the single ion detection

One fundamental question is raised from the previous section whether it is possible to optically detect and coherently address the other species of rare earth impurities at single-ion level.

There exist 17 elements in lanthanide series. They are marked with red squares in the chemistry table (Fig. 2.5). More than 290 types of rare earth doped laser glasses have been synthesized so far, for example, Y_2SiO_5, $LiYF_4$, LiF_3, CaF_2 and NYF_4, etc. Finding suitable rare earth species doped in certain laser glasses is essential to detect single rare earth ions in solids. Towards the optical detection of single rare earth ions in solids through the $4f^n \leftrightarrow 4f^{n-1}5d$ transitions, several fundamental and technological requirements are raised:

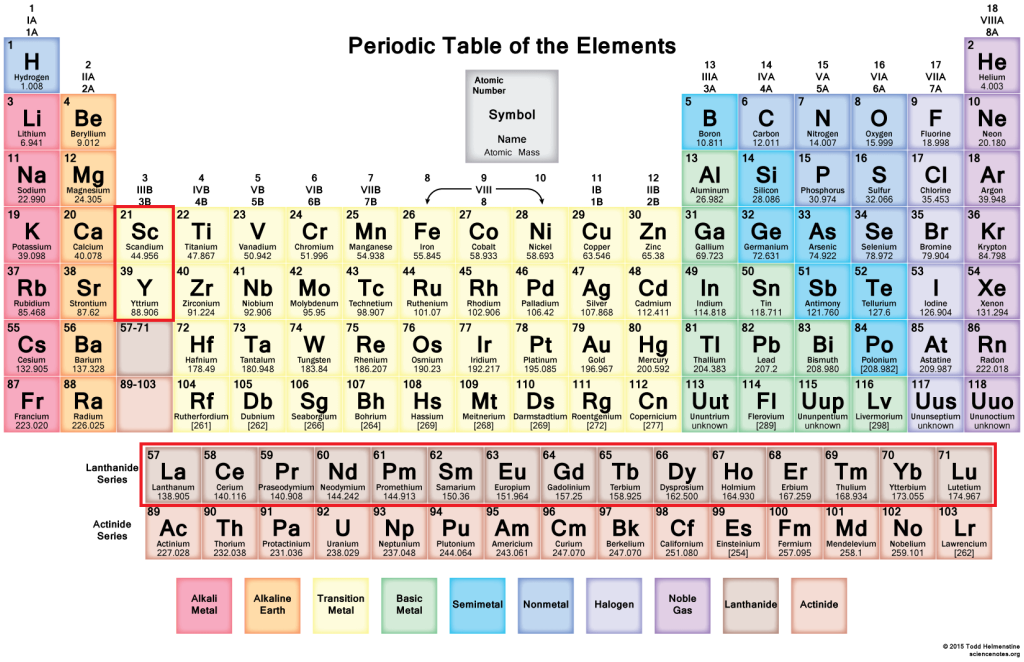

Figure 2.5: Element table, with rare earth elements marked with red squares.

1. Optical properties of the emitters. For most of rare earth elements the high efficiency $4f^n \rightarrow 4f^{n-1}5d$ transitions normally occur in the UV range [102]. However, with the current technology, the performance of the optical microscopy in UV range is unsatisfied. Especially if the wavelength is shorter than 350 nm, the transmission efficiency of the optics, the achromaticity of the UV objective lens, and the detection efficiency of the single photon detectors are dreadful. In addition, UV laser is uncommon and difficult to efficiently operate. While optical microscopy operating in the visible spectral range is a mature technology . It displays much better performance in terms of optical transition, and detection efficiency. Most solid-state based single photon emitters have been detected in the visible spectral range [14, 16]. Finding the rare earth doped solids which their $4f^n \rightarrow 4f^{n-1}5d$ transitions are in NUV and visible range, is critical in this approach.

2. The quality of the crystal. Individual impurities can be optically resolved in either spatial or frequency domain. Normally single emitters embedded in condensed matter phases suffer with spectral jumps and diffusions [58, 103, 104], which broaden the transition linewidths and spoil the spectral properties of single ions. Thus resolving single rare earth ions in the frequency domain is not a favorable approach in this dissertation. Here we prefer to resolve single rare earth ions in the septal domain. It indicates the optical detection of one and only one single ion in the focus volume, which requires a high demand of the number of impurities of the crystal. Ultra-pure laser glasses are desired to have very few number of ions in the detection volume. Meanwhile, as one of the ideal host material, the crystal should also provide big energy band gap, high thermal conductivity and preferably small electron and nuclear spin baths.

Among almost 300 types of laser glasses, yttrium aluminum garnet (YAG) and lutetium aluminum garnet (LuAG) crystals attract the interests due to the following reasons. These two crystals provide a biggest red shift in the emission spectrum among all the laser glasses. For example, the $4f5d \leftrightarrow 4f^2$ transitions of Pr:YAG is located at 300∼450 nm which can be detected by single photon detectors. The same transitions of Pr:$YAlO_3$ is in the range of 200∼320 nm, which is difficult to measure by single photon detectors. In addition, both crystals can be purified, indicating the possibility to provide ultra-pure host material with low impurities in the crystals.

Within all 17 lanthanide elements embedded in YAG or (LuAG), trivalent praseodymium and cerium doped YAG (or LuAG) fit our purpose, since their $4f^n \rightarrow 4f^{n-1}5d$ transitions are located near UV or even in the visible range with short optical lifetime and high quantum efficiency, indicating high fluorescence yield. In spite of detecting single praseodymium ions in YAG, optical detection and coherent manipulation of single trivalent cerium ions in YAG and LuAG particular attracts our attention.

2.2.1 Rare earth doped YAG crystal

As it is introduced among all the laser crystals, YAG is one of the most favorable crystals for us, it produces the biggest spectral shift in the red range from the embedded emitters. YAG crystal presents several impressive chemical, mechanical and optical properties, such as compound stability, mechanical robustness, and most importantly, optical isotropy and transparency throughout a huge spectral range 200∼4,000 nm due to 6.2 eV band gap [105, 106].

Material	Formula	Mohs scale	Refractive index	Thermal conductivity ($W \cdot m^{-1} \cdot K^{-1}$)	Density ($\times 10^3 kg/m^3$)
YAG	$Y_3Al_5O_{12}$	8.5	1.83 (@ 633 nm)	14	4.55
LuAG	$Lu_3Al_5O_{12}$	8.4	1.84 (@ 633 nm)	8.3	6.71
YSO	Y_2SiO_5	5.6	1.78 (@ 633 nm)	4.5	4.44

Table 2.1: Physical properties of YAG, LuAG and YSO crystals [107].

The physical properties of YAG crystal is shown in Tab. 2.1. The lattice structure of the YAG is drawn in Fig. 2.6, where the cubic lattice structure of YAG crystal has 12.01 Å

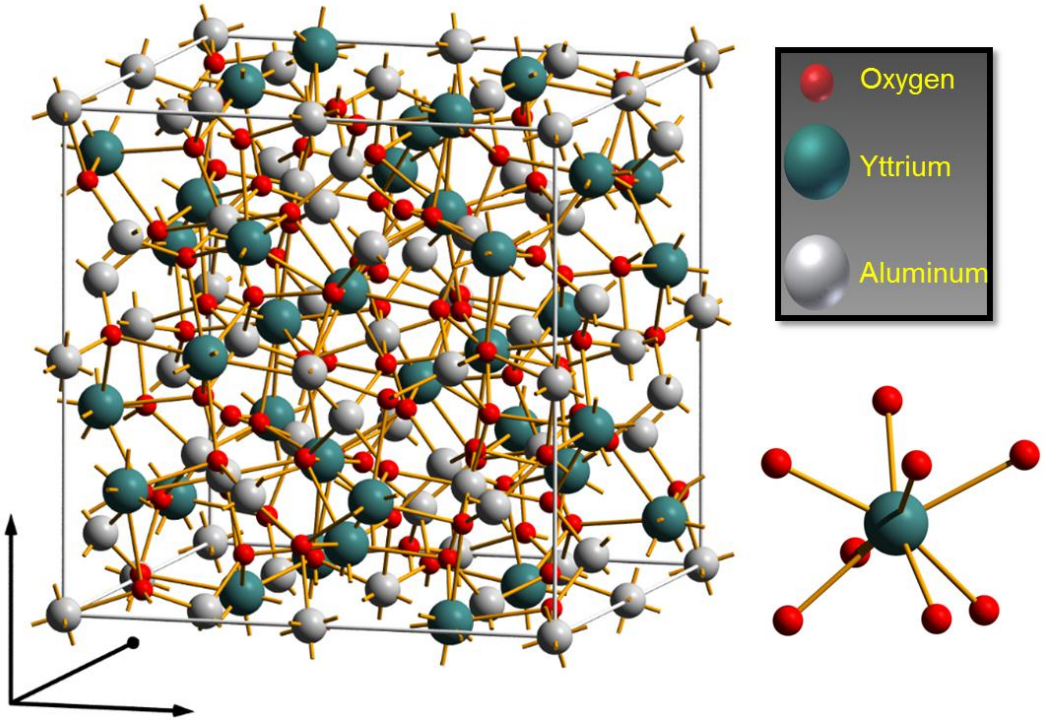

Figure 2.6: Lattice structure of the yttrium aluminum garnet crystal, where yttrium ions, oxygen ions, and aluminum ions correspond to green, red and white spheres respectively.

lattice parameter [108]. Eight formula units are contained in one cubic unit cell, indicating a total number of 160 ions [105]. In YAG crystal, each trivalent yttrium ions is surrounded by eight oxygen ions, presenting a dodecahedron with D_2 point symmetry [109]. The size of the trivalent yttrium ions is ∼102 pm, while the size of trivalent praseodymium and cerium ions is 113 pm and 114 pm, respectively. It implies that yttrium ions can easily be substituted by praseodymium or cerium ions upon doping of YAG crystal. Furthermore, the isotopes and nuclear spin properties of each element in YAG crystal have been introduced in Tab. 2.2. YAG has a strong nuclear spin bath, which is mainly contributed by the aluminum ions. Each of the ^{27}Al ions contains nuclear spin 5/2 with magnetic moment 3.64 μ_N.

Isotope	Mass	Natural abundance (%)	Nuclear spin (I)	Magnetic moment (μ/μ_N)
^{89}Y	89	100	1/2	-0.14
^{27}Al	27	100	5/2	3.6
^{16}O	16	99.8	0	0
^{28}Si	28	92.2	0	0
^{29}Si	29	4.7	1/2	-0.56
^{175}Lu	175	97.4	7/2	2.2
^{176}Lu	176	2.6	7	3.2
^{140}Ce	140	88.4	0	0
^{141}Pr	141	100	5/2	4.1

Table 2.2: Isotope data of YAG, LuAG and YSO crystal and Pr and Ce ions. Data is acquired from [110].

Pr doped YAG crystal

A frozen-gas model can be applied to describe the rare earth ions in solids, where the ions are treated as individual and free ions within additional crystal field perturbation introduced by the host material [111]. When trivalent praseodymium ions are doped in YAG crystal, the $4f^2$ energy levels are split by the total Hamiltonian as shown in Fig. 2.7, where H_{Pr} is given as [112]:

$$H_{Pr} = H_0 + H_C + H_{SO} + H_{CF} + H_{HF}, \tag{2.1}$$

where H_0 is the central Coulomb potential of the core of praseodymium ion, H_C corresponds to the Coulomb interaction between two unpaired electrons in $4f$ states, H_{SO} yields the spin-orbit coupling. In addition, unlike free atoms, as soon as rare earth color centers are doped into a solid state matrix, they are surrounded by charged neighbors providing a static electric field, which is named crystal field (represented by H_{CF}). On top of it, praseodymium ions contain nuclear spins 5/2 with the additional hyperfine interaction Hamiltonian H_{HF} [113].

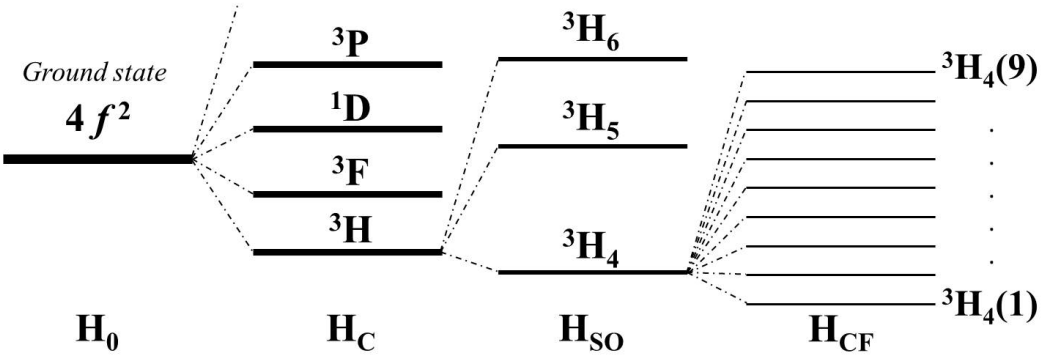

Figure 2.7: Energy levels of Pr:YAG.

The interaction Hamiltonian splits the $4f^2$ states into 96 sublevels. The optical transitions in between the $4f^2$ states are parity forbidden transitions indicating weak oscillator strength with long optical lifetime [92]. For example, the $^3\mathrm{H}_4 \leftrightarrow ^1\mathrm{D}_2$ transition is located at 609 nm. The lifetime of $^1\mathrm{D}_2$ state is 200 μs [114]. The $^3\mathrm{H}_4 \leftrightarrow ^3\mathrm{P}_0$ transition is located at 488 nm with the optical lifetime of 8 μs. In comparison with the long lived $4f^2$ states, the $4f5d$ states have an optical lifetime of 18 ns [92]. Furthermore, the parity allowed $4f^2 \leftrightarrow 4f5d$ transitions present strong oscillator strength with quantum efficiency close to unity [115]. The absorption spectrum of the $4f^2 \leftrightarrow 4f5d$ transition of Pr:YAG is plotted in Fig. 2.8(b) [116], showing 180∼320 nm spectral range. However, it is not a simple task to excite Pr:YAG through $^3\mathrm{H}_4 \rightarrow 4f5d$ transitions with single-step excitation, since the UV laser is not available in the lab. Meanwhile, such high pumping photon energy generates enormous downconverted fluorescence from the chemical contaminants which reduce the contrast.

On the other hand, the $^3\mathrm{H}_4 \rightarrow 4f5d$ transitions can be achieved by using excitation lasers in visible light range only, which is known as excited state absorption (ESA) process of Pr:YAG. Praseodymium ions can be pumped to the first excited state through $4f \rightarrow 4f$ transitions, for example $^3\mathrm{H}_4 \rightarrow ^3\mathrm{P}_0$ or $^3\mathrm{H}_4 \rightarrow ^1\mathrm{D}_2$ transitions by 488 nm or 609 nm laser

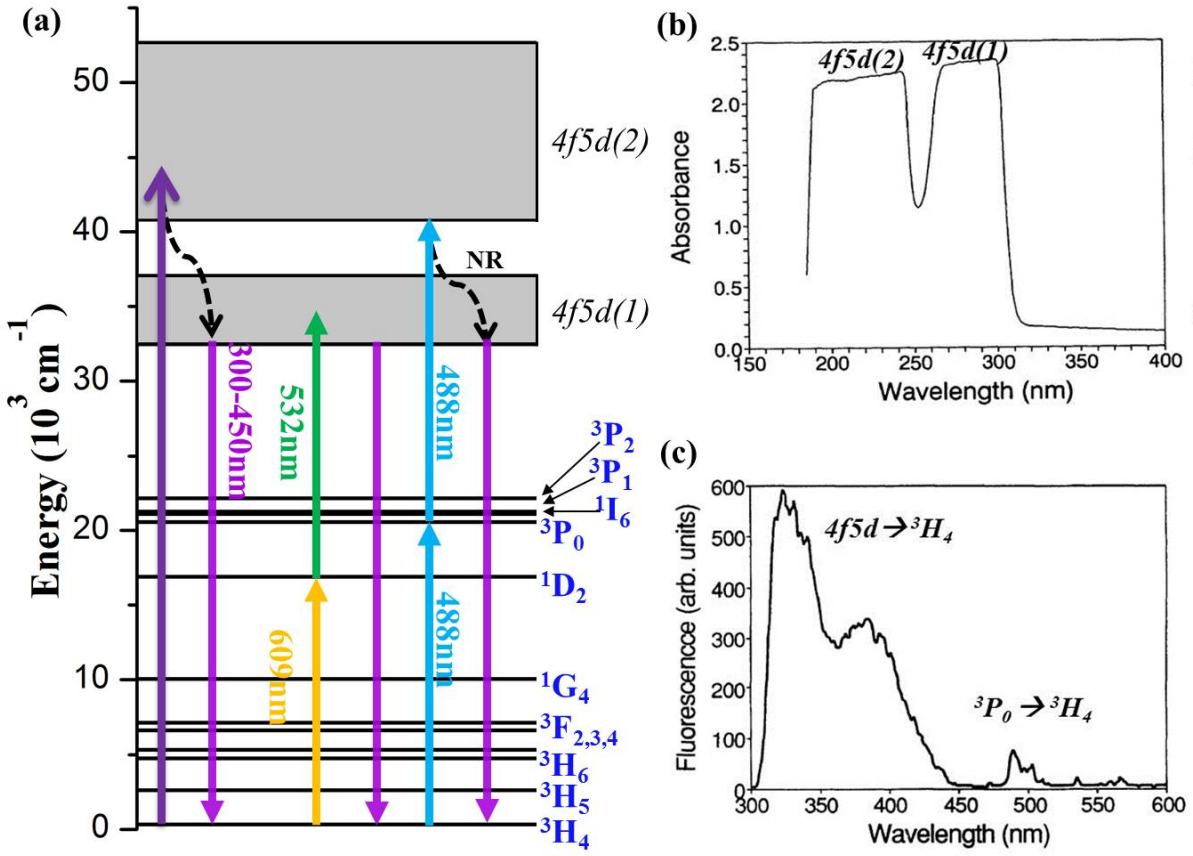

Figure 2.8: (a) Optical transitions of Pr:YAG. NR indicates the non-radiative decay channels. (b) The absorbance spectrum of $4f^2 \rightarrow 4f5d$ transition of Pr:YAG. (c) The emission spectrum of Pr:YAG. Figures are reproduced from [116].

respectively. During the time Pr ions stay in the long lived first excited state, by absorbing an additional photon wavelength at 488 nm or 532 nm, they can be simply promoted to the higher lying second excited state $4f5d$ states (see Fig. 2.8(a)). The emission from the $4f5d$ states is in the wavelength range of 300∼450 nm as shown in Fig. 2.8(c) [116]. Since the upconverted emission photons have higher photon energy compared to the excitation photons, the scattering light and downconverted fluorescence from the background can be filtered out efficiently by picking up right filters, resulting in extreme high signal-to-noise ratio [73].

This upconversion microscopy technique is applied in this dissertation, to demonstrate the coherent manipulation of single praseodymium nuclear spins in YAG crystal, which will be presented in Chapter 7. In addition, the details of upconversion microscopy is described in the Appendix.

Ce doped YAG crystal

Trivalent cerium ions doped in YAG is the second species of rare earth ions, which shows the possibility to be detected at single-ion level. Unlike the Pr doped YAG, when the cerium ion embedded in the YAG crystal, it has only one unpaired electron without

any nuclear spins. The Coulomb interaction between unpaired electrons term H_c and hyperfine interaction H_{HF} is excluded in the total Hamiltonian H_{Ce}, which is described as following [117, 118]:

$$H_{Ce} = H_0 + H_{SO} + H_{CF} + H_B, \tag{2.2}$$

there is an additional term H_B represents the Zeeman interaction between the Ce:YAG ion with the external magnetic field.

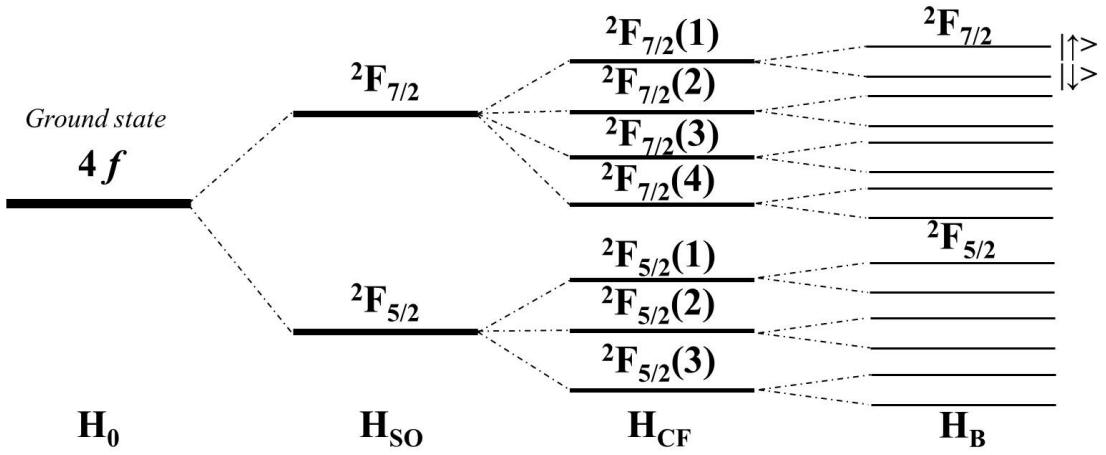

Figure 2.9: Energy level of the ground $4f$ states of Ce:YAG.

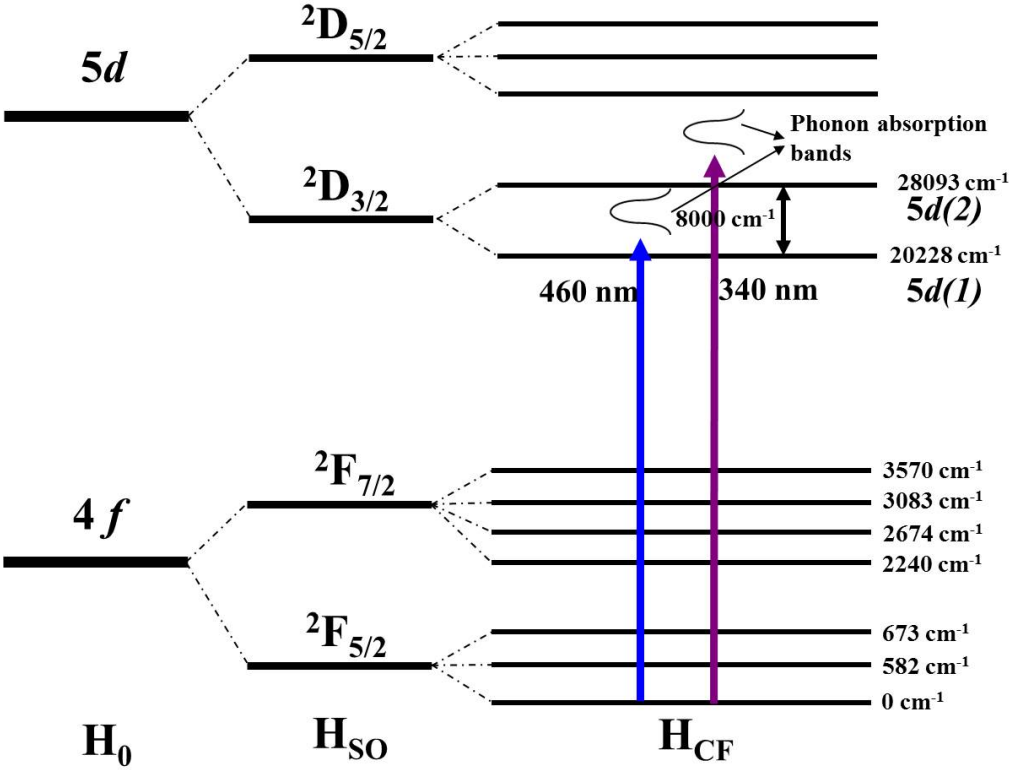

Figure 2.10: $4f \rightarrow 5d$ optical transitions of Ce:YAG.

In comparison with Pr:YAG and other rare earth ions, the energy level of Ce:YAG is simpler as presented in Fig. 2.9. The single unpaired electron of the $4f$ states split to two fine structures $^2F_{7/2}$ and $^2F_{5/2}$ due to the spin-orbital interaction. The crystal field lift off two energy levels to seven Kramers' doublets. The degeneracy of the Kramers doublets is removed if the external magnetic field is applied, resulting in 14 eigenlevels [117].

The spin-orbital coupling and crystal field interaction split the $5d$ state into five Kramers's doublets as plotted in Fig. 2.10. The lowest Kramers' doublets of the excited states present 8,000 cm^{-1} energy difference, indicating spectral selective in the excited states.

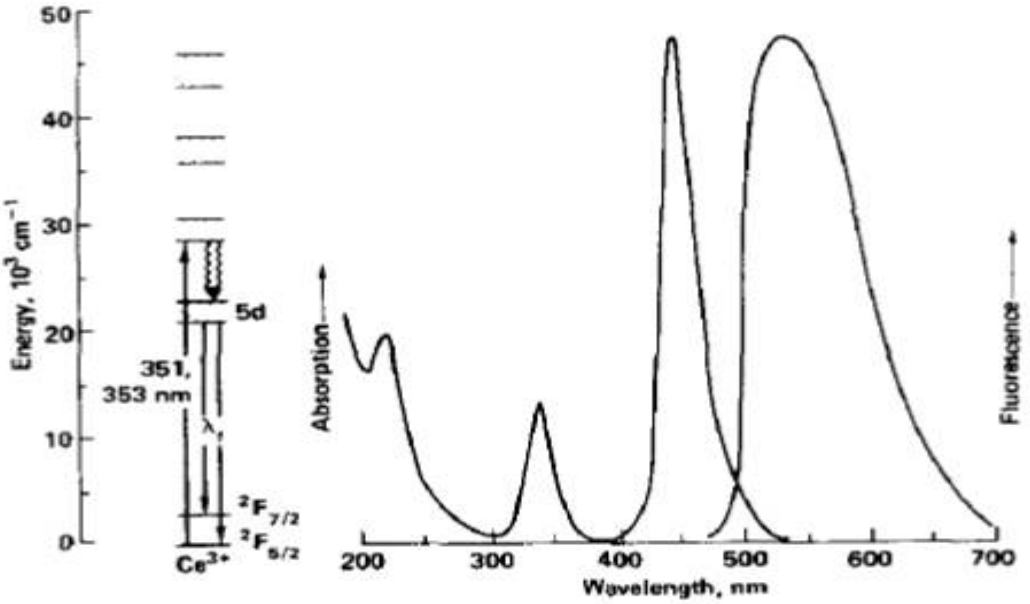

Figure 2.11: Absorption and emission spectrum of Ce:YAG, recorded under ambient conditions. The figure is reproduced from [119].

The absorption and emission spectrum of the Ce:YAG recorded under ambient conditions are expressed in Fig. 2.11 [119]. In the absorption spectra, cerium has two peaks located at 340 and 460 nm. These two peaks correspond to the transitions between $4f \rightarrow 5d(1)$ and $4f \rightarrow 5d(2)$. The linewidth of the transitions is broad, owing to the strong phonon coupling. The fluorescence spectrum of Ce:YAG is in the range of 489∼700 nm with strong phonon-assisted emission. The zero phonon line (ZPL) of Ce:YAG can not be observed at room temperature, which is located at 489 nm [120]. In addition, the $4f \rightarrow 5d$ transitions of the Ce:YAG are parity allowed, with strong oscillator strength and close to unity quantum efficiency [121]. The optical lifetime of the $5d$ states is 60 ns [122]. It yields strong fluorescence signal when Ce:YAG is efficiently excited.

Trivalent cerium ions doped in crystals present impressive optical properties with strong emission photon flux, which is the reason it can be detected at single-ion level. The optical detection of a single cerium ion in crystals will be introduced in this dissertation. However, other groups tried to resolve individual Ce ions in crystals for years, but the attempts of detecting single Ce ions have not yet been successful [123, 124].

2.2.2 Ce doped LuAG crystal

Lutetium Aluminum Garnet(LuAG) has formula $Lu_3Al_5O_{12}$, is another type of laser glasses, which shows similar physical properties as YAG (see Tab. 2.1). LuAG crystal also offers the opportunity to resolve rare earth impurities at single-ion level. LuAG has a cubic crystal structure with D_2 symmetry of Lu^{3+} sites. In comparison with Y^{3+}, Lu^{3+} presents much stronger nuclear spins as shown in Tab. 2.2. In addition, there are two isotopes of Lu^{3+}: ^{175}Lu with natural abundance 97.4% with nuclear spin 7/2 and magnetic moment 2.2 μ_N, and ^{176}Lu with natural abundance 2.6% with nuclear spin 7 and magnetic moment 3.2 μ_N, respectively.

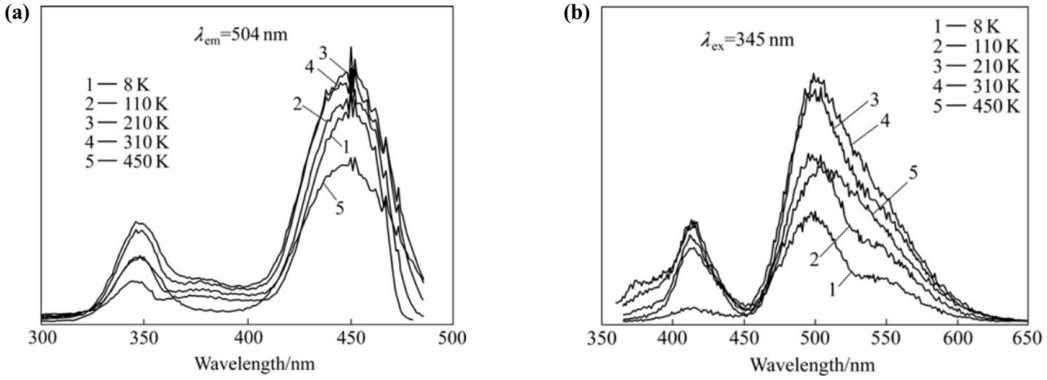

Figure 2.12: Absorption and emission spectrum of Ce:LuAG. Figures are reproduced from [125].

When trivalent cerium ions doped in LuAG crystal, it feels similar crystal field as in YAG. The absorption and emission spectrum of Ce:LuAG is introduced in Fig. 2.12, where both spectrum show ∼10 nm blue shift in comparison with Ce:YAG [125]. The optical lifetime of the 5d states of Ce:LuAG is ∼50 ns with also near unit quantum efficiency [126].

2.2.3 Ce doped yttrium orthosilicate crystal

Yttrium Orthosilicate is one of the most popular host materials in rare earth ion based quantum information processing, because it shows weak spin bath. The physical properties of YSO crystal are introduced in Tab. 2.1. In YSO crystal, ^{16}O, ^{28}Si, and ^{30}Si show no nuclear spins (see Tab. 2.2), ^{89}Y contains nuclear spin 1/2 with $\mu_Y = -0.14\mu_N$, and ^{29}Si presents nuclear spin 1/2 with $\mu_{\mathrm{Si}} = 0.56\mu_N$. Such nuclear spin bath indicates weak interaction of rare earth ions with the local environment, resulting in long lived coherence time of the spin transitions [79, 127]. Examples include quantum memories, two-qubit quantum gates and storage of quantum information have been demonstrated with rare earth ensembles in YSO crystal. In 2015, six hours coherence time between ensemble Eu^{3+} nuclear spin transitions in YSO host has been reported [63]. If rare earth ions can be detected and coherently manipulated at single-ion level in YSO crystal, it will offer long lived qubits for more complex quantum operations [81].

There exist two crystallographic forms of Y_2SiO_5, so called X1- and X2- Y_2SiO_5 crystals (see Fig. 9.5). They form different phases at different growth temperature, with X1-

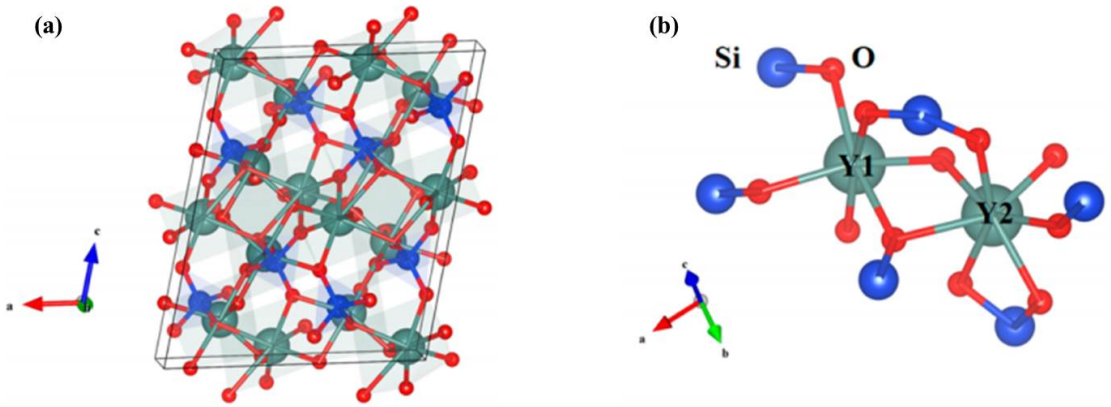

Figure 2.13: Lattice structure of X2-Y_2SiO_5. The figure is reproduced from [128].

corresponding to low temperature phase and X2- represents high temperature phase [129]. Therefore, only high temperature phase X2-YSO is under consideration here, since it represents bulk crystals grown by Czochralski method. In a unit cell of X2-YSO crystal, it shows C_{2h}^6 symmetry with 1.041, 0.6726 and 1.249 nm lattice constants with an angel of 102.65° in between two axis. In X2-YSO, it contains two different sites (see Fig. 2.13), due to different local environments resulting in two types of crystal fields. The crystal fields of X2-phase Ce:YSO crystal has been calculated in [128].

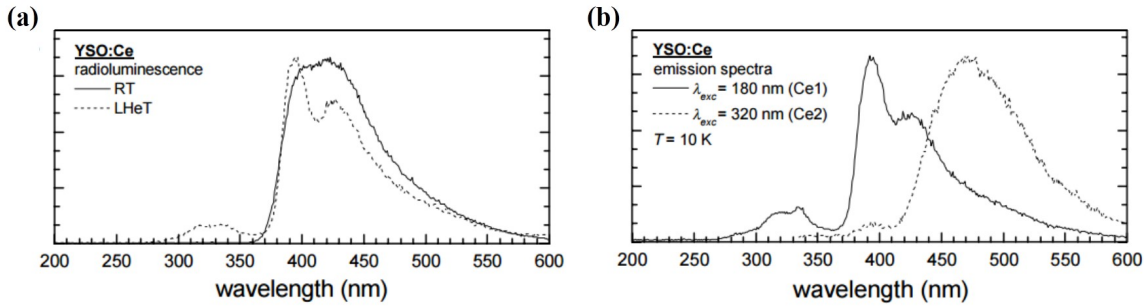

Figure 2.14: (a) Emission spectrum of Ce:YSO located in site 1. (b) Emission spectrum of Ce:YSO located in site 2. Figures are reproduced from [130].

Two sites of Ce doped X2-YSO also present different optical properties as plotted in Fig. 2.14 [130]. UV laser wavelength shorter than 370 nm is required to excite both sites of Ce in YSO crystal. They present different spectrum. One of them shows emission spectrum in the range of 350∼600 nm with a peak at 425 nm, while the other expresses emission spectrum from 400 nm to 600 nm with a maximum peak around 475 nm. The optical lifetimes of two sites are 40 and 55 ns respectively [131].

2.3 Summary

In this chapter, several different approaches of resolving individual Pr or Er ions in solids have been reviewed. The requirements of detecting single rare earth impurities have been introduced. Meanwhile, the potential candidates of single ion detection have been

presented.

The general physical properties of Pr and Ce doped YAG, LuAG and YSO crystals have been introduced. Trivalent cerium ions present impressive optical properties, since their parity allowed $4f \rightarrow 5d$ transitions show strong oscillator strength with high quantum efficiency. The optical detection and coherently manipulation of single Ce ions in different crystals will be introduced in the following chapters.

Chapter 3

Optical detection of a single Ce in YAG crystal

Optical detection of a single rare earth ion requires resolving the single ion either in the spatial domain or in the spectral domain. At room temperature, strong phonon coupling restricts resolving single rare earth ions in the spectral domain. On the other hand, to identify single rare earth ions in the spatial domain, we should obtain if and only if one ion in the focus volume. In YAG crystal, the radius of the exciting beam is limited by $\lambda/2/n_{YAG}$, where n_{YAG} is 1.82. If the excitation laser wavelength is at 460 nm, the excitation radius is ∼126 nm. It indicates that the maximum impurity level relative to yttrium ions in YAG crystal should be below 36 ppb (parts per billion). In our previous study, we estimated the praseodymium impurities in the purest YAG crystal (ultrapure YAG crystal from Scientific Materials) is ∼40 ppt (parts per trillion). It suggests that, in the ultrapure YAG crystal, the concentration of other species of rare earth ions might be low enough to be resolved at single-ion level.

Trivalent Ce ions in YAG crystal present a very promising optical properties. Its $4f \rightarrow 5d$ transition is located in the visible light range [119]. The quantum efficiency is close to the unit and the optical lifetime of the $5d$ states is ∼60 ns [121]. Owing to the high excitation-emission-reexcitation cycling efficiency, single Ce ion in YAG is predicted to emit 1.7×10^7 photons per second. It is possible to detect such strong fluorescence intensity of a single Ce ion in YAG by means of optical microscopy.

In this chapter, we discover a new type of photostable single photon emitter in YAG crystal by means of photon correlation measurements. The single photon emitter is proved to be single trivalent Ce ions by spectroscopic and lifetime measurements. On top of it, the coherent properties of single Ce excited state spin properties has been characterized. The coherent precession of single Ce electron spin is observed with the mapping of the spin state direct onto the polarization state of the emitted photons. The results offer us a new platform for exploring single Ce ions as single rare earth solid-state qubits.

3.1 Single photon emitters in YAG crystal

We mount the ¡1 1 1¿ oriented ultra pure YAG crystal in our home-built room temperature confocal microscope. The crystal is scanned by a 460 nm excitation light which is operated by a frequency doubled femtosecond Ti:Sapphire laser at 920 nm. The fluorescence signal of the YAG crystal is split into two detection paths and collected by an APD. In the spectral domain a window from 485 nm to 630 nm is open for detect the emitted photons. More details about the experimental condition are presented in the Appendix.

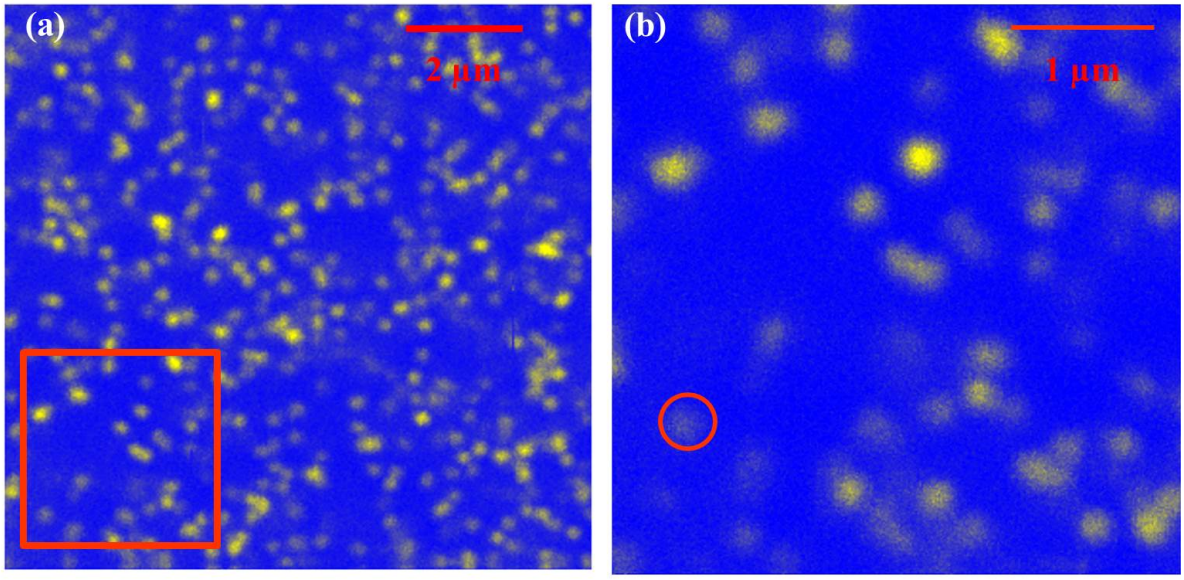

Figure 3.1: (a) Laser scanning image of single Ce ions in YAG. Scanning range is 10×10 μm^2. (b) Zoomed in scanning image of the red area in (a). The scanning range is 4×4 μm^2

The laser scanning image of the ultra pure YAG crystal is presented in Fig. 3.1. Quite some amount of bright individual spots can be determined in Fig. 3.1(a). In the 4×4 μm^2 laser scanning image (see Fig. 3.1(b)) individual spots are clearly resolved. The average distance in between the bright spots is ∼0.75 μm. When we perform the second order correlation function measurements on one of the dim spots as marked in Fig. 3.1(b), at zero delay, the peak vanishes (Fig. 3.2(a)). The antibunching behavior indicates that the marked spot is a single photon emitter. We also monitor the fluorescence yield of this single photon emitter in a long time scale (a couple of hours). It displays good photostability at room temperature.

More experiments have been performed to understand this single photon emitter properly. The optical lifetime of the single photon emitter is measured as shown in Fig. 3.2(b). It presents ∼64 ns optical lifetime fitted by a single exponential decay. The literature value of, the optical lifetime of Ce:YAG 5*d* excited state is 60 ns which is in agreement with the lifetime we measured from the single color center. The emission spectrum of this single impurity is also obtained with 460 nm excitation (Fig. 3.3(a)). It presents strong phonon-assisted emission in 485 ∼ 650 nm range without any sharp peaks. We also acquire the emission spectrum of Ce:YAG bulk crystal as shown in Fig. 3.3(b). As soon as we correlate the lifetime and spectrum of single color center with Ce:YAG bulk crystal, it shows the

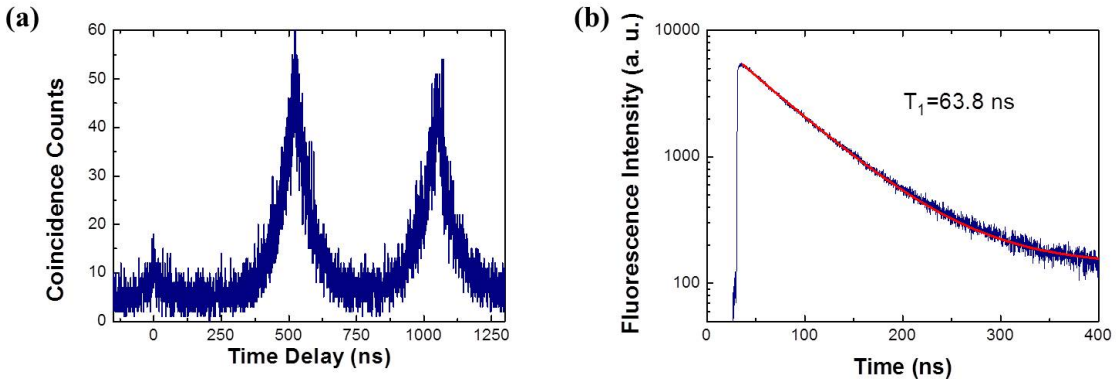

Figure 3.2: (a) The photon correlation measurement of an individual bright spot in YAG. It presents antibunching behavior indicating a single photon emitter in YAG crystal. (b) Optical lifetime measurement of the single photon emitter in YAG crystal.

high possibility to deduce that the single photon emitter we are studying is single trivalent Ce ions embedded in YAG crystal. However, Ce:YAG doesn't present sharp peaks in the emission spectrum. The unambiguously identification that single photon emitter is a Ce ion in YAG is absent. It is indispensable to find a unique feature that represents the species. For example, NV^- center in diamond presents ODMR lines at 2.87 GHz, Pr:YAG shows upconversion transition at 486.9 and 488.2 nm. In case of Ce:YAG, it presents the light induced magnetization of its excited spin states.

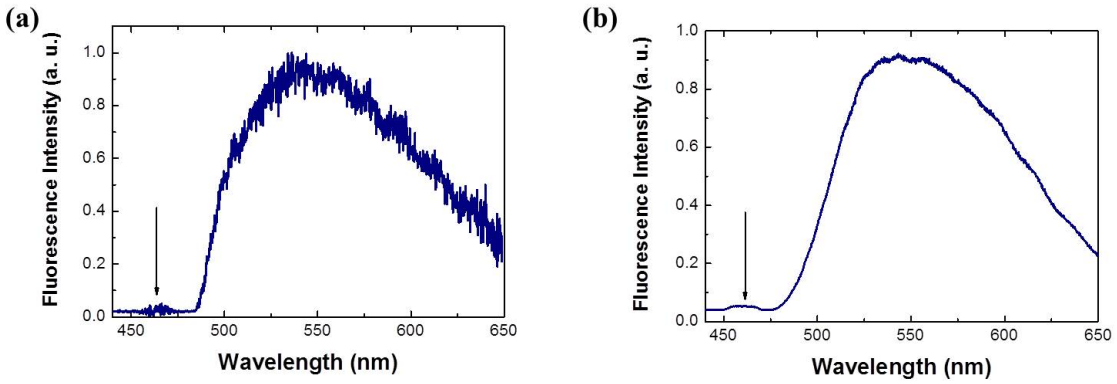

Figure 3.3: (a) Emission spectrum of single color center in YAG. (b) Emission spectrum of Ce:YAG bulk crystal.

3.2 Optical selection rules of Ce:YAG

Ce:YAG presents a Faraday effect due to its spin-flip transitions. It is introduced in the previous chapter that the energy level of Ce:YAG is split by spin-orbit coupling and crystal field. The Hamiltonian can be described by the following equation:

$$H_{\text{total}} = H_0 + H_{\text{SO}} + H_{\text{CF}}, \tag{3.1}$$

here $H_0 + H_{\mathrm{SO}}$ represents of a free trivalent Ce ion. Spin-orbit coupling H_{SO} and crystal field interaction H_{CF} is given by:

$$H_{\mathrm{SO}} = \lambda \mathbf{L} \cdot \mathbf{S}. \tag{3.2}$$

$$H_{\mathrm{CF}} = \sum_{L=0}^{L_{max}} \sum_{m=-L}^{L} A_{L,m} \langle r^L \rangle Y_{L,m}(\theta, \varphi). \tag{3.3}$$

In Eq. (3.2) $\mathbf{L}$ is the orbital momentum operator and $\mathbf{S}$ represents the spin operators. λ indicates the strength of the spin-orbit coupling. λ yields 647 in $4f$ states and 991 in $5d$ states. In Eq. (3.3) $L_{max} = 6$ or 4 for the $4f$ and $5d$ states respectively. $Y_{L,m}(\theta, \varphi)$ is the spherical harmonic. $A_{L,m}\langle r^L \rangle$ represents the crystal field parameter which is given in Tab. (3.1) [117, 118].

State	$A_{20}\langle r^2 \rangle$	$A_{22}\langle r^2 \rangle$	$A_{40}\langle r^4 \rangle$	$A_{42}\langle r^4 \rangle$	$A_{44}\langle r^4 \rangle$
$4f$	-465	-96	-3739	-380	1602
$5d$	-6099	-1259	-50042	-5374	19626
State	$A_{60}\langle r^6 \rangle$	$A_{62}\langle r^6 \rangle$	$A_{64}\langle r^6 \rangle$	$A_{66}\langle r^6 \rangle$	
$4f$	901	307	2136	246	

Table 3.1: Crystal field parameters of different energy levels of Ce:YAG crystal.

When an external magnetic field is applied to YAG crystal, Zeeman term will be introduced in the total Hamiltonian:

$$H_{\mathrm{Zeeman}} = \mu_B \mathbf{B}(\mathbf{L} + \mathbf{2S}), \tag{3.4}$$

where μ_B represents the Bohr magneton. $\mathbf{B}$ corresponds to the external magnetic field.

The eigenfunctions $|L, L_z, S, S_z\rangle$ in the natural basis can be obtained by diagonalizing the total Hamiltonian in Eq. (6.10). In the $4f$ states, $L = 3$, while in the $5d$ states $L = 2$. The wavefunction is given by the following:

$$\psi_n = \sum_{L_Z, S_Z} a_{L_Z, S_Z} |L, L_Z, S, S_Z\rangle., \tag{3.5}$$

where n is from 1 to 14 in $4f$ states and 1 to 10 in $5d$ states.

The matrix element of the external electromagnetic fields acting in between the ground and the excited states is given by:

$$\mu_{nm} = \langle \psi_n^{4f} | e \cdot \mathbf{r} | \psi_m^{5d} \rangle, \tag{3.6}$$

here e means the charge of the electron and $\mathbf{r}$ yields the electron position operator. If the excitation light is circularly polarized, Eq. (3.6) yields:

$$\mu_{nm} = \langle \psi_n^{4f} | x_{\mathrm{lab}} \pm \imath y_{\mathrm{lab}} | \psi_m^{5d} \rangle, \tag{3.7}$$

here "+" represents σ_+ photons and "−" represents σ_- photons. x_{lab} and y_{lab} are the $x-$ and $y-$ axis in terms of the lab coordinates represented by the coordinates of Ce local frame.

Under the experimental conditions, only the lowest $5d$ state can be pumped by 460 nm laser. The oscillation dipole strength of the $5d$ state to $4f$ states with circularly polarized photons is given by Tab. 3.2. It should be noticed that the laser beam direction defines the quantization axis ($\vec{k}$ direction) [132].

$\|5d\downarrow\rangle \leftrightarrow$	$\|4f(1)\uparrow\rangle$	$\|4f(2)\uparrow\rangle$	$\|4f(3)\uparrow\rangle$	$\|4f(4)\uparrow\rangle$	$\|4f(5)\uparrow\rangle$	$\|4f(6)\uparrow\rangle$	$\|4f(7)\uparrow\rangle$
	0.0007	0.012	0.243	0.0007	0.0034	0.017	0.0005
$\|5d\uparrow\rangle \leftrightarrow$	$\|4f(1)\downarrow\rangle$	$\|4f(2)\downarrow\rangle$	$\|4f(3)\downarrow\rangle$	$\|4f(4)\downarrow\rangle$	$\|4f(5)\downarrow\rangle$	$\|4f(6)\downarrow\rangle$	$\|4f(7)\downarrow\rangle$
	0.286	0.006	0.002	0.184	0.0007	0.051	0.018

Table 3.2: Dipolar oscillator strengths of different optical transitions [132].

If single Ce decays from $|5d(1)\uparrow\rangle \rightarrow |4f(1)\downarrow\rangle$ (or $|5d(1)\downarrow\rangle \rightarrow |4f(1)\uparrow\rangle$), it emits a σ_+ (or σ_-) photon. It indicates that the excited spin state of single Ce ion is directly mapping onto the polarization state of the fluorescence photon, which suggests the interface between a single rare earth ion and a single photon.

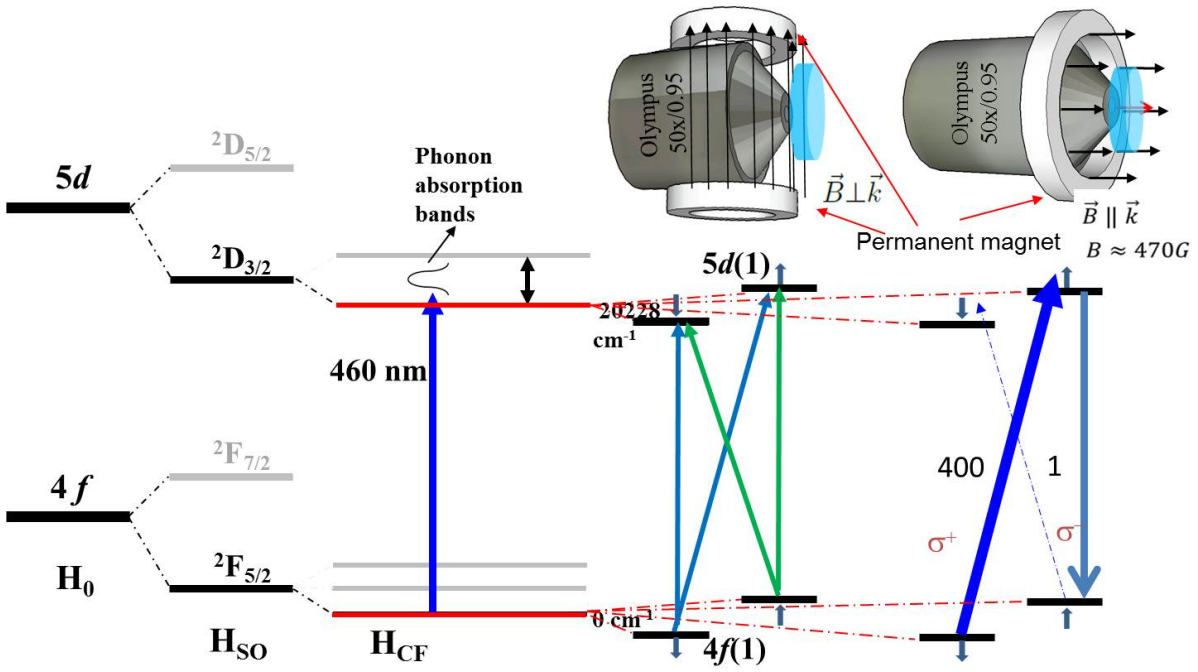

Figure 3.4: Ce:YAG energy level, and its selection rules correspond to different directions of the external magnetic field.

The applied external magnetic field removes of the degeneracy of the Kramers doublets (Fig. 3.4). If the external magnetic field is perpendicular to the quantization axis ($\vec{B} \perp \vec{k}$), both spin-flip and spin-nonflip transitions are allowed. With the forming of the V systems, the lowest excited states $|5d\uparrow\rangle$ and $|5d\downarrow\rangle$ precesses with a Larmor frequency ω:

$$\omega = \frac{\mu_B g \vec{B}}{\hbar}, \tag{3.8}$$

where μ_B is the Bohr magneton, g represents the g factor of the lowest excited states. With this external magnetic field, it yields to a new wave function in the excited states as following:

$$|\psi\rangle = \frac{1}{\sqrt{2}}(|5d(1)\uparrow\rangle + e^{-i\omega t}|5d(1)\downarrow\rangle). \tag{3.9}$$

Equation(3.9) indicates an oscillatory behavior in the excited states $5d$ known as Larmor precession [133]. Due to the high ratio of the oscillator strengths of $|5d(1)\uparrow\rangle \rightarrow |4f(1)\downarrow\rangle$ and $|5d(1)\downarrow\rangle \rightarrow |4f(1)\uparrow\rangle$ transitions (400:1 ratio is calculated) excited state oscillation will be projected to the polarized state of the fluorescence (σ_+ or σ_- photons). Different polarization of the fluorescence signal with external magnetic field has been calculated as shown in Fig. 3.5(a). The damping of the oscillation is caused by the dephasing process from the interaction of the excited spin states with the local spin bath.

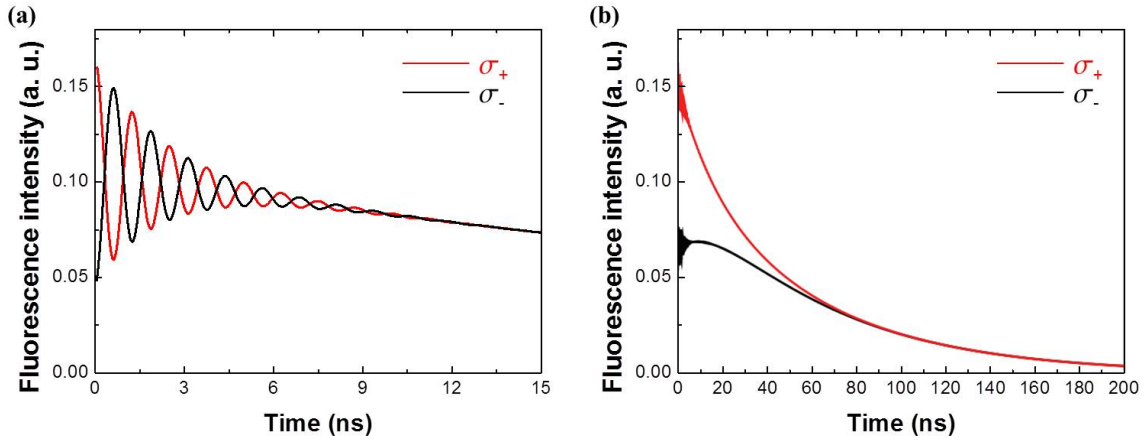

Figure 3.5: Simulated different polarization fluroescence signals with different external magnetic field. (a) $|\vec{B}|$= 250 G, $\vec{B} \perp \vec{k}$. (b) $|\vec{B}|$= 500 G, $\vec{B} \parallel \vec{k}$.

If the external magnetic field is parallel to the quantization axis ($\vec{B} \parallel \vec{k}$), only spin-flip transitions are allowed indicated by the disappearance of the Larmor precession. Owing to the different diploe oscillator strengths with different polarization of the excitation lasers, the population in the $5d(\uparrow)$ and $5d(\downarrow)$ is in nonequilibrium. It results in the difference in the fluorescence corresponding to σ_+ and σ_- polarizations in the beginning of the decay, as shown in Fig. 3.5(b).

3.3 Mapping the excited states of a single Ce ion onto the polarization of emission photons

To confirm the theoretical prediction of the excited state dynamics of a single Ce ion in YAG, the following experiments are performed. As soon as the single Ce ion is localized under the home-built confocal microscopy, circularly polarized light (σ_+ photons)

is applied to initialize Ce to the excited state $|5d(1)\uparrow\rangle$. A set of $\lambda/4$ waveplate-$\lambda/2$ waveplate-polarization beam splitter is settled to filter out one type of the polarization (e.g. σ_- photon) from the fluorescence. The fluorescence of single Ce (e.g. σ_+ photon) is detected by a single photon detector in the spectral range 485∼525 nm to ensure the good contrast of the mapping. An external magnetic field is directed either perpendicular ($\vec{B} \perp \vec{k}$, $|\vec{B}| = 250$ G) or parallel ($\vec{B} \parallel \vec{k}$, $|\vec{B}| = 500$ G) to the laser beam direction.

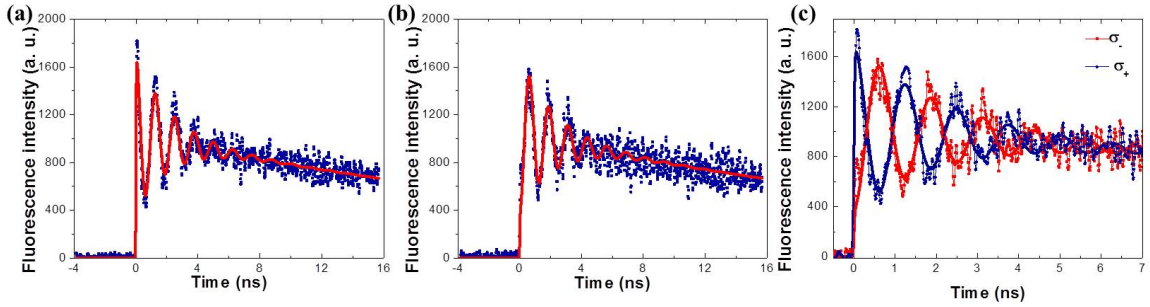

Figure 3.6: Larmor precession of the excited spin state of a single Ce ion, where the external magnetic field is $\vec{B} \perp \vec{k}$, $|\vec{B}| = 250$ G. The single Ce ion is excited by a circularly polarized (σ_+) 460 nm femtosecond pulsed laser. (a) Temporal behavior of the fluorescence of a single Ce ion with σ_+ photons detection. (b) Temporal behavior of the fluorescence of a single Ce ion with σ_- photons detection. (c) Observation of π phase shift of two types of emitted photons.

If the magnetic field is applied perpendicular to the laser beam direction, the temporal behavior of the fluorescence of a single Ce ion is recorded. Figure.3.6(a) displays the temporal behavior of the detected σ_+ fluorescence signals from a single Ce ion. It presents a high peak at the beginning, and oscillating with high frequency. On the other hand, signal corresponding to σ_- polarized light shows π phase shift in respect to the σ_+ signal as depicted in Fig 3.6(b). When the laser is applied, it shows minimal fluorescence intensity, and rises up the maximal intensity in 0.6 ns. We plot the temporal behavior of both σ_+ and σ_- fluorescence together in Fig. 3.6(c), the oscillation of σ_+ and σ_- signals presents π phase shift.

We are able to deduce two important parameters from the oscillations. The g-factor of the excited state is given by:

$$g = \frac{\omega\hbar}{\mu_B|\vec{B}|}, \tag{3.10}$$

where ω represents the oscillating frequency. It indicates g factor of the $5d(1)$ excited spin states to be 2.2. Furthermore, by calculating the damping time of the Larmor precession, the dephasing time (T_2^*) of the $5d(1)$ excited state of a single Ce ion is determined to be 2.2 ns. It is not surprised to discover such short dephasing time, since YAG crystal contains numerous of ^{27}Al ions which have nuclear spin 5/2. The strong ^{27}Al nuclear spin bath leads to the short T_2^* time of the excited spin states.

The indirect proof of such strong nuclear spin bath is given by Fig. 3.7. When the external magnetic field is removed, the Larmor precession of the excited spin states has been detected with different polarizations. Even at zero magnetic field, the quantum beat signal can still be resolved. Around 40 G magnetic field is obtained by determining the Larmor precession frequency. Such strong magnetic field is mainly contributed by the ^{27}Al nuclear

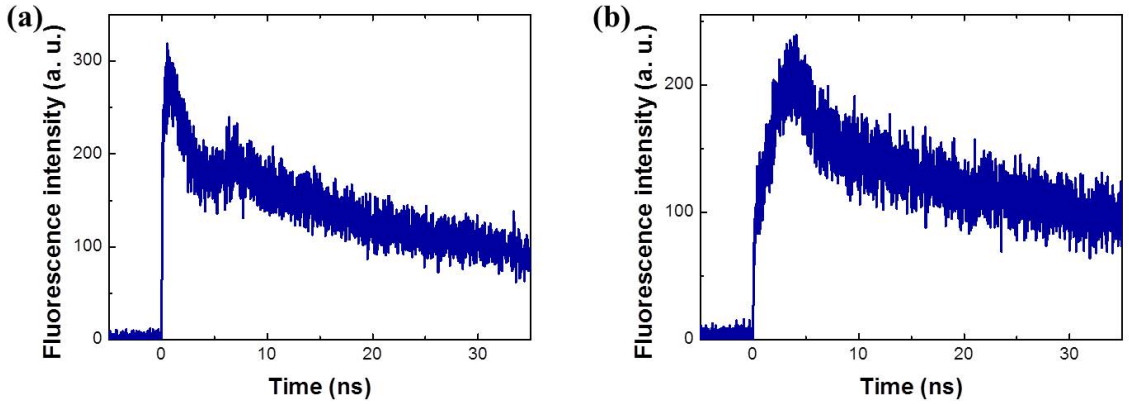

Figure 3.7: Larmor precession of the excited spin state of a single Ce ion under zero magnetic field. The single Ce ion is excited by a circularly polarized (σ_+) 460 nm femtosecond pulsed laser. (a) Temporal behavior of the fluorescence of a single Ce ion with σ_+ photons detection. (b) Temporal behavior of the fluorescence of a single Ce ion with σ_- photons detection. (c) Observation of π phase shift of two types of emitted photons.

spin bath. It indicates if low spin matrix host material is alternated, the Larmor precession time will be extended.

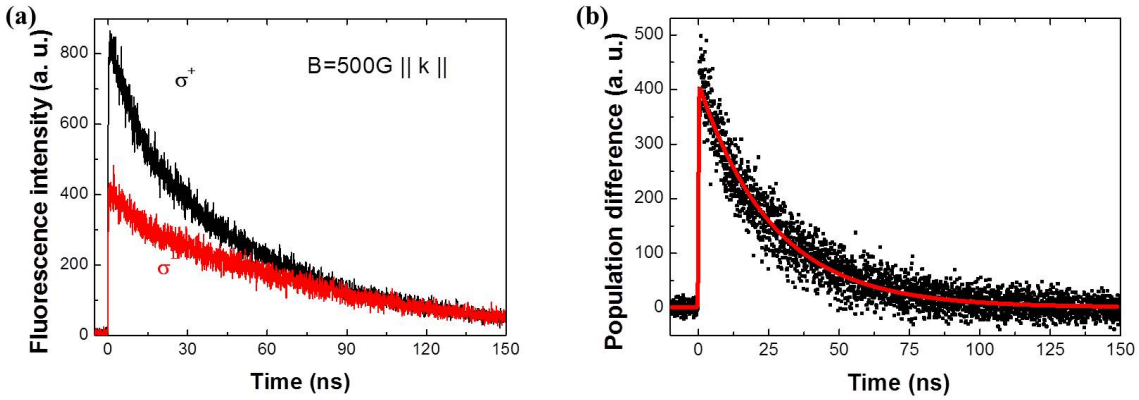

Figure 3.8: Larmor precession of the excited spin state of a single Ce ion under parallel magnetic field. (a) Temporal behavior of the fluorescence of a single Ce ion with σ_+ photons (black curve) and σ_- (red curve) detection. (b) Population difference between $|5d(1)\uparrow\rangle$ and $5d(2)\downarrow\rangle$.

We also applied the magnetic field (500 G) which is parallel to the laser beam direction. It is similar to the simulation result, the Larmor precession of the excited states vanishes as shown in Fig. 3.8(a). At the starting point, the fluorescence signal of the single Ce ion corresponds to σ_+ and σ_- polarizations presenting remarkably difference. The difference of the fluorescence indicates the non-equilibrium populations of $|5d(1)\uparrow\rangle$ and $|5d(2)\downarrow\rangle$ which is due to different dipole oscillation strength. After 90 ns, the fluorescence intensities merge to the same level owing to the spin-flip process. The population difference between two excited spin states is obtained by subtracting two decay curves (see Fig. 3.8(b)). This difference indicates 26 ns spin-lattice relaxation time of the lowest excited states.

3.4 Conclusion and outlook

In this chapter, optical detection of the second species of single rare earth ions in solids namely single Ce ions in YAG crystal has been demonstrated at room temperature. Under the confocal microscopy, single Ce ions have been optically resolved in an ultra pure YAG crystal. The results have been confirmed by antibunching, lifetime and emission spectrum measurements. Ce:YAG presents a special optical property. Its optical selection rules are changed by different directions of the external magnetic field. Thus, Ce can be optically initialized to one of the lowest excited spin states by circularly polarized light. The spin state is mapped onto the polarization state of a single photon. When the external magnetic field is perpendicular to the quantization axis, the Larmor precession of the excited spin state has been observed by monitoring the temporal behavior of fluorescence of a certain polarization. Furthermore, the coherence properties of a single Ce excited spin state has been measured presenting 26 ns spin-lattice relaxation time and 2.2 ns depasing time. Such short coherent time of Ce:YAG excited spin states is not suitable to explore single Ce ions as solid-state qubits. Two improvements are introduced to prolong the short coherence time of single Ce ions.

1. Picking up low spin matrix host crystals. As it is mentioned in the previous chapter that the depasing time is mainly induced by the hyperfine interaction of strong ^{27}Al nuclear spin bath. The choice of the low spin bath material, for example, Y_2SiO_5 crystal, will enlarge the depasing time. The preliminary results are shown in Fig. 3.9, where the Larmor precession of the excited spin state of Ce:YSO 100 ppm nanoparticles have been observed. The dephasing time of the excited spin state is ∼17 ns, which is already influence by the spin-lattice relaxation time. However, the optical lifetime of the excited state (∼65 ns) set the upper-limitation of the coherence time of Ce $|5d\rangle$ states, which is invincible.

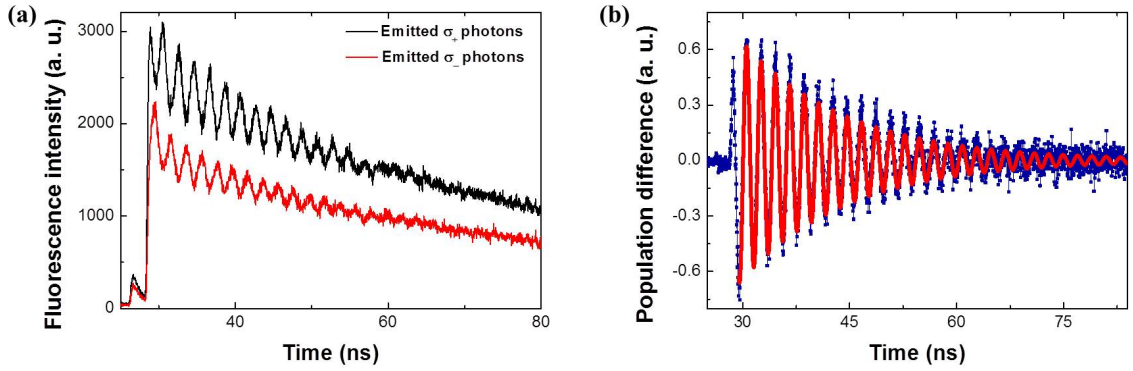

Figure 3.9: Larmor precession of the excited spin state of a Ce:YSO (100 ppm) nanoparticle. (a) Temporal behavior of the fluorescence of a single Ce ion with σ_+ photons (black curve) and σ_- (red curve) detection. (b) Population difference between $|5d(1)\uparrow\rangle$ and $5d(2)\downarrow\rangle$.

2. Exploring Ce:YAG ground states spin qubits. The mechanism of spin-lattice relaxation of Ce:YAG is Orbach relaxation. At room temperature, the T_1 time of Ce:YAG $4f$ levels is fast (picoseconds range). If the crystal is cooled down at cryogenic temperature, the spin-lattice relaxation of the ground spin states will be promisingly suppressed, indicating the prolonging of the ground state T_1 time by a few orders of magnitude. Afterward it

offers the possibility to study the coherent properties of single Ce ground spin states.

However, in current experimental conditions, single Ce ions are optically resolved by a 1.3 N.A. oil immersion objective lens at room temperature. When the YAG crystal is cooled down to cryogenic temperature, the oil immersion objective lens can not be utilized since the oil will be frozen. The N.A. of the air objective lens is lower than the oil one, indicates low fluorescence collection efficiency, spectral resolution and signal-to-noise ratio. Nanophotonic devices should be introduced to overcome this barrier, solid immersion lenses (SILs) as one of the standard and common photonic devices which is under our consideration. SILs can be fabricated on the surface of YAG crystal by means of focus ion beam milling. Under the SILs, the collection efficiency, spectral resolution and signal-to-noise ratio has been dramatically improved (for more details please see Appendix). The combination of SILs and a high N.A. air objective lens, will give us the opportunity to optically identify single Ce ions at cryogenic temperature and to explore its coherent properties of ground spin states.

Chapter 4

Coherent properties of single Ce ions

In the previous chapter, the optical detection of single Ce ions in YAG has been demonstrated at room temperature. The short spin coherence time (T_2^* ~2.2 ns) blocks the further application of single Ce ions as quantum devices. Nevertheless, the ground states of Ce ions are $4f$ levels, which are screened by filled $5s$ and $5p$ levels, indicating much weaker coupling to the environment. However, the ground state spin properties can not be observed at room temperature, due to the fast spin-lattice relaxation time. The spin relaxation mechanism of Ce:YAG ground state is Orbach relaxation,which features a temperature dependence of T_1 as [134]:

$$T_1 = \frac{1}{c \cdot \Delta} exp(\frac{\Delta}{kT}), \tag{4.1}$$

where T is the temperature, and k is the Boltzmann constant. Δ represents the energy difference between the lowest Kramers doublet and the second lowest $4f$ state, which is 228 cm^{-1}. Equation(4.1) explains why the spin-relaxation time will be significantly prolonged at cryogenic temperature compared to room temperature. Following this expectation, in this chapter, the YAG crystal is cooled down to $\approx$ 3.5 K to extend the T_1 time of Ce:YAG ground spin states. With long T_1 time, high fidelity optical initialization and readout, and coherent manipulation of single Ce electron spin have been demonstrated. It is an essential step to explore single rare earth ions as single rare earth solid-state qubits.

4.1 Optical spin initialization and readout

Before studying the coherent properties, the first step is to initialize the spin and subsequently read it out, which is a basic requirement to use single Ce spin as stationary qubits. To realize such requirement, an optical pumping method based on well chosen selection rules is applied here. Specifically, in a 500 Gauss external magnetic field aligned perpendicular to the sample surface, the spin-flip transition between $|4f\downarrow\rangle$ and $|5d\uparrow\rangle$ is 396 times stronger than the transition between $|4f\uparrow\rangle$ and $|5d\downarrow\rangle$ under σ^+ circularly polarized excitation, as shown in Fig. 4.1(a). Since the spontaneous decay from $5d$ state back to the two ground $4f$ states is equal, repeated optical excitation pumps the ion into $|4f\uparrow\rangle$ state and therefore initializes the Ce spin. The ratio of 396:1 in optical transition

strength between $4f$ and $5d$ under circularly polarized excitation grants a high selectivity and enables spin-dependent fluorescence and as such an optical spin detection. Under σ^+ circularly polarized excitation, Ce ions only generate fluorescence in $|4f\downarrow\rangle$. While under σ^- circularly polarized excitation, the fluorescence intensity is proportional to the probability of Ce to be in $|4f\uparrow\rangle$ spin state. Both ways are able to readout the spin.

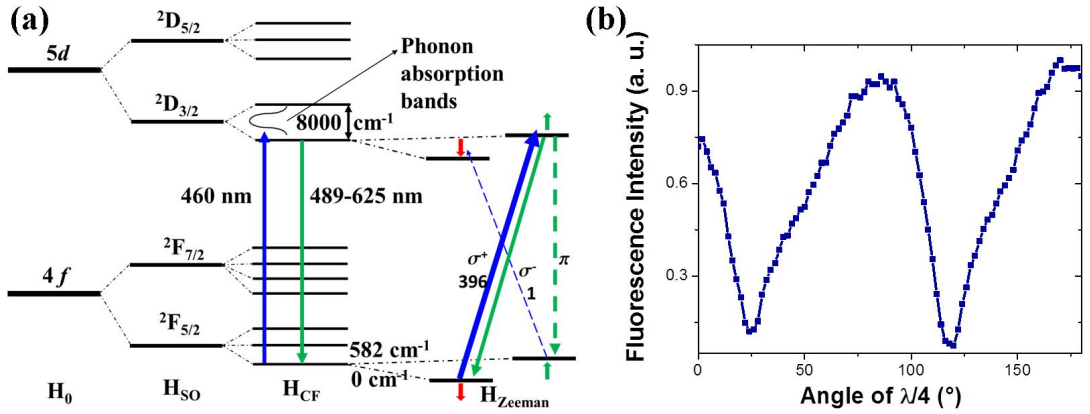

Figure 4.1: (a) Energy levels of Ce:YAG with selection rules of optical transitions at low temperature. (b) Fluorescence intensity of a single Ce ion corresponds to the rotation angle of $\lambda/4$ waveplate.

To experimentally characterize the above process, an ultra-pure YAG crystal is cooled down to ≈ 3.5 K. A permanent magnet is settled on the air objective lens to generate a 500 G magnetic field perpendicular to the sample surface. A confocal microscopy is used for detecting single Ce ions. Solid immersion lenses (SILs) are milled by focus ion beam on the surface of YAG crystals to increase the spatial resolution and collection efficiency (for more details of the SILs and experimental setup please see Appendix). It has to be noted, that the π polarized photon, propagating perpendicular to the laser beam direction, can not be detected in the described setup and thus can not contribute to the measured fluorescence intensity. We first study the polarization dependence of the Ce ion fluorescence.

When single Ce ions are optically resolved at low temperature, a $\lambda/4$ waveplate is inserted into the excitation path to change the polarization of the excitation laser. Figure 4.1(b) shows the fluorescence intensity of a single Ce ion as a function of the angle of the $\lambda/4$ waveplate. It shows strong fluorescence yield when the excitation photons are linearly polarized and weak yield when the excitation photons are circularly polarized. The linearly polarized photons can be decomposed to the combination of σ^+ and σ^- photons, and therefore both $|4f\downarrow\rangle \rightarrow |5d\uparrow\rangle$ and $|4f\uparrow\rangle \rightarrow |5d\downarrow\rangle$ transitions are allowed, resulting in high fluorescence yield. When Ce ions are excited by only σ^+ (or σ^-) polarized photons, after several loops, they will eventually stay in the "dark state" $|4f\uparrow\rangle$ (or $|4f\downarrow\rangle$) and cannot be excited any longer. It yields minimal fluorescence intensity, which not only indicates the initialization of single Ce ions, but also calibrates the optimal photon polarization required for initialization. The asymmetry of Fig. 4.1(b) curve is caused by an imperfect $\lambda/4$ waveplate.

To quantify the number of excitation loops required for initialization, a pulse sequence is applied as shown in Fig. 4.2(a). A train of circularly polarized laser pulses is generated to

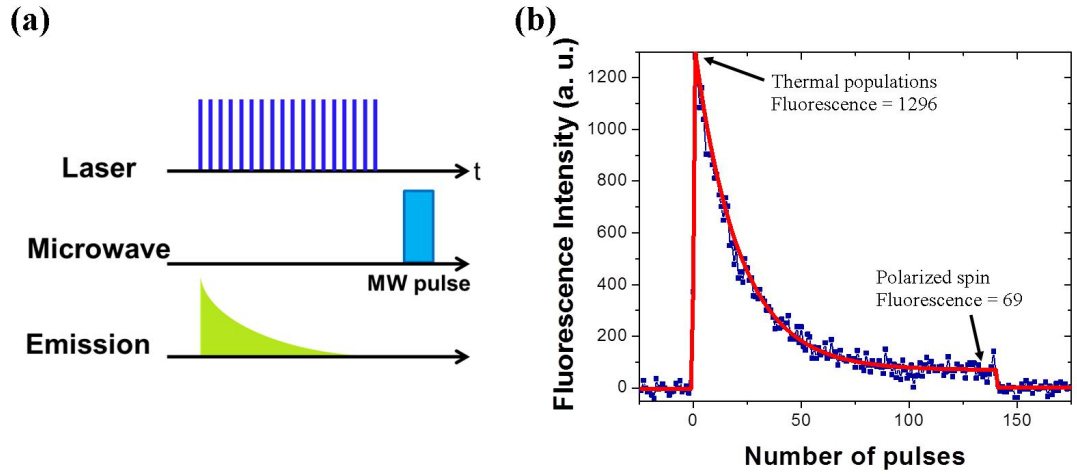

Figure 4.2: (a) Schematic diagram of the MW and laser pulse sequences to observe the dynamics of the optical pumping process. (b) Fluorescence intensity of a single Ce ion as a function of the number of laser pulses.

excite single Ce ions. This sequence is then used up to ten thousands of times to acquire data points shown in subsequent figures. In order to guarantee that the Ce ion starts from the thermodynamic equilibrium for every new pulse sequence, a waiting time τ is introduced in between two trains of laser pulses($\tau > 5T_1$ in milliseconds range. T_1 will be described with more details in the next section). In the experiment, to speed up this process, a MW pulse with the duration time 3 μs is introduced as the white noise source. The dependence of fluorescence intensity of a single Ce ion on the number of initialization laser pulses is plotted in Fig. 4.2(b). At the beginning, the lowest Kramers doublets are under thermodynamic equilibrium resulting in high fluorescence yield $I_T \propto \eta P_B(n = 0)$. η represents the collection efficiency. P_B corresponds to the probability that Ce stays in the bright state($|4f\uparrow\rangle$). It is 1/2 when the ion is in thermodynamic equilibrium. After around 135 excitation pulses, the Ce is optically pumped to the "dark state" ($|4f\downarrow\rangle$) with low fluorescence yield $I_D \propto \eta P_B(n = 135)$. From these two values, one can obtain the initialization fidelity in $|4f\downarrow\rangle$ state according to the following equation:

$$f = (1 - \frac{I_D}{2 \times I_T}). \tag{4.2}$$

In the described experiment 97.5%initialization fidelity is achieved. A further optimization of the experimental conditions like the quality of the circularly polarized photons, and the performance of the SIL can increase the fidelity up to 99.74% according to the theoretical prediction.

4.2 Spin-lattice relaxation time of single Ce ions

When a spin is initialized, it will unavoidably relax back to thermodynamic equilibrium due to interaction with the phonons in the lattice. This process is known as spin-lattice relaxation. The spin relaxation time T_1 characterizes how fast this spin is depolarized.

It also sets an upper limitation of the quantum system's coherent time by noting the following formula [135].

$$\frac{1}{T_2} = \frac{1}{2T_1} + \frac{1}{T_2^*}, \tag{4.3}$$

where T_2 represents the spin-spin relaxation time, and T_2^* indicates the dephasing time of the spin evolution. It yields from Eq. (4.3) that T_2 is no longer than $2T_1$.

Figure 4.3(a) presents the schematic diagram of a standard pulse sequence for T_1 measurements: the single Ce ion is initialized in the "dark" state ($|4f\downarrow\rangle$) by the first train of circularly polarized laser pulses. It then experiences a spin-lattice relaxation in a waiting time τ which is finally detected by the second train of the laser pulses. In addition, the second train of the laser pulses initializes the Ce ion again to the "dark state". To increase the contrast, the single photon detector is gated to readout Ce spin state only during the first four laser pulses. The experimental data is plotted in Fig. 4.3(b). T_1 time ~4.5 ms is obtained by fitting the curve. Normally, the T_1 lifetime of rare earth spin transitions can approach a couple of hours or even days. It is not clear so far what causes the relatively short lifetime of Ce spin transitions. With the measured T_1 time of single Ce spin qubits. In principle, a T_2 time of 9 ms could be achieved.

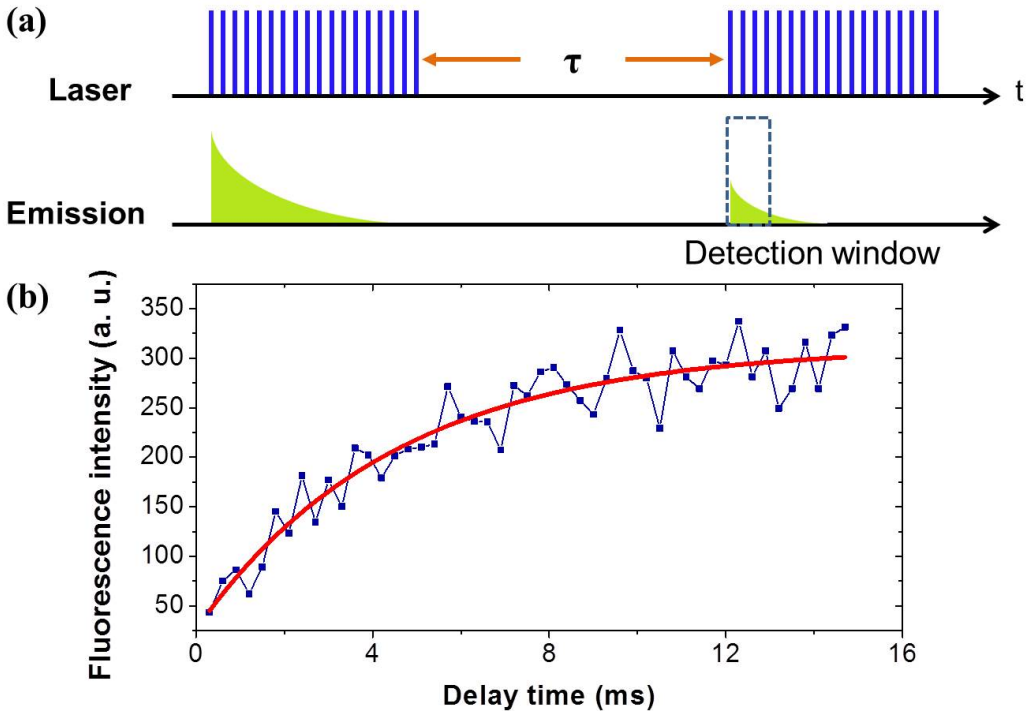

Figure 4.3: (a) Schematic diagram of the laser pulse sequences to record the spin-lattice relaxation time of single Ce ions. (b) Fluorescence intensity of a single Ce ion as a function of the delay time in between two pulse train.

4.3 Coherent manipulation of single Ce ions

With a rough knowledge about the magnetic filed the Zeeman splitting of Ce:YAG ground states could in principle be achieved. It offers the opportunity of operating microwave (MW) radiation to coherently drive the single Ce spin transitions. In the experiment, a MW waveguide structure is fabricated on the surface of the crystal right beside the SILs (for more details about the fabrication of MW structure please see Appendix). By the MW radiation, the single Ce spin transition is coherently manipulated.

4.3.1 Ground state spin transitions

In an external magnetic field of 500 Gauss, the Zeeman splitting of Ce:YAG ground states is in the range of MW frequency. It varies from 500 MHz up to 1.6 GHz depending on the specific site of Ce ion in YAG. To acquire the ground state spin transition frequency, the MW frequency is swept while the circularly polarized laser is applied simultaneously, as shown in Fig.4(a).

When the frequency of the MW is out of the resonance of the ground state spin transition, the Ce ion stays in the "dark state"($|4f\uparrow\rangle$) due to the optical pumping. The fluorescence intensity stays as low as the background level. If the MW frequency is on resonance of the ground spin transitions, the ion is pumped back to the bright spin state ($|4f\downarrow\rangle$) by absorbing a MW photon, and yield high fluorescence intensity in the optical excitation. This method is known as optically detected magnetic resonance(ODMR) [12]. Owing to the high initialization fidelity of the spin states, ODMR of a single Ce spin transition displays fairly high contrast (see Fig. 7.4 (b)).

By repeating the ODMR measurements on more than 20 individual single Ce ions, we finally obtain all the six resonance frequencies corresponding to the six different sites in YAG crystal (Fig.7.4(c)), as introduced in Chapter II. The resonance frequencies are at 651 MHz, 1312 MHz, 1508 MHz, 1532 MHz, 1556 MHz and 1571 MHz respectively.

With the optical initialization and the acquirement of the energy difference in between the ground state transitions, coherent manipulation of single Ce electron spins can be attempted.

4.3.2 Rabi oscillations of single Ce ions

In a two-level system, when an external electromagnetic field is introduced, which is on resonance with the two level system, this external field will induce the oscillation of the population in between the two-level system. This is namely Rabi oscillation, indicating the ability of coherently controlling the two-level system. To realize single Ce ions as stationary qubits, it is important to coherently manipulate their single electron spins. Observation of Rabi oscillations of the spin transition is the next step of coherently controlling single Ce spin qubits.

As soon as the Zeeman splitting of the ground spin states is determined by ODMR spectroscopy, a strong MW field can be applied on resonance with the spin transitions to

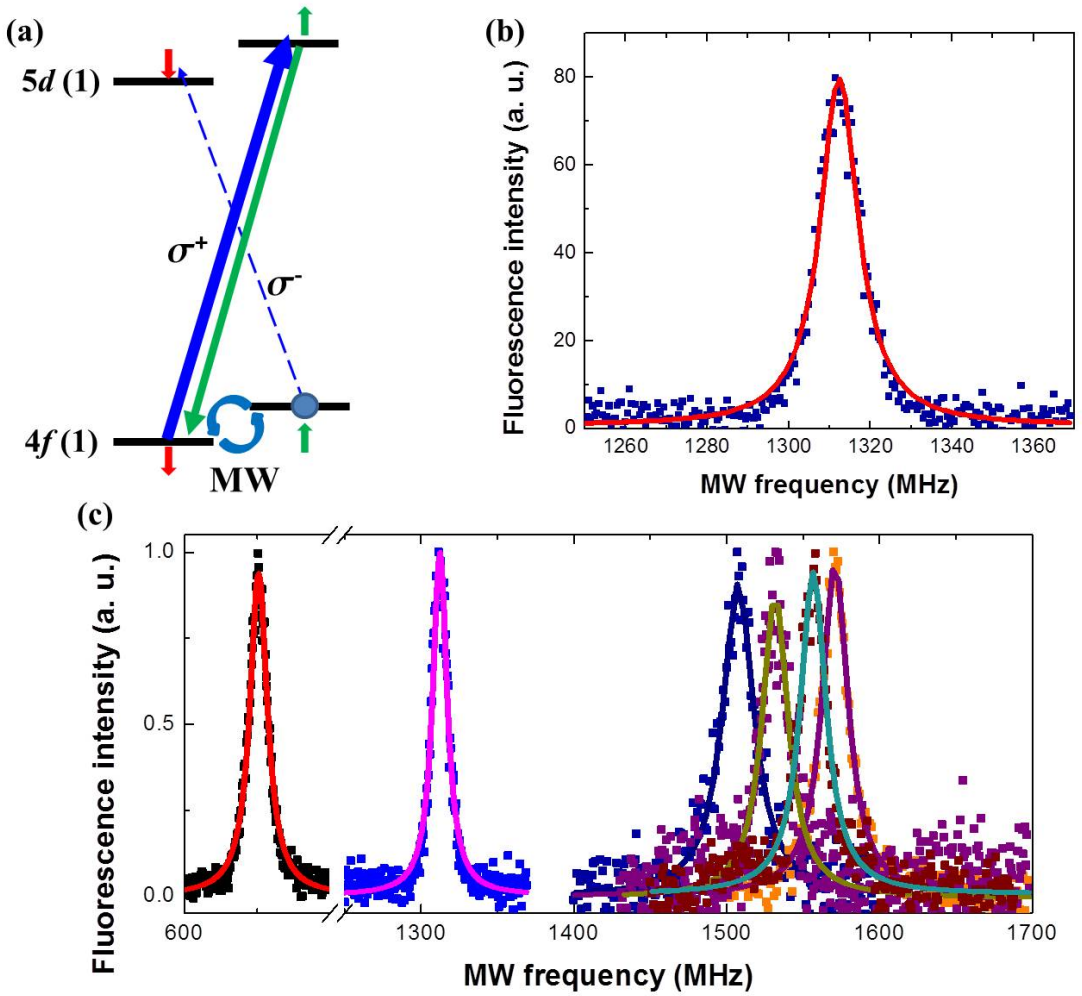

Figure 4.4: (a) Level structure of single Ce ions with external MW radiation. (b) ODMR of a single Ce ion, which the spin resonance frequency is at 1312 MHz. (c) ODMR signal of single Ce ions orientated differently in YAG.

drive the electron spin coherently. In the experiment, a train of circularly polarized laser pulses is generated to initialize the Ce spin state as shown in Fig. 7.5(a). After the optical pumping, the laser is turned off, and the MW source is switched on with certain duration time to drive single Ce spins. When the coherent manipulation of a single electron spin is done, another train of the laser is generated to readout the population of the spin state, and initialize the Ce ion back to the "dark state", in preparation for the next measurement. The single photon detector is gated to readout the Ce fluorescence intensity during the first four laser pulses to acquire good contrast.

Figure 7.5 shows the Rabi oscillation of a single Ce ion. The Rabi oscillation signal presents good contrast owing to the high-fidelity initialization. Unfortunately, the Rabi oscillation of a single Ce ion vanishes out quickly within 3 μs. It indicates strong interaction of the Ce ion with the local environment which is mainly caused by strong ^{27}Al nuclear spin bath. The observed Rabi oscillation of single Ce offers the further investigation of the transverse relaxation time of single Ce spin states to understand the quick vanishing of the Rabi oscillation.

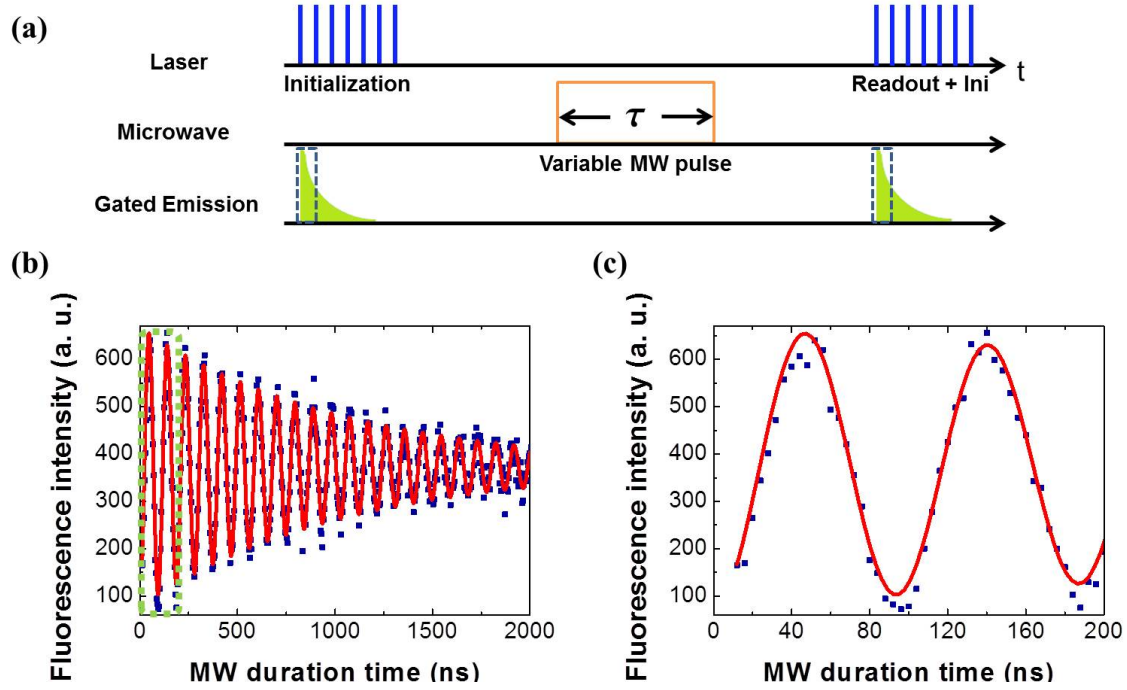

Figure 4.5: (a) Schematic diagram of pulse sequences for Rabi oscillation measurements. (b) Rabi oscillation of a single Ce ion, the ground state splitting at 650 MHz (c) Zoomed in curve of (b), to show the Rabi oscillation in the first two periods, with this the π and $\pi/2$ pulses can be determined.

4.3.3 Free induction decay

The Rabi oscillations observed in the previous section indicate the coherently driving of a single Ce electron spin. In the high contrast Rabi oscillation, the $\pi/2$ and π pulses can be determined. The free induction decay (FID) of single Ce ion is performed, to study the dephasing process in the electron spin evolution. The pulse sequences of the FID measurements are presented in Fig. 4.6(a), known as Ramsey sequences, where the MW $\pi/2$ pulses are applied to flip the electron spin in the Bloch sphere. The evolution of the spin state has been displayed on the Bloch sphere (see Fig. 4.6(b)).

The FID measurement of a single Ce ion is plotted in Fig. 4.6(c). Approximately 100 ns T_2^* time of single Ce spin states is obtained which is also in agreement with the Fourier transform of ODMR linewidth. Such short T_2^* time is mainly caused by the strong fluctuations of the local environment during the spin evolution. Two predicted sources might contribute to such strong environment fluctuations. (1) Strong nuclear spin bath induced by intrinsic ^{27}Al spins. (2) Electron spin bath generated by the impurities in the YAG crystal for example Cr, Fe, and vacancies in the crystal. The simulation (Fig. 4.6(c) red curve) of the FID process is performed by only considering the ^{27}Al nuclear spin bath. It shows fairly good agreement with the experimental results.

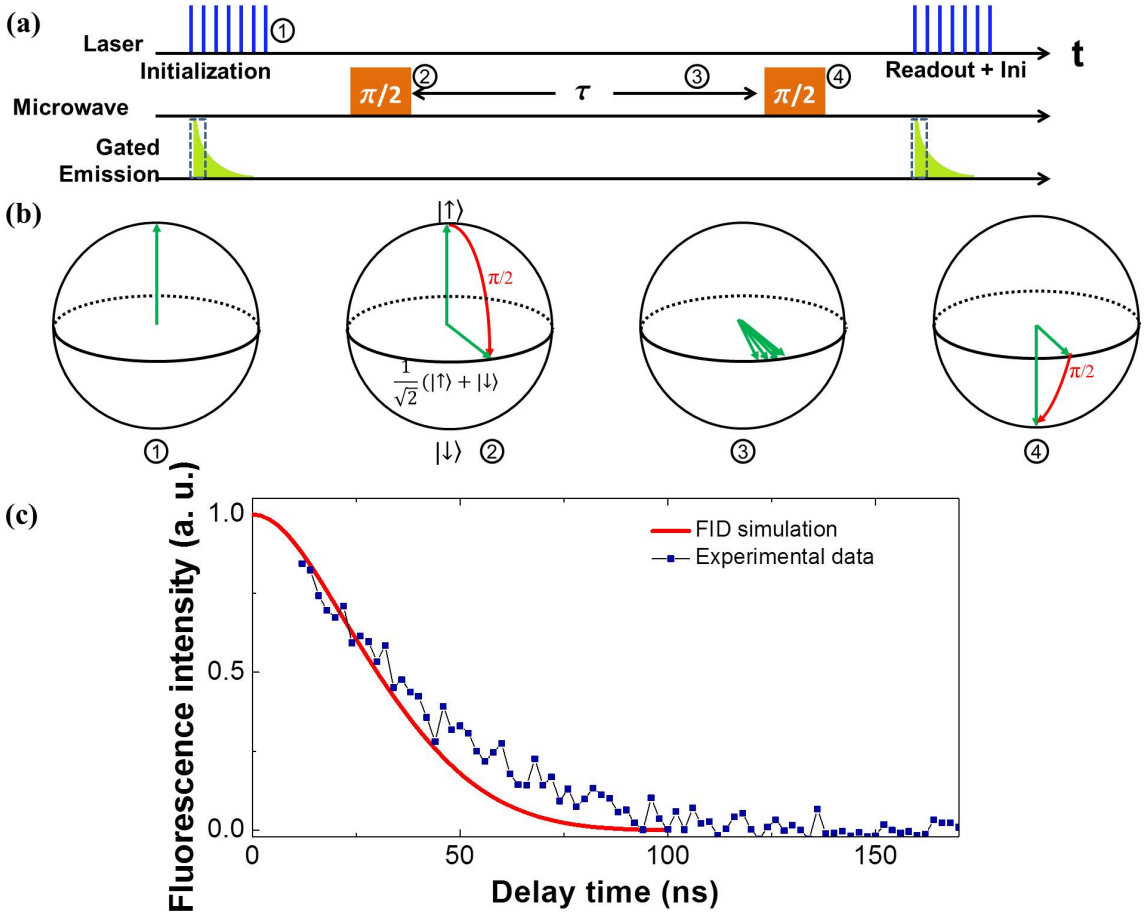

Figure 4.6: (a) Schematic diagram of pulse sequences for FID measurements. (b) Spin state evolution on the Bloch sphere. (1) Optically initialize the spin state ($|4f\uparrow\rangle$ "dark state"). (2) Rotate electron spin into the horizontal plane $\frac{1}{\sqrt{2}}|\uparrow\rangle + |\downarrow\rangle$ by applying MW $\pi/2$ pulse. (3) Dephase the electron spin freely during the delay time τ. (4) Apply the second $\pi/2$ pulse to project the electron spin into either $|\uparrow\rangle$ or $|\downarrow\rangle$ states. (5) Readout the state information by the second train of laser pulses. Meanwhile re-initialized the spin state to $|\uparrow\rangle$ 'dark state'. (c) FID measurements on a single Ce ion the ODMR resonant at 650 MHz showing ~100 ns T_2^* time.

4.3.4 Hahn echo of single Ce ions

There is a technique to suppress this fast dephasing process in the FID, which is known as spin (Hahn) echo sequence (see Fig. 4.7(a)) [136], where an additional MW π pulse is applied to flip the evolution direction. The spin evolution on the Block sphere is plotted in Fig. 4.7(b). In comparison with the FID pulse sequences, after duration time τ the electron spin dephases freely③, a MW π pulse is generated to reverse the evolution of the spin 180° around the X axis ($|\uparrow\rangle$, $|\downarrow\rangle$ direction) ④. It dephases to the opposite direction. The π pulse compensates the inhomogeneous dephasing of the Ce spin, resulting in the refocusing of the spin ⑥. The second $\pi/2$ pulse is applied to project the electron spin into either $|\uparrow\rangle$ or $|\downarrow\rangle$ state. Eventually, another train of the laser pulses is generated to readout the spin state and polarizes the spin to $|\uparrow\rangle$.

With the suppressed dephasing process, the decoherence time of the single electron spin is obtained as T_2 in the spin echo measurements. Hahn echo measurements of two dif-

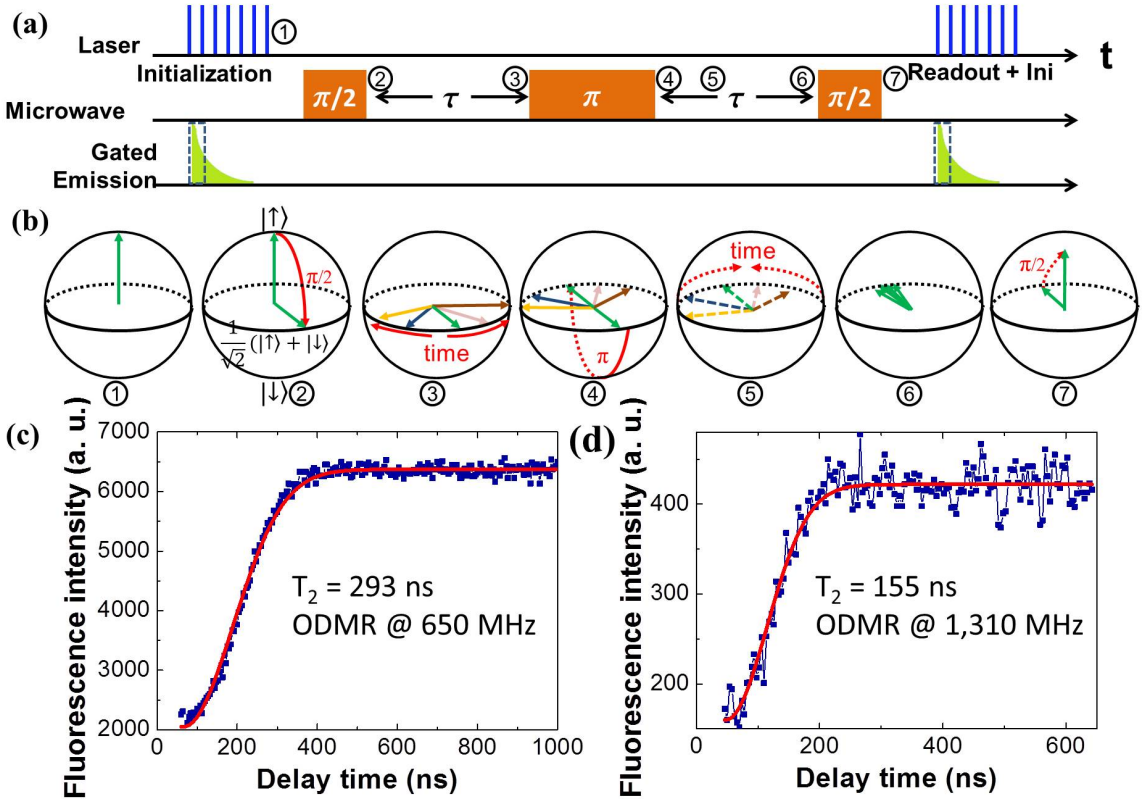

Figure 4.7: (a) Schematic diagram of pulse sequences for Hahn echo measurements. (b) Spin state evolution on the Bloch sphere. (c) Hahn echo measurements on a single Ce ion the ODMR resonant at 650 MHz. (d) Hahn echo measurements on a single Ce ion the ODMR resonant at 1,310 MHz.

ferent Ce ions are presented in Fig 4.7(c), (d). Single Ce ions showing different ODMR lines indicates the different orientation axis in the crystal. The one ODMR resonance at 650 MHz corresponds to 293 ns spin-spin relaxation time. It is longer than the T_2 time of another Ce center, whose the ODMR resonance is at 1,310 MHz. It indicates that the local environment influences the single Ce decoherence differently.

The T_2 and T_2^* time of single Ce ions are approximately four orders of magnitude shorter than their T_1 time. Such short coherence time might restrict further application, like exploring single Ce qubits as rare earth based quantum devices. It is indispensable to discover the origin, which leads to such short coherence time, and develops the method to overcome this obstacle. Eventually, extend the coherence time of single Ce spin qubit in order to demonstrate more applications.

4.4 Dynamical decoupling of single Ce spins

In solid state systems, the surrounding spin bath is usually playing an important role in reducing the center spin's coherence time. For Ce spins in crystals, every unit cell contains 40 ^{27}Al nuclear spins. In addition to the intrinsic ^{27}Al nuclear spin bath, there are many impurities and defects in the crystal acting as electron spin bath. Both spin baths result

in the decoherence of Ce electron spin. To figure out and quantify the influence of two spin baths respectively, dynamical decoupling(DD) methods are employed here.

DD as an evolution of Hahn echo sequence is widely studied and applied in the field of NMR and ESR since the 1950s [136, 137]. Recently with the development of quantum information [138, 139], DD is reviewed and developed as a standard tool, not only to extend the coherence time of qubit [140, 141], but also to investigate the spin bath in the noise spectroscopy [135]. There are various types of DD pulse sequences in the DD family. In terms of the robust against systematical pulse errors, such as periodic dynamical decoupling (PDD), Carr-Purcell-Meiboom-Gill (CPMG) [142, 143] pulse sequences are studied here.

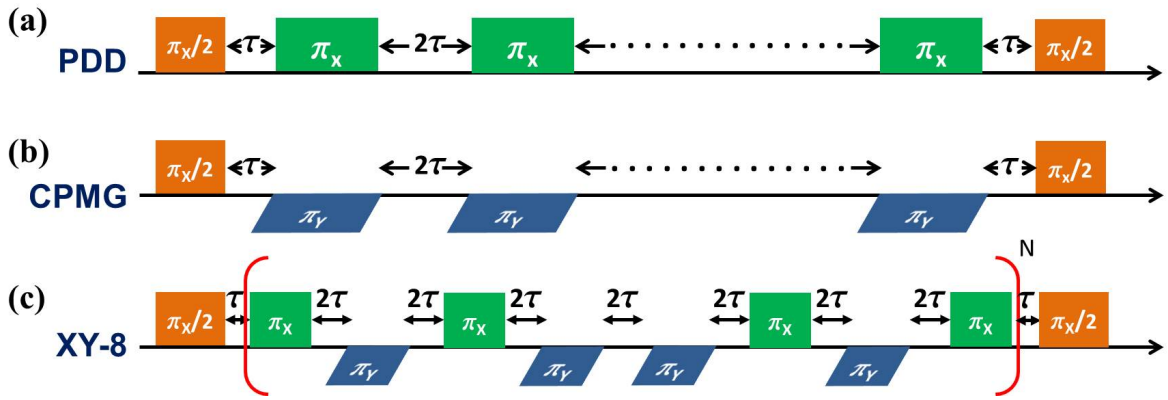

Figure 4.8: Schematic diagram of three types of dynamical decoupling pulse sequences: PDD, CPMG and XY-8.

PDD is similar to Hahn echo. It refocuses the spin evolution by periodically applying π pulses which are in phase with the $\pi/2$ pulse (see Fig. 4.8(a)). However, this in-phase property makes the PDD sequence very sensitive to the pulse errors. As shown in Fig. 4.9 (a) and (b), both the pulse angle error $\Delta\theta$ and phase angle error $\Delta\phi$ accumulate with the increasing number of π pulses. It results in an additional dephasing process of the spin coherence.

The experimental results of PDD applied in single Ce spin are shown in Fig. 4.9 (d). The T_2 time is prolonged with increasing number of π pulses. With 10 π pulses, the T_2 time is prolonged from 163 ns to 1.6 μs. However, the amplitude of coherence also decreases dramatically as the number of π pulses increase. It is difficult to observe any signal when the number of pulses is more than 10. Technically, π pulses are generated by the PulseBlaster card with only 2 ns time resolution. The normal duration of the π pulses is $\sim$22 ns, which is only 10 times higher than the time resolution of the PulseBlaster card. It reveals imperfections of the π pulses. The fidelity of the coherence decreases with increasing number of π pulses as plotted in Fig. 4.9(c). In general, the DD pulse sequence is capable of extending the coherence time of single Ce ions. However, current PDD technique doesn't show large space to improve the situation, due to the imperfections of the MW pulses. If we can find a more robust DD pulse sequence, the Ce ion might be decoupled from the environment better.

CPMG pulse sequences are introduced to overcome the issue of the inaccuracy of MW pulses. As shown in Fig. 4.8, in CPMG pulse sequences, all the π pulses have a 90° phase

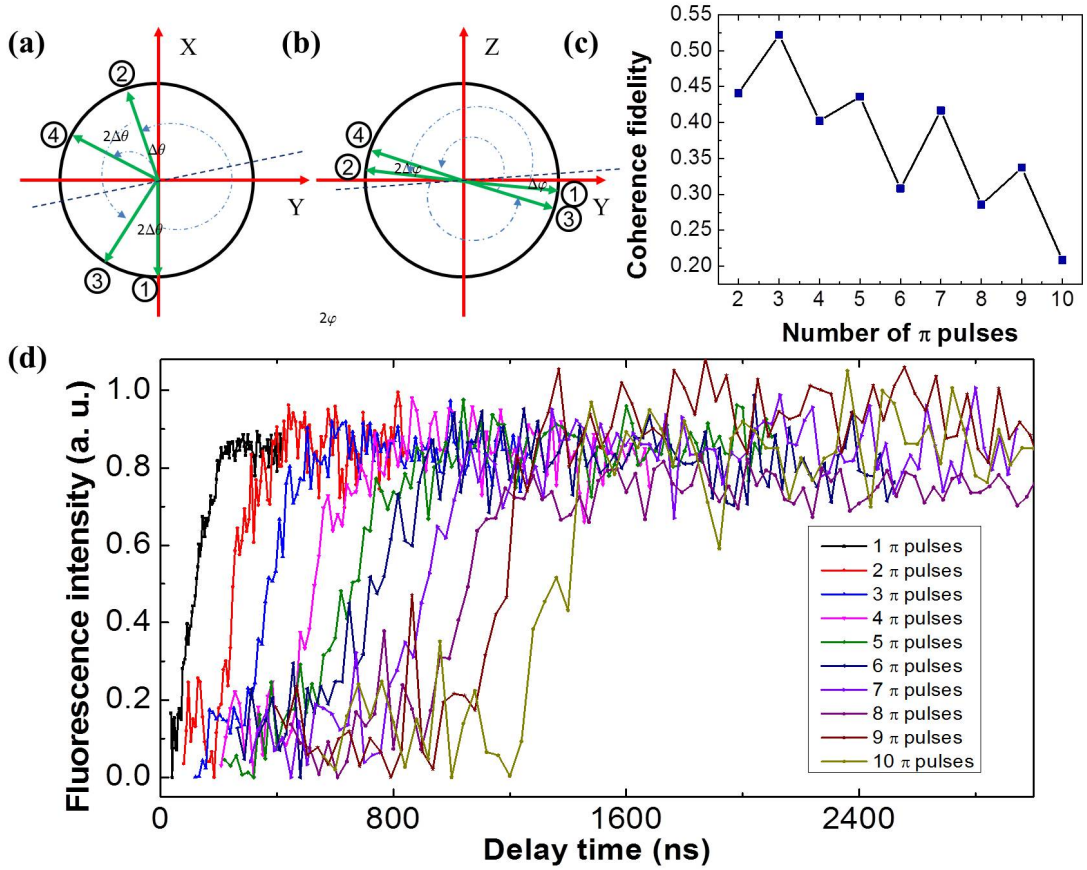

Figure 4.9: (a) Accumulation of pulse angle error. (b) Accumulation of pulse phase error. (c) Fidelity with the number of π pulses. (d) PDD of a single Ce ion, the resonance frequency of the ODMR line is 650 MHz. All the curves have been normalized.

shift. By doing so, the evolution of spin state is locked along the Y axis and therefore the pulse error accumulation effect is removed. This prediction is in agreement with the experimental results presented in Fig. 4.10(b). In comparison with PDD pulse sequence, the fidelity of the coherence is preserved much better under CPMG pulse sequences. No obvious decay of the signal (coherence) contrast is observed up to 1,000 pulses as shown in Fig. 4.10(c). With the significant improvement, we finally applied 24,576 pulses to extend the coherence time by four orders of magnitude, from 290 ns to 2.0 ms. However, the prolonging of T_2 time with number of π_Y pulses is not yet achieving $2T_1$ time. It is restricted either by the phase angle error accumulation in the YZ plane or the intrinsic material issue.

A disadvantage of CPMG sequence is that its robustness to pulse errors only holds for the initial state along Y direction. XY-8 shown in Fig. 4.8(c) is known as robust pulse sequences without this limitation [144]. The combination of π_X and π_Y pulses is helpful to suppress both the pulse angle and phase angle errors for the arbitrary initial state. The XY-8 pulse sequence is not performed in the experiment since its performance is similar to the CPMG pulse sequence in extending the coherence time.

Moreover, Fig. 4.11 shows the simulated decoherence time corresponding to the number of

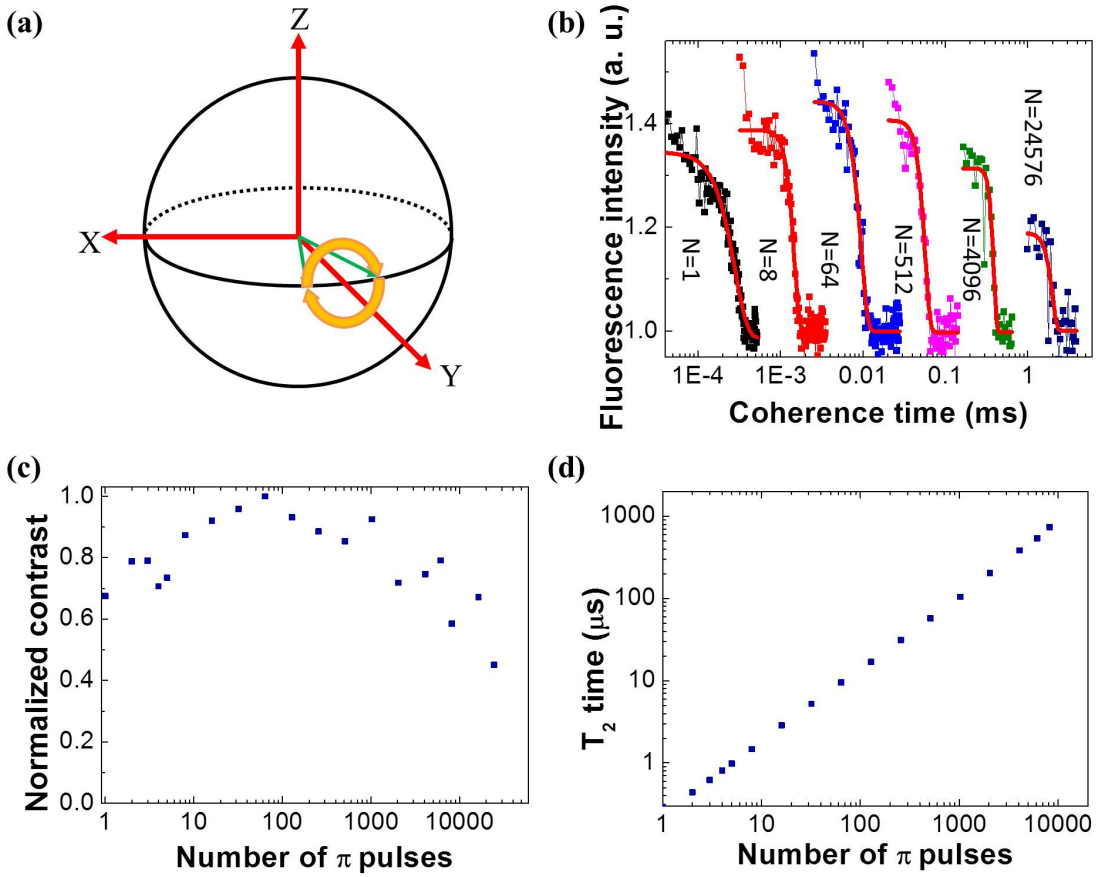

Figure 4.10: (a) Schematic diagram of pulse sequences for CPMG. (b) Spin state evolution on the Bloch sphere. (c) CPMG of a single Ce ion, the resonance frequency of the ODMR line is 650 MHz. All curves have been normalized. (d) The relation between number of π pulses and prolonged T_2 time.

π_y pulses by CCE method, where only ^{27}Al nuclear spin bath is under consideration (the spin properties of ^{27}Al are introduced in Chapter II). The decoherence of the Ce ion shows same order of magnitude as the experimental data. It suggests that the Al nuclear spin is the major source leading to the decoherence process in single Ce spin qubits. However, the simulated results didn't perfectly fit the experiment data. It indicates that electron spin baths also influence the decoherence of single Ce ions. Normally both electron and nuclear spin baths influence the decoherence process of single qubits. The former behaves like a classical macroscopic environment, where the noise spectrum is a continuous function, modeled as a Lorentzian function with long spectral tails. This results in $T_2 \sim N^{2/3}$ relation between decoherence time to the number of π_Y pulses. In comparison, the nuclear spin bath indicates a hard cutoff in the noise spectrum, revealing a linear dependence of the decoherence time on the number of π_Y pulses [140].

The relation between the number of CPMG π_Y pulses and decoherence time of single Ce spin qubits is investigated and plotted in Fig. 4.10(d). $T_2 \sim N^{0.88}$ is obtained by fitting the experimental data. It suggests that the decoherence process of single Ce spin qubits is influenced by both electron and nuclear spin baths. In YAG crystal, the electron spin bath comes from the impurities in the crystal such as residual transition metals like Cr^{3+}

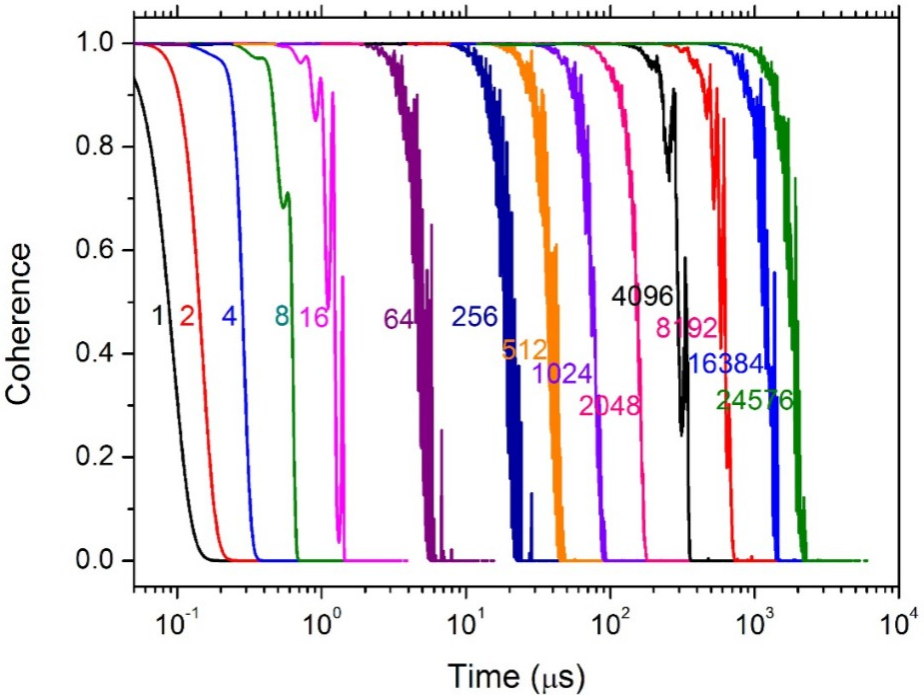

Figure 4.11: Calculated decoherence time with the number of π_y pulses. The noise only from Al nuclear spins is considered. The figure is reproduced from [145].

and Fe^{3+}, and vacancies introduced during the crystal growth, while the nuclear spin bath is mainly contributed by intrinsic ^{27}Al nuclear. We can also deduce from the data that changing to a low spin host material such as Y_2SiO_5 crystal will help to prolong the coherence time of single Ce spin qubits.

4.5 Coherent properties of single Ce ions in LuAG crystal

In the previous section, the noise spectrum of the local environment of single Ce ions in YAG has been studied. It reveals that single Ce ions have a strong interaction with the host crystals. If a low spin matrix (or a high spin matrix) host crystal is selected, the decoherence time of single Ce qubits will be improved (or get worse). To confirm the influence of nuclear spin bath with the decoherence time of Ce qubits, Ce ions doped in LuAG have been investigated.

Lutetium aluminum garnet ($Lu_3Al_5O_12$, LuAG), is another type of laser crystals. It has very similar lattice structure to YAG as introduced in Chapter II. Regarding the optical properties of Ce: LuAG, it is similar to Ce:YAG. The maximum absorption wavelength is around 450 nm. The fluorescence shows strong phonon assisted sideband emission in the range of 470-625 nm. The optical lifetime of the lowest $5d$ states is ∼70 ns. It has also the same optical selection rules as Ce:YAG, so that circularly polarized light induces the optical pumping in the ground state. In an ultra-pure LuAG crystal, single Ce ions are optically resolved under the confocal microscope as displayed in Fig. 4.12(a).

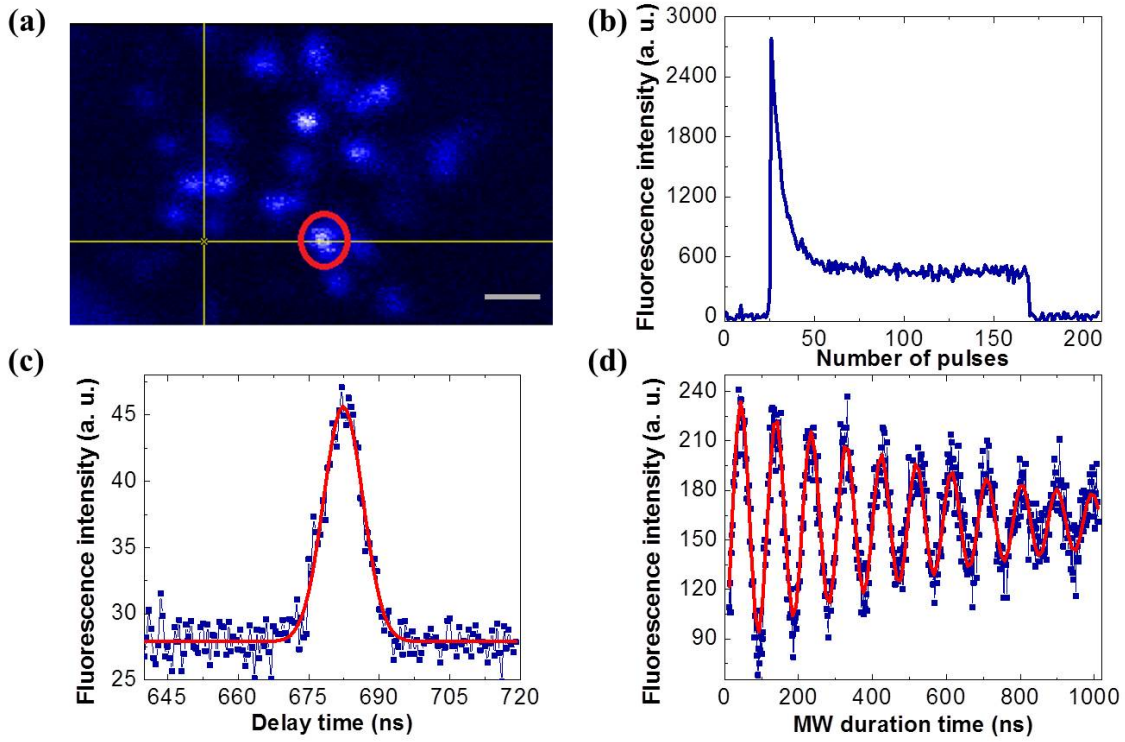

Figure 4.12: (a) Laser scanning image of single Ce ions in LuAG crystal. Scalar bar represents 1 μm. (b) Optical initialization of single Ce:LuAG. (c) ODMR of a single Ce ion in LuAG presents a resonance line at 680 MHz. (d) Rabi oscillation of a single Ce ion in LuAG.

To survey the coherent properties of single Ce ions in LuAG, the experiments have been performed with the same condition as previously. The ground spin state of Ce:LuAG is able to be optically initialized by a train of circularly polarized laser pulses as demonstrated in Fig. 4.12(b). Following to the spin state initialization, the ODMR spectrum of the ground spin states has been obtained as shown in 4.12(c). The splitting of the ground spin states is 680 MHz with 10 MHz FWHM. After the acquirement of the ground state spin transition, the resonance MW radiation is chopped so as to observe the Rabi oscillation as expressed in Fig. 4.12(d).The Rabi oscillation of a single Ce:LuAG vanishes in 1$\sim$2 μs, indicating strong fluctuations of the local environment.

After the obtainment of Rabi oscillation, the Ramsey pulse sequence is applied to determine the dephasing process of single Ce ions in LuAG as illustrated in Fig. 4.13(a). The FID signal reveals the T_2^* of Ce ions in LuAG to be $\sim$70 ns. To investigate the decoherence time of single Ce in LuAG, Hahn echo is performed where the data is plotted in Fig. 4.13(b), showing $\sim$260 ns T_2 time. In comparison with Ce:YAG, both T_2 and T_2^* time of Ce:LuAG ground spin states are reduced. Such fast dephasing and decoherence processes are mainly caused by the strong local nuclear spin bath, where the ^{169}Lu and ^{175}Lu represents much stronger nuclear spin momentum in comparison to ^{89}Y (for more details please see Chapter II).

The CPMG pulse sequence is applied here, not only to extend the coherence time, but also to characterize the noise spectrum. It is shown in Fig. 4.13(c) that the coherence time is prolonged with the increasing the number of π_Y pulses. As it is introduced previously, the

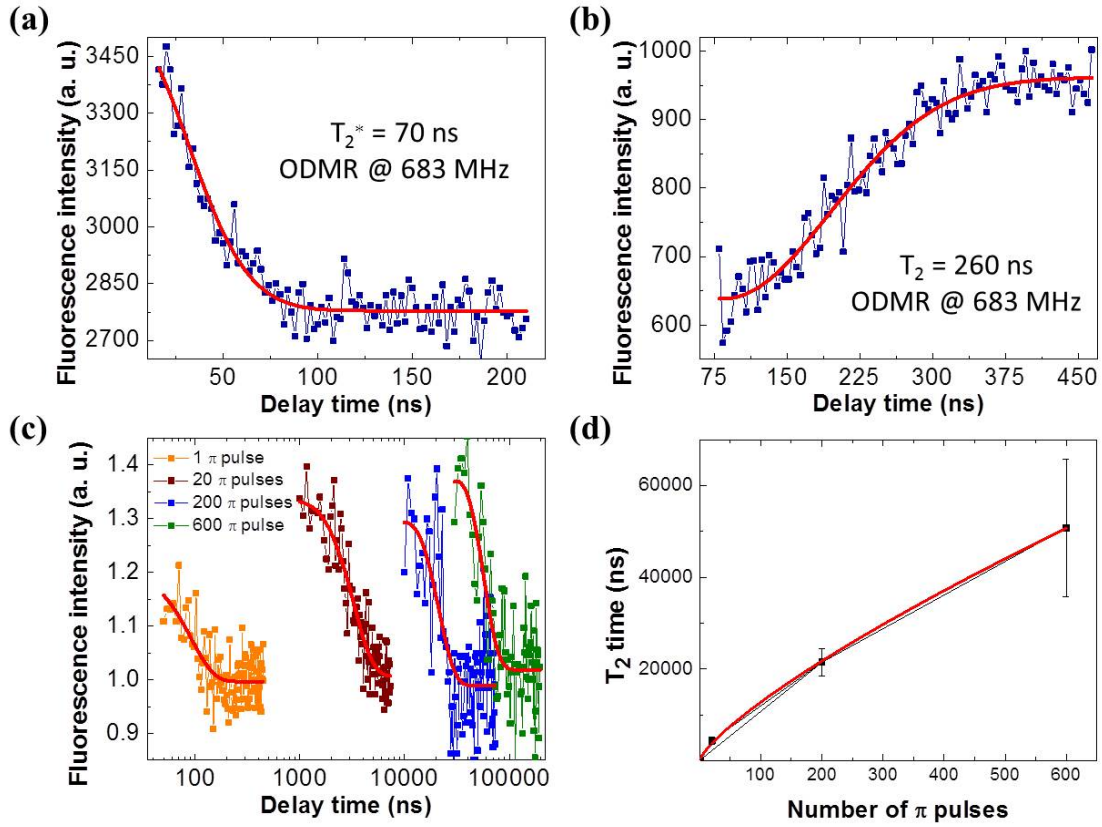

Figure 4.13: (a)FID curve of a single Ce:LuAG revealing ∼70 ns T_2^* time. (b) Hahn echo measurement suggests ∼260 ns T_2 time of single Ce:LuAG. (c) CPMG of a single Ce ion in LuAG. (d) The relation between the number of π pulses and prolonged T_2 time of a single Ce in LuAG.

nuclear spin bath of single Ce ions in LuAG is stronger than in YAG crystals. This yields to shortening of T_2 and T_2^* time. In addition, when we plot the dependence of number of decoupling pulses with the prolonged decoherence time (Fig. 4.13(d)), it suggests that $T_2 \sim N^{0.78}$. The noise spectrum shows that the electron spin bath contributes more in comparison with the case in YAG. It also implies that different host material contains various impurities resulting in different noise spectrum. For the next step, the improvement of the performance of the matrix materials is essential. When low weak spin bath host crystal, for example, Y_2SiO_5 crystal, is used, the nuclear spin bath interacts with Ce will be weaker in comparison with the current situations. It indicates the extension of the coherence time of single Ce spin qubits, which will offer more complex quantum operations.

4.6 Conclusion and outlook

In this chapter, the coherent properties of single electron spins of Ce in YAG and LuAG have been investigated at cryogenic temperature. Single Ce electron spins present impressive coherent properties as one of the good candidates of solid-state qubits. With the prolonged T_1 time and special optical selection rules, the ground spin state of a

single Ce ion has been optical initialized with more than 97.5% fidelity. By assistance of MW radiation, ODMR of single Ce ions has been performed so as to determine the resonance of ground state spin transition. Coherent manipulation of single Ce ground spin states including Rabi, FID, Hahn echo has been demonstrated. We also prolonged the coherence time of single Ce spin qubits by the DD pulse sequences. Meanwhile, the acquirement of the noise spectrum suggests that both nuclear and electron spin baths affect the spin qubit intensively. Shifting to a low spin bath material will significantly suppress the nuclear spin bath. Another spin noise induced by the electron spin bath can be reduced by carefully removing the impurities and defects in the host material, for example, improve the crystal growth procedure or perform the post-growth annealing.

Furthermore, the optical excitation of single Ce ions through phonon sideband transition has one restrict requirement. There exists one and if only one Ce ion in the focal volume. Otherwise, additional Ce ions will introduce background and influence the operation fidelity. It indicates the huge challenge to scale the system up by this approach. Meanwhile, the spin states of single Ce ions are driven by MW radiation. The operation duration time is more than 20 ns. It is technically arduous to fast coherent manipulation of spin transition by MW radiation.

On the contrary, resonant excitation and all-optical addressing single qubits attract more attentions since it offers several incomparable advantages. For example, exciting single Ce ions through the ZPLs display the capability of spectral selectivity. In addition, the forming of the Λ system will construct a new platform for fast and accurate addressing single Ce spin qubits all-optically. In general, the resonant excitation and all-optically addressing single Ce spin qubits will pave the way to construct all-optical addressable solid-state qubits.

Chapter 5

Single Ce ions under CW laser excitation

Due to the close proximity of optically excited states to band edges in the solid state, photo-induced phenomenon like photo-ionization and charge dynamics [146], are often found in solid-state systems like quantum dots [147] and NV centers in diamond [148]. Solid-state quantum systems suffer from these unwanted photo-induced dynamics. For single rare earth ions, charge dynamics is not yet clear whether these effects exist.

In this chapter, we observe the photo-induced fluorescence dynamics of single Ce ions with a CW laser excitation. A novel method is developed to suppress these unwanted dynamics. Moreover, an extended charge dynamics model is proposed to understand the underlying processes. This result allows us to realize all-optical addressing of single Ce qubits in the following chapter.

5.1 Fluorescence time trace of Ce ions under CW laser excitation

In Chapter III and IV, single Ce ions show good photostability (constant fluorescence) under pulsed laser excitation even for a couple of days. However, if a single Ce ion in YAG bulk crystal is instead excited through a CW laser, the fluorescence, continuously monitored by an APD, shows interesting dynamics. As shown in Fig. 5.1(b), the fluorescence intensity presents high yield at the beginning of the CW laser excitation, and decays smoothly to the background level in a few seconds. Note that the low fluorescence intensity by pulsed laser is due to low laser power.

To exclude the effect of sample selection, we also studied the fluorescence of Ce:YAG nanoparticles under the same experimental conditions. Ce:YAG nanoparticles are prepared by a sol-gel pyrolysis method with a typical diameter ∼40 nm. The dopant concentration of Ce is 100 ppm, so that each single nanoparticle contains in average 50∼100 Ce centers. As shown in Fig. 5.2(b), the fluorescence intensity of a single Ce:YAG nanoparticle shows the same decay behavior with a much faster decay rate. The fluorescence decay

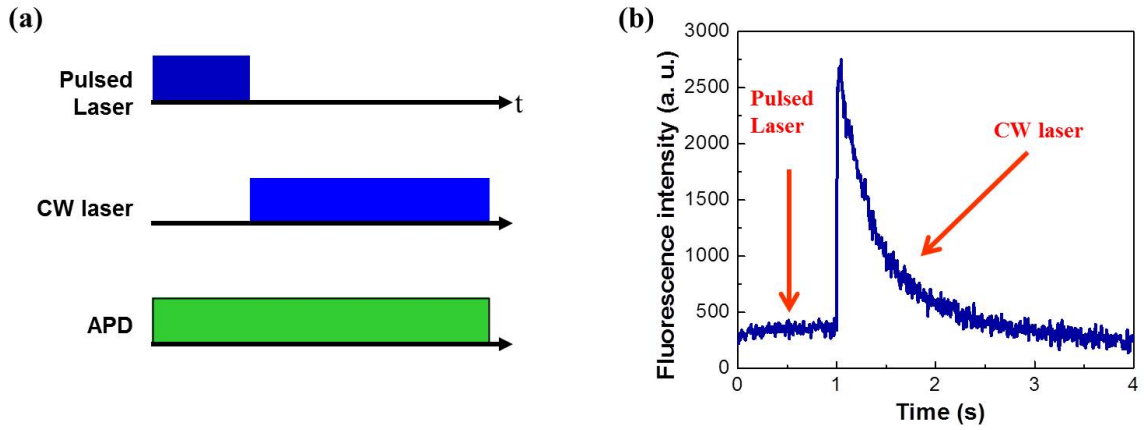

Figure 5.1: Fluorescence time trace of a single Ce ion under a CW laser excitation. (a) Scheme of pulse sequence: the femtosecond pulsed laser is irradiated for 1 s. When it is switched off, a CW laser is turned on simultaneously. The APD is constantly monitoring the fluorescence of the single Ce ion. The femtosecond pulse laser wavelength at 448 nm has a repetition rate of 2.5 MHz with 10 μW average laser power. The CW laser is a blue diode laser operating at a wavelength of 451 nm, and its power is 150 μW. (b) Fluorescence time trace of a single Ce ion under pulsed and CW lasers excitation. It should be noted that this decay curve is taken as time traces, i.e. continuous monitoring the fluorescence intensity of the single ion.

is thus a common phenomenon in different samples, indicating that it is photo-induced by the CW laser excitation. These results explain why in previous studies the attempts of detecting single Ce ions under CW laser excitation were unsuccessful.

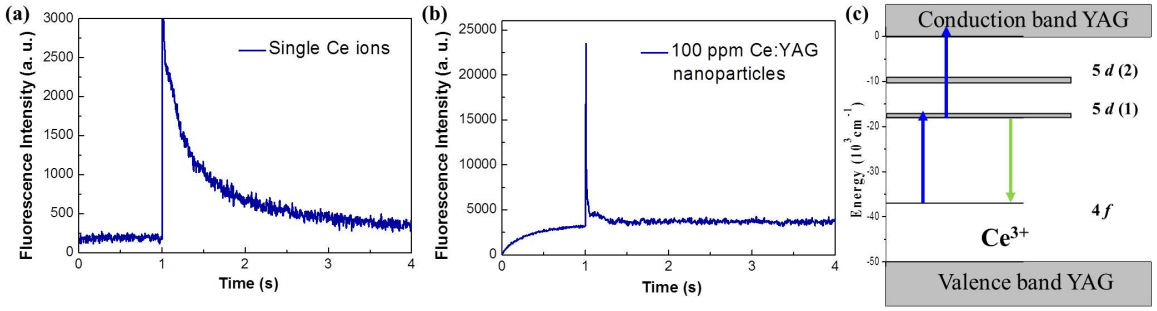

Figure 5.2: Fluorescence time trace of Ce ions under CW excitation (a) single Ce ions in YAG bulk crystal. (b) tens of Ce ions in YAG nanoparticles (10 ppm). (c) Scheme of photo-induced charge dynamics of Ce:YAG.

Normally, non-photostable single photon emitters in solids produce either photo-bleaching or photo-blinking. Photo-bleaching is the photo-induced alteration of single emitters, e.g. organic molecules, such that it is permanently unable to fluoresce (see Fig. 5.3(a) [146]). When a single photon emitter shows photo-blinking, it alternates between a bright state and a dark state, resulting a step-wise fluorescence signal. For example, charge dynamics phenomenon show in quantum dots (Fig. 5.3(c)), and NV centers in diamond present photo-blinks due to the charge dynamics in between NV^- and NV^0 states (Fig. 5.3(c) [148]). However, the fluorescence decay of single Ce ions (Fig. 5.1) is quite

unusual and distinct from the charge dynamics described here.

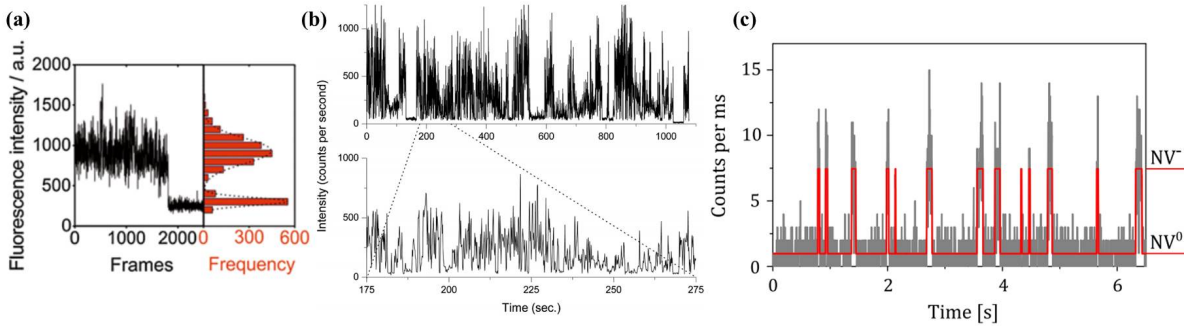

Figure 5.3: Fluorescence time trace of three types of single photon emitters. (a) Single molecule performs photo-bleaching. (b) Quantum dots show photo-blinking. (c) NV centers in diamond display charge dynamics in between NV^- and NV^0 states. Figures are reproduced from [146–148]

From the literature we learn that as soon as Ce^{3+} is pumped to the excited state [149], it has a possibility to absorb one more photon, be promoted to the conduction band and be photo-ionized to Ce^{4+} [150, 151], where the Ce^{4+} is non-fluorescing (see Fig. 5.2(c)). It can explain why Ce ions do not show fluorescence anymore after a short time of CW laser excitation (the end of decay curve). However, the gradual fluorescence decay of single Ce ions is counterintuitive. How this process happens and why single ions finally stay at Ce^{4+} is not clear. Importantly, the identification and application of resonant excitations of single Ce ions are also blocked by this non-desired photo-induced process since a narrow linewidth single mode CW laser is required to resolve the optical transitions. Finding a method to suppress it is essential for applications relying on resonant excitations, like all-optical control of single Ce spin qubits.

5.2 Suppressing the fluorescence decay of a single cerium ion with engineered laser sequence

The gradual decay from a single Ce fluorescence time trace suggests that exciting Ce ions by CW laser are insufficient. In comparison, single Ce ions show good photostability under the femtosecond pulse laser excitation. It indicates that the pulsed laser plays the key role of keeping Ce photo-stable. A preliminary experiment is performed as presented in Fig. 5.4. The pulsed laser and CW laser are switched alternatingly. The plotted fluorescence time trace of the Ce ion shows that after 1 s low power of the pulsed laser irradiation, the Ce again displays high fluorescence yield when the CW laser is switched on. It suggests that the femtosecond laser pulses by some means improve the performance of the single Ce ions.

To investigate how the pulsed laser interfaces with Ce ions, the following experiments have been performed:

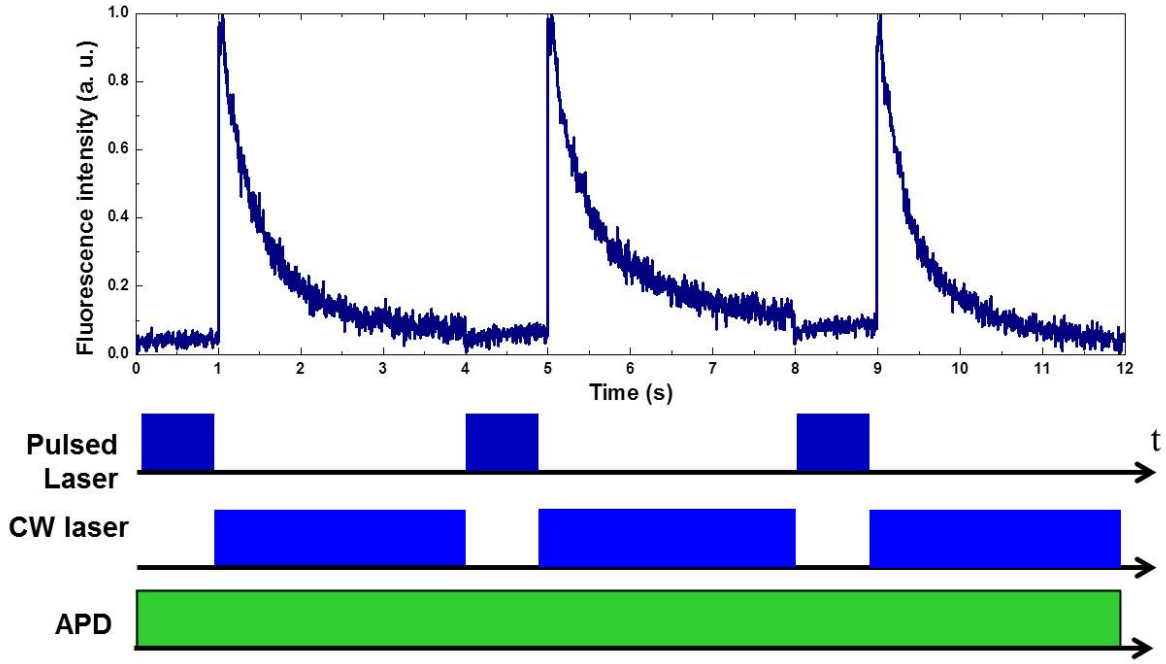

Figure 5.4: (a) Fluorescence time trace of a single Ce ion under pulsed and CW lasers excitation. (b) Scheme of laser pulse sequences.

1. Varying the pulsed laser power. To figure out the power dependence in the photo-induced process, the power of the femtosecond pulsed laser is varied, as shown in Fig. 5.5(a). The pulse sequence is similar to Fig. 5.1(a). After the single Ce goes "dark", the femtosecond pulsed laser is generated within 2 s time. When the pulse laser is switched off, the CW laser is turned on. As presented in Fig. 5.5(a), each curve corresponds to different pulse laser power (from 5 μW to 180 μW). It is important to monitor the fluorescence intensity of single Ce ions when the CW laser is switched on, which corresponds to the starting peaks of the decay curves ("starting point" at 2 seconds in Fig. 5.5(a)). These peaks indicate whether a single Ce has been brought "normal"(bright) after the pulsed laser irradiation.

The "starting point" (Fig. 5.5(b)) shows low fluorescence yield when the pulse laser power is kept low (5, 10 μW). It alludes that at the "starting point" Ce is not fluorescing with high efficiency. As soon as the pulse laser power is higher than 20 μW, fluorescence intensity at the "starting point" stays at the same level. It indicates that Ce is completely "normal" again by the pulsed laser irradiation. In addition, the CW laser displays huge power fluctuation in the first 0.2 s operation time, resulting in the wiggling around 2.1 s in the fluorescence time trace.

2. Varying the duration time of the pulsed laser. We keep the pulsed laser power low (5 μW). The duration time of the pulsed laser is varied from 0.1 s to 3 s. The CW laser power is kept at the same condition as in previous experiments. The fluorescence time trace of a Ce is recorded and plotted in Fig. 5.6(a). If the operation time of the pulsed laser is short (0.1 s), Ce displays almost no fluorescence when the CW laser is turned on. With increasing repumping time of the pulsed laser, the "starting point" of the

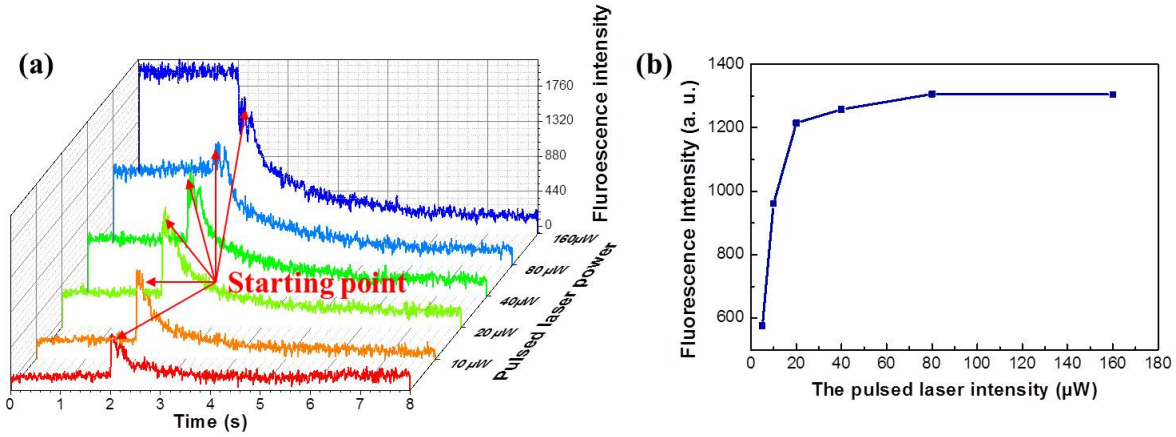

Figure 5.5: (a) Fluorescence time trace of a Ce ion. The CW laser is kept in the same condition. The pulse laser is operating on the wavelength at 440 nm with reputation rate 2.5 MHz, which its power is varying from 5 μW to 160 μW. The CW laser has wavelength at 450 nm, power is 150 μW. (b) Fluorescence yield of the "starting point" of the single Ce ion when the CW laser is switched on.

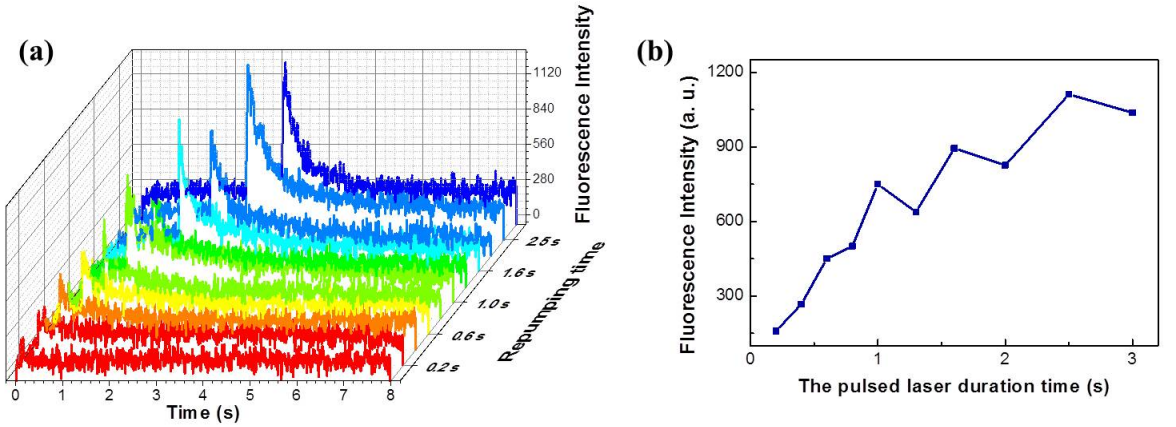

Figure 5.6: (a) The relation between pulsed laser irradiation time and Ce fluorescence decay. The pulsed laser power is kept low ($\sim$ 5 μW). The duration time of the pulsed laser is changed. Meanwhile, the CW laser power is constant. (b) Fluorescence yield of the "starting point" of the single Ce ion when the CW laser is switched on.

fluorescence time trace rises up. It indicates that the photo-induced dynamics starts to overcome after long time irradiation of the pulsed laser.

3. Varying the wavelength of the pulsed laser. The power of the CW and the pulsed laser is kept constant, while the wavelength of the pulsed laser is tuned from 405 nm to 448 nm. The "starting point" displayed in Fig. 5.7(a) reveals, there is no difference in between 415 nm to 448 nm. However, if the wavelength of the pulsed laser is shorter than 410 nm, it might cause reduced Ce^{3+} fluorescence at the "starting point". It is also necessary to point out that the band gap of the YAG crystal is 6 eV. If the excitation laser wavelength is shorter than 206 nm (two-photon absorption of 412 nm), the electrons will be directly excited from valence band to conduction band.

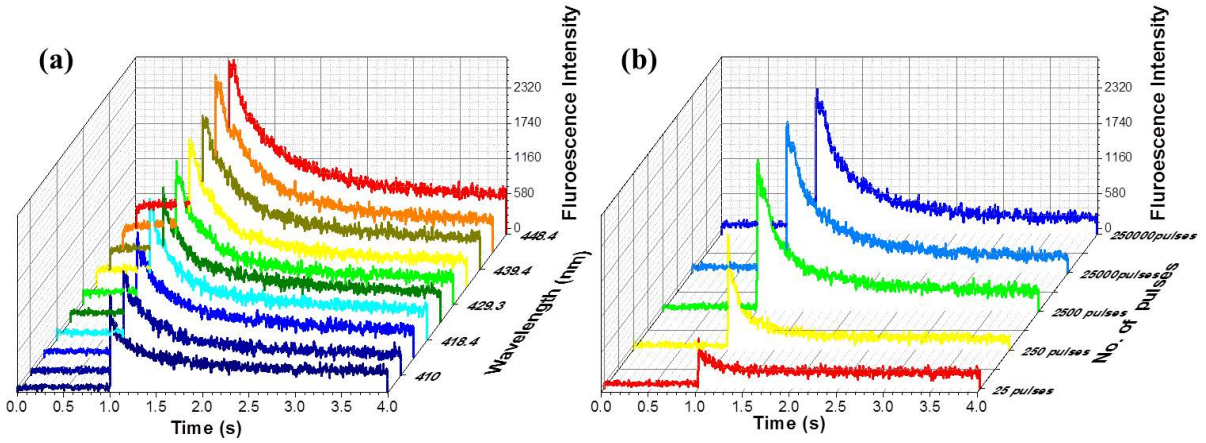

Figure 5.7: (a) Fluorescence time trace of a Ce ion. The CW laser is kept constant. The wavelength of the pulsed laser is tuned from 405 nm to 448 nm. (b) Varying the number of laser pulses. The power of the pulsed laser is kept high (460 μW with 2.5 MHz repetition rate, the wavelength at 424 nm). The number of laser pulses is varied from 25 to 250,000. Meanwhile, the CW laser power is constant.

All the evidence presented here indicate that irradiation of the pulsed laser somehow restores the single Ce ion who was non-fluorescing after the CW laser excitation. To figure out how many laser pulses which are needed to restore the Ce fluroescence back, the number of laser pulses is varied. In the experiment, the power of the femtosecond pulse laser is kept high (460 μW with 2.5 MHz repetition rate, the wavelength at 424 nm). The number of laser pulses is varied from 25 pulses to 250,000 pulses. Meanwhile, the CW laser power is constant. As presented in Fig. 5.7(b) that after 25 pulses irradiation, the "restoration" is insufficiency. It suggests that at least 250 femtosecond laser pulses in 1 s are required to bring the Ce ions back to Ce^{3+}. It should be noticed that if 7% collection efficiency is under consideration, 250 laser pulses per second contributes less than 17 photons per second as additional background.

Furthermore, for the laser pulse length, we observe that femtosecond laser definitely can re-charge the Ce ion and the pulsed CW or even a picosecond laser will not help the Ce ions to go back to Ce^{3+}. This suggests that repumping Ce ions depend on a critical pulse length. When either laser pulse length is shorter than this critical pulse length, for example, the femtosecond laser pulse, the restoring process works. When the pulse length is longer than the critical pulse length, such as 10 picosecond laser, the restoring process fails.

5.3 Proposed model of single Ce photo-induced dynamics

In this section, a model is proposed to understand the single Ce photo-induced dynamics. It includes the excited state absorption, electron transfer through deep level traps and two-photon excitation processes.

5.3.1 Excited state absorption

To understand the photo-induced dynamics, we first consider excited-state absorption process induced by the CW laser excitation. Figure 5.2(c) displays the band gap of YAG crystal and the relevant energy levels of Ce^{3+} within it. Since the energy gap between the conduction band and $5d$ state is smaller than the CW photon energy, the electron staying in $4f$ state can be pumped to the conduction band through excited-state absorption. Consequently, the ions are converted from state Ce^{3+} to the non-fluorescing Ce^{4+} state and will stay at Ce^{4+} state. So the CW laser itself can only result in fluorescence dynamics like photo-bleaching in single molecules. However, the fluorescence decay rather than a jump is not understood using the current model.

5.3.2 Deep level traps in YAG crystal

Regarding the literature, scientists reported that in YAG crystals, rare earth ions can be surrounded by a lot of impurities, for example, Cr, Fe impurities, Al and O induced vacancies introduced when the crystal was grown [152]. Some of these impurities play a critical role of deep level traps lying in between the conduction and valence band of YAG crystal (see Fig. 5.8(d)) [153, 154]. However, the precise location of the deep level traps is still under investigation. We assume here that deep level traps are lying in between the lowest $5d$ states and the conduction band. We correlate the observed counterintuitive gradual fluorescence decay with the reported deep level traps, and propose the following photo-induced dynamics:

Under the CW laser excitation, the single Ce ion is excited to the $5d$ excited state. It might decay back to the $4f$ state with an emitted photon. However, it is also possible that it absorbs an additional photon and is promoted to the conduction band. Thus Ce^{3+} is photo-ionized to non-fluorescing Ce^{4+} ions. Once the Ce^{3+} has been photo-ionized to Ce^{4+} states, by tunneling from nearby deep level trap the Ce ion might capture an electron to compensate the lost one, thus recovering into the Ce^{3+} charge state. (Also another possibility is that the electron in the deep level traps is excited to the conduction band, and eventually, scattered and re-captured by the Ce ion.) As the result, Ce ion is converted back to fluorescing Ce^{3+}. If the CW laser is constantly irradiating, the Ce^{3+} ion is photo-ionized to Ce^{4+} from time to time. Donors in the deep level traps are successively transferred to converted Ce^{4+} into Ce^{3+}. The decline in fluorescence indicates a gradual reduction of the number of donors and the correlated probability to the gradual decrease of the fluorescence intensity. Eventually the deep level traps are empty resulting in Ce staying in non-fluorescing Ce^{4+} state as shown in Fig. 5.8(a), (c).

According to the proposed model, we perform the CW laser power dependent measurements with the fluorescence decay of single Ce ions to understand smooth gradual decay behavior of Ce ions. As shown in Fig. 5.9, the fluorescence time traces of a single Ce ion are recorded with different CW laser power, while the pulse laser power and the duration time are constant. The pulse sequence is the same as Fig. 5.1. First, the single Ce ion is optically initialized by the pulsed laser. After one second, we switch off the pulsed laser

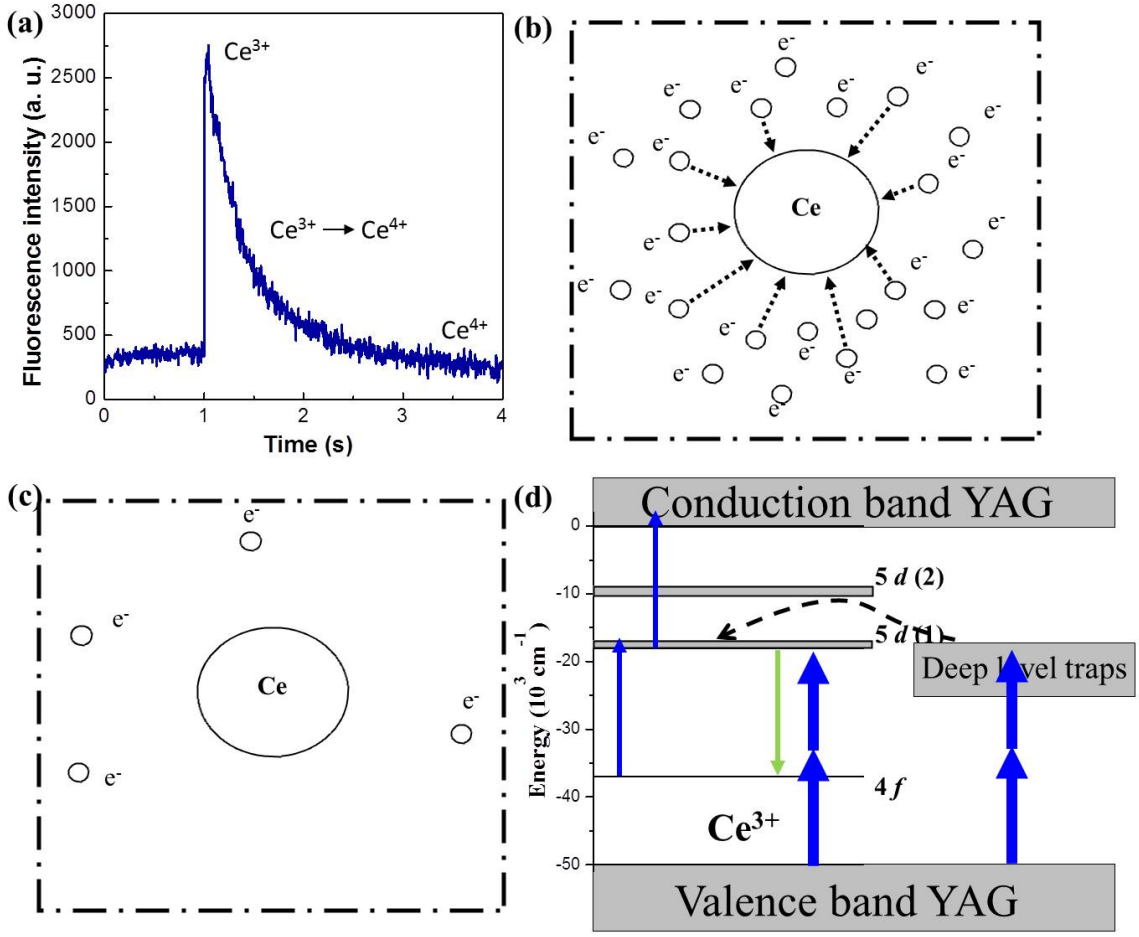

Figure 5.8: (a) Fluorescence time trace of a Ce ion. High fluorescence yield corresponds to the trivalent state of cerium and low fluorescence yield represents Ce^{4+} state. (b) Donors in the deep level traps are empty and resulting Ce stays in Ce^{4+} states. (c) Electrons in the deep level traps are restored by high peak intensity femtosecond laser pulses. (d) The proposed model for the charge dynamics of single Ce ions.

and turn on a CW laser simultaneously. Each decay curve corresponds to different CW laser power between 50 μW to 500 μW. It can be clearly observed in Fig. 5.9, if the CW laser power is high, the Ce ion shows strong fluorescence intensity at the "starting point". Meanwhile, the increase of the CW laser power indicates the faster decay rate in the decay curves. This phenomenon implies the correlation of the decay speed with the CW laser power and excitation-emission-reexcitation cycling speed.

5.3.3 Two-photon excitation process

When the non-fluorescing Ce ion is irradiated by the high peak power femtosecond laser pulses, Ce can be excited again by the CW laser, indicating the possibility of restoring the deep level traps (see Fig. 5.8(d)). We suspect that there is some two-photon excitation process involving in this pulsed laser irradiation. Once we shift our Ce:YAG optical setup to another optical table and couple the femtosecond pulsed laser through

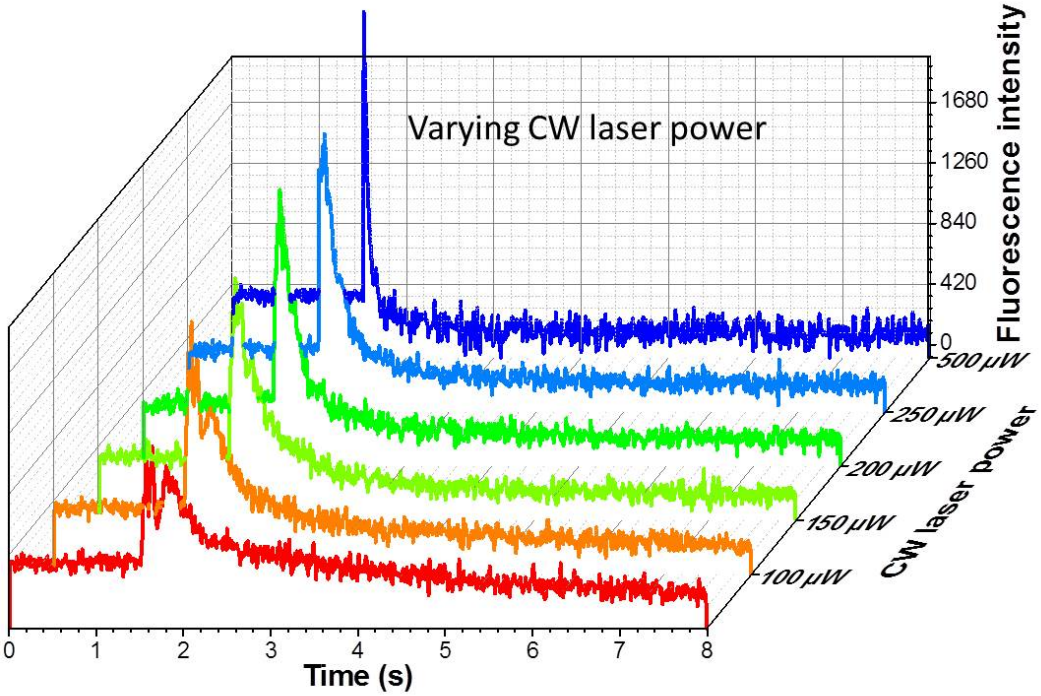

Figure 5.9: Fluorescence time trace of a single Ce ion under different CW laser excitation power (from 50 μW $\sim$ 500 μW).

a 12 m optical fiber to the confocal microscopy. Surprisingly, we found that, after the femtosecond laser pulses propagating in 12 m optical fiber, it can not light up single Ce ions anymore. We thus shortened the optical fiber from 12 m to 8 m. As the result, single Ce ions can be excited and resolved afterwards. However, the fluorescence scanning image presents a fairly low contrast. This evidence suggests that single Ce ions can not be efficiently excited when the femtosecond laser pulses have been extended to picosecond laser pulses with the same average laser power. This indirect evidence suggests that a two-photon excitation process is involved in this Ce:YAG photo-induced dynamics. The pulses can either promote the electrons from the valence band to deep level traps or bring the electrons directly to the 5*d* states of the Ce ion. Thus it shows strong power and irradiation time dependence to the pulsed laser. When the deep level traps are fully restored, the system reaches its initial condition, where the single Ce ion is brought back to the Ce^{3+} charge state by the help of the donor electrons in the deep level traps.

Although we don't fully understand this photo-induced charge dynamics process in single Ce ions, the evidence is observed show that the high peak intensity laser pulses sufficiently re-active the non-fluorescing Ce ions. Therefore, in the spectroscopy experiments we can apply a low repetition rate pulsed laser to keep the Ce ion photostable, simultaneously a single mode CW laser can be used to resonantly excite single Ce ions.

5.4 Conclusion

In this chapter, the counterintuitive fluorescence time trace of single photon emitters namely a single Ce ion in YAG crystal has been observed, which presents a gradual decay curve in the fluorescence time trace when it is under a CW laser excitation. A possible picture is drawn to explain this phenomenon, where deep level traps in the band gap are introduced as the donors to convert Ce back to Ce^{3+}. So far this is only a proposed model, more experiments such as thermal luminescence or solid state spectroscopy, should be carefully performed to either support or optimize this model.

Unfortunately, the observation indicates that the attempts of resonant excitation Ce ions by CW laser will be unsuccessful. However, we also notice that Ce shows good photostability under femtosecond pulsed laser irradiation. The studies suggest that the femtosecond laser pulses induce the two-photon absorption which restores the donor electrons in the deep level traps. Therefore, if the femtosecond pulsed laser and CW laser is applied simultaneously, Ce shows good photostability. With the combination of low repetition rate femtosecond pulsed laser and CW laser offers a new way to excite Ce ions through its resonant optical transitions and coherent addressing single Ce spin qubit all-optically.

Chapter 6

All-optical addressing single Ce spin qubits

In Chapter IV, high fidelity optical initialization, coherent manipulation and optical readout of single Ce spin qubits have been demonstrated. It paves a way to study the interfacing of the light and single rare earth solid-state qubits. Compared to the techniques for microwave manipulation as shown before, all-optical control is a fast and precise approach to coherently manipulate single solid-state qubits. It is an essential step towards the development of integrated nanophotonic systems using single rare earth ions.

In Chapter V, the charge dynamics of single Ce ions has been studied. High peak intensity femtosecond laser pulses efficiently suppress the charge dynamics of Ce ions. It results in the good photostability of a Ce ion when it is excited under the combination of low repetition rate femtosecond pulsed laser and a CW laser. In this Chapter, high-resolution spectroscopy of single Ce ions in YAG is performed. Four narrow and spectral stable optical transitions can form two Λ system. Utilizing either of the Λ system, the preparation of coherent dark states of a single Ce spin qubit has been demonstrated. Exciting single Ce ions resonantly and addressing its spin states all-optically offers more degree of freedom to coherently control single Ce spin qubits.

6.1 Theory of coherent population trapping

Coherent population trapping(CPT) [155] and related physical phenomena (electromagnetically induced transparency [156, 157], slow light [158], lasing without inversion [159], etc.) as one of the common techniques in quantum optics have been discovered and developed in several decades [160]. It is a consequence of quantum interference effect between two excitation pathways when two ground levels are both excited to a common excited state. CPT was initially used in quantum ensembles to initialize, unitarily manipulate and readout the quantum states all-optically. Recent years, it has been demonstrated at single-ion level in atom systems and solids resulting in the all-optical addressing of single spin qubits [161–165], which is a key tool for precise and fast control of single qubits [166, 167].

Consider a three-level system interacting coherently with two external electromagnetic fields: probe and coupling field. The three-level Λ system is shown in Fig. 6.1(a), that $|g_1\rangle$ and $|g_2\rangle$ are ground states, and they share a common excited state $|e\rangle$. In the Λ system, state $|g_1\rangle$ and $|e\rangle$ are on resonance with frequency $\omega_p = \omega_e - \omega_{g1}$. While state $|g_2\rangle$ and $|e\rangle$ are on resonance with frequency $\omega_c = \omega_e - \omega_{g2}$. The frequency detuning Δ_1 and Δ_2 are introduced from the resonant transitions ω_p and ω_c respectively. Γ_{eg1} and Γ_{eg2} correspond to the radiative decay rates from the excited state $|e\rangle$ to two ground states $|g_1\rangle$ and $|g_2\rangle$.

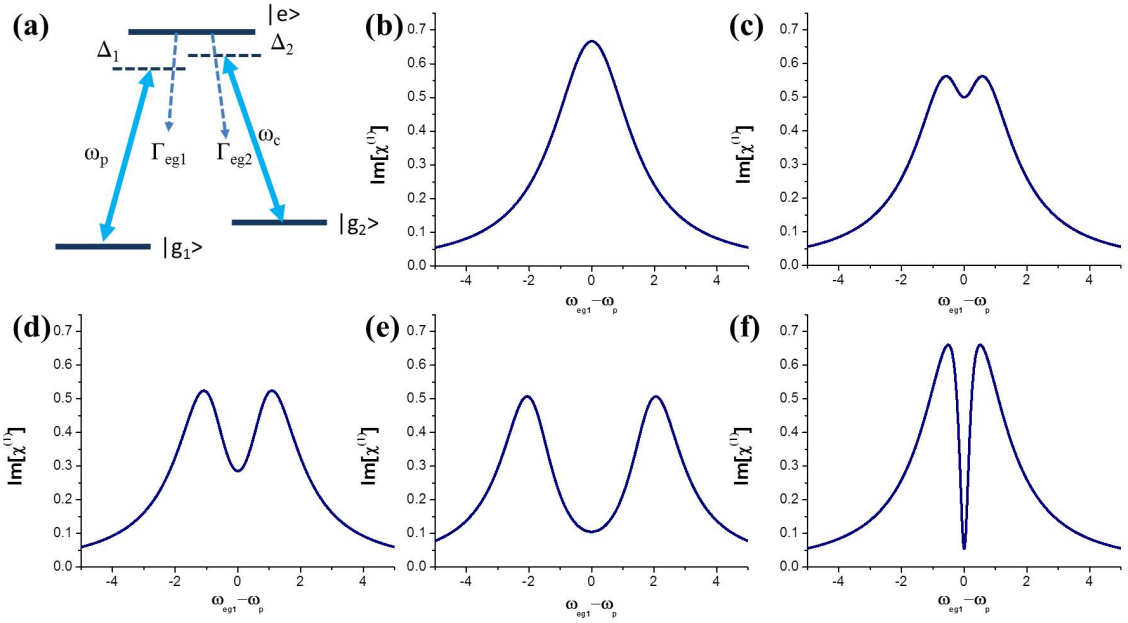

Figure 6.1: (a) A three-level Λ system coherently interacts with two external electromagnetic fields. (b)-(f) Absorption spectrum with different parameters. (b) $\gamma_{g_2g_1} = 1$, $\gamma_{eg_1} = 3$, and $\Omega_c = 0$. (c) $\gamma_{g_2g_1} = 1$, $\gamma_{eg_1} = 3$, and $\Omega_c = 1$. (d) $\gamma_{g_2g_1} = 1$, $\gamma_{eg_1} = 3$, and $\Omega_c = 2$. (e) $\gamma_{g_2g_1} = 1$, $\gamma_{eg_1} = 3$, and $\Omega_c = 4$. (f) $\gamma_{g_2g_1} = 0.03$, $\gamma_{eg_1} = 3$, and $\Omega_c = 1$.

When the three-level system is interacting with the external electromagnetic field, the CPT Hamiltonian is described by:

$$H_{CPT} = H_0 + H_1. \tag{6.1}$$

In Eq. 6.1 H_0 is the Hamiltonian of the three-level system without external electromagnetic fields. H_1 represents the perturbation induced by the applied external field which is defined by:

$$H_1 = -q\mathbf{E} \cdot \mathbf{r}, \tag{6.2}$$

here q is the charge of the electron. $\mathbf{E}$ and $\mathbf{r}$ represent electric field and a position vector. With the rotation wave approximation, the H_{CPT} is written as [160]:

$$H_{\mathrm{CPT}} = \frac{1}{2}\hbar \begin{pmatrix} 0 & 0 & \Omega_p \\ 0 & -2(\Delta_1 - \Delta_2) & \Omega_c \\ \Omega_p & \Omega_c & -2\Delta_1 \end{pmatrix}, \tag{6.3}$$

where Ω_p and Ω_c represent the optical Rabi frequency in between the $|\mathrm{g}_1\rangle \leftrightarrow |\mathrm{e}\rangle$ and $|\mathrm{g}_2\rangle \leftrightarrow |\mathrm{e}\rangle$ transitions caused by probe and coupling field.

The eigenstates of the H_{CPT} are calculated as [160]:

$$|a^+\rangle = \sin\theta \sin\phi|g_1\rangle + \cos\phi|e\rangle + \cos\theta \sin\phi|g_2\rangle, \tag{6.4}$$

$$|a^-\rangle = \sin\theta \sin\phi|g_1\rangle - \cos\phi|e\rangle + \cos\theta \cos\phi|g_2\rangle, \tag{6.5}$$

$$|a^0\rangle = \cos\theta|g_1\rangle - \sin\theta|g_2\rangle, \tag{6.6}$$

in which $\theta = \arctan(\frac{\Omega_p}{\Omega_c})$ and $\phi = \frac{1}{2}\arctan(\frac{\sqrt{\Omega_p^2+\Omega_c^2}}{\Delta_1})$.

Here, $|a^0\rangle$ is particularly interesting to us, since it can be obtained from Eq. 6.6 that:

$$\langle e|H_{\mathrm{CPT}}|a^0\rangle = 0. \tag{6.7}$$

Equation6.7 suggests no contribution of state $|e\rangle$ to states $|a^0\rangle$. In this case, the population of the excited state is 0, indicating no absorption and fluorescence from the system. It results in state $|a^0\rangle$ as the dark state. This is so called coherent population trapping.

If the probe field is much weaker than the coupling field, it yields to $\Omega_p \ll \Omega_c$. It yields the θ in Eq. 6.3 close to 0. The $|a^0\rangle$ state turns to $|a^0\rangle = |g_1\rangle$. In addition, as soon as the detuning of the probe field $\Delta_1 = 0$ (probe field is on resonance with the transition $|g_1\rangle \leftrightarrow |e\rangle$), $|a^+\rangle$ and $|a^-\rangle$ are written as: $|a^+\rangle = \frac{1}{\sqrt{2}}(|g_1\rangle + |g_2\rangle)$ and $|a^-\rangle = \frac{1}{\sqrt{2}}(|g_1\rangle - |g_2\rangle)$. These are normally described as dressed state picture.

Followed by the master equation for the atomic density operator, the first order susceptibility $\chi^{(1)}$ is given by [160]:

$$\chi^{(1)}(-\omega_p, \omega_p) = \frac{|\mu|^2\varrho}{\epsilon_0\hbar} \times \left[\frac{4\delta(|\Omega_c|^2 - 4\delta\Delta_1) - 4\Delta_1\gamma_{g_2g_1}^2}{||\Omega_c|^2 + (\gamma_{eg_1} + i2\Delta_1)(\gamma_{g_2g_1} + i2\delta)|^2} + i\frac{8\delta^2\gamma_{eg_1} + 2\gamma_{g_1g_2}(|\Omega_c|^2 + \gamma_{g_2g_1}\gamma_{eg_1}}{||\Omega_c|^2 + (\gamma_{eg_1} + i2\Delta_1)(\gamma_{g_2g_1} + i2\delta)|^2} \right] \tag{6.8}$$

where γ_{eg_1}, $\gamma_{g_2g_1}$ represent to the coherent decay rates from $|e\rangle$ to $|g_1\rangle$ and from $|g_2\rangle$ to $|g_1\rangle$ respectively. δ is the two photon detuning: $\delta = \Delta_1 - \Delta_2$. When the probe and pump field are both on resonance with the optical transitions $\delta = \Delta_1 = 0$, three parameters $\gamma_{g_2g_1}$, Ω_c and γ_{eg_1} remain important. In Eq. 6.8 the imaginary part of the susceptibility $Im[\chi^{(1)}]$ represents to the dissipation of the field by the system [160], which is represented by the PLE spectrum of the three-level system.

The simulation of the $Im[\chi^{(1)}]$ corresponds to different ratio between $\gamma_{g_2g_1}$, γ_{eg_1} and Ω_c is shown in Fig. 6.1(b)-(f). If the coupling field is zero (Fig. 6.1(b)), the PLE spectrum presents a lorentz like line shape, where the linewidth is determined by the coherence decay rate of the excited state γ_{eg_1}. When the coupling field is applied, a dip appears when the probe field frequency is on resonance with ω_{eg_1}. It indicates the successful preparation of coherent dark states in between the ground states $|g_1\rangle$ and $|g_2\rangle$. The width of the dip is limited by the coherence decay rate of the ground states $\gamma_{g_2g_1}$. As soon as

the coupling power is heightened, the dip at the middle of the PLE spectrum goes deeper as shown in Fig. 6.1(c)-(e). The width of the dip is broadened if the coupling field is strong, which is known as power broadening effect. If the coupling field is weak and the coherence decay rate of the ground state is relatively long as displaced in Fig. 6.1(f), PLE spectrum of the CPT process expresses a narrow and sharp dip going down to the background level.

In the case of single Ce ions embedded in YAG, to generate the coherent dark states of single Ce spin qubits, two requirements should be under consideration.

(1) The construction of the Λ system. It is introduced in Chapter 3 if the external magnetic field is perpendicular to the laser beam direction, both spin-flip and non-flip transitions are allowed. To achieve this condition, we set-up an external magnetic field (see Appendix). The external magnetic field ($\vec{B}$ ∼450 G) dominates the optical selection rules of Ce:YAG, indicating the permission of four optical transitions between the lowest Kramers doublets of the ground state and of the excited state, as presented in Fig. 6.2, where the Λ system can be formed.

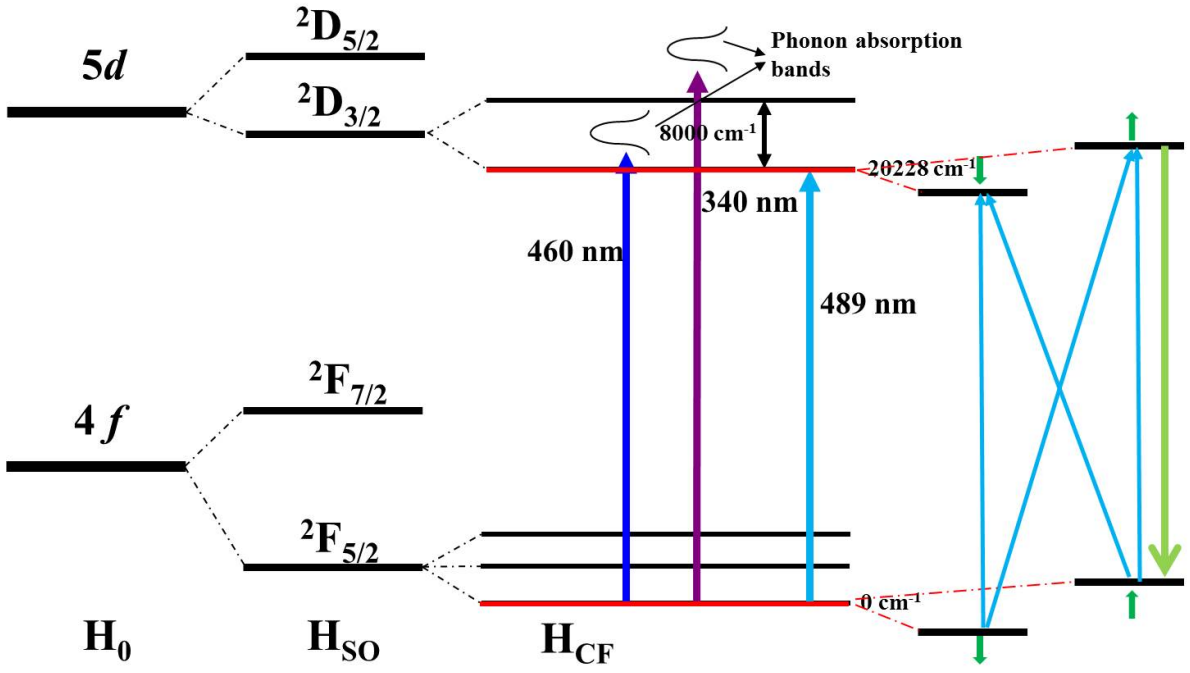

Figure 6.2: The energy level and the selection rules of the optical transitions of single Ce ions in YAG.

(2) Acquirement of resonant transitions of single Ce ions. It is essential to resonant excite single Ce ions through the optical transitions to achieve the all-optical addressing of single electron spin qubits. On top of that, if the transition linewidth is broad (bigger than the ground state splitting) or presents huge spectral diffusion, the CPT signal will be almost invisible. The obtainment the ZPLs of single Ce ions and determine the resonant transition quality by means of photoluminescence excitation(PLE) spectrum is the next step.

6.2 Emission spectrum of Ce:YAG

As it is introduced in Chapter III, the emission spectrum of Ce:YAG shows broad phonon assisted sideband. Under ambient conditions, the ZPL of Ce:YAG is invisible due to the strong phonon coupling. To know the up boundary of the temperature when the ZPL is resolvable, the emission spectrum of Ce:YAG are measured at different temperatures. The preliminary results of temperature dependence of Ce:YAG emission spectrum is shown in Fig. 6.3. A Ce:YAG bulk crystal (1%) is cooled down in the cryostat experiment setup. A laser wavelength of 450 nm is applied to excite the Ce:YAG through phonon sideband transition. The fluorescence photons from Ce:YAG have been collected and recorded by a spectrometer. Figure 6.3(a) shows the full range of the emission spectrum corresponding to the different temperature. It reveals broadband phonon-assisted emission of Ce:YAG. If the temperature is higher than 100 K, the ZPL of Ce:YAG can not be acquired. Higher resolution spectrum have been performed with a finer optical grating to resolve the ZPLs more precisely. The dependency of Ce emission spectrum with different temperature has been plotted in Fig. 6.3(b). Ce:YAG ZPL appears when the crystal temperature is below 80 K. If the lowest temperature is achieved,(∼3.5 K) a sharp and narrow ZPL is clearly presented. The ZPL of Ce:YAG is located around 489 nm with 0.46 nm FWHM (∼600 GHz).

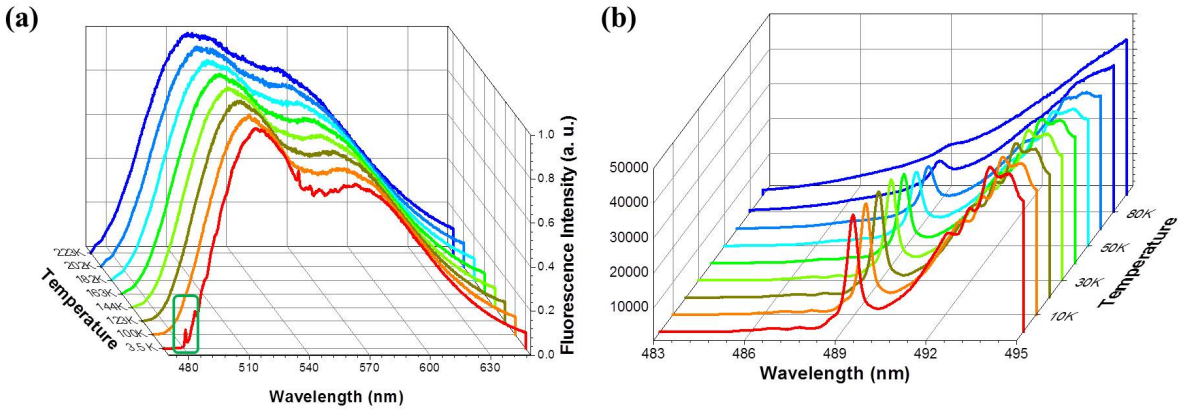

Figure 6.3: The dependence of emission spectrum of Ce:YAG bulk crystal with temperature. (a) The emission spectrum of Ce:YAG in full range spectrum (b) The emission spectrum of Ce:YAG with high resolution.

The Ce:YAG bulk measurements suggest that to acquire good quality of ZPLs, the temperature of the YAG crystal has to be kept low (∼3.5 K). To determine the ZPLs of single Ce ions, the experiment is performed with the lowest setup temperature (3.5 K). When a single Ce is excited by the pumping laser, its emission spectrum is recorded and presented in Fig. 6.4. The emission spectrum of a single Ce ion is similar comparing to the ensemble spectrum. Broadband phonon-assisted emission of a single Ce ion has been clearly obtained with a sharp ZPL located around 489 nm. The linewidth of the ZPL of a single Ce ion is limited by the resolution of the spectrometer. Due to the big inhomogeneous broadening of Ce:YAG crystal (∼600 GHz), the ZPL positions of individual Ce ions disperse in a wide range. For example, Fig. 6.4(c) shows two sharp ZPLs of single Ce ions, both are simultaneously optically excited. The ZPLs are located in two different

positions. It implies the possibility of selectively excite individual Ce ion in the spectral domain. With the acquirement of the ZPL position of single Ce ions, the PLE of single Ce ion can be measured to determine the optical transition quality.

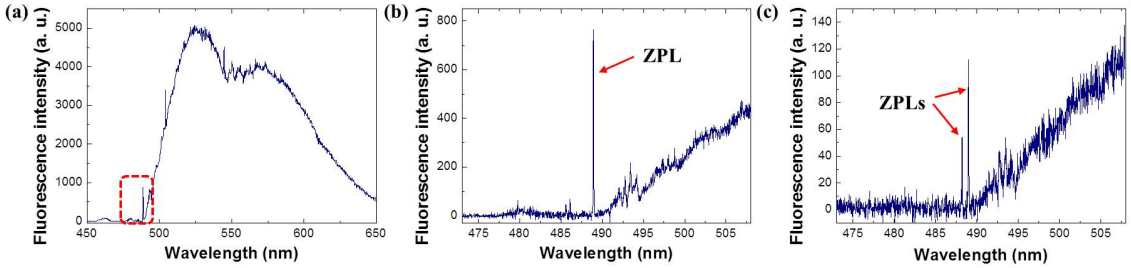

Figure 6.4: The emission spectrum of single Ce ions in YAG crystal temperature at ∼3.5 K. (a) Emission spectrum of a single Ce ion with full range. (b) The emission spectrum of a single Ce ion with high resolution. (c) The emission spectrum of two individual Ce ions

6.3 Excitation spectrum of single Ce ions

The acquirement of the PLE spectrum of single Ce ions is performed in the following way: A single mode narrow linewidth (∼500 kHz) CW laser (wavelength of 489.15 nm, Toptica Photonics DL pro) is swept across the ZPL position, while a 440 nm pulse laser with 2.5 kHz repetition rate is applied to ensure the good photostability (see Chapter 5). The excitation spectrum of single native Ce ions in YAG has been displayed in Fig. 7.3(a) with four well resolved optical excitation-transitions lines. These four excitation lines represent four optical transitions between two pairs of spin states of the lowest $4f$ and $5d$ levels as indicated in Fig. 7.3(a). Two strong peaks on the sides (the blue and red peaks) are corresponding to the spin-flip transitions (D1 and D4 transitions), and two weak peak at the center (the green and the orange peaks) are representing to two spin non-flip transitions (D2 and D3 transitions). The different fluorescence intensities of each peaks imply the different dipole oscillation strength between the transitions. The excitation spectrum show good optical transition linewidth, which the FWHM is $\sim 2\pi \times 80$ MHz. FWHM of the transitions is broader than $2\pi \times 4$ MHz excited state lifetime (70 ns) limited linewidth. This broadening is mainly contributed by the dephasing process caused by strong ^{27}Al nuclear spin bath, which is an intrinsic property of the host material.

The fluorescence intensity of a single Ce ion is recorded during each successive frequency sweep through the optical transitions as expressed in Fig. 7.3(b). Stable optical transition lines are presented without obvious spectral jumps and diffusion. When zoom into one of the excitation lines (D1) and the line centers for each sweep are shown in Fig. 6.6. As one can see, spectral jumps do not exceed 20 MHz, while the optical linewidth of natural Ce impurities is 80 MHz. Thus, the instability is within the original linewidth. This contrasts the behavior of NV centers in diamond, single Pr ions in YSO crystal, for which spectral jumps as high as more than the optical linewidths are routinely observed. The forming of the Λ system with spectral stability and narrow optical transitions of single Ce ions offers an opportunity of precision addressing single Ce ion spins all-optically.

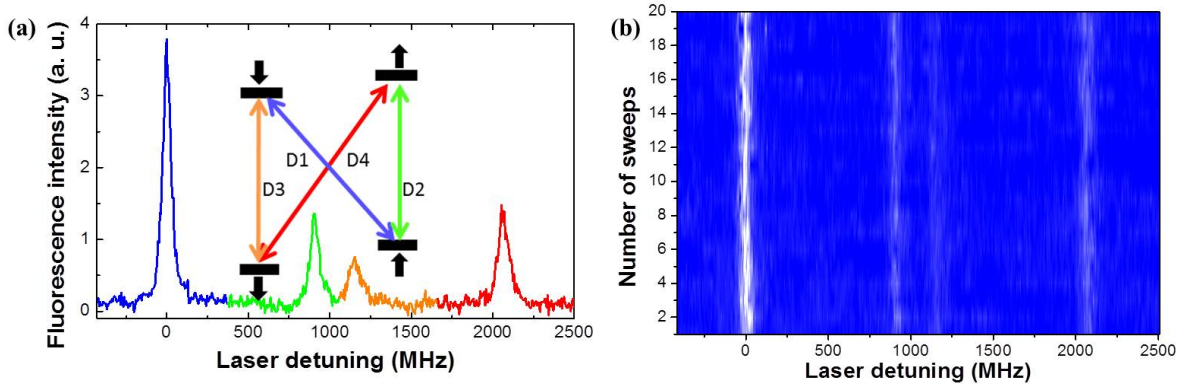

Figure 6.5: (a) Photoluminescence excitation spectrum of the single Ce ion, four resonance lines correspond to the optical transitions between the lowest Kramers doublets of the ground and the excited states. (b) 20 successive excitation sweeps of the single Ce ion.

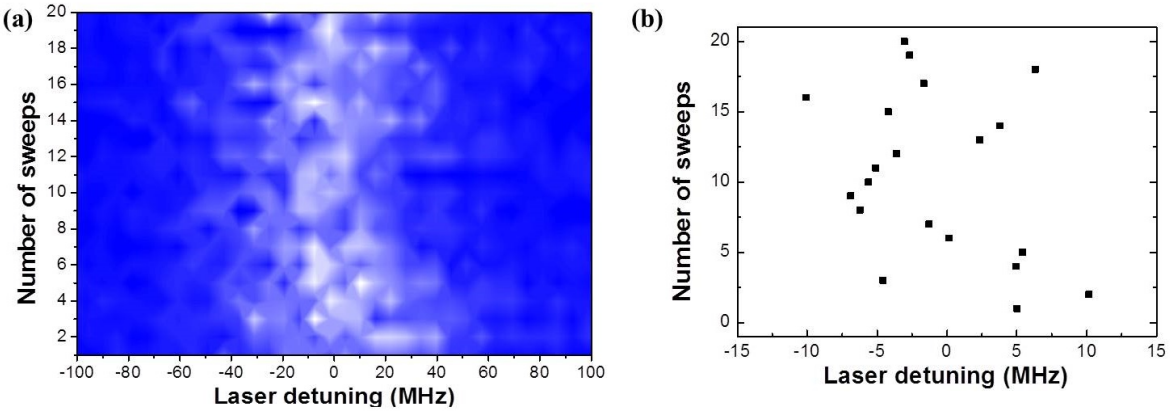

Figure 6.6: (a) Successive sweeps around one resonance transition. (b) The center position of the resonance transition corresponds to the sweeps.

6.4 All-optical generation of coherent dark states of a single Ce spin

6.4.1 Coherent population trapping of single Ce spin states

From the excitation spectrum of single Ce ions obtained in the previous section, four different optical transitions have been resolved. Two of these optical transitions $D1$, $D3$ (or $D2$, $D4$) can be used to form a Λ system (see Fig. 6.7(a)). The Λ system offers the opportunity to generate the coherent dark states of single Ce spin qubits.

In the experiment, one laser is fixed on resonance with $D1$ transition acting as the pump laser. Another laser known as probe laser is swept around the $D3$ transition (experiment details are introduced in Appendix). The fluorescence intensity of single Ce ions corresponding to the probe laser frequency is plotted in Fig. 6.7(a). It shows a broad peak with a dip at the center, where drops down nearly to the background level. The frequency of the dip is the center of the $D3$ transition, indicating no Ce emission when both probe

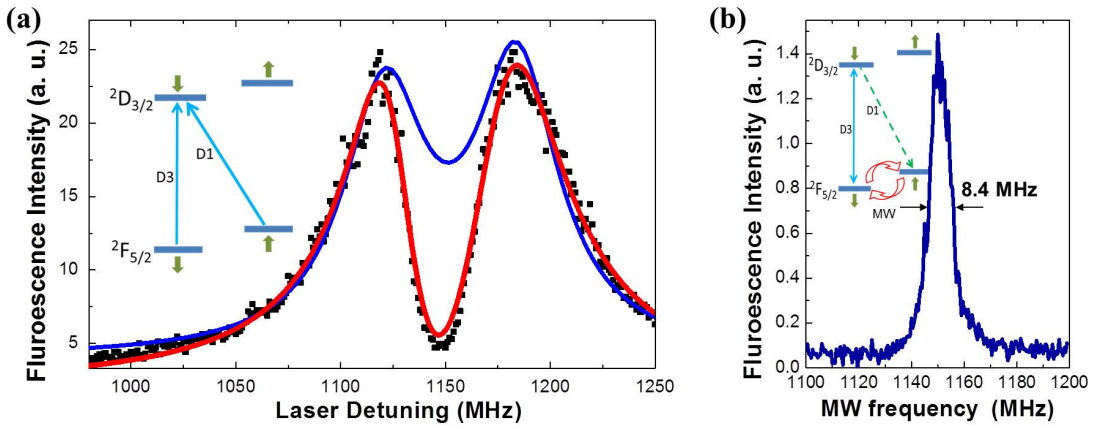

Figure 6.7: (a) CPT of a single Ce ion. The red curve shows the fitting of the CPT. The blue curve represents the simulated Rabi splitting process. (Inset) Scheme of the single Ce spin CPT. The pump laser is on resonance with $D1$ transition. The probe laser is swept through $D3$ transition. (b) ODMR of the single Ce ion. (Inset) Scheme of single Ce ions ODMR. The ground spin state is optically polarized by $D3$, the spin non-flip transition.

and pump lasers are on resonance. The forming of the dip indicates that the ground spin state is coherently trapped in a dark superposition state.

The width of the CPT dip is $\sim 2\pi \times 35$ MHz, which is influenced by several decoherence process, such as the intrinsic ground spin state dephasing and the power broadening caused by probe laser power. To figure out the CPT linewidth, the ODMR has been performed to obtain the intrinsic dephasing rate of the ground-state spin transition. The excitation laser is applied on resonance with the $D3$ transition to initialize the Ce ion into $|4f\uparrow\rangle$. MW radiation is swept through resonance of the ground-state spin transition. We keep the power of both MW and laser low to prevent the power broadening. When the MW is not in resonant with the spin transition, the Ce spin remains in $|4f\uparrow\rangle$, with low fluorescence level. If the MW is on-resonance, the Ce spin is repumped to $|4f\downarrow\rangle$, resulting in the dramatically increasing the fluorescence yield as shown in Fig. 6.7(b). The linewidth of the ODMR curve is $2\pi \times 8.4$ MHz, in agreement with the previous observation in Chapter 4. In previous work, an external magnetic field was settled to have spin-flip transitions of single Ce ions. Through phonon absorption sideband transition, fidelity of spin initialization was more than 97%. However, resonant excitation of the single Ce ion shows a more robust way to initial and readout its spin state. By comparing the dark state and coherently mixed state in the ODMR signal (Fig. 6.7(b)), the fidelity of spin initialization is more than 98%. With this method, accurately alignment of the external magnetic field to have high contrast selection rules was not necessary. Furthermore, narrow linewidth resonant transitions offer the opportunity to individually and independently excite, initialize, manipulate and readout single cerium ions even they were close to each other.

6.4.2 Studying of the CPT dip

To understand the width of measured CPT dip theoretically, we consider the four-level system $|4f\uparrow\rangle$, $|4f\downarrow\rangle$, $|5d\uparrow\rangle$, $|5d\downarrow\rangle$ as shown in Fig. 6.7(a) which are related to the CPT process. Two ground states $|4f\uparrow\rangle$, $|4f\downarrow\rangle$ and one excited state $|5d\downarrow\rangle$ form the Λ system, while $|5d\uparrow\rangle$ is an auxiliary state. A master equation is introduced to describe the dynamics of the laser-driven 4 level system:

$$\frac{d\rho}{dt} = \frac{1}{i\hbar}[H_{int}, \rho] + \mathscr{L}[\rho], \tag{6.9}$$

where the interaction Hamiltonian is

$$H_{int} = \begin{pmatrix} 0 & 0 & \Omega_{13}/2 & 0 \\ 0 & \Delta_1 - \Delta_2 & \Omega_{23}/2 & 0 \\ \Omega_{13}/2 & \Omega_{23}/2 & \Delta_1 & 0 \\ 0 & 0 & 0 & 0 \end{pmatrix}, \tag{6.10}$$

where Ω_{23} and Ω_{13} represent the Rabi frequency induced by coupling and probe laser on-resonance with $D1$ and $D3$ transitions respectively. The detuning of the pump and probe laser is expressed by Δ_2 and Δ_1. The Lindbald superoperator $\mathscr{L}[\rho]$ describing the spontaneous emission process is given by [164]:

$$\mathscr{L}[\rho] = \sum \mathscr{L}_{ij}[\rho] = -\frac{1}{2}\sum(\mathcal{C}_{ij}^{\dagger}\mathcal{C}_{ij}\rho + \rho\mathcal{C}_{ij}^{\dagger}\mathcal{C}_{ij}) + \sum \mathcal{C}_{ij}\rho\mathcal{C}_{ij}^{\dagger}, \tag{6.11}$$

here the collapse operator $\mathcal{C}_{ij}$ is related to the transition rates Γ_{ij}:

$$\mathcal{C}_{ij} = \sqrt{\Gamma_{ij}}|j\rangle\langle i|. \tag{6.12}$$

In the Lindbald superoperator $\mathscr{L}[\rho]$, the spontaneous decays of state $|4f\uparrow\rangle$ is $\sim 2\pi\times 3$ MHz. The pure dephasing rate is $\sim 2\pi\times 4$ MHz in the ground spin states. The spin-flip transitions between state $|5d\downarrow\rangle$ and $|5d\uparrow\rangle$ is $\sim 2\pi\times 3$ MHz, while the dephasing rate of the optical coherence is $\sim 2\pi\times 80$ MHz. Power boarding induced by high Rabi frequency of the pump laser is the only unknown parameter which can be fitted.

The steady state solution of the master equation $\frac{d\rho}{dt} = 0$ is solved. The density matrix ρ is obtained, which is applied to explain the experimental data. When the pump laser introduced Rabi frequency $\Omega_{23} \approx 62$ MHz, the fitting curve(the red curve in Fig. 6.7(a)) shows good agreement with the experiment data. The blue curve in Fig. 6.7(a) represents the Rabi splitting caused by such pump laser power presenting a much shallower dip. It also indicates that the observed dip is related to the successful generation of a coherent dark state of a single Ce spin.

The CPT dip linewidth as a function of the pump laser power has been measured to quantify the power broadening effect in the CPT process. The dip linewidth shows the linearly dependence of the pump laser intensity , as indicated in Fig. 6.8(a). By a linear fit, the intercept of the dip linewidth is $\sim 10.7 \pm 3.2$ MHz. It is related to the CPT process without power broadening. The fitted value is in agreement with the intrinsic linewidth 8.4 MHz acquired from the ODMR signal. Furthermore, detuning effects of the pump laser on the CPT process are also investigated as indicated in Fig. 6.8(b), (c). The pump

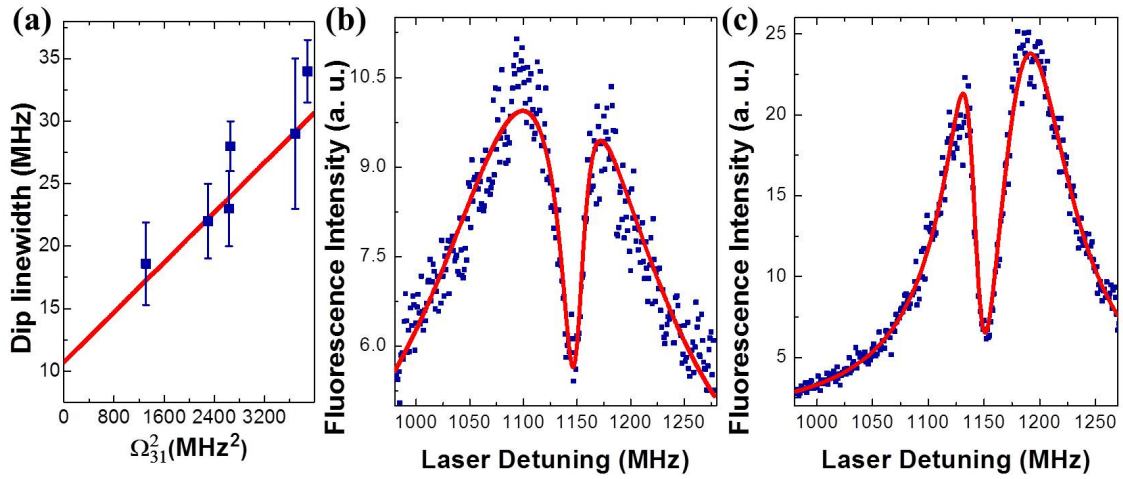

Figure 6.8: (a) The CPT dip linewidth corresponds to the pump laser induced Rabi frequency. (b)Pumper laser is detuned from the resonance +26 MHz. (c) Pumper laser is detuned from the resonance -25 MHz.

laser frequency is detuned from the resonance frequency($D1$) +26 MHz and -25 MHz respectively. The CPT dips remain at 1.15 GHz, while the fidelity of CPT dips is reduced when the pump laser frequency is not matching the resonance transition. It implies that the CPT process presents the highest fidelity when both pump and probe laser are on resonance($D1$ and $D3$ respectively.

6.5 Conclusion

In conclusion, in this chapter, the resonant excitation of single Ce ions in YAG has been achieved. Based on the Λ system in the optical transitions, all-optical generation of coherent dark states of single Ce ions has been demonstrated by CPT method. The CPT method is capable of fast controlling a single spin with picoseconds or nanoseconds time scalar due to the strong optical transition dipole of Ce:YAG. Comparing to, coherent manipulation of single Ce spin with complicated MW pulse sequence as introduced in Chapter 4, the all-optical approach is more convenient to unitary manipulate a single Ce spin in the Bloch sphere. In addition, the PLE of single Ce ions shows $\sim 2\pi \times 80$ MHz transition linewidth, with good spectral stability. It offers an opportunity to spectrally select, excite and coherent manipulate a single rare earth spin qubit without influencing the surroundings. In general, it paves a new and novel way to all-optical manipulate single rare earth spin qubits.

Chapter 7

Spectroscopy of single praseodymium ions in YAG

Due to the natural isolation from the environment, nuclear spin has very long coherence time. It is regarded as a promising candidate for quantum memory [168]. Especially nuclear spin with optical access provides an opportunity for realizing the effective optical quantum memory, a necessary element for quantum repeater network. Based on the optical access and well-developed ultrafast optical control techniques, such nuclear spin can also be much more functional in conventional quantum registers [40,169].

In this chapter, under cryogenic temperature, we optically identified single Pr ions in YAG , another species of rare earth ion with nuclear spin 5/2. The PLE of a single Pr ion has been observed. We also demonstrated the coherent addressing a single nuclear spin of Pr ion by RF radiation. Furthermore, we provided all-optical control of a single trivalent Pr ion in YAG. The observation of PLE, ODMR and the all-optical control of single Pr ions offers us an opportunity to explore single Pr nuclear spins as memory qubits.

7.1 Optical detection of single Pr ions in YAG

As introduced in Chapter 2, Pr:YAG has the energy structure as shown in Fig. 7.1. The presence of crystal field lifts the $2J+1$ fold degeneracy and hence the ground state $^3H_4$ is split into nine sublevels. The lowest three sublevels have energy difference 0 cm^{-1}, 19 cm^{-1} and 50 cm^{-1} respectively [170]. Due to the magnetic hyperfine interaction to Pr^{3+} nuclear spin 5/2, each energy level splits further. The splitting is dominated by the second order hyperfine interaction which can be described by a Hamiltonian that takes the same form as the Hamiltonian for electric quadrupolar interactions. For this reason, the hyperfine levels with different I_z^2 split up but hyperfine levels $\pm I_z$ are still doubly degenerate under zero magnetic field. For ground state $^3H_4(1)$ the hyperfine splittings are 33.4 MHz and 41.6 MHz, and for excited state $^3P_0$ they are 1.8 MHz and 2.9 MHz [171].

In 2012, the first optical detection of single Pr ions in YAG has been demonstrated in our group [83]. The efficient detection relies on the upconversion process (see Fig. 2 (a)) to induce strong fluorescence yield, as well as using a high N.A. oil immersion objective lens

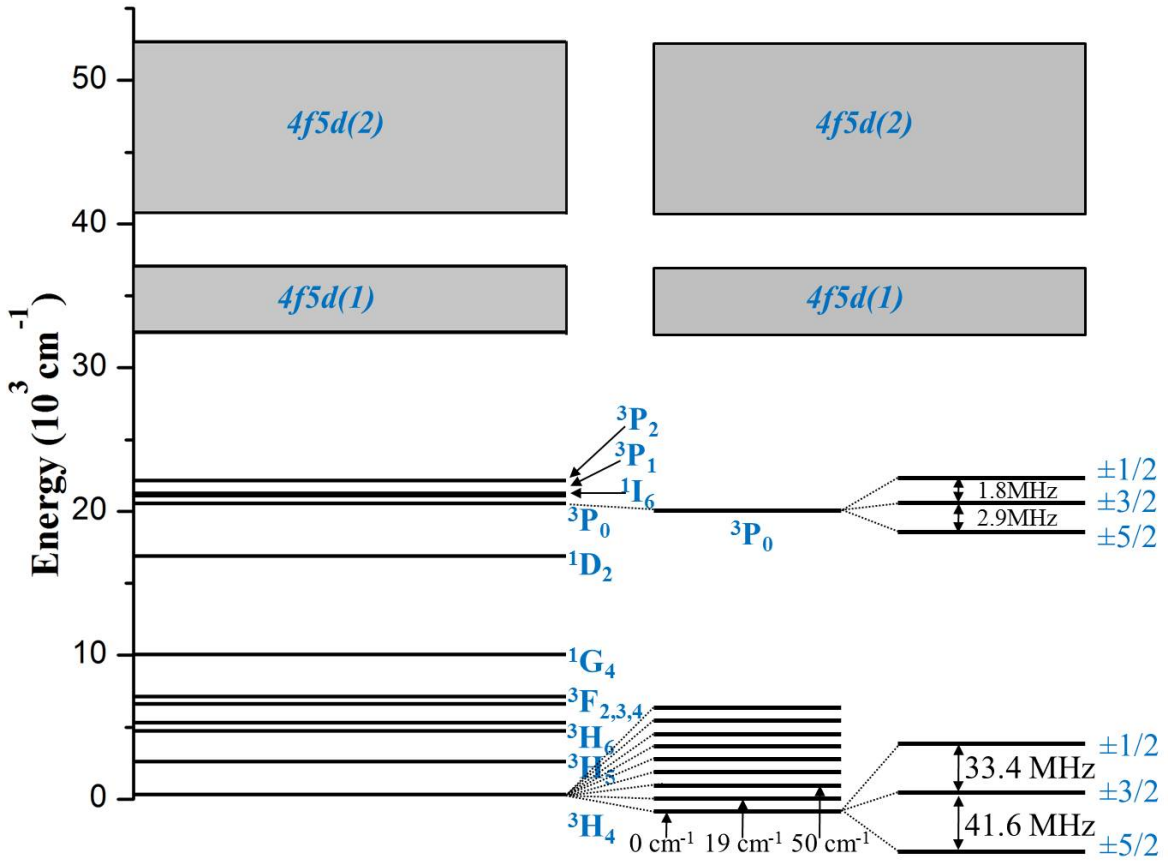

Figure 7.1: Energy level of Pr:YAG. The lowest energy ground state $^3H_4(1)$ shows Zeeman splitting 33.4 and 41.6 MHz and the first excited state $^3P_0$ presents hyperfine splitting 1.8 and 2.9 MHz respectively.

to achieve high collection efficiency. However, since the experiment has been performed at room temperature, the coherence time of Pr ions is dominated by the electron phonon coupling. The T_1 time of Pr:YAG nuclear spins is too short (<1 ns) to be observed.

In this chapter, we cooled down YAG till cryogenic temperature to suppress the phonon effect and enhance the spin coherence time of single Pr^{3+} ions. This improvement enables to resolve the hyperfine transitions of single Pr^{3+} ions and coherently manipulate them. Furthermore, to overcome the absence of high N.A. oil objective lens at low temperature, solid immersion lenses have been fabricated on the surface of YAG crystal by focus ion beam milling [172]. Under the SILs, excitation laser power, collection efficiency and spectral resolution of the upconverting microscopy has been improved [173]. The upconversion process is performed by a blue laser to excite Pr ions to the first excited state, as well as a high power laser with wavelength at 532 nm (∼10 mW laser power) to subsequently promote the Pr ions to the higher $4f5d$ state. More than 400 times fluorescence enhancement by this upconversion process can in principle be achieved in comparison with the direct $^3P_0 \rightarrow ^3 H_4$ transitions. To first localize single Pr ions, the blue laser is applied with wavelength at 487 nm and laser power about 1 mW. By performing spatial scanning and collecting the UV photons in the wavelength range of 300-400 nm, the upconversion scanning microscopy image of single Pr ions under the SIL is obtained and shown in Fig. 7.2.

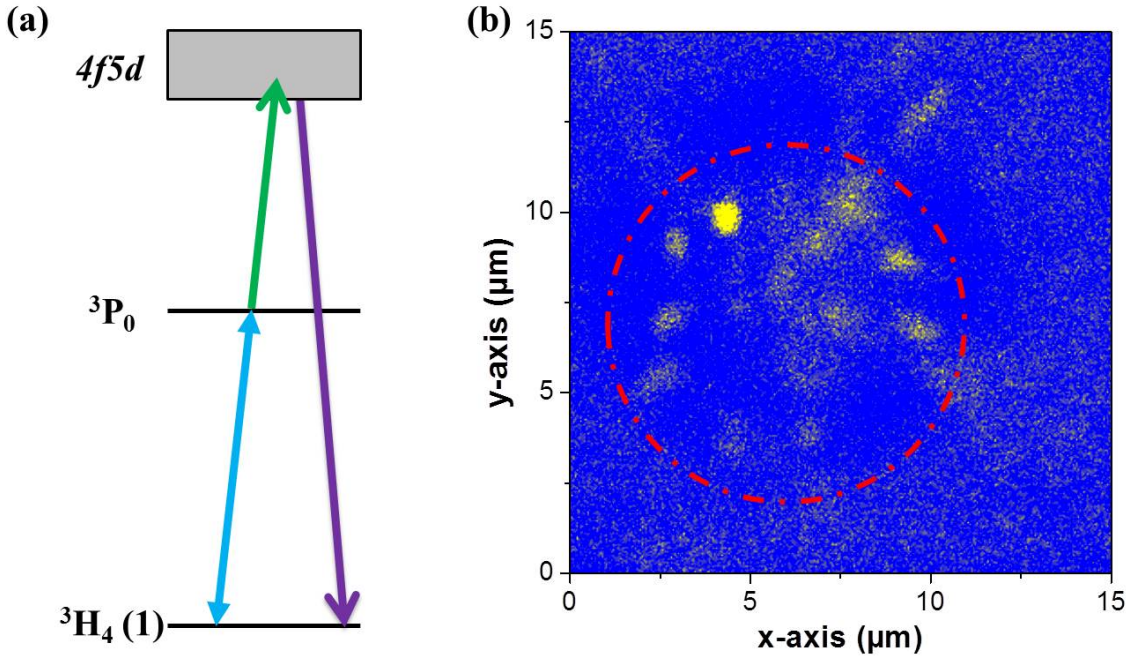

Figure 7.2: (a) Single Pr ions is excited to the first excited state by a broadband 487 nm wavelength diode laser. A second laser (wavelength at 532 nm) is applied to promote the Pr ion to higher $4f5d$ state to achieve the upconversion process .(b) Upconversion scanning microscopy images of single Pr ions under a SIL. Single Pr ions have been well resolved by air objective lens.

Every bright spot in the image corresponds to individual Pr ions.

7.2 Upconverted PLE of single Pr ions in YAG

With the above improvements, we first extend the reach of our previous study to the ground state energy structure through the PLE measurement.

For this measurement, we switch the blue laser to a narrow line width single mode laser (Toptica photonics) and sweep its frequency through the $^3H_4 \rightarrow ^3P_0$ transitions. The high power green laser (wavelength at 532 nm) is using the same setting as in the upconversion scanning microscopy image measurement.

To avoid the power broadening effect, the single mode laser is kept in low power ($\sim$5 μW laser power). The obtained upconverted PLE spectra shows there well resolved optical transitions (Fig. 7.3(b)). The frequency difference of theses three transitions are 32.7 and 42.3 MHz respectively which exactly corresponds to the hyperfine splitting of the ground state $^3H_4(1)$. However, since the width of the optical transitions is $\sim 2\pi \times 6$ MHz, the hyperfine splitting of the excited state $^3P_0$ are not resolved in the spectra. The intrinsic optical linewidth should be much narrower than $2\pi \times 6$ MHz, according to the measurements in ensemble Pr ions. And the linewidth of the single mode laser is around 1 MHz. These two values mean that the width measured here is induced either due to the spectral diffusion or by the power broadening. The power broadening effect can be investigated by

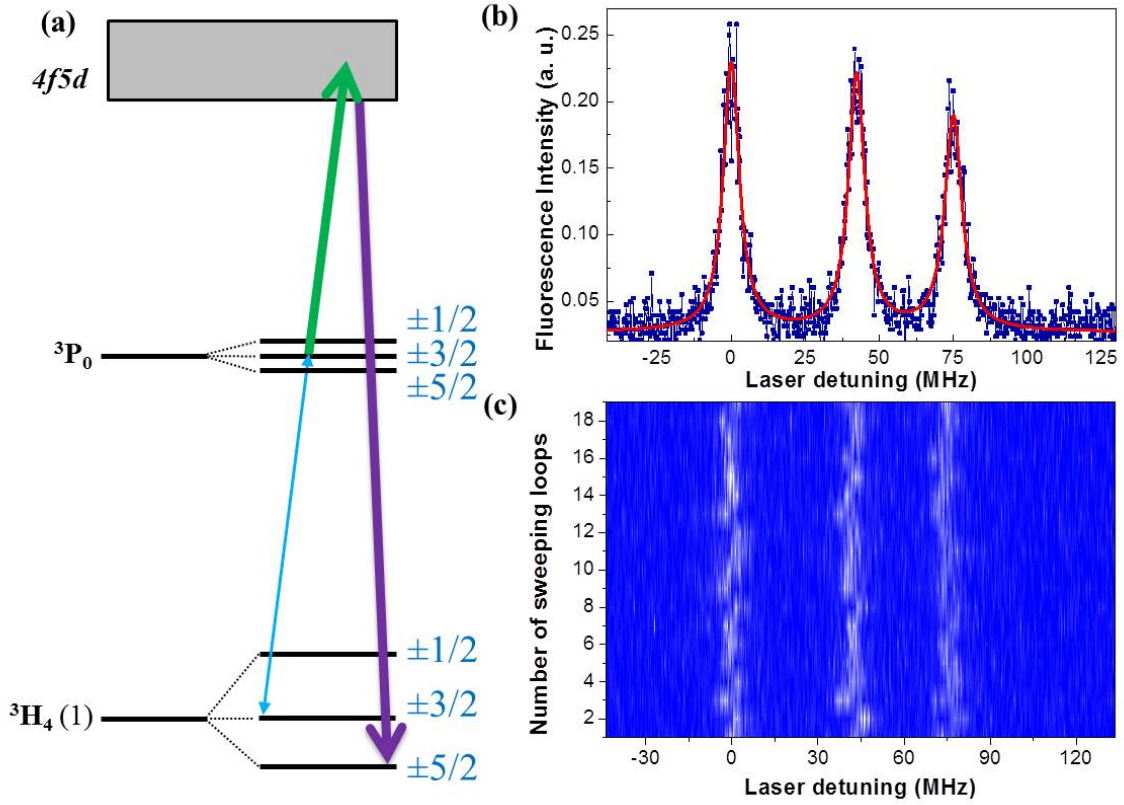

Figure 7.3: Upconverted PLE of a single Pr ion in YAG.(a) Energy diagram of the PLE, a single mode narrow linewidth laser wavelength at 487 nm is swept across the ground state Zeeman splitting levels. Second green laser wavelength at 532 nm is applied to readout the spin states by upconversion process. (b) Upconverted PLE spectrum of a single Pr ion, indicating ∼8 MHz optical transition linewidth. (c) Successive upconverted PLE sweeps of a single Pr ion. It suggests that the optical transition lines are stable.

further reducing the laser power. However since the fluorescence signal decays quadratically as laser power reduces, the signal accumulation becomes an issue . In current 5 μW blue laser power, the fluorescence counts with 200 per second are already trouble for the measurements.

The successive upconverted PLE sweeps of a single Pr ion is demonstrated in Fig. 7.3(c) showing almost the same line shape as in Fig. 7.3(b). According to the above discussion, the spectral diffusion induced linewidth is at most $2\pi\times6$ MHz. Compared to the PLE spectrum of single Pr ions in other crystals [96], like YSO nanoparticle [74, 174]s, the PLE spectrum of single Pr ion in YAG presents higher signal-to-noise ratio and better photostability with less spectral diffusion.

7.3 Upconverted ODMR of single Pr ions in YAG

The obtainment of the hyperfine splitting resolved PLE spectrum of single Pr ion enables the resonant optical initialization of the ground spin state. This allows us to further study the coherent spin property of single Pr nuclear spins. Here the upconverted ODMR is

performed to acquire the hyperfine splitting and study the spin properties. In addition, applying two lasers (487 nm and 532 nm) to realize the spin initialization and spin readout through the upconversion process, the ODMR measurements requires an RF source to induce spin transitions between different nuclear spin state (see Fig. 7.4(a)).

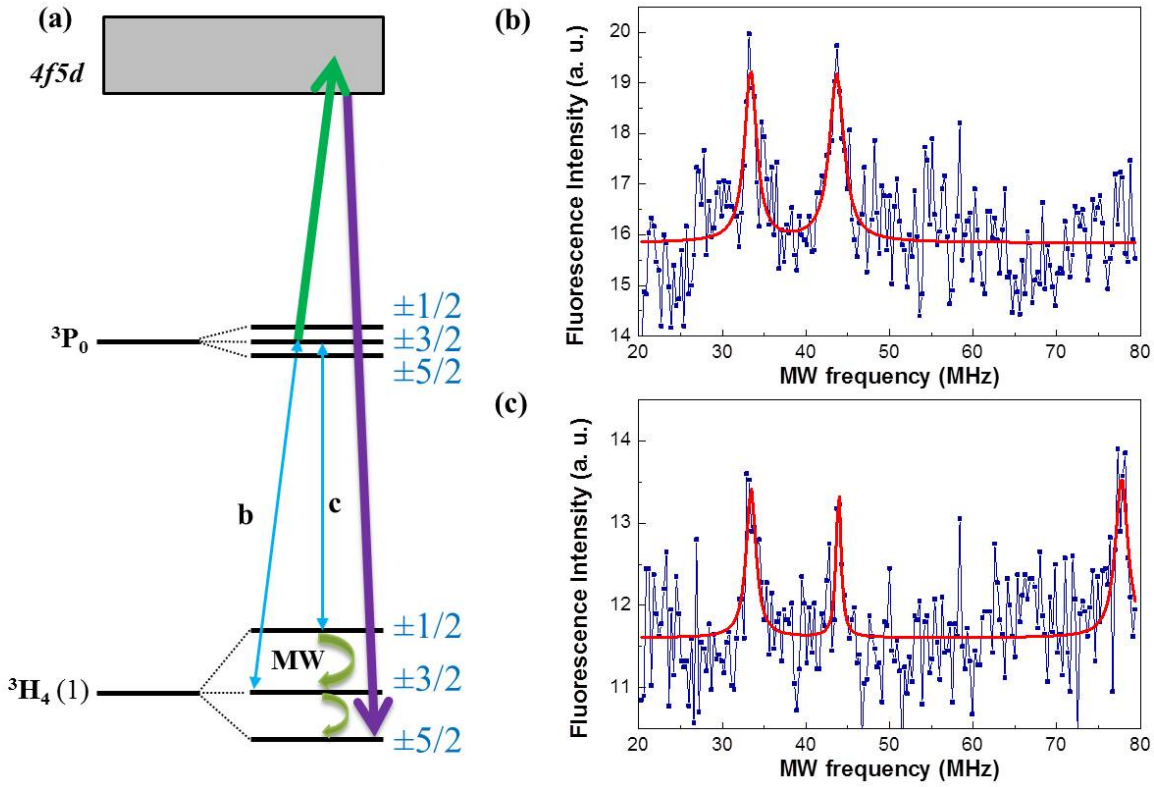

Figure 7.4: Upconverted ODMR of a single Pr ion in YAG.(a) Energy diagram of the ODMR, the single mode narrow linewidth laser is on resonance with either of the optical transitions. (b) and (c) Upconverted ODMR spectrum of a single Pr ion in YAG. The laser frequency is on resonance with $^3H_4(\pm 3/2) \rightarrow^3 P_0$ transition (or $^3H_4(\pm 1/2) \rightarrow^3 P_0$ transition) The linewidth of ODMR spectrum is ∼1 MHz.

Experimentally, the single mode laser frequency is tuned on resonance with one of the optical transition *b* or *c* in Fig. 7.4(a). With the RF frequency sweeps, the upconverted ODMR spectra of a single Pr ion is shown in Fig. 7.4(b) and (c).If the excitation laser is on resonance with $^3H_4(\pm 3/2) \rightarrow^3 P_0$ transition, it presents two peaks with frequency at 33.4 and 43.7 MHz (see Fig.7.4(b)). On the other hand, when the laser is on resonance with $^3H_4(\pm 1/2) \rightarrow^3 P_0$ transition(or on resonance with $^3H_4(\pm 5/2) \rightarrow^3 P_0$ transition), one more peak with frequency at 78 MHz appears in the ODMR spectrum. This additional peak appears due to two reasons. One reason is that the transitions from ±1/2 to ±5/2 are allowed due to the state mixture between different spin sublevels. The other one is the population between ±1/2 and ±5/2 is different under $^3H_4(\pm 1/2) \rightarrow^3 P_0$ transition(or on resonance with $^3H_4(\pm 5/2) \rightarrow^3 P_0$ transition)

The linewidth of the ODMR spectrum is ∼1 MHz, which is one order of magnitude narrower than the ODMR linewidth of single Ce:YAG. It indicates that the single Pr nuclear spin qubits have at least ten times longer T_2^* time than single Ce electron spin qubits. However, this linewidth is still much larger than the theoretical expectation value,

which should be three orders of magnitude smaller than linewidth of the single Ce electron spin qubits. One main reason is that in Pr:YAG spin-lattice relaxation mechanism is Orbach relaxation. The second lowest ground state ($^3H_4(2)$) is only 19 cm^{-1} higher than the ground state ($^3H_4(1)$). In the current 3.5K experimental condition, the phonon effect is not sufficiently suppressed. This results in short spin coherent time which can also be indirectly seen from the ODMR measurements. For example, the baseline with more than zero fluorescence intensity in Fig. 7.4(b) shows that spin is partially relaxed back to $\pm 3/2$ state, indicating the spin-lattice relaxation time is comparable with the time for single ODMR measurement. To precisely study the spin coherence property like T_2 and T_1time, either the contrast or the fluorescence signal requires being improved. The contrast enhancement needs lower temperature condition. Meanwhile, a higher UV transmission and collection efficiency objective lens, or good optical cavities can be a practical way to increase the fluorescence counts.

7.4 Optical Rabi of single Pr ions in YAG

Since the optical lifetime of the $^3P_0$ state is 8μs, it has been suggested to explore Pr ions as qubits through their optical transitions. Here we demonstrate the coherent optical control of this qubit. The Pr optical transitions are coherently driven by means of optical Rabi as soon as the driving frequency is higher than the optical lifetime of the excited states. Meanwhile, with the high the driving laser power (~1 mW), the optical transition lines are merged (~100 MHz linewidth) resulting in the failure of optical pumping.

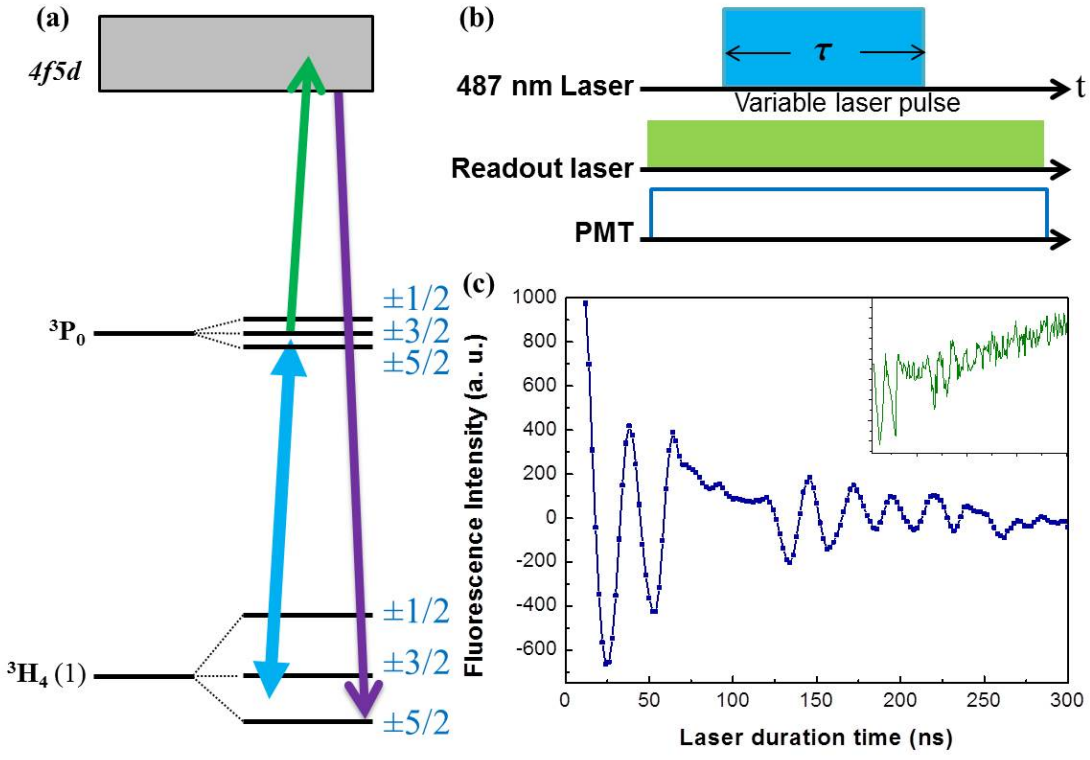

Figure 7.5: Optical Rabi of single Pr ion

In the experiment, the blue laser frequency at 487 nm is applied as the external driving field. Single Pr ion is coherently driving in between the $^3H_4$ and $^3P_0$ states (Fig. 7.5(a)). A green laser is constantly shining to accomplish the upconversion process. The duration time of the blue laser is various as shown in Fig. 7.5(b). The measured data is shown in the inset figure in Fig. 7.5(c). It displays the optical Rabi oscillation of a single Pr ion in between $^3H_4$ and $^3P_0$ states. The baseline is raising up with the increasing of the various time. It is due to the fact that the 487 nm wavelength blue laser can also achieve the upconversion process, contributing the fluorescence signal in the mixed state. A linearly correction function is introduced to eliminate this effect, where the corrected of the optical Rabi oscillation is plotted in Fig. 7.5(c).It presents a good contrast, however, the oscillation vanishes in a short time ($\sim$100 ns). We believe that high blue laser power induces not only increasing baseline but also decreasing coherent time in between $^3H_4$ and $^3P_0$ states. The obtainment of the optical Rabi oscillation of single Pr ions paves a way to fast and precise control of single Pr qubits all-optically [175, 176].

7.5 Conclusion

In this chapter, spectroscopic studying of single Pr ions in YAG has been performed at cryogenic temperature. The single Pr ions in YAG show narrow optical transition linewidth and stable optical transition. However, the intrinsic spin property is concealed by the electron phonon coupling even at 3.5K. It suggests that the full application of single Pr ions should be performed at much lower temperature. Moreover, we can improve the total collection efficiency of the single Pr fluorescence once Pr ions are coupled to photonic devices like nano-rods or photonic cavities. The good optical property and spin property of single Pr ions in YAG will offer a new opportunity of exploring the long lived nuclear spins as qubits in quantum nodes.

Chapter 8

Nanoscale engineering rare earth ions by ion implantation in solid state hosts

In previous chapters, spectroscopy of single rare earth ions (Ce and Pr) in solids (YAG and LuAG) has been investigated. Single rare earth species show remarkably narrow and stable optical transitions and good coherent properties. The demonstration of optical detection, initialization and readout, coherent manipulation of single rare earth spin qubits offers a new platform for investigating and exploring rare earth dopants as single solid-state qubits. However, so far, all the experiments are based on native single rare earth ions, namely, intrinsic impurities in the hosts. The distance between individual rare earth ions is 1$\sim$2 μm, indicating no coupling between single rare earth ions. Controlled fabrication of single rare earth ions in desired positions is a key for coupling individual rare earth ion qubits.

Ion implantation is a well-known method to generate ions locally in host materials. It has been widely used in semiconductor industry, as one of the common doping methods [177, 178]. Recently ion implantation has been applied in solid state quantum physics region [57, 179, 180], to produce single qubits in special positions [181–183]. So far, only a couple of reports show that rare earth ions have been created by ion implantation [184–186], and a yield estimation could not be achieved previously since the single rare earth ion detection is required.

In this chapter, nanoscale engineering rare earth doping in YAG has been demonstrated by means of ion implantation. Due to the ability of single rare earth detection, the production yield of Ce and Pr implantation have been measured. Different implantation energies, doses and annealing parameters correlated with the production yield has been studied. We also study the spectroscopic properties of single implanted Ce ions, which presents narrow and stable optical and spin transitions.

8.1 Mask preparation

Here, ion implantation has been performed by a FIB system in Prof. Andreas Wieck's group, Ruhr-Universität Bochum. Ions are accelerated in a range of 75∼300 keV in the FIB system, then impinge upon the sample. Implanted ions enter and collide with target ions and electrons. It results in the replacement of target ions in the host material with the implanted ions. Afterward, a post-implantation annealing procedure is applied to recover crystallinity, and to increase the implantation yield. The implantation yield η is given by:

$$\eta = \frac{N}{N_0}, \tag{8.1}$$

where N corresponds to the number of ions replacing the target ions in the material, which eventually converted into the fluorescing emitters. N_0 represents the dose of implanted ions.

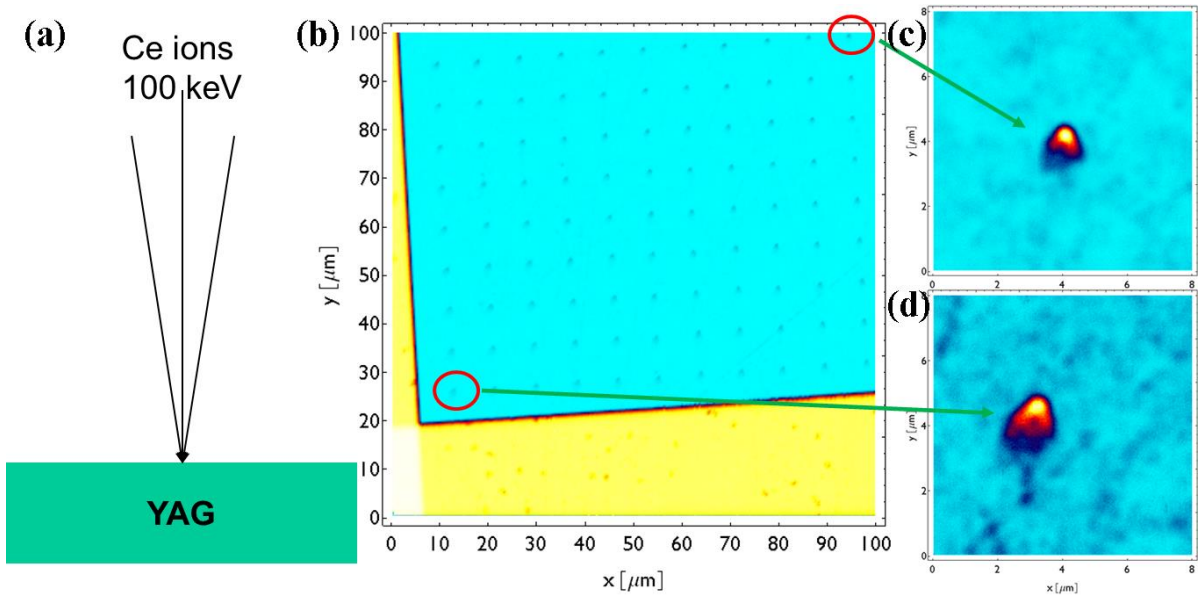

Figure 8.1: (a) Schematic diagram of ion implantation by means of FIB. (b) Preliminary results of Ce implantation, the laser scanning image of Ce implanted YAG. (c) and (d) Zoomed in figure of (b), shows asymmetry dots.

A preliminary experiment is performed as presented in Fig. 8.1(a). Ce ions accelerated till 100 keV are implanted through the FIB system into the YAG sample. After post-implantation annealing, the laser scanning image of the implanted region is shown in Fig. 8.1(b), where an array is clearly seen. The bright spots correspond to the Ce implanted spots. However, the zoomed in scanning images (Fig. 8.1(c)(d)) display asymmetric spots instead of symmetric ones. It indicates an unstable FIB system and fluctuating ion dose during the ion implantation. In this case, it is impossible to estimate the production yield due to the unprecise acquire of implantation dose and implanted area. To overcome these problems, a special mask is introduced.

The procedure of mask preparation is shown in Fig. 8.2:

(a) SiO_2 nanoparticles (430 nm diameter) are spin-coated on a surface polished YAG

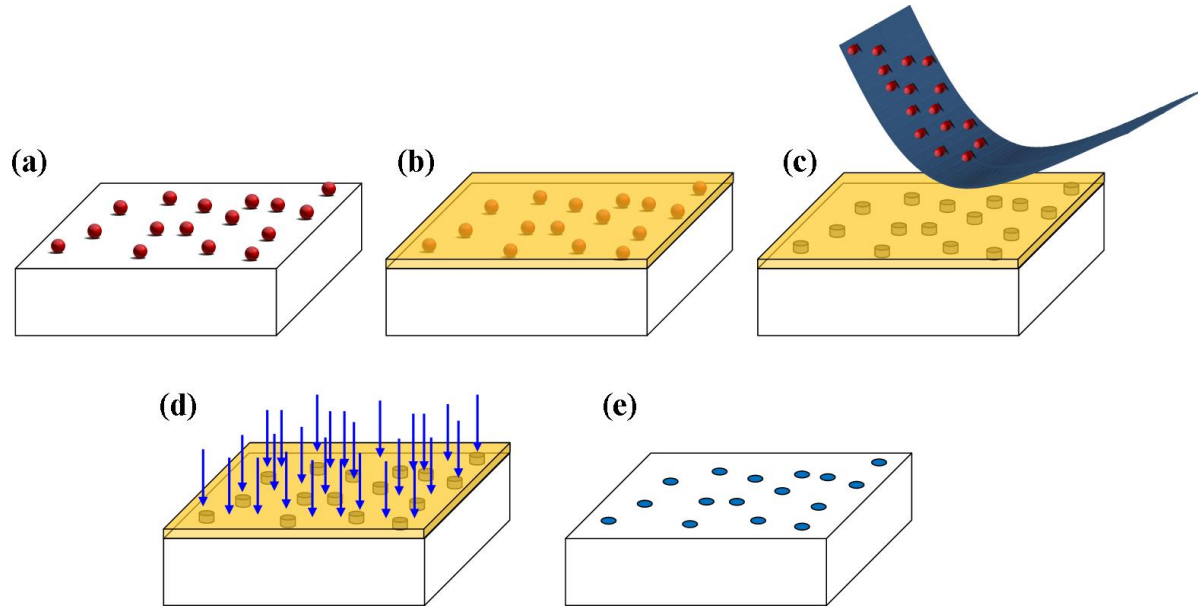

Figure 8.2: (a) Spin-coat SiO_2 nanoparticles on surface polished YAG crystal. (b) Evaporation of Cu metal layer on the surface of YAG crystal. (c) Lift-off SiO_2 nanoparticles with holes remaining. (d) Ion implantation (e) Wet chemistry etching and post-implantation annealing.

crystal.

(b) Copper is evaporated on the surface of YAG crystal.

(c) Scotch tape is applied to lift-off the SiO_2 nanoparticles and leave holes behind.

(d) Rare earth ions are implanted by FIB system. When the ion beam is on the mask, they are stopped by the mask. When the ion beam is on top of the hole, ions go through the holes and strike the crystal.

(e) After ion implantation, the mask is removed by wet chemistry etching and a post-implantation annealing is performed to recover the crystallinity and improve the production yield.

The implantation energy range of the FIB system is 75∼300 keV. To stop the implanted ions completely, a properly thick (200 nm) metal mask is needed. Experimentally 215 nm SiO_2 nanoparticles are picked to produce the metal mask. Their SEM image is presented in Fig. 8.3(a) showing uniform size and spherical shape. The thickness of the copper layer is 200 nm. After scotch tape lift-off process, nano-holes radius around 220 nm is remained on the surface, as shown in Fig. 8.3(b).

With the help of the proper implantation mask, the FIB system can be operated in "continuous scanning mode", where the instability of the FIB system, unprecise values of implantation dose and areas are eliminated by averaging out.

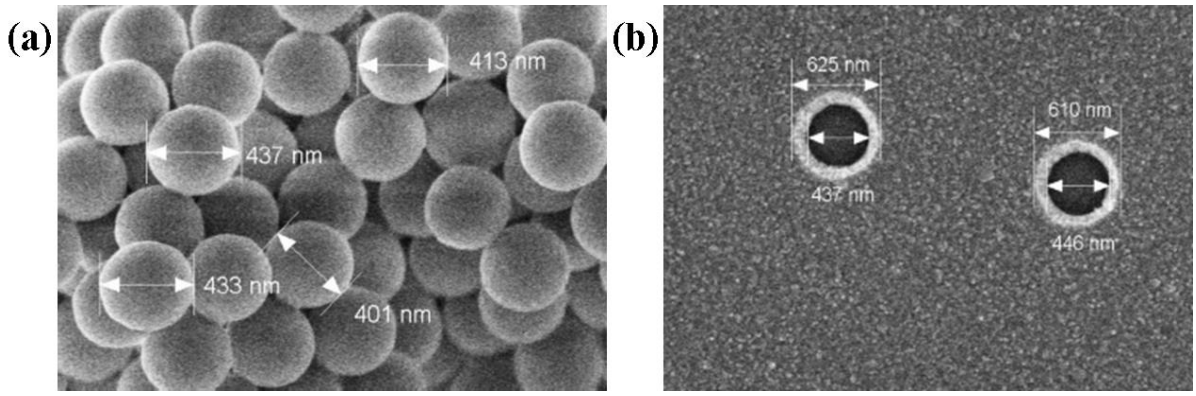

Figure 8.3: (a) SEM image of SiO_2 nanoparticles shows uniform size 215 nm radius. (b) SEM image of the copper mask after the lift-off process (Fig. 8.2(b)) presents ∼220 nm radius nano-holes.

8.2 Pr ion implantations

After the mask is produced, rare earth ions can be implanted through the nano-holes with precise acquire of implantation dose and area. Once the fluorescence intensity ratio between implanted spots with single rare earth ions is obtained, we can estimate the production yield of ion implantation.

Single Pr ions are the first rare earth species which can be optically detected in our lab since 2012. With the help of the upconverting microscope, the fluorescence intensity of Pr:YAG can be measured precisely with negligible background contribution.

In the experiment, Pr^{3+} ions are implanted through the metal mask by FIB system which were introduced above. The implanted Pr^{3+} energy is 75, 150, 200, 300 keV with the dose range from $10^{12} \sim 10^{14}$ ions/cm^2 for each energy. After the implantation, the mask has been removed. The post-implantation annealing process is performed under the air at 1,200°C with 24 hours to recover the implantation induced damage.

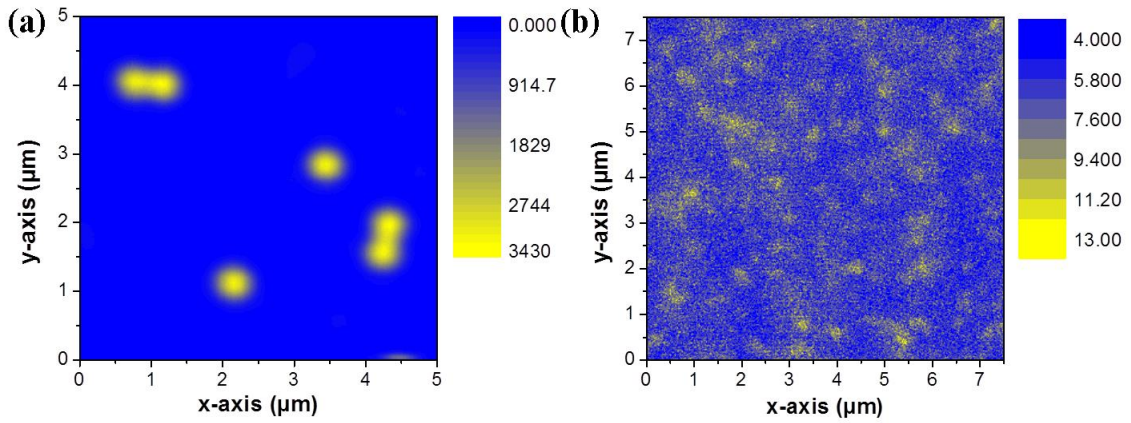

Figure 8.4: Upconversion fluorescence scanning image of (a) Pr implanted YAG. (b) Single Pr ions in ultra-pure YAG crystal.

The upconversion fluorescence scanning image of one of the Pr ion implanted samples is

shown in Fig. 8.4(a). The implantation energy is 225 keV with 6.85×10^{11} ions/cm^2 dose. Compared to the fluorescence image at single-ion level as presented in Fig. 8.4(b), the implanted spots shows at least three orders of magnitude bright fluorescence intensities.

In the well-resolved Pr implanted spots, the upconversion fluorescence intensities have been obtained. The number of Pr ions (N) is estimated by:

$$N = \alpha \frac{I}{I_0}, \tag{8.2}$$

here I correspond to the fluorescence intensity of Pr implanted spots. I_0 represents the fluorescence intensity of single Pr ions in YAG. Since the actual size of the nano-hole ($\sim$200 nm) is bigger than the point spread function ($\sim$120 nm), an additional coefficient factor α is introduced to compensate this difference (for more details please see [187]). In our upconversion microscopy, $\alpha = 1.6$. Equation 8.1 yields to:

$$\eta = \alpha \frac{I}{I_0 N_0}. \tag{8.3}$$

This infers the production yield of implanted Pr ions in YAG. The production yield of Pr implanted ions corresponding to different implantation energies and fluences is plotted in Fig. 8.5. The production yield varies from 6.03% (75 keV energy and 5.02×10^{13} ions/cm^2) to 91% (300 keV and 9.1×10^{11} ions/cm^2).

In Fig. 8.5 several phenomenon can be determined:

1). Higher implantation energies refer to higher production yield. For higher implantation energies, the struggle of implanted Pr ions is larger and the travel distance is longer yielding to bigger implantation volume. Meanwhile implanted Pr ions with higher energy generate more defects and show higher chance to replace the yttrium ions. The post-implantation annealing process helps the Pr ions displacing yttrium ions and settling in crystal lattice.

2). In the same implantation energy, higher fluence induces lower production yield. When the implantation energy is constant, the implanted volume is constant and sees a varying fluence. It indicates that the local density increases with the increasing of the fluence. It yields the lower possibility for Pr ions substituting local yttrium ions. Eventually, the higher the fluence is, the lower the production yield it will be.

Additionally, there are several components contribute the errors in Fig. 8.5: The fluence value measured through the Faraday Cup in the implantation system; the varying size of the nano-holes; the accuracy of the obtained point spread function; the fluorescence intensity difference in between different implantation spots and individual single Pr emitters.

8.3 Ce ions implantations

Similar to Pr case, Ce ions are also implanted in YAG crystal through the FIB implantation system. Owing to the optical detection of single Ce ions in YAG, the production yield of implanted Ce ions can be quantified.

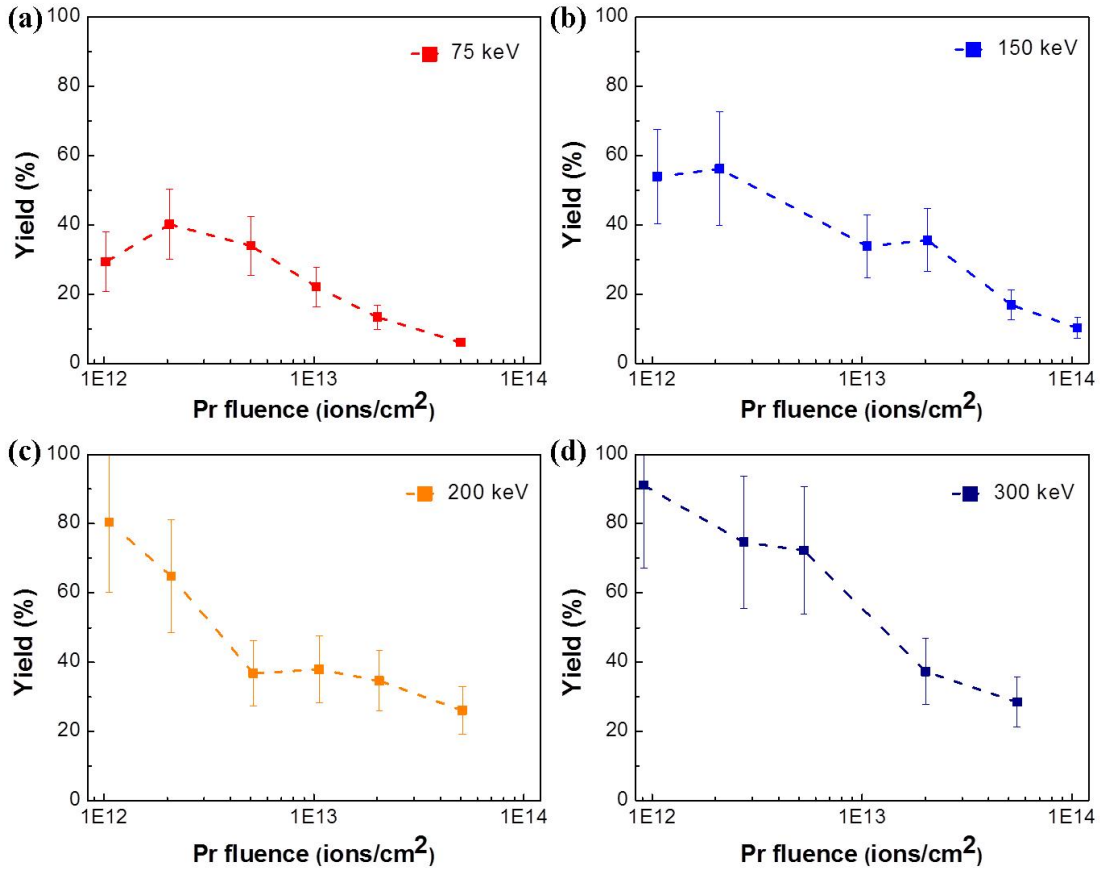

Figure 8.5: Production yield of Pr implanted YAG. The implanted energies are 75, 150, 200, 300 keV with varying fluence respectively

Ce ions are implanted through the metal mask with nano-holes. The implantation energy of Ce ions is 75, 150, 200, and 300 keV with varying fluence from $10^{12} \sim 10^{14}$ ions/cm^2. The post-implantation annealing is set at 1,200°C for 24 hours in reducing atmosphere (Ar/H_2: 95/5 under 1 mbar) to recover the lattice damaging and to avoid the oxidizing atmosphere, which might induce Ce inactivation.

One of the fluorescence scanning images of Ce implanted YAG has been shown in Fig. 8.6(a), where Ce ions were implanted with 150 keV energy and 1.06×10^{12} ions/cm^2. Bright spots corresponding to implanted Ce ions show strong fluorescence intensity, which is at least two orders magnitude higher than the fluorescence signal from a single Ce ion with same experiment conditions (see Fig. 8.6(b)).

With the factor $\alpha = 3.02$ in this case (related to the point spread function as introduced previously), and obtainment of the fluorescence intensity ratio between the implanted spots and native Ce ions, the production yield of implanted Ce is determined as shown in Fig. 8.7.

The implanted Ce ions display similar phenomena as implanted Pr ions. In the same fluence, the production yield increases with the increasing of the ion energies. On the other hand, while the implantation energy is the same, the higher fluence presents, the lower production yield shows. Due to the charge dynamics effect as introduced in the

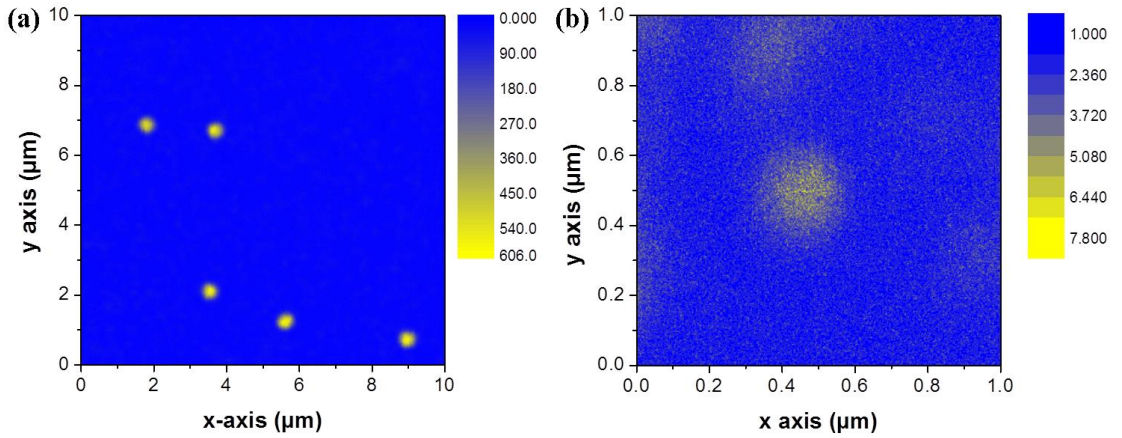

Figure 8.6: fluorescence scanning image of (a) Ce implanted YAG, with implanted energy 75 keV and fluence of 1.06×10^{11} ions/cm^2. (b) Single Ce ions in pure YAG crystal.

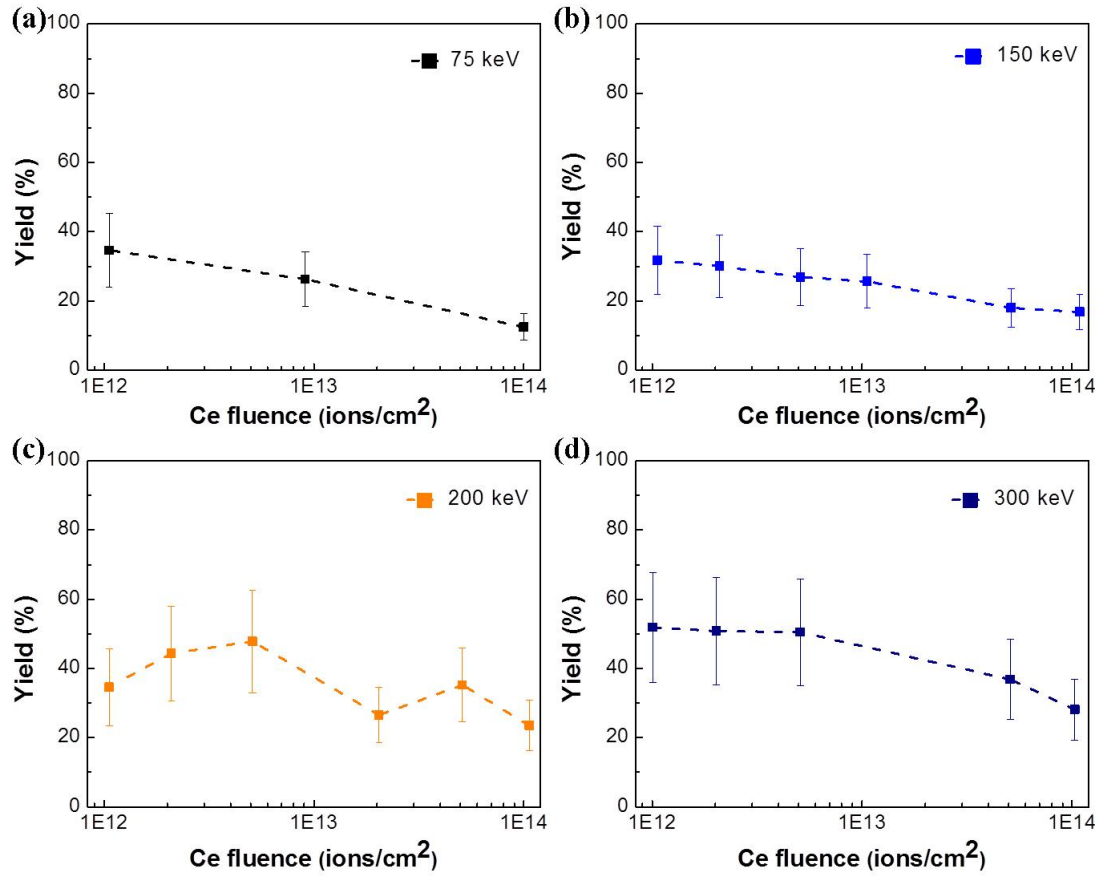

Figure 8.7: Production yield of Ce implanted YAG. The implanted energies are 75, 150, 200, 300 keV with varying fluence respectively

previous chapter, the production yield is not as high as implanted Pr ions. The highest yield of about 53% is achieved when the implantation energy reaches 300 keV with the lowest fluence (10^{12} ions/cm^2).

8.4 Spectroscopy of implanted single rare earth ions

The demonstration of the nanoscale generation of Pr and Ce ions in the crystal, and the quantification of the production yields of the ion implantation indicates an important step towards coupling single rare earth qubits close to each other [188]. However, the ion implantation might introduce additional strain with the damaged lattice structure, which might affect the optical and spin properties of single solid-state qubits, for example, NV centers generated by ion implantation show strong spectral diffusion and short spin coherence time [189].

It is essential to study the spectroscopic performance of implanted rare earth ions at single-ion level to evaluate the influence of the ion implantation to spin and optical properties of single rare earth (Ce) qubits.

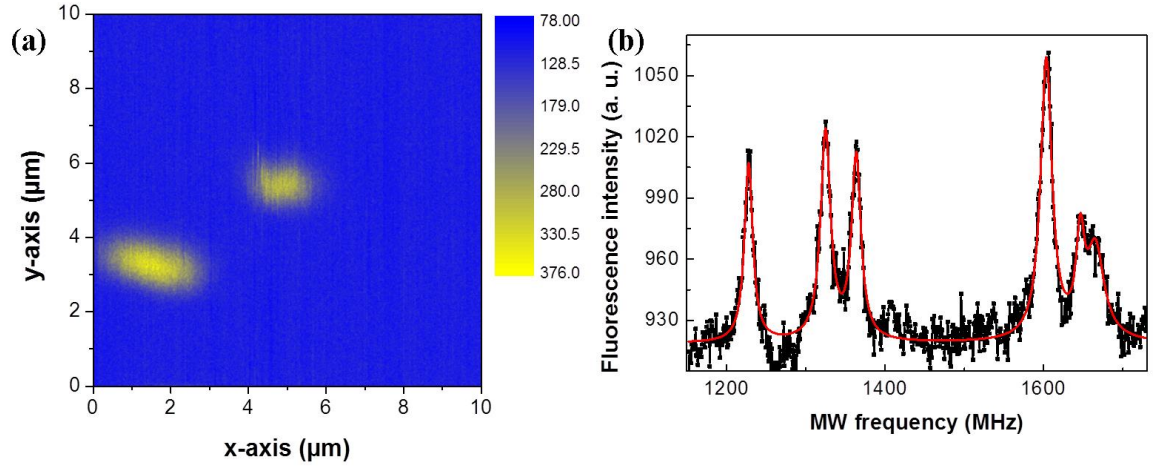

Figure 8.8: (a) Fluorescence scanning image of implanted Ce ions in YAG at low temperature. The excitation laser wavelength is at 450 nm. (b) ODMR of implanted Ce ions showing six different ground spin transitions.

The experimental condition is the same as the one introduced in Chapter IV. A YAG crystal with implanted Ce ions is mounted on the cold finger sample holder and cooled down to ∼3.5 K. Implanted Ce:YAG spots are excited and localized by a laser wavelength at 450 nm (Fig. 8.8(a)). Due to the selection rules presented in Chapter IV, the circularly polarized laser beam is applied to optically initialize the spin states, meanwhile, the frequency of the MW radiation is swept. The ODMR spectra of implanted Ce spots have been recorded as shown Fig. 8.8(b). In the ODMR spectrum, six different ground state spin transitions have been observed with resonance frequency at 1,228 MHz, 1,325 MHz, 1,354 MHz, 1604 MHz, 1,646 MHz and 1,665 MHz respectively. In comparison with single Ce ions in YAG, ODMR spectra of ensemble Ce ions show much lower initialization fidelity. However, ODMR linewidths of implanted Ce:YAG is ∼10 MHz which is equivalent to the ODMR linewidths of single Ce ions. It is the evidence that the ground state spin transitions of Ce:YAG are not influenced by the ion implantation.

The ZPL linewidth of implanted Ce:YAG is $\sim 2\pi \times 550$ GHz. It gives the possibility

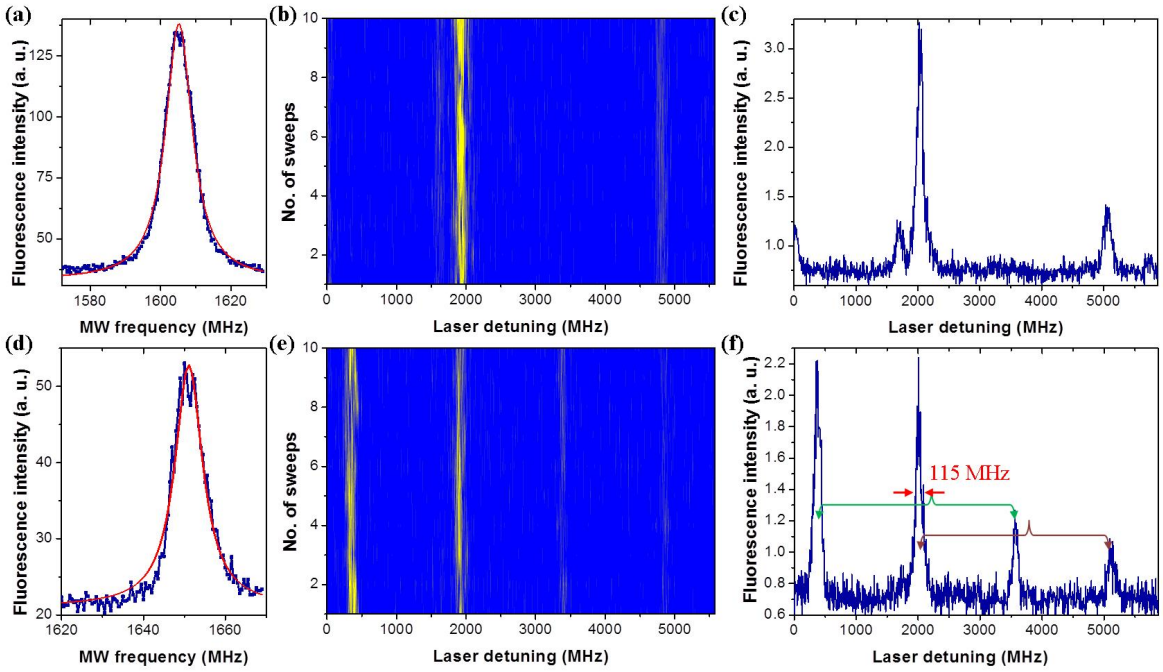

Figure 8.9: (a), (d) ODMR spectrum of single Ce ions created by ion implantation. Single Ce ions are optically initialized by resonant excitation as introduced in Chapter 6. The resonance frequencies of the ground state spin transitions are at 1605 MHz and 1650 MHz respectively. (b), (e) Successive PLE sweeps of single Ce ions in an implanted spot.(c), (f) Excitation spectrum of single Ce ions in the implanted spot.

to spectrally select, excite, and manipulate single Ce ions without affecting to other Ce ions close. Once an implanted spot is localized, the narrow linewidth single mode laser wavelength around 489 nm is applied to resonantly excite Ce ions and to obtain the PLE spectrum. During the sweeping of the laser frequency, a certain frequency MW radiation(on resonance with one of the ground state transitions) is generated to avoid the optical pumping. In the experiment, when the MW frequency is at 1,605 MHz (see Fig. 8.9(a)), one PLE spectrum is obtained as shown in Fig. 8.9(b). The PLE spectrum presents two peaks with narrow linewidth ($\sim 2\ \pi \times 110$ MHz). The successive PLE sweeps of the single Ce ion present no spectral jumps and spectral diffusion of a single Ce ion in the implanted spot (see Fig. 8.9(c)).

However, in the host material, the Ce impurities are high. It is impossible to distinguish whether the acquired PLE was contributed by an implanted single Ce ion or a native single Ce center which is originally in the implanted spot. To unambiguously confirm that the implanted Ce ions represent remarkably good optical properties, a second PLE measurement is performed at the same implanted spot. The frequency of the MW radiation now is at 1,650 MHz (see Fig. 8.9(d)), while this PLE spectrum is acquired. In Fig. 8.9(e) and (f), four resonant transition lines are resolved with narrow transition linewidth ($\sim 2\ \pi \times 115$ MHz). By the frequency difference, it can be deduced that these four optical transition lines correspond to two single Ce ions with same ground state splitting. Consecutive frequency sweeps of two single Ce ions illustrate also narrow optical transition lines with good optical stability (no spectral jumps and diffusion). The

linewidths of optical transitions of implanted single Ce ions are slightly broader than native single Ce ions which might be caused by extra strain introduced during ion implantation.

With the PLE spectra of three individual Ce ions in one implanted spot, it is apparent that optical properties of single Ce ions created by ion implantation are almost as good as native single Ce ions.

Implanted single Ce ions present high performance in both PLE and ODMR spectra. There exists minority evidence, which the ion implantation influence the optical properties and spin properties of single Ce qubits.

8.5 Conclusion

In this chapter, the nanoscale engineering rare earth ions (Pr and Ce) in the crystal(YAG) have been demonstrated by means of FIB implantation. Due to the precise acquirement of implantation dose and area, fluorescence intensities of single Pr and Ce ions, the production yield of ion implantation has been studied. With the lowest fluence in the FIB implantation system, Pr ions show 91% production yield, while Ce ions present 53% production yield.

The spectroscopic properties of implanted single Ce ions has been studied at low temperature. In comparison with the other solid-state systems, e.g. defects in diamond and quantum dots [190], implanted Ce ions show minimal influence by the damaging of the lattice structure. Narrow and stable spin and optical transitions from implanted Ce ions suggest that the spin and optical properties of implanted single Ce ions are as good as native single Ce ions. These results give an opportunity to locally generate single rare earth ions in a nanoscale volume close to the crystal surface and make precision optical control of single Ce qubits.

Chapter 9

Outlook

In the previous chapters, spectroscopic studying of single rare earth qubits in solids have been investigated. The remarkable spin and optical properties of single Ce and Pr ions give an opportunity to explore single rare earth ions to single rare earth solid-state qubits, which might be served as building blocks for constructing scalable quantum networks. Studying and alternating different species of single rare earth qubits for various quantum applications is essential to accomplish the ambitious goal.

In this chapter, various methods are proposed to improve the optical and spin properties of single rare earth qubits. Eventually, CQED approach is raised to not only enhance the optical properties of single ions but provide quantum channels to entangle two or many separate quantum nodes.

9.1 Ce as a readout ion–Pr Ce energy transfer

It is introduced that the $5d \rightarrow 4f$ transitions of Ce:YAG emit photons wavelength in the range of 485∼650 nm, where the optical elements in the experimental setup present good performance, meanwhile single photon detectors display high quantum efficiency. The lifetime of the $5d$ state is 60 ns with quantum efficiency close to unit. It results in strong fluorescence photon flux from Ce:YAG even at single-ion level (close to 100 kHz count rate). However, single Ce ions have only electron spins instead of nuclear spins, indicating strong influence by the local environment, resulting in 200 ns coherence time. On the other hand, single Pr ions in YAG contain nuclear spins, yielding to much weaker coupling with the environment, indicating long-lived nuclear spin qubits. However, Pr ions show more barrier for proper harness optically. The first excited state $^3P_0$ presents a lifetime of 8 μs, yielding to low excitation-emission-reexcitation rate. It makes almost impossible to detect and manipulate Pr^{3+} at single-ion level from this $4f \leftrightarrow 4f$ transitions. The second excited state $4f5d$ is located in much higher energy level, resulting fluorescence emission wavelength in the range of 300∼450 nm. Normally optical elements perform much worse in the UV range in terms of transmission and achromatic. Although the lifetime of $4f5d$ state is 18 ns, less than 10 kHz photons are eventually detected in current experiment conditions. If we can keep the essence, go the dregs for both systems, namely combining

the spin properties of Pr ions and optical properties of Ce ions, we are able to coherently manipulate single nuclear spin of Pr ions and readout the quantum information by single Ce ions (it is similar to [82]).

Here we propose a new scheme of coupling single Pr ions and Ce ions by means of the fluorescence resonance energy transfer (FRET) since the $^3P_0 \rightarrow ^3H_4$ optical transitions of Pr:YAG is at 486.9 and 488.2 nm, and the ZPL of $5d \rightarrow 4f$ transition of Ce:YAG is located at 489 nm. These close transitions might offer the opportunity of the FRET in between these two species. Moreover preliminary results of FRET at a-few-ion level has been demonstrated in both downconversion and upconversion approach [191–193].

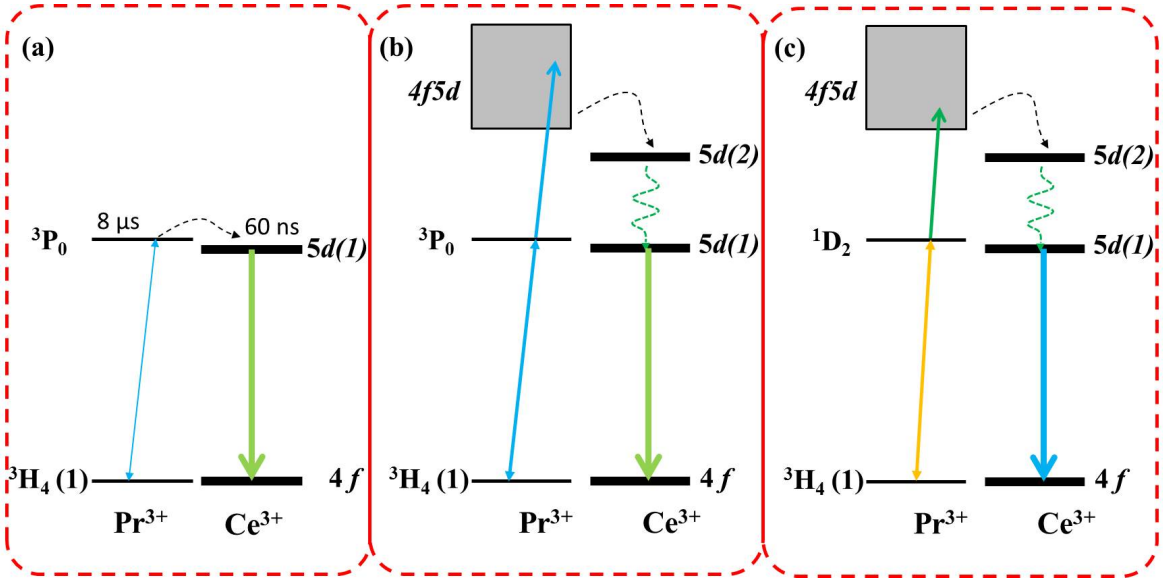

Figure 9.1: Energy transfer of Pr and Ce ions in YAG. (a) Energy is transferred through $^3P_0$ state of Pr ions to $5d(1)$ states of Ce ions. (b) Another scheme of the energy transfer, through the $4f5d$ states of Pr ions to $5d(2)$ states of Ce ions. (c) Upconversion energy transfer, where Pr ions are excited by 609 nm and 532 nm laser and the emitted photon wavelength at 489 nm.

In the downconversion FRET approach, Pr ions are excited to the $^3P_0$ state by a 487 nm laser. The energy is either transferred from $^3P_0$ state of Pr ions to the $5d(1)$ state of Ce ions as shown in Fig. 9.1(a), or Pr ion is promoted further to $4f5d$ state by the excited state absorption, and transfer its energy to the $5d(2)$ level of Ce ions (Fig. 9.1(b)) [194, 195]. Eventually, the dowconverted fluorescence emitted from Ce:YAG has been recorded. Regarding the upconversion FRET approach, the Pr ion is first excited to long lived $^1D_2$ state. It is promoted further to the $4f5d$ level when it absorbs another photon. The energy is transferred from the $4f5d$ states of Pr to the $5d(1)$ state of Ce, resulting in the emission in the upconversion region in comparison with the excitation laser wavelength (532 and 609 nm) (see Fig. 9.1(c)). The observation of Pr and Ce energy transfer offers a new platform to construct the hybrid quantum system.

9.1.1 Energy transfer through $^3P_0$ state

In the experiment, 100 pm Ce:YAG nanoparticles (contain 50∼100 Ce ions in each individual nanoparticles) are spin-coated on the glass substrate. A tunable diode laser wave-

length in the range of 485∼490 nm is applied to excite the nanoparticles. In the detection channel, a 538 nm longpass filter is inset to block the scattering from the excitation laser. When a single Ce:YAG nanoparticle is localized under the home-built confocal microscopy operating under ambient conditions, the excitation spectrum of a Ce:YAG nanoparticle is obtained by sweeping the frequency of the diode laser as shown in Fig. 9.2(d). It presents two peaks located at 486.9 and 488.2 nm, which is in agreement with the excitation spectrum of Pr:YAG (see Fig. 9.2(e)). It indicates that Pr ions are excited in the Ce:YAG nanoparticles. The emission spectrum of the Ce:YAG nanoparticle is obtained when the laser is on and off resonance with the Pr:YAG $^3H_4 \rightarrow ^3P_0$ transitions as plotted in Fig. 9.2(a) and (b). If we subtract two spectra as displayed in Fig. 9.2(c), an emission spectrum of Ce:YAG can be obtained. This means in 100 ppm Ce, 0 ppm Pr ions doped YAG nanoparticles, the excitation spectrum of Pr:YAG is observed with the emission of Ce:YAG signals. From our previous knowledge that in yttrium powder, it always contains many impurities such as Er, Pr and Ce ions. Sometimes Pr ions can be detected even under pure YAG nanoparticles. It indicates that in this type of the synthesized YAG nanoparticles, low concentration (1∼5 ppm) Pr impurities is always contained. After we correlate all the evidence, a brief conclusion can be deduced when a 488.2 nm wavelength laser shines on the Ce:YAG nanoparticle, Pr ions as impurities in the Ce:YAG nanoparticle have been excited. Pr ions transfer their energy to the nearby Ce ions. Eventually, Ce ions decay back to the ground state with fluorescing photons. It results in the observation of both excitation spectrum of Pr ions and emission spectrum of Ce ions.

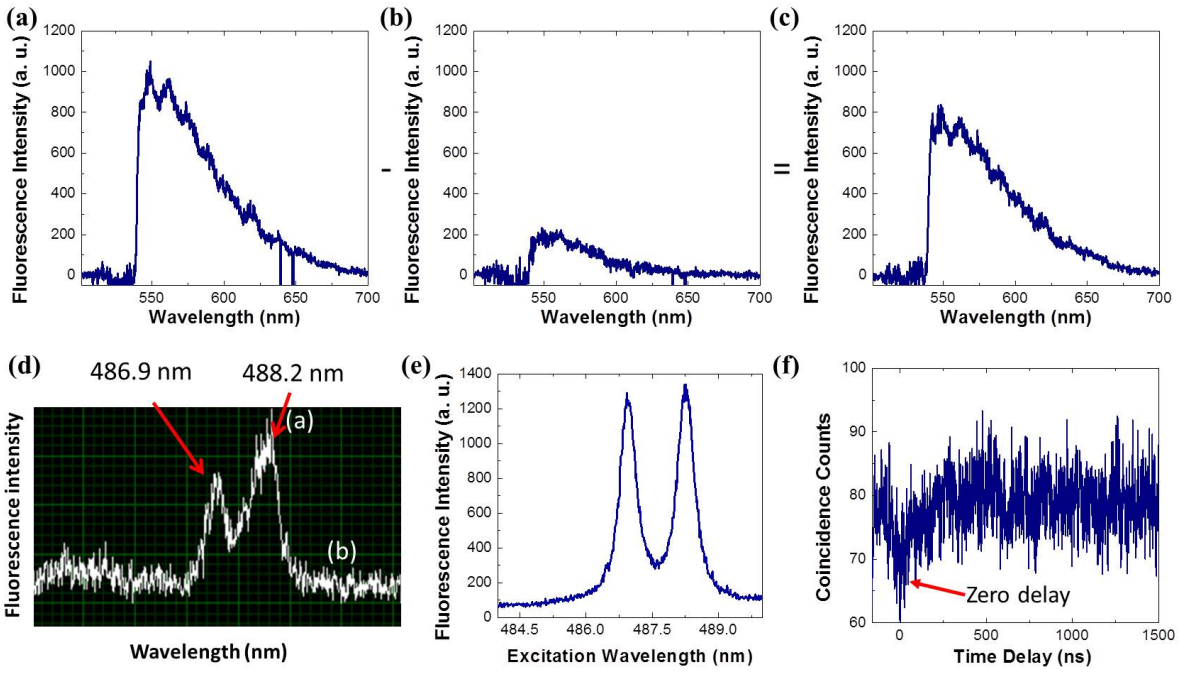

Figure 9.2: (a) The emission spectrum of Ce:YAG when it is excited at 488.2 nm. (b) Emission spectrum of Ce:YAG when it is excited around 490 nm. (c) The subtraction of (a) and (b), displays Ce emission spectrum. (d) The excitation spectrum of the Ce:YAG nanoparticle. The diode laser frequency is swept from 485 nm to 491 nm. (e) The excitation spectrum of Pr:YAG. (d) The second order correlation measurements of 100 ppm Ce:YAG nanoparticle, when it is excited at 488.2 nm, showing a dip at zero delay time. It indicates that the detected fluorescence is contributed by a few (2, or 3) single photon emitters at Ce:YAG nanoparticles

Interestingly, when the second order correlation measurement of the Ce:YAG nanoparticle is performed as presented in Fig. 9.2(f), a dip is clearly resolved at zero delay time. It indicates the anti-bunching behavior of the excited Ce:YAG nanoparticle. The observed $g^{(2)}(0) > 0.5$, implies a few emitters (2 or 3 actually) contributing in the detected fluorescence signals. Normally 100 ppm Ce:YAG nanoparticles contain in average 50∼100 Ce ions inside. The measured $g^{(2)}$ function suggest that 2 or 3 Pr ions in the nanoparticle are excited by the 488.2 nm laser. They eventually transfer their energy to nearby Ce ions and resulting in high efficiency Ce emissions. Previously Pr ions in YAG can not be detected at single-ion level by the downconversion microscopy since the excitation-emission-reexcitation cycling efficiency is too low. When Ce ions are brought nearby Pr ions, Ce ions can play a role in readout ion by means of FRET process. At cryogenic temperature, it might offer a new approach to coherent manipulate the nuclear spin of single Pr ions. Instead of readout the nuclear spin of Pr:YAG by upconverted UV emission painfully, a Ce ion is set as a readout ion to readout the nuclear spin of Pr ions by visible photon emission with high fluorescence efficiency.

9.1.2 Energy transfer through $^1D_2$ state

Another approach we proposed here is to readout Pr ions through the upconverted FRET process as shown in Fig. 9.1(c). The upconversion process of Pr ions in YAG can be accomplished not only by a 488 nm laser but by a combination of 532 nm and 609 nm lasers through $^3H_4 \rightarrow ^1 D_2 \rightarrow 4f5d$ transitions. On the other hand, it is introduced in Chapter VI that the ZPLs of Ce:YAG show ∼500 GHz inhomogeneous broadening at cryogenic temperature, while the homogeneous linewidth of a single Ce ion is close ∼100 MHz. The high resolution spectrometer can determine the number of fluorescing Ce ions by their emission spectra, if the number of Ce ions is not many (see Chapter VI). In principle, the upconversion FRET process can be observed by the combination of upconversion process of Pr ions and well resolved ZPL of single Ce ions.

A special treatment of the sample is required for this proposal. Pr and Ce ions are co-implanted in a un-doped YAG crystal through the same mask by means of FIB implantation (a same method which is introduced in Chapter VIII). The dosage of Pr ions is fixed to be 4.19×10^{13} ions/cm^2. The dosage of Ce ions exists two opinions, either high (3.35×10^{13} ions/cm^2) or low (8.37×10^{12} ions/cm^2) dose. In the co-doped spot, two different concentrations of Pr-Ce are introduced. Post-implantation annealing is carried out to recover the lattice structure.

The experiment is performed at cryogenic temperature. The crystal is mounted at the cold finger cryostat. Two lasers wavelength at 532 and 609 nm are combined to excite Pr ions through $^3H_4 \rightarrow ^1 D_2 \rightarrow 4f5d$ transition. The detection window is in the range of 485∼500 nm spectrally. For the high Ce dose area, the emission spectra are obtained as plotted in Fig. 9.3(a). Two strong peaks (486.9 and 488.2 nm) corresponding to $^3P_0 \rightarrow ^3 H_4$ transitions are observed. Meanwhile, a weak peak located at 489 nm is resolved, which represents to the ZPL of Ce ions. When we take a close look at the ZPL position of Ce:YAG (see Fig. 9.3(d)), the inhomogeneous broadening of ZPL is determined to show ∼800 GHz FWHM linewidth. The linewidth of high dosage Ce ZPL is in agree with our previous results. It indicates that a large number of Pr ions transfer their energy to many

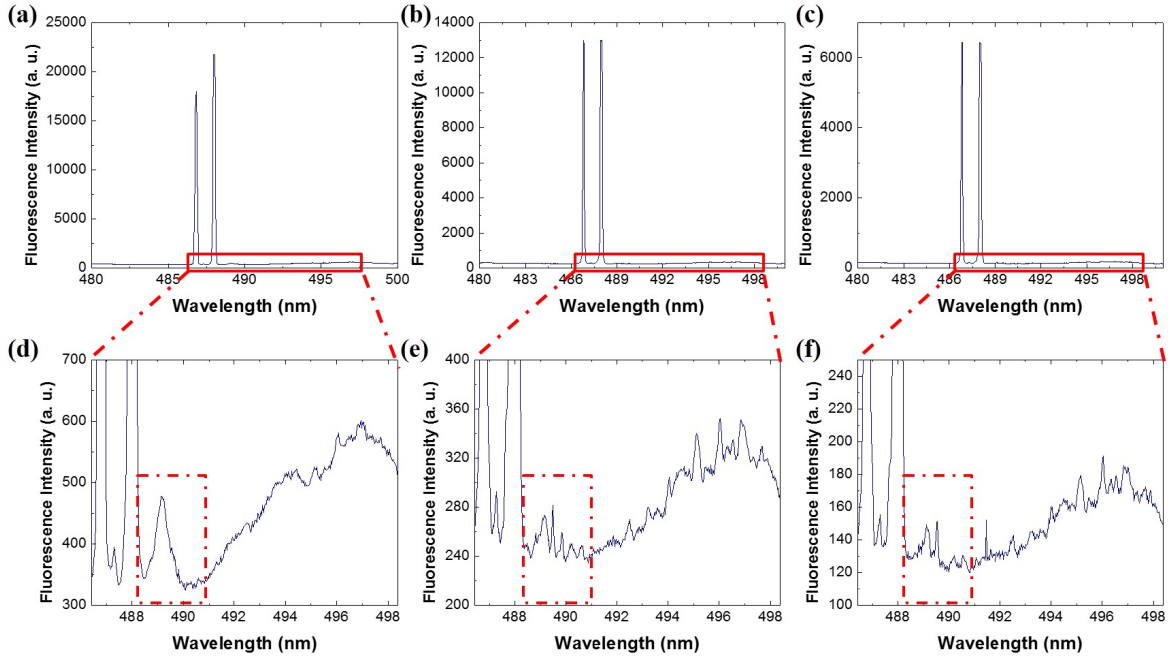

Figure 9.3: The emission spectrum of the Pr and Ce co-implanted spots acquired by a high resolution spectrometer. The spots are excited by 532 and 609 nm lasers. (a) Ce ions are implanted in the dosage of 3.35×10^{13} ions/cm^2. (b) and (c) Ce are implanted in the dosage of 8.37×10^{12} ions/cm^2. (d)-(f) Zoom in spectra of (a)-(c) respectively. The ZPL lines of Ce:YAG is resolved which located at 489 nm.

Ce ions. It is impossible to resolve the ZPL from single Ce ions since the number of fluorescing Ce ions is high.

The same measurements are performed in the low dose region. The emission spectra taken by different spots are presented in Fig. 9.3 (b) and (c). They look similar to the one obtained from Ce high dose area. However, if we zoom in the ZPL region (Fig. 9.3(e) and (f)), we clearly notice that the ZPLs of Ce ions are different in comparison to the ZPLs of ensemble Ce ions. Some sharp and discrete peaks appear in the inhomogeneous domain of ZPL position. Two different spots display different ZPL spectra. It indicates when numerously Pr ions are pumped by the excitation lasers, a few Pr ions transfer their energy to nearby Ce ions, resulting in the fluorescing of Ce at a-few-ion level. It presents the second evidence of FRET between Pr and Ce in close to single-ion level.

In general, the FRET of Pr and Ce in close to single-ion level has been observed in two situations. It offers a possibility of taking advantage of the single Ce ions to readout quantum information of nearby single rare earth qubits which is difficult to be detected optically owing to their long optical lifetime. This is a novel approach to construct hybrid quantum systems.

9.2 Evidence of single Ce ions in YSO crystal

In this dissertation, the solid state hosts where the single Pr and Ce ions are embedded in, are either YAG or LuAG crystals. They present excellent optical properties, however,

both types of the crystals contain numerous intrinsic nuclear spins, resulting in short coherence time of the single rare-earth solid-state qubits. In comparison, Y_2SiO_5 crystal is a well known and studied crystal due to its low spin bath., The general physical and optical properties of trivalent cerium doped YSO crystal is introduced in Chapter II. If single rare earth ions can be detected and coherently manipulated in YSO crystal, it will offer long lived qubits, which is suitable for more complex quantum operations. The investigation of Ce doped YSO crystal has been carried on [123, 196], however, the attempts of detecting single Ce ions in YSO crystals is so far unsuccessful [123, 124].

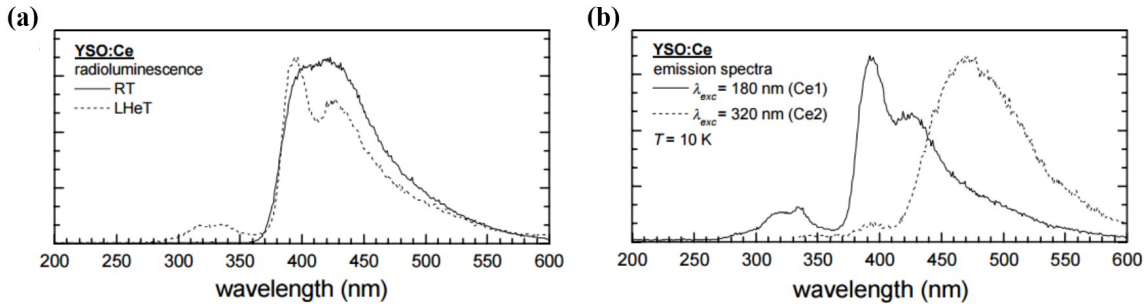

Figure 9.4: (a) Emission spectrum of Ce:YSO located in site 1. (b) Emission spectrum of Ce:YSO located in site 2. Figures are reproduced from [130].

We accidently figure out that one of the undoped YSO crystal presents the evidence that Ce^{3+} might be detected at single-ion level. The experiment conditions are following: A Ti:Sapphire femtosecond pulsed laser is generated with wavelength around 730 nm. The laser frequency has been doubled by an SHG crystal which is regarded as the excitation light source. The optical elements present low transmission efficiency in UV range, resulting in only 260 nW laser power being left after the photonic crystal fiber. The crystal is mounted on a home-built UV confocal microscopy operating under ambient conditions, where a 400 nm long pass filter is served as the dichroic mirror. It indicates that the fluorescence wavelength shorter than 400 nm is not detectable. Due to the poor UV transmission, only a 0.85 N.A. air objective lens fulfills the task. To enhance the collection efficiency and spectral resolution, SILs are fabricated on the top of the undoped YSO crystal by means of FIB milling. Since in the YSO crystal, Ce contains two different sites emitting in different spectral range. Two different filter sites are introduced to distinguish different sites of Ce:YSO in spectrally (400∼425 nm and 475∼625 nm).

The laser scanning images of undoped YSO under the SIL are displayed in Fig. 9.5. In the spectral domain, optical filters are introduced in the range of 475∼625 nm to detect the emitted photons from site 2 Ce:YSO, as shown in Fig. 9.5(a) and (c), who are scanned in different depth. Individual bright spots have been resolved, however, the impurities are still high. It is arduous to perform the photon statistic measurements on the individual bright spots due to the low signal-to-noise ratio. Figure 9.5(b) and (d) are acquired in the same area and depth as Fig. 9.5(a) and (c), while, the detection window is in the range of 400∼425 nm which is desirable for site 1 Ce:YSO emission. Individual bright spots are identified, while their positions are different in comparison with Fig. 9.5(a) and (c). It indicates that in this undoped YSO crystal, two species of individual emitters have been identified in both spectral and spatial domains, which might be the evidence of detecting X1- and X2-sites single Ce ions in YSO.

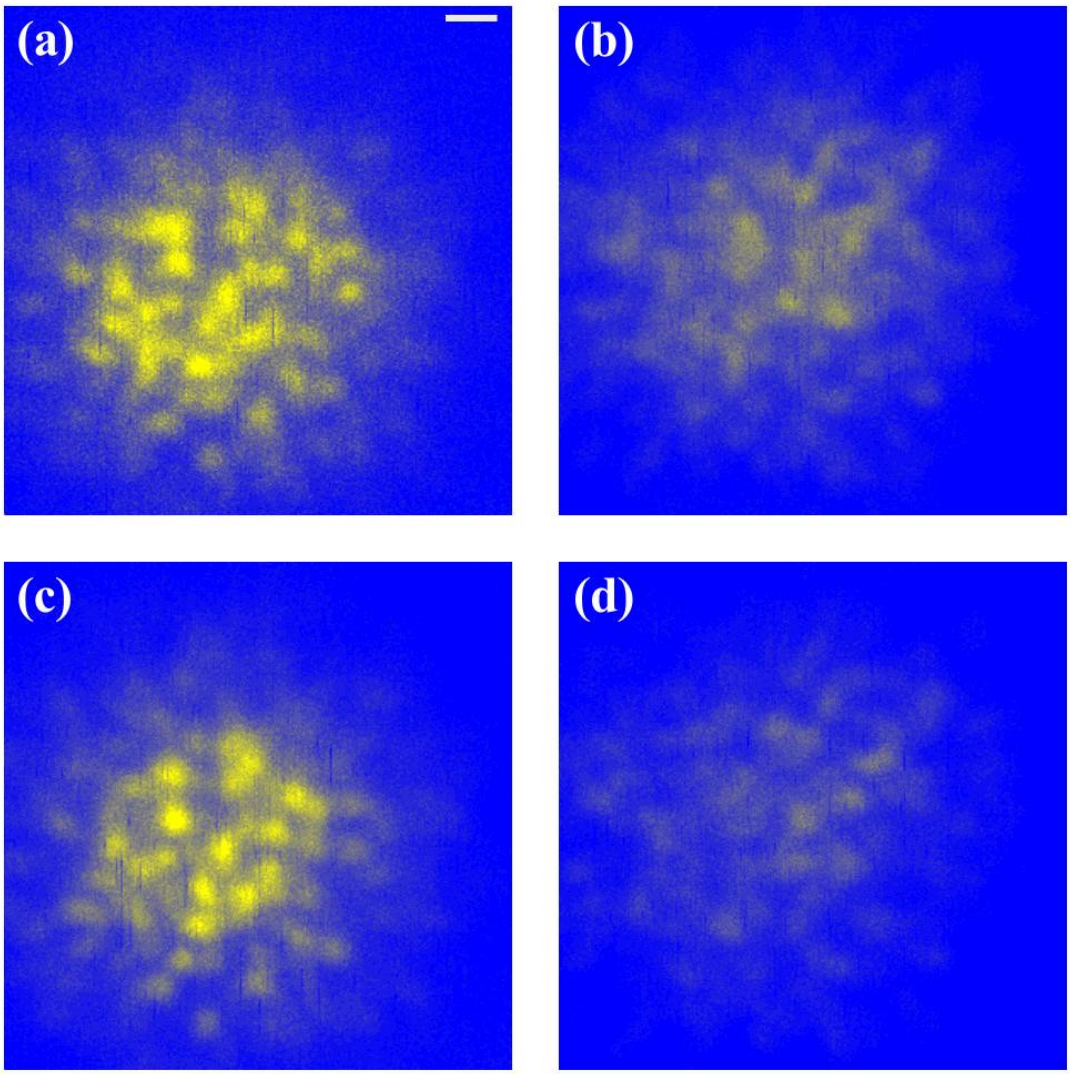

Figure 9.5: (a) Fluorescence scanning image of undoped YSO crystal under a SIL, detection range 475∼625 nm. Scalar bar represents 1 μm. (b) Fluorescence scanning image of undoped YSO crystal same area as (a), spectral range 400∼425 nm. (c) Fluorescence scanning image of undoped YSO crystal under a SIL, another area compared to (a) and (b), detection range 475∼625 nm. (d) Fluorescence scanning image of undoped YSO crystal same area as (c), spectral range 400∼425 nm.

The second order correlation function measurements of single impurities in undoped YSO crystal have been acquired. After normalization, some single bright spots show the $g^{(2)}$ <0.5, indicating the spots are corresponding to the single photon emitters. However, owing to poor signal-to-noise ratio (around 1:1), the dip of the $g^{(2)}$ function doesn't approach to zero.

To evaluate the single color centers in undoped YSO crystal, the emission spectrum is obtained. The sample is excited by a 375 nm UV laser. The fluorescence of the color centers wavelength longer than 400 nm is detected by the spectrometer. To characterize the wavelength dependency of the transmission in the experiment setup, the emission

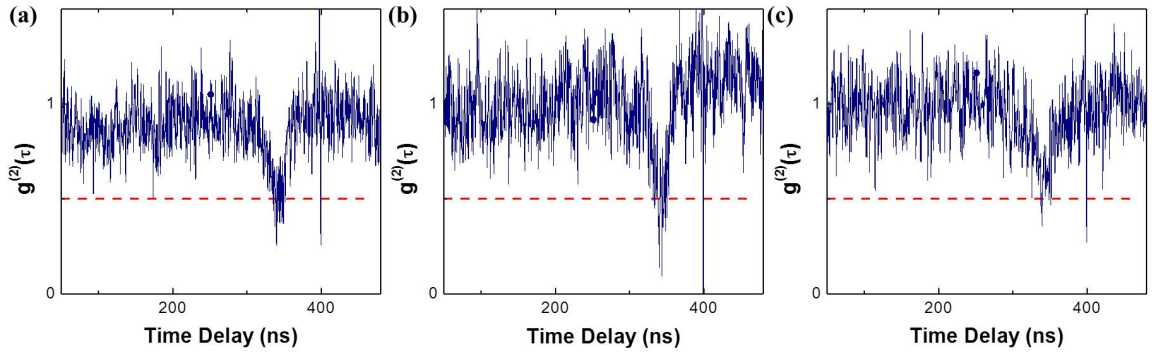

Figure 9.6: The second order correlation function of single impurities in YSO crystal.

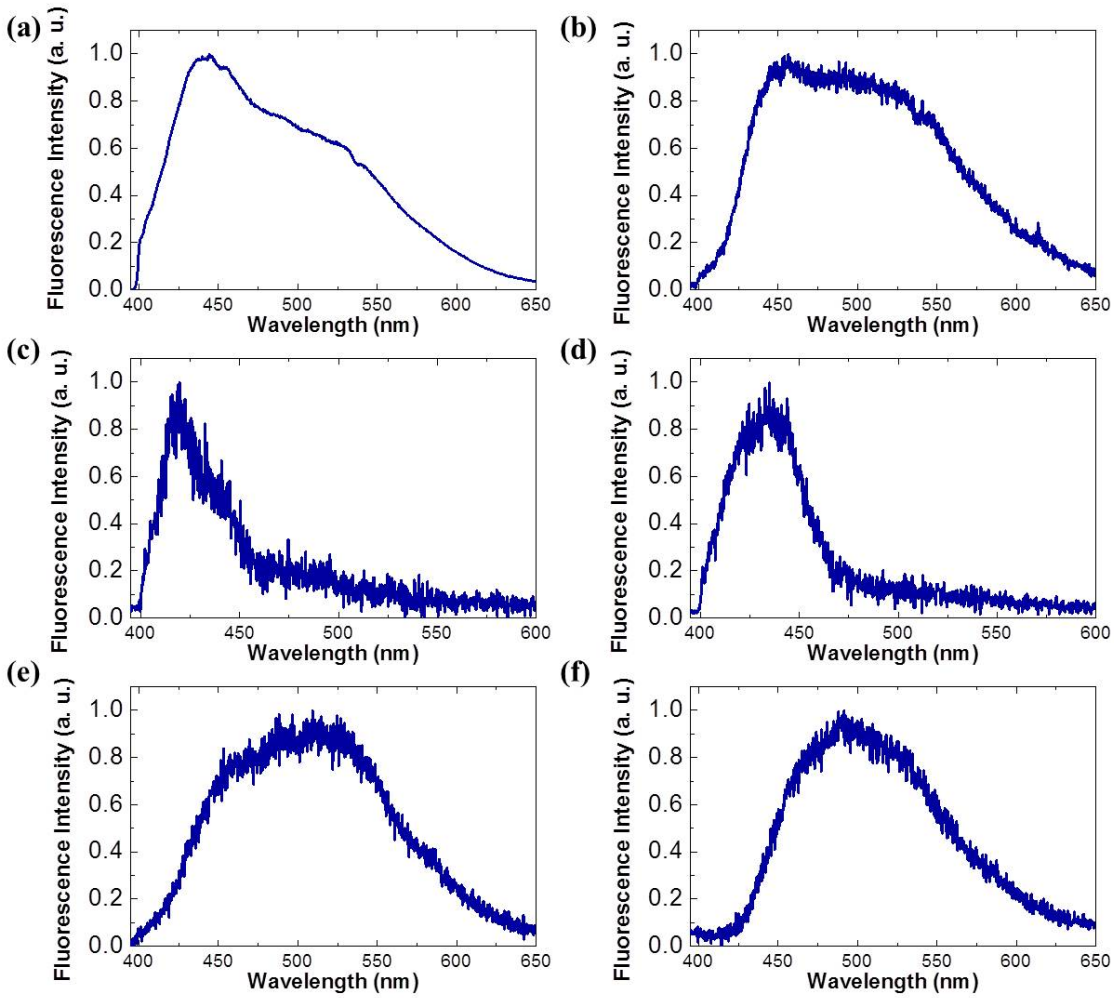

Figure 9.7: (a) The emission spectrum of Ce:YSO bulk crystal. (b) The emission spectrum of Ce^{3+} implanted YSO crystal. (c)-(f) The emission spectrum of single bright spots in YSO crystal, presenting different spectrum range. Noting owing to high impurities, emission spectrum from the other spots might contribute the spectrum of a single bright spot

spectrum of a Ce:YSO bulk crystal is measured as shown in Fig. 9.7(a). It displays different shape compared to the literature (see Fig. 9.4). The spectrum rises up from 400 nm, with

a peak position at 423 nm. A long tail in the spectrum is presented after the peak. The rising slope (400∼425 nm) is mainly caused by the non-ideal optical elements in the detection path, where mirrors and lenses are all chosen in the visible light range indicating poor transmission efficiency if the photon wavelength close to 400 nm. The long tail is contributed by the emission from X2-site of Ce in YSO crystal, whose peak location is at 475 nm. It also suggests that in Ce:YSO bulk crystal, the concentration of Ce in X1- is higher than X2-sites. The emission spectrum of Ce^{3+} implanted YSO spot has been measured and presented in Fig. 9.7(b). The emission spectrum of individual color centers in undoped YSO crystal have been acquired as displayed in Fig. 9.7(c)-(f). Two different types of emission spectrum can be clearly distinguished. Figure9.7(c), (d) express peaks close to 425 nm. Figure9.7(c) and (d) shows a sharper cut-off edge after the peak compared to the ensemble measurements. It indicates the background contributed by X2-site of Ce:YSO is well excluded. The long tail in Fig. 9.7(b) is dedicated by X2-site of Ce:YSO. Figure9.7(e) and (f) illustrate spectrum alike to Fig. 9.4(b) where peaks are located around 475 nm. The evidence might imply that these are the fluorescence from X2-site of Ce:YSO.

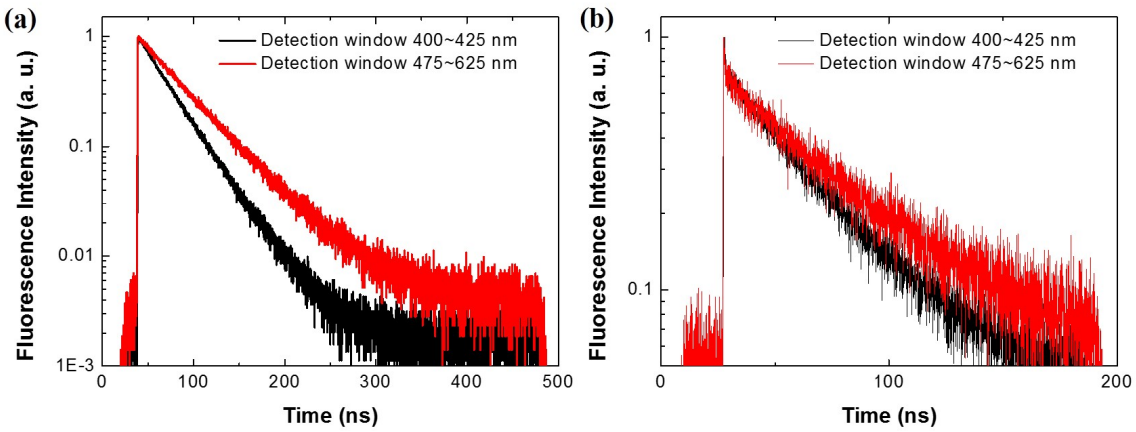

Figure 9.8: Lifetime measurements with two detection windows 400∼425 nm (black curves) and 475∼625 nm (red curves) ranges represents to two different sites. (a) Ce:YSO bulk crystal. (b) Single bright spots in undoped YSO crystal.

To confirm this hypothesis, the lifetime of these two species of color centers in YSO crystal has also been investigated. We first obtain the optical lifetime in Ce:YSO bulk crystal in two different spectral range (Fig. 9.8(a)). The black curve is obtained in the spectral range 400∼425 nm, where the fluorescence signal is mainly from the X1-site of Ce:YSO, showing a 33 ns decay time. In the red curve, the detection window is 475∼625 nm, where the fluorescence signal is mainly from the X2-site of Ce:YSO. It presents a 47 ns lifetime from the excited state. Same experiments have been performed in two species of color centers in the undoped YSO crystal (see Fig. 9.8(b)). The black curve measured in the range 400∼425 nm displays a lifetime of 35 ns, while the red one reveals a 48 ns lifetime, which is correlated to the Ce:YSO ensemble results.

In conclusion, the experiment data of individual bright spots in undoped YSO crystal expresses two different species of color centers. They show different performance in the lifetime, spectral and spatial domains, which is in agreement with the X1- and X2- sites

of Ce:YSO in the bulk crystal. It suggests the evidence of detecting Ce at single-ion level in YSO crystal.

Unfortunately, neither these color centers nor Ce:YSO bulk crystal present the quantum beats in the excited states alike Ce:YAG. Moreover, we also attempt to initialize the ground spin state of single Ce ions in YSO by circularly polarized light at low temperature. The birefringent effect of the YSO crystal obstructs the selection rules resulting in the failure of the optical pumping. Nevertheless, if we equip a single mode laser wavelength at 371 nm, single Ce ions in YSO can be excited resonantly. It will offer a new opportunity to initialize the ground spin state as demonstrated in Chapter VI. When the spin state of Ce:YSO is initialized, the coherent properties of single Ce ions in YSO crystal can be explored. Owing to the low spin bath, it will turn into a longer lived spin qubit. On top of it, the hyperfine interaction of nearby of ^{29}Si will offer additional long lived nuclear spin qubits, which can serve as quantum registers. The detection of single Ce ions in YSO may establish a new stage for constructing hybrid quantum system, where the Ce electron spin is used as a processing unit and long lived ^{29}Si nuclear spin is regarded as a storage unit.

9.3 CQED in single rare-earth ions in solids

The interaction between a two-level system and an external electromagnetic field will be strongly enhanced if it is placed into a high-finesse resonant cavity. With sufficiently small mode volume and large Q-factor of the cavity, it is possible to realize optical non-linearity with a single ion and a single photon in the cavity [197]. The interaction between an ion and electromagnetic filed has two important parameters: The critical ion number $N_A = \kappa\gamma/g^2$ and the saturation photon number $N_P = \gamma^2/3g^2$, in which κ is the decay rate of the cavity, γ represents the spontaneous decay rate of an ion, and g indicates the coupling strength between the cavity and an ion. N_A refers to the number of ions required to change the resonance of the cavity. N_P represents the number of photons needed to saturate an ion. In the cavity if $N_P < 1$ and $N_A < 1$, it is known as 'strong coupling regime'. It will show strong non-linear effects, for example; only one photon and one ion will appear in the cavity. It is predicted that so far the CQED effect in the strong coupling regime has the highest efficiency of interfacing flying qubits (photons here) with stationary qubits (ions in the cavity). It will also give an opportunity to couple two stationary qubits [198].

The CQED research with atoms has demonstrated pioneering results. For example; realization of a one-atom laser in the cavity [199], deterministic generation of single photons from single atom in a cavity [200]; an elementary quantum network of single atoms in cavities [201], etc. Meanwhile, the CQED approach is transferred into solid-state hosts, such as demonstration of CQED with quantum dots [15, 34, 35], enhancement of the zero-phonon line of nitrogen-vacancy centers in diamond by a photonic crystal cavity [202], and coupling ensemble rare-earth ions in a nanobeam resonator [63, 203], etc. Apart from demonstration of the coupling between ions and cavities [204], enormous progress has been achieved in opto-mechanical resonators and on-chip photonic integrated circuits [205]. The combination of an ability to detect and manipulate single rare-earth ions and fabricate high-Q cavities, will give an opportunity to couple single rare-earth ions in a resonator cavity in the 'strong coupling regime' to demonstrate CQED with single rare-earth ions.

Technically, attempts of directly fabricating optical cavities on host materials are not successful. It is still challenging to produce low insertion loss thin films made by optical glasses. To overcome this issue, several approaches have been arisen up to couple rare earth ions in the optical cavities, for example, fabricating the nano-photonic devices on the crystal by means of FIB milling, coupling rare earth nanoparticles to a fiber based Fabry-Perot cavity. Here, we propose a new approach, which is coupling single rare earth ions through a high quality external cavity by its evanescence tail.

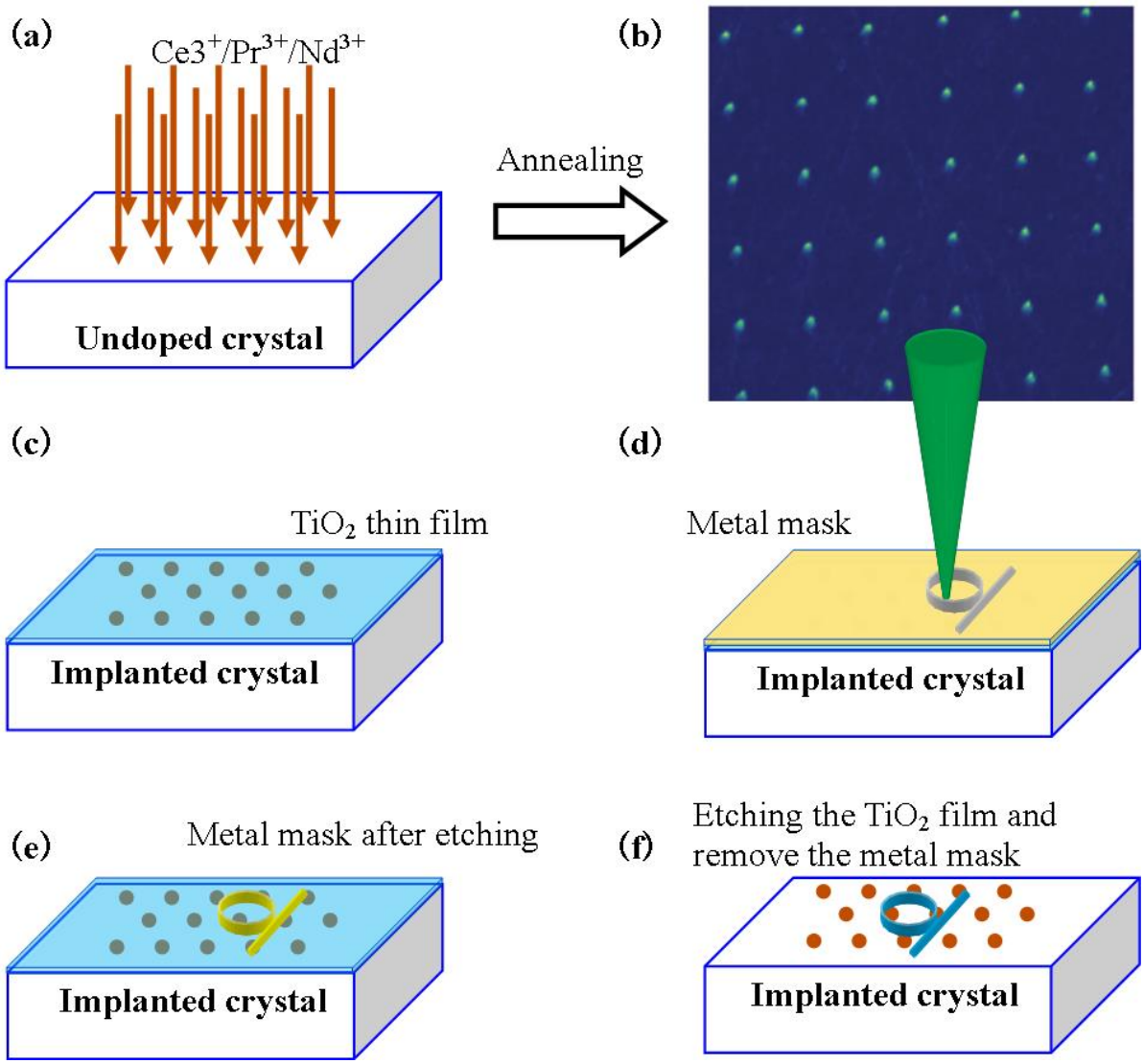

Figure 9.9: Methodology of fabricating optical resonators. (a) Engineer rare earth species near the surface of the crystal by ion implantation. (b) An annealing is performed after ion implantation. (c) Low optical losses TiO_2 thin film is spattered on the crystal. (d) Evaporate a thin metal layer as the mask, and shape the mask by means of E-beam or optical lithography. (e) Produce the metal mask. (f) Etch the TiO_2 film by reactive ion etching so as to create the optical cavity by TiO_2 film.

The methodology of fabricating optical resonators on the crystal is presented in Fig. 9.9.

(1) Nanoscale engineering rare earth ions near the surface of the crystal by means of

ion implantation. To couple the rare earth ions to the cavities with evanescence tail, the location of the rare earth ions are essential. If the rare earth ions are close to the cavities, the coupling efficiency is high. The knowledge we acquired from Chapter VII indicates that rare earth ions can be artificially fabricated near the surface of the sample with high production yield. The current evidence shows that the spin and optical properties of implanted single Ce ions is well preserved.

(2) Coating high optical quality thin film on the crystal. Here, TiO_2 thin film (350∼700 nm) is sputtered. It shows low insertion loss ∼0.5 dB/cm with high reflective index (∼2.4) in the literature.

(3) The Producing of metal masks for the resonators. We evaporate a thin metal layer (∼50 nm Ni) on top of the TiO_2 films. The metal mask is manufactured by means of E-beam or optical lithography.

(4) Fabricating resonators. The TiO_2 thin film is etched through the metal mask by reactive ion etching. After removing the residue metal, the cavities are eventually fabricated.

(5) Test the performance of the cavities and attempt to couple single rare earth qubits to the cavities.

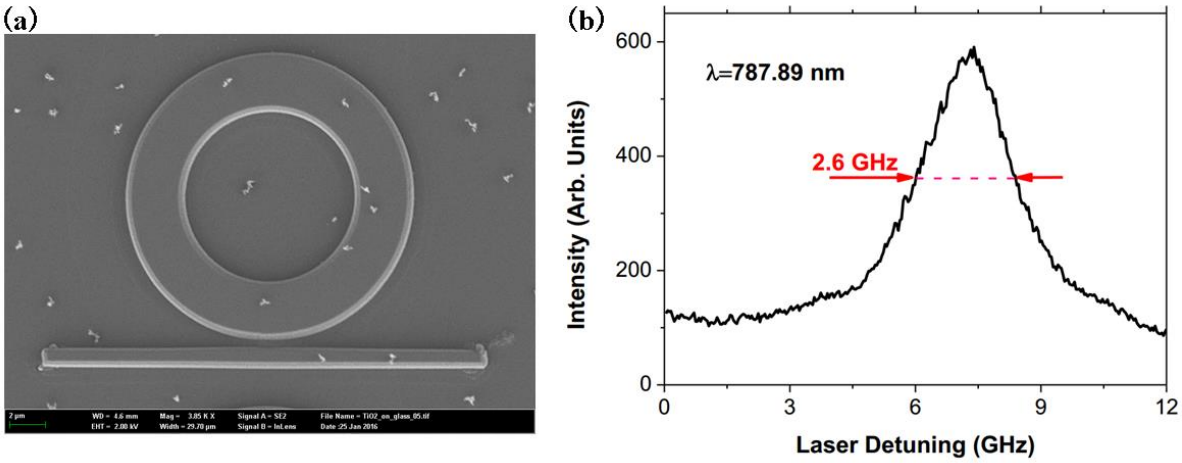

Figure 9.10: WGM cavity made by TiO_2 film on glass substrate. (a) SEM image of a WGM cavity. (b)The cavity shows resonance linewidth 2.6 GHz at 789.89 nm, indicating 146,000 Q factor.

So far, the recipe of processing whispering gallery mode (WGM) cavities made by TiO_2 has been demonstrated on a glass substrate. The SEM image of a whispering gallery mode (WGM) cavity is shown in Fig. 9.10(a). It contains an 8 μm radius WMG cavity coupled to a 25 μm long fiber. A narrow linewidth (∼500 kHz) single mode laser is applied to sweep its frequency across the resonant line of the WGM cavity. It presents resonance linewidth 2.6 GHz at 789.89 nm (see Fig. 9.10(b)), indicating the Q factor of the cavity to be 146,000. We believe, if this recipe is adapt to the TiO_2 films on YAG crystal, CQED based on single rare earth ions will be demonstrated. It will offer

us a new platform to achieve the interfacing of single photon and single rare earth ion. As an example, vacuum Rabi splitting of the optical transitions will appear when the coupling is "strong". Furthermore, as soon as the CQED is achieved, the lifetime of the rare earth ion will be dramatically reduced due to the Purcell effect, which might offer us a new platform for detecting and manipulating rare earth ions at single ion level. Most importantly, with the accomplishment of CQED, cavities will act as quantum channels to entangle individual quantum nodes (single rare earth solid-state qubits here). This will be a novel and essential approach to construct scalable quantum network based on single rare earth solid-state qubits (Fig. 9.11).

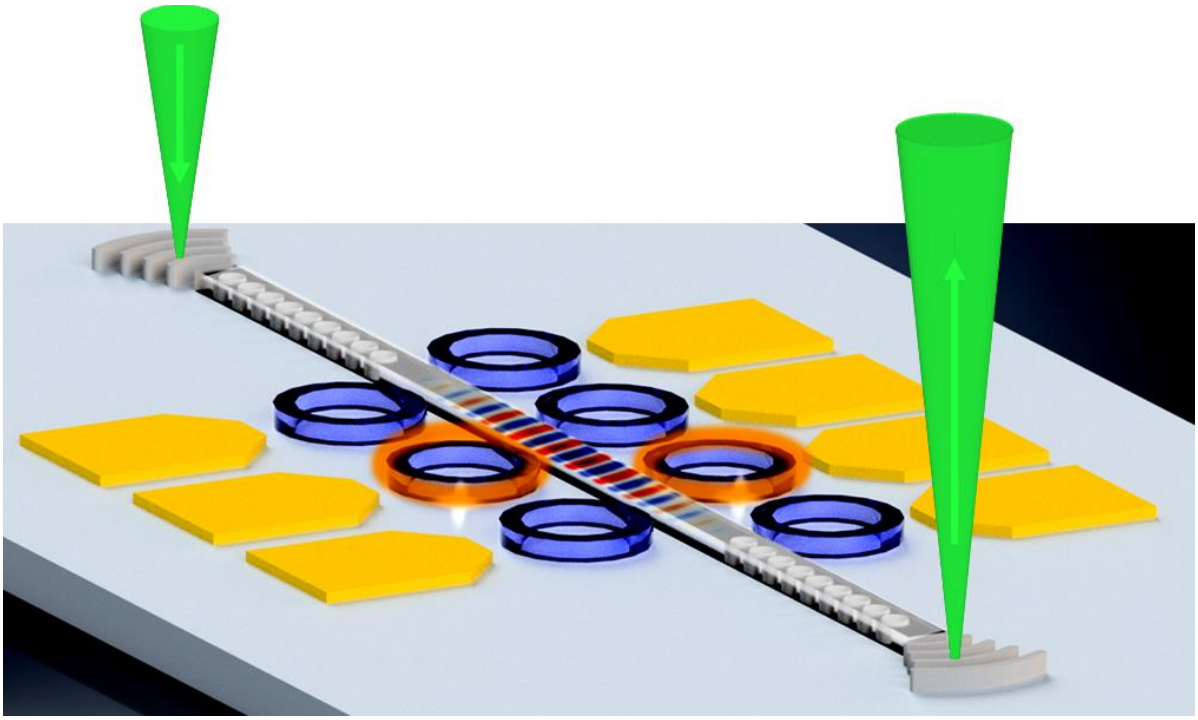

Figure 9.11: Constructing scalable quantum network based on single rare earth solid-state qubits. Individual rare earth solid-state qubits are coupled through the cavities. Each of the WGM cavities is coupled to a common cavity bus. Bright spots represent the entangled single rare earth ions. Electrodes are introduced to tune the resonance frequency of the WGM cavities on and off resonance with the common cavity bus.

Appendix A

Appendix

A.1 The optical microscopy under ambient conditions

Spectroscopy of single rare earth ions in solids normally yields low fluorescence intensity. High collection efficiency is required to detect their weak emission photons. On the other hand, due to their small cross sections, the high laser intensity is desired to properly excit the single ions. Because of high impurities in the crystal, high spatial resolution and signal-to-noise ratio are another two essential requirements to optically detect single rare earth elements in solids. Laser scanning confocal microscopy focuses the laser beam to the diffraction limitation, which produces high laser intensity on the sample. It also provides high collection efficiency, spatial resolution and signal-to-noise ratio, which fulfills all the requirements above.

Figure A.1 is the schematic representation of the home-built laser scanning confocal microscopy used to detect single Ce^{3+} ions in YAG crystal under ambient conditions. In the setup, a 475 nm long pass filter is served as the dichroic mirror. A high numerical aperture oil immersion objective lens (Zeiss, 1.3 N. A.) is used to achieve spatial resolution close to 200 nm in x, y dimension and 1 μm in z dimension. Combination of 475 long-pass filter and 625 short-pass filter are applied to spectrally exclude the signal from the excitation laser and the other fluorescing background, for example, emission from Cr:YAG. Two single-photon avalanche photodiode(APD) are settled as Hanbury-Brown Twiss interferometry, to detect the fluorescence signal from single Ce^{3+} ions. Meanwhile, APD generates an electrical pulse when it detects a photon. These electrical pulses are connected to a time-correlated single photon counting(TCSPC). By measuring the time-correlation between two APDs the number of single emitters in the optical detection volume can be determined (when the number of single emitters is less than three).

The laser system is shown in Fig. A.1: A femtosecond pulsed Ti:Sapphire laser wavelength at 920 nm is pumped by a 9 W CW laser at 532 nm. The fundamental repetition rate of the pulsed laser is 77 MHz, while it can be changed by a pulse picker. The optical frequency of the pulsed laser is doubled by a second-harmonic generation(SHG) crystal from 920 nm to 460 nm to excite the single Ce ions. To achieve the spin-flip transitions of Ce:YAG, circularly polarized excitation photons are required, a combination of a linear polarizer

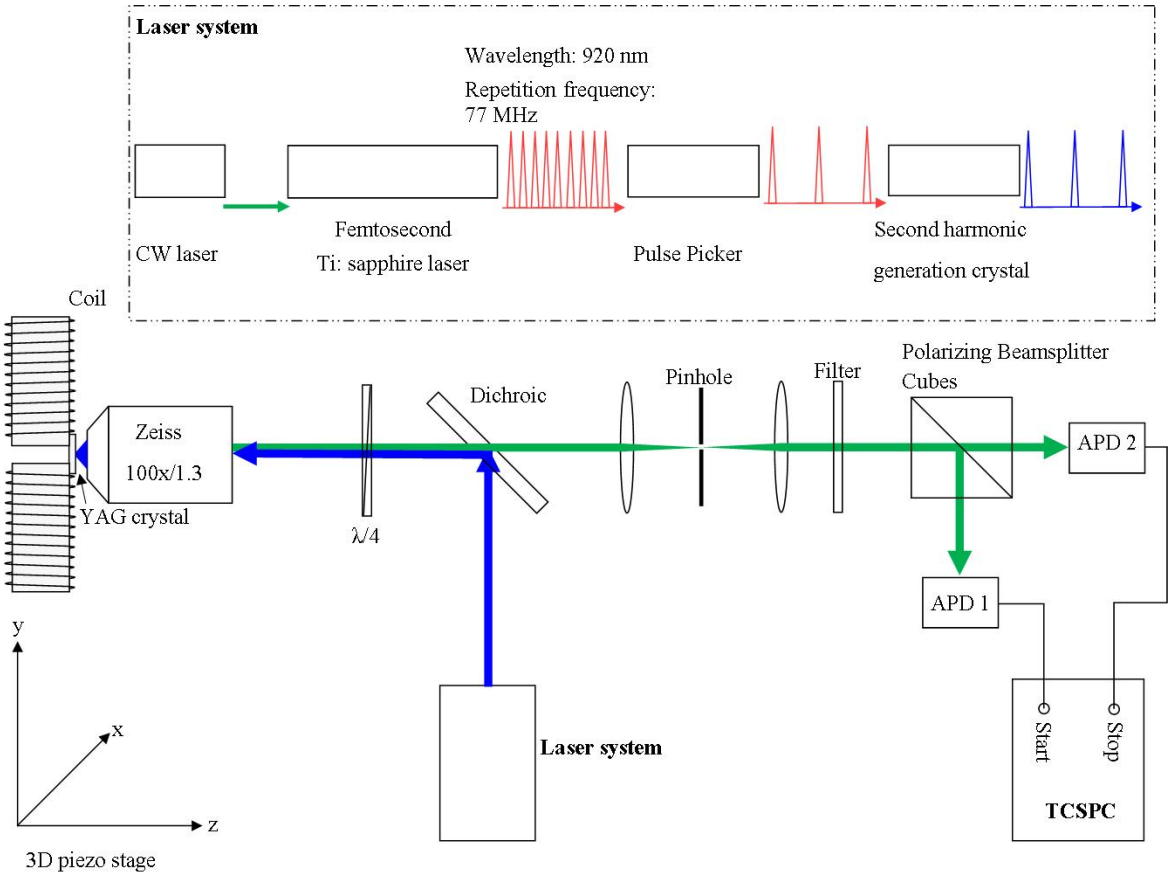

Figure A.1: Experiment setup under ambient conditions. CW: continuous wave, $\lambda/4$: quarter waveplate, APD: avalanche photodiode, TCSPC: time-correlated single photon counting

and a quarter waveplate is introduced to polarize the excitation photons circularly.

A home-made magnet coil is settled near the sample. It can produce either 500 G $\vec{B}$ field along the laser propagation direction or 250 G $\vec{B}$ field perpendicular to the laser direction. With these two different directions of the $\vec{B}$ field, two different selection rules are achieved as described in Chapter III.

A.2 Low temperature experiments setup

A.2.1 Konti-cryostat

The low temperature experiments have been performed in the Konti-cryostat, which its draft is shown in Fig. A.2. The Konti-cryostat is a continuous helium flow cryostat which the helium is supplied from one external helium tank. It offers a broad manipulating temperature range. The lowest temperature it achieves on the heat exchange is 2.7 K. In the experiment, the samples were mounted on the cold finger, while the cold finger is fixed among the heat exchanger. The temperature of the sample is ~3.5 K. A 3D motor stage is applied to move the sample and approach the sample to the focus of the objective lens

To achieve the highest collection efficiency of the optical microscopy, a high N.A. (0.95 N. A.) air objective lens with short working distance (∼300 μm) is mounted in the Konti-cryostat with high vacuum. Once the sample is cooled down, the temperature of the objective lens is still close to room temperature indicating less deforming of the objective lens due to the temperature changing. To acquire the laser scanning fluorescence image of the sample, the objective lens is mounted on a 3D piezo driven stage. In addition, the Konti-cryostat has one optical access with a UV anti-reflected coating window.

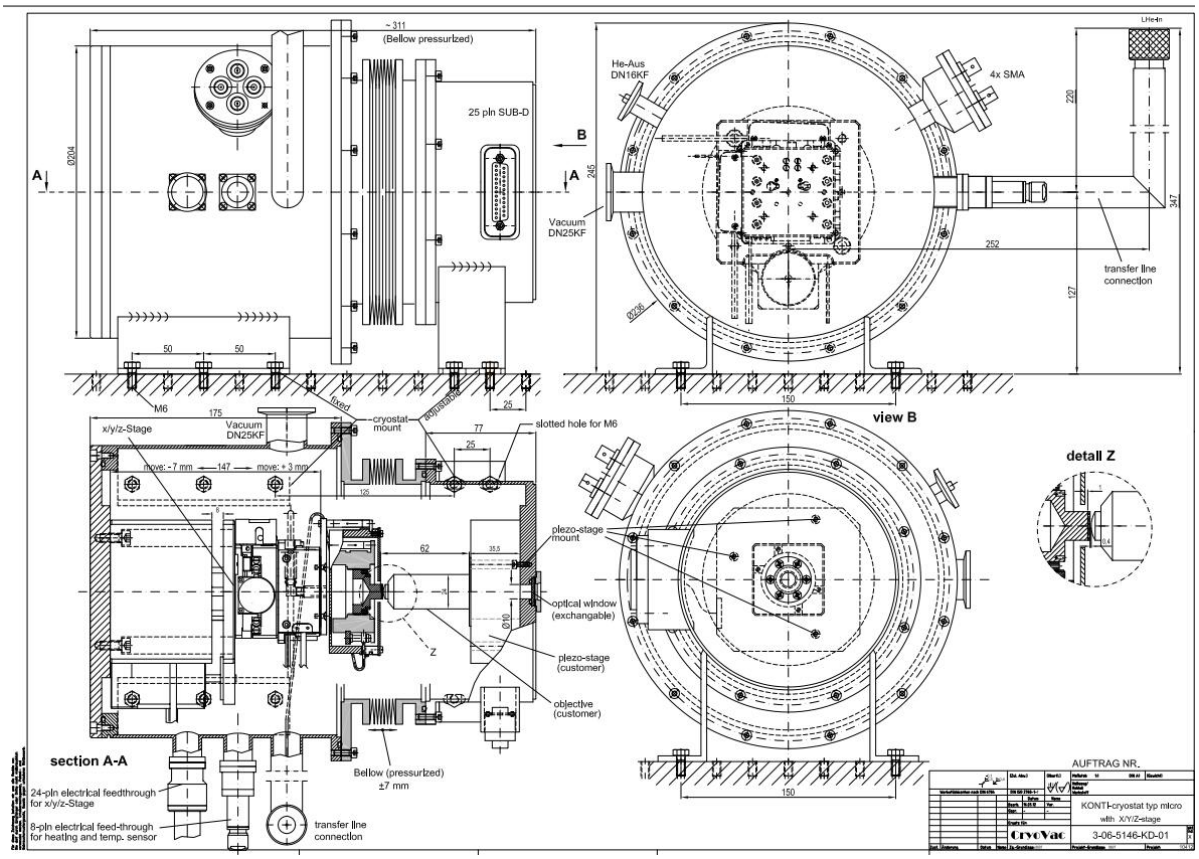

Figure A.2: The draft of the Knoti-cryostat.

A.2.2 Low temperature experiment setup for Ce:YAG

Laser system

Three different low temperature experiments of single Ce ions in YAG have been described in this dissertation corresponding to three different laser systems:

I. Measurements of coherent properties of single Ce^{3+} electron spin qubit. Single Ce ions are optically excited, initialized, and readout through phonon sideband transition. A pulsed laser wavelength at 460 nm is applied to excite single Ce ions and suppress the charge dynamics. A same laser system as room temperature experiment setup is applied

to achieve this purpose (see Fig. A.1).

II. Observation of excitation spectra of native and nanoscale engineered single Ce^{3+} ions. Single Ce ions are resonantly excited through the optical transition between the lowest ground and excited states. In the experiment, a diode laser with external cavity (Toptica DL Pro diode laser) the wavelength of 489.15 nm is applied. The laser linewidth is ∼ 500-1,000 kHz. Laser frequency can be accurately swept by changing by the driving piezo of the external optical grating. The scanning range of the diode laser is ∼6 GHz, which covers four resonant transitions of Ce ions. Additionally, the femtosecond laser is also applied (430 nm wavelength, the repetition rate is 2.5 kHz) to keep the Ce ion photostable under CW laser excitation.

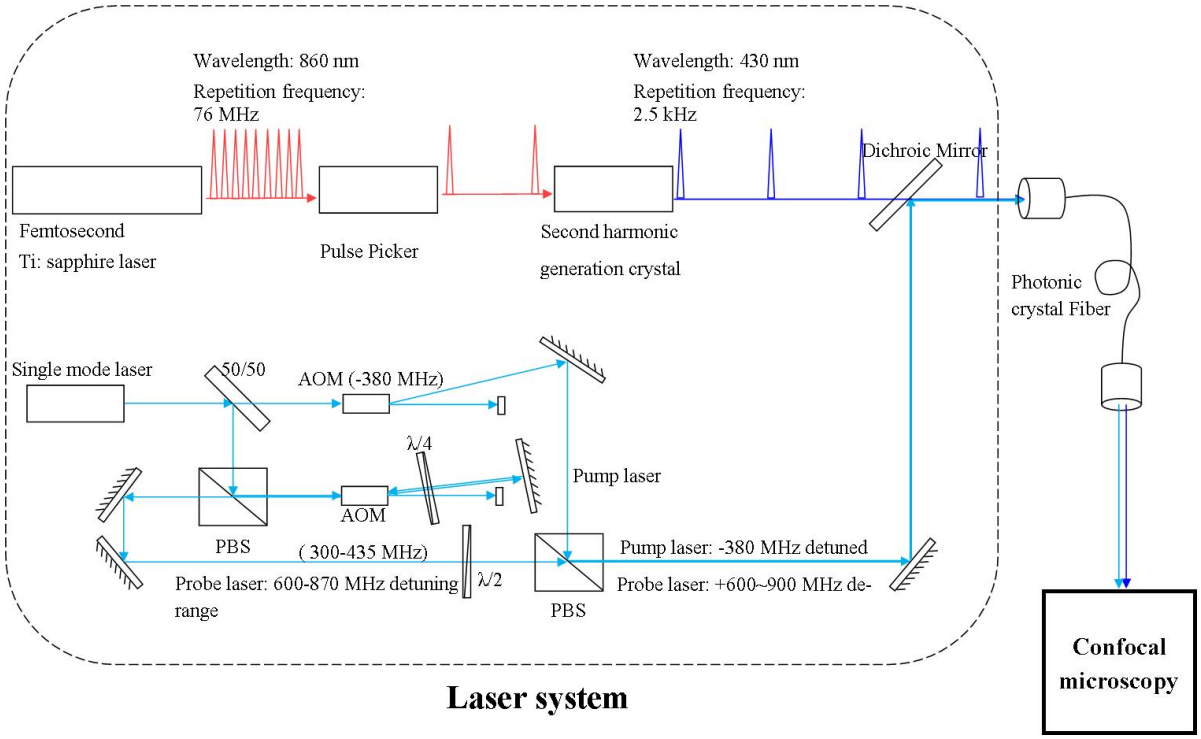

Figure A.3: Laser system for all-optical preparation of coherent dark states of a single Ce ion. AOM: acousto-optic modulator; PBS: polarizing beamsplitter cube; $\lambda/4$: quarter waveplate.

III. All-optical preparation of coherent dark states of a single Ce^{3+} ion. To prepare the coherent dark states, the single mode laser described in II is split into two optical paths by using a 50/50 beam splitter (see Fig. A.3). One laser goes through an acousto-optic modulator (AOM). The first order diffraction laser beam has a -380 MHz detuned frequency serving as the pump laser. Another laser beam is pushed through a double-pass AOM to have a 600-780 MHz frequency sweeping range acting as the probe laser. Subsequently, these two laser beams are coupled by a polarizing beamsplitter cube. The frequency difference of two laser beams is in the range of 980-1,250 MHz. A pulsed laser described above is still applied (430 nm wavelength, and the repetition rate is 2.5 kHz), to suppress the charge state dynamics of single Ce ions. At the end, the pulsed laser, the pump and the probe laser are combined together by a dichroic mirror and propagated to the confocal

microscopy.

Low temperature confocal microscopy

The confocal microscope operating at cryogenic temperature (see Fig. A.4) is similar with the one working under ambient conditions. To mount the sample on the cold finger, nickel and copper are deposited on the back side of YAG. Indium is introduced to connect the sample and the cold finger sample holder to provide high thermal conductivity. In the experiment, the cold finger is cooled down to ∼2.7 K and the temperature of the YAG sample is below 3.5 K. In the cryogenic temperature environment, the oil immersion objective lens can not be applied since the immersion oil would be frozen. A high N. A. air objective lens (0.95 N. A.) is used to excite a single Ce ion and collect its fluorescence. In the detection part, the fluorescence of a single Ce is obtained either by a spectrometer or by the single photon detector.

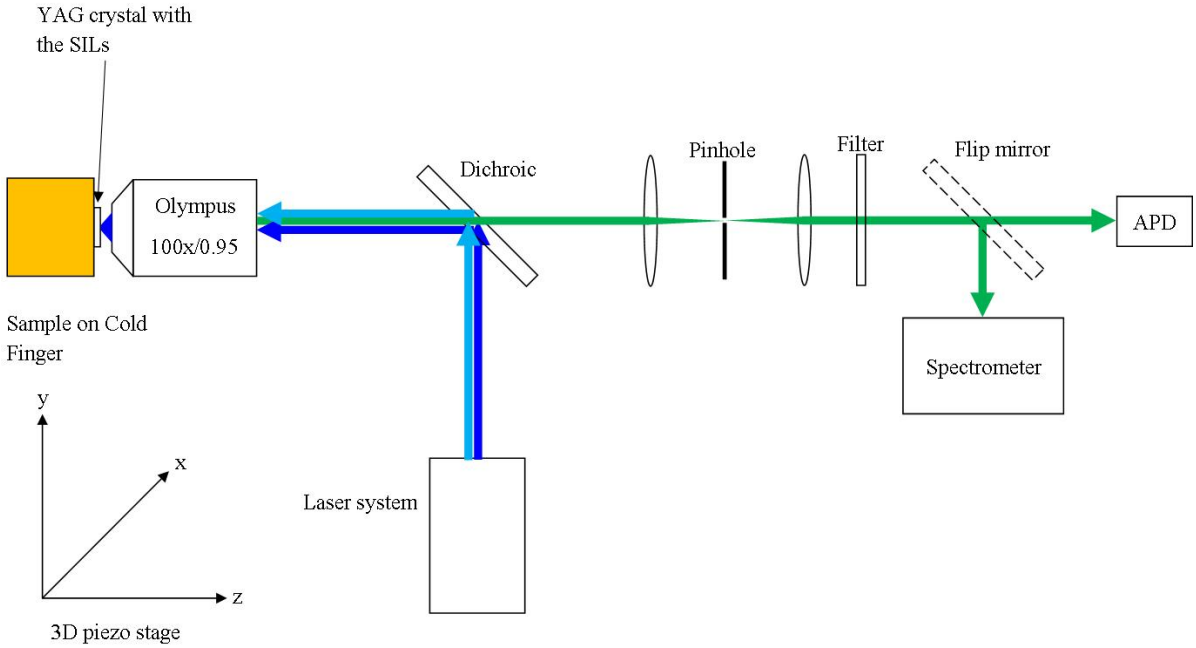

Figure A.4: Laser system for all-optical preparation of coherent dark states of a single Ce ion. AOM: acousto-optic modulator; PBS: polarizing beamsplitter cube; $\lambda/4$: quarter waveplate.

External magnetic field

In the low temperature experiment, an external magnetic field is settled to produce certain selection rules for the optical transitions of Ce ions. However, unlike the room temperature optical setup, the space of the Konti-cryostat experiment setup is limited. Only Two different magnetic field can be generated by using permanent magnets. In Fig. A.5 (a), (b), one permanent magnet is mounted on the objective lens to generate ∼500 G magnetic field, which is parallel to the $\vec{k}$ (laser beam direction). Under this magnetic field, only spin-flip transitions are allowed. In Fig. A.5(c),(d), two permanent magnets are mounted on

the objective lens, providing ∼500 G magnetic field perpendicular to the $\vec{k}$. It removes the degeneracy of present Kramer's doublets and provides both spin flip and non-flip transitions to form Λ systems of Ce:YAG.

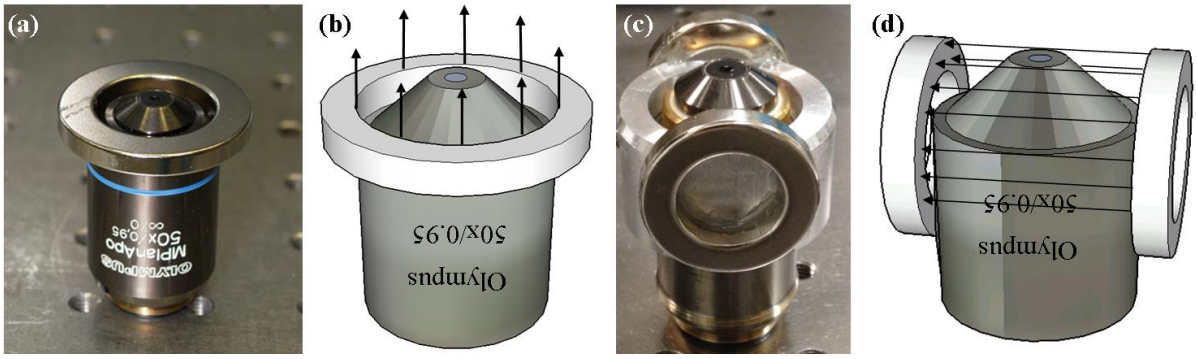

Figure A.5: (a)(b), external magnetic field ∼500 G parallel to the $\vec{k}$. (c) (d), external magnetic field ∼500 G perpendicular to the $\vec{k}$

A.2.3 Low temperature experiment setup for Pr:YAG

Single Pr ions in YAG is excited, manipulated and detected under a upconverting micoroscpe, which the scheme is shown in Fig. A.6. The upconversion microscopy technique has two major advantages compared to confocal microscope. First, the upconverting microscope is a background-free microscopy. The background is generated by downconverted fluorescence of chemical contaminants, optical devices, and scattered laser light. They all have the same or longer wavelength than the excitation laser. In contrast, upconverted fluorescence emitted by single Pr ions has a shorter wavelength than the excitation photons. Owing to the different spectral range of the emission signal and background, a short pass filter can be used to block fluorescent background and transmit the upconverted emission photons simultaneously. Therefore, the negligible background contribution results in high signal-to-noise ratio. Second, in a confocal microscope, a small pinhole is needed to reject fluorescence originating from the planes above and below the focus plane to increase the special resolution in z-plane. In comparison, the upconversion process as one of the nonlinear excitation mechanism indicates highly localized excitation volume. Only the ions within this volume are excited and contribute to the fluorescence signal, while ions outside this volume keep dark. The use of a pinhole is obsolete, which increases the transmission efficiency by omitting the pinhole.

A.3 Solid immersion lenses

In low temperature experiments, the absence of a high N.A. oil immersion objective lens causes the dramatically reducing of collection efficiency, spatial resolution and signal-to-noise ratio of detecting a single rare earth ion. Single rare earth ions can be barely resolved by using only an air objective lens, which blocks the further manipulation of single rare earth qubits. Several methods are raised up to overcome this issue, such as taking advantage of near-field microscopy, nano-photonic devices, surface plasma enhancement

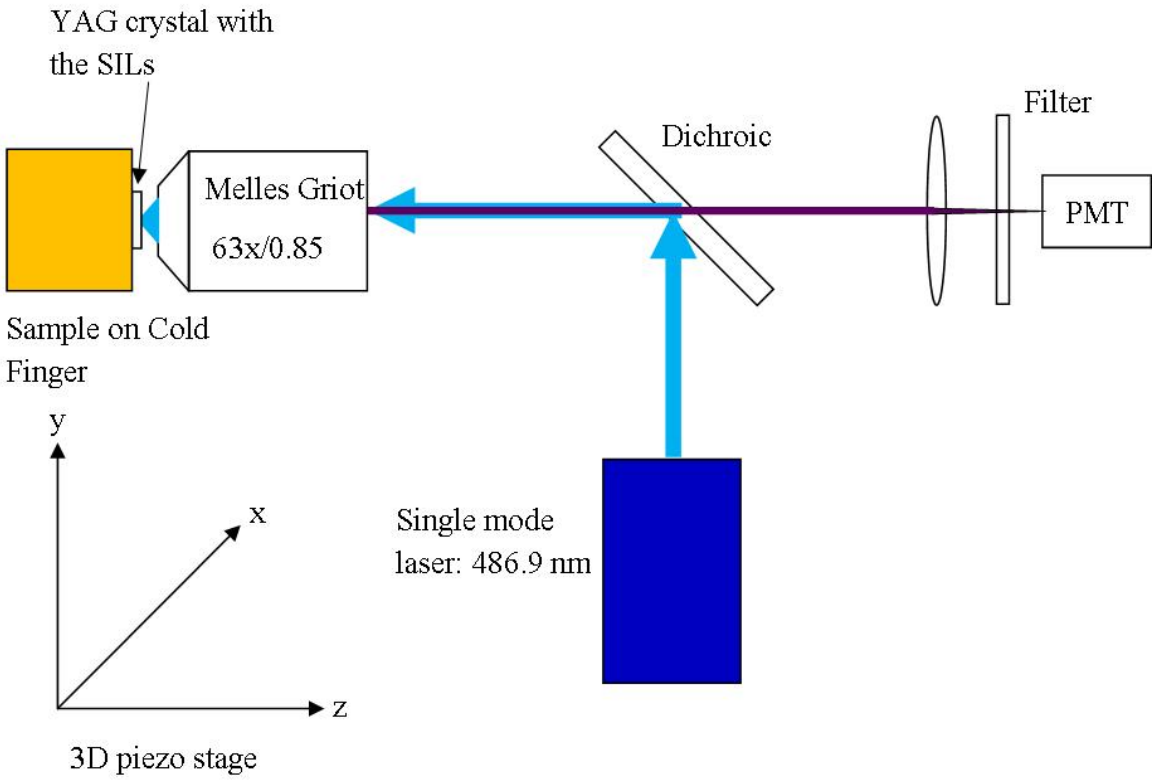

Figure A.6: The upconverting microscope operating at low temperature

and solid immersion lenses (SILs). SILs have been used in optical microscopy in the last two decades to improve its special resolution and the collection efficiency. The collection efficiency is enhanced by avoiding interface refraction from a SIL, and therefore, the effective N.A. of the optical microscope is increased.

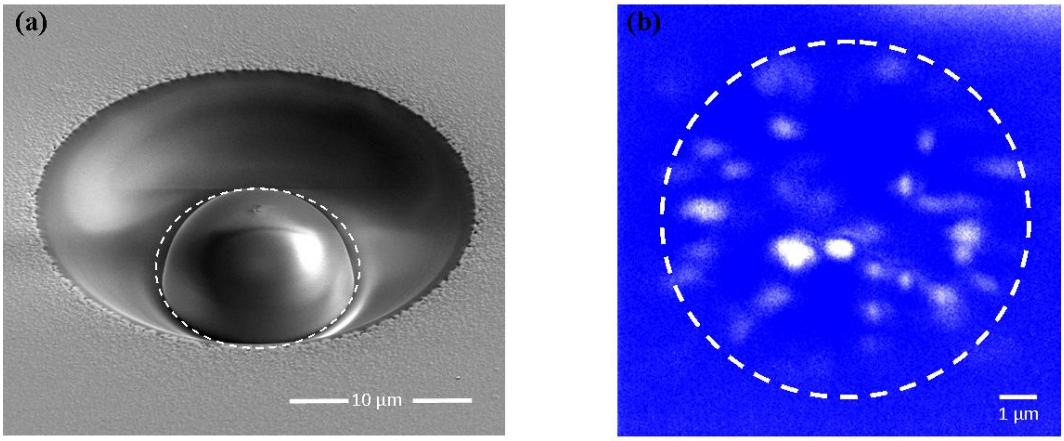

Figure A.7: (a).(b) The SEM image of a solid immersion lens on YAG crystal. (c) laser scanning microscopy image of single Ce ions in YAG under a SIL.

In the experiments, SILs are fabricated directly on the surface of the YAG crystals by means of FIB milling. Figure A.7 (b) shows the SEM image of the sample where a shape of hemispherical SIL with the diameter of 10 μm is located directly on the surface of a

YAG crystal. A laser scanning microscopy image of single Ce ions under the SIL with a scanning depth ~ 7 μm is present in Fig. A.7(c). In the image, single isolated bright spots correspond to single Ce ions. With the help of the SILs, single rare earth ions can be well detected with high spatial resolution with strong photon flux.

A.4 Microwave waveguide

In the experiments, external magnetic field introduces the ground state splitting of single Ce ions from 600 MHz till 1.7 GHz. Microwave (MW) radiation is applied to coherently manipulate the single electron spin (see Fig. A.8 (a)). To coherently manipulate single electron with MW radiation, a high power MW amplifier (50 dB amplification) is applied to a MW synthesizer (Rothde & Schwarz SMT 03). A MW switch (Mini-Circuits) is utilized to chopper the MW to generate π and $\pi/2$ pulses.

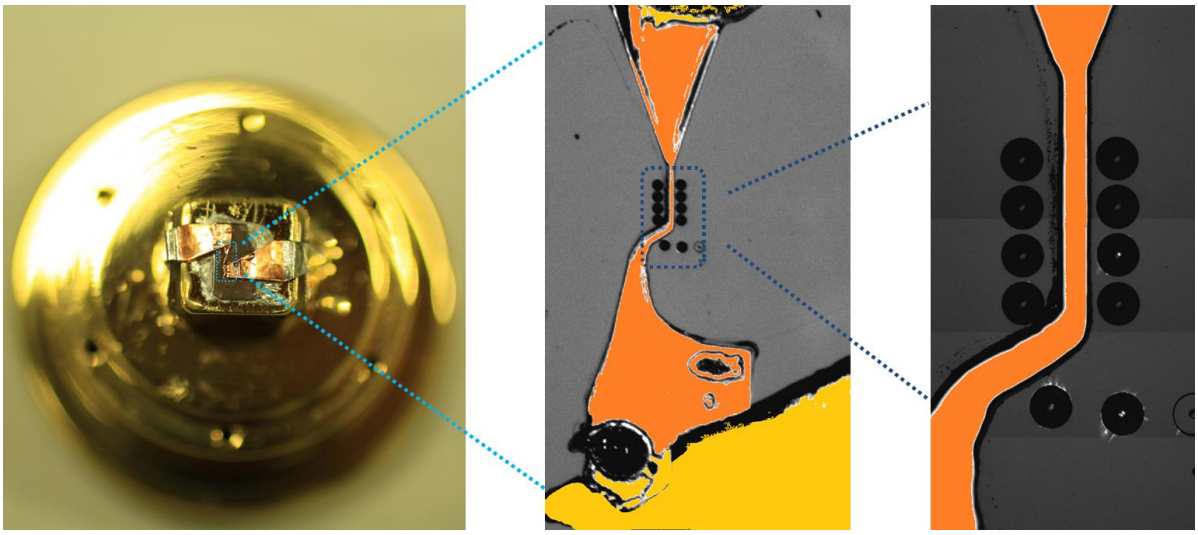

Figure A.8: (a) The cold finger sample holder with a YAG sample mounted on it. (b) Copper waveguide (orange color) is positioned next to the SILs. (c) A magnified microscope image of the SILs and the MW waveguide.

In Fig. A.8(b), a fabricated single copper MW waveguide is positioned next to the SILs to have high MW radiation power in the sample. A magnified microscope image is present in Fig. A.8 (c), where 10 SILs are on the sample and a MW waveguide (orange color) is precisely positioned next to the SILs by means of photolithography. The MW waveguide has ~ 20 μm width with $\sim$10 μm thickness and $\sim$1.5 mm length.

MW waveguide is fabricated next to the sample to gain high MW power. A recipe (see Fig. A.9 (a)-(g)) is developed to precisely place the MW waveguide to the desired position.

(a) Clean the surface of YAG bulk crystal. The crystal is cleaned with acetone and isopropanol solution. Afterward a plasma clean is introduced to remove the residual organic solvent and terminate the surface by O_2.

(b) Deposit copper layer. On the surface of the crystal, 50 nm copper laser is deposited by e-gun evaporation.

(c) Spin-coat photoresist. Positive photoresist (AZ 9240) is spin coated on the sample with 3 min soft baking at 110 °C afterward.

(d) Localize the positions of the SILs. The home-built laser writing system is combined with a laser scanning microscope. The image of the surface is acquired by scanning the sample with a 706 nm diode laser. A special mask is designed when the positions of the SILs are localized. A 405 nm diode laser is used to expose the photoresist along the mask.

(e) Develop the photoresist. After the exposure, the developer is helped to remove the exposed photoresist. The sample is immersed in a copper sulfate solution to have electrical plating with copper. After 10 min, additional 20 μm thickness copper layer is grown in the exposed area on the YAG crystal.

(f) Remove the residual photoresist. Acetone is introduced to remove the residual photoresist.

(g) Eliminate the thin copper layer. Iron chloride solution is used to eliminate the thin copper layer deposited in (b).

At the end, a desired copper MW waveguide is precisely positioned on the surface of the crystal. Two copper arms are mounted on both ends of the waveguide to induce MW from the MW wire to the MW waveguide. The MW loss is only 6 dB even without impedance/matching to the outer MW source.

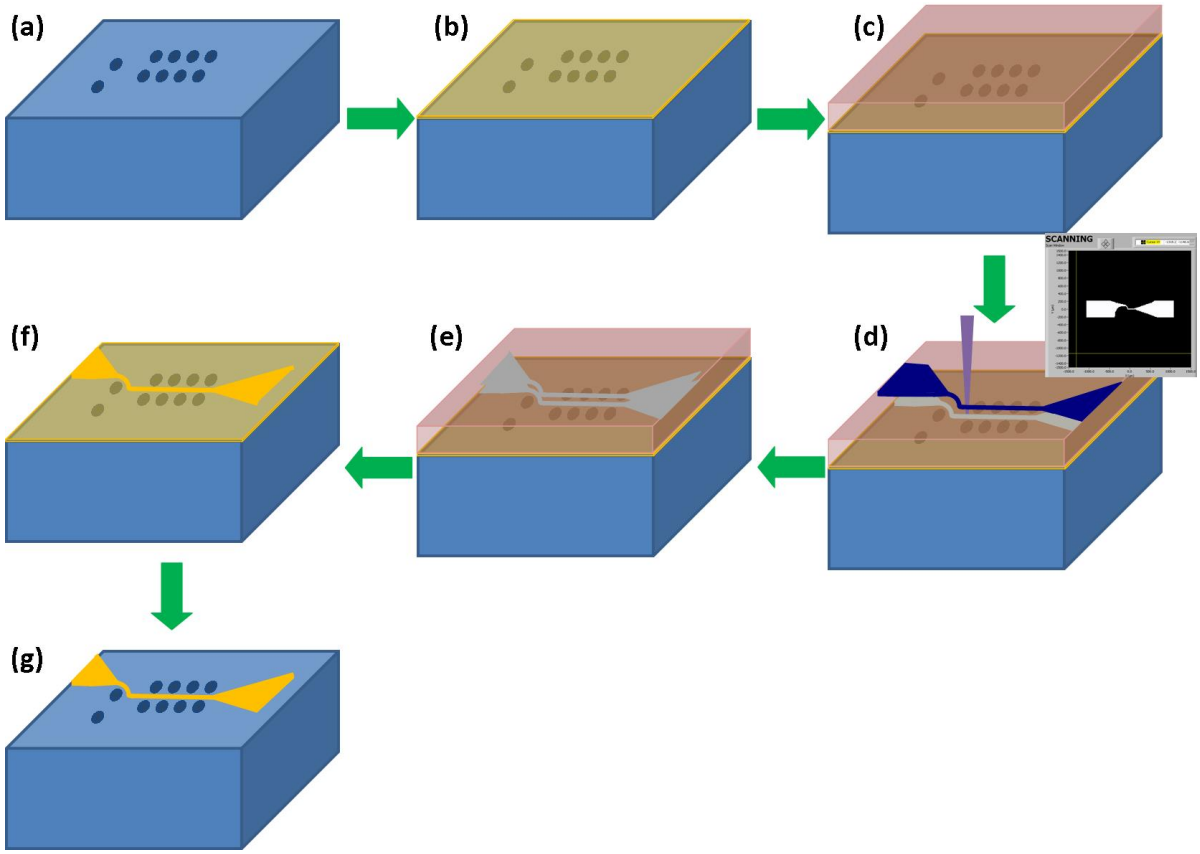

Figure A.9: The procedure of producing the MW waveguide. (a) Clean the sample. (b) Deposit 50 nm copper layer. (c) Spin coat photoresist. (d) Localize the position of the SILs and laser writing. (e) Develop photoresist and copper electrical plating. (f) Remove the photoresist. (g) Eliminate the deposited copper layer.

List of Figures

Bibliography

[1] H. J. Kimble, M. Dagenais, and L. Mandel. Photon Antibunching in Resonance Fluorescence. *Physical Review Letters*, 39(11):691–695, 1977.

[2] R. J. Glauber. Photon Correlations. *Physical Review Letters*, 10(3):84–86, 1963.

[3] R. J. Glauber. The Quantum Theory of Optical Coherence. *Physical Review*, 130(6):2529, 1963.

[4] H. Paul. Photon Antibunching. *Reviews of Modern Physics*, 54(4):1061, 1982.

[5] W. Neuhauser, M. Hohenstatt, P.E. Toschek, and H. Dehmelt. Localized Visible Ba^+ Mono-Ion Oscillator. *Physical Review A*, 22(3):1137, 1980.

[6] W. Paul. Electromagnetic Traps for Charged and Neutral Particles. *Reviews of Modern Physics*, 62(3):531, 1990.

[7] Nobel Prize in Physics 1989. https : //www.nobelprize.org.

[8] W. E. Moerner and L. Kador. Optical Detection and Spectroscopy of Single Molecules in a Solid. *Physical Review Letters*, 62(21):2535, 1989.

[9] M. Orrit and J. Bernard. Single Pentacene Molecules Detected by Fluorescence Excitation in a P-Terphenyl Crystal. *Physical Review Letters*, 65(21):2716, 1990.

[10] W. E. Moerner and M. Orrit. Illuminating single molecules in condensed matter. *Science*, 283(5408):1670–1676, 1999.

[11] Th. Basché, W. E. Moerner, M. Orrit, and H. Talon. Photon Antibunching in the Fluorescence of a Single Dye Molecule Trapped in a Solid. *Physical Review Letters*, 69:1516–1519, 1992.

[12] J. Wrachtrup, C. Von Borczyskowski, J. Bernard, M. Orritt, and R. Brown. Optical Detection of Magnetic Resonance in a Single Molecule. *Nature*, 363:244–245, 1993.

[13] K.D. Weston, P.J. Carson, H. Metiu, and S.K. Buratto. Room-Temperature Fluorescence Characteristics of Single Dye Molecules Adsorbed on a Glass Surface. *The Journal of Chemical Physics*, 109:7474, 1998.

[14] B. Lounis and W. E. Moerner. Single Photons on Demand from a Single Molecule at Room Temperature. *Nature*, 407:491–493, 2000.

[15] P. Michler, A. Kiraz, W. V. Schoenfeld, P. M. Petroff, Lidong Zhang, E. Hu, and A. Imamoglu. A Quantum Dot Single-Photon Turnstile Device. *Science*, 290:2282–2285, 2000.

[16] C. Santori, M. Pelton, G. Solomon, Y. Dale, and Y. Yamamoto. Triggered Single Photons from a Quantum Dot. *Physical Review Letters*, 86:1502–1505, 2001.

[17] J. R. Petta, A. C. Johnson, J. M. Taylor, E. A. Laird, A. Yacoby, M. D. Lukin, C. M. Marcus, M. P. Hanson, and A. C. Gossard. Coherent Manipulation of Coupled Electron Spins in Semiconductor Quantum Dots. *Science*, 309(5744):2180–2184, 2005.

[18] A. Gruber, A. Dräbenstedt, C. Tietz, L. Fleury, J. Wrachtrup, and C. von Borczyskowski. Scanning Confocal Optical Microscopy and Magnetic Resonance on Single Defect Centers. *Science*, 276(5321):2012–2014, 1997.

[19] C. Kurtsiefer, S. Mayer, P. Zarda, and H. Weinfurter. Stable Solid-State Source of Single Photons. *Physical Review Letters*, 85(2):290–293, 2000.

[20] C. Wang, C. Kurtsiefer, H. Weinfurter, and B. Burchard. Single Photon Emission from SiV Centres in Diamond Produced by Ion Implantation. *Journal of Physics B: Atomic, Molecular and Optical Physics*, 39(1):37, 2005.

[21] E Wu, J.R. Rabeau, G. Roger, F. Treussart, H. Zeng, P. Grangier, S. Prawer, and J. Roch. Room Temperature Triggered Single-Photon Source in the Near Infrared. *New Journal of Physics*, 9(12):434, 2007.

[22] W. F. Koehl, B. B. Buckley, F. J. Heremans, G. Calusine, and D. D. Awschalom. Room Temperature Coherent Control of Defect Spin Qubits in Silicon Carbide. *Nature*, 479(7371):84–87, 2011.

[23] A. J. Morfa, B. C. Gibson, M. Karg, T. J. Karle, A. D. Greentree, P. Mulvaney, and S. Tomljenovic-Hanic. Single-Photon Emission and Quantum Characterization of Zinc Oxide Defects. *Nano Letters*, 12(2):949–954, 2012.

[24] A. Beveratos, R. Brouri, T. Gacoin, A. Villing, J. Poizat, and P. Grangier. Single photon quantum cryptography. *Physical Review Letters*, 89(18):187901, 2002.

[25] V. Jacques, E Wu, T. Toury, F. Treussart, A. Aspect, P. Grangier, and J. Roch. Single-Photon Wavefront-Splitting Interference. *The European Physical Journal D-Atomic, Molecular, Optical and Plasma Physics*, 35(3):561–565, 2005.

[26] V. Jacques, E Wu, F. Grosshans, F. Treussart, P. Grangier, A. Aspect, and J. Roch. Experimental Realization of Wheeler's Delayed-Choice Gedanken Experiment. *Science*, 315(5814):966–968, 2007.

[27] E. Betzig, J.K. Trautman, T.D. Harris, J.S. Weiner, and R.L. Kostelak. Breaking the Diffraction Barrier: Optical Microscopy on a Nanometric Scale. *Science*, 251(5000):1468–1470, 1991.

[28] E. Betzig and R. J. Chichester. Single Molecules Observed by Near-Field Scanning Optical Microscopy. *Science*, 262(5138):1422–1425, 1993.

[29] E. Betzig, G. H. Patterson, R. Sougrat, O. W. Lindwasser, S. Olenych, Juan S. B., M. W. Davidson, J. Lippincott-Schwartz, and H. F. Hess. Imaging Intracellular Fluorescent Proteins at Nanometer Resolution. *Science*, 313(5793):1642–1645, 2006.

[30] M. J Rust, M. Bates, and X. Zhuang. Sub-Diffraction-Limit Imaging by Stochastic Optical Reconstruction Microscopy (STORM). *Nature Methods*, 3(10):793–796, 2006.

[31] M. Bates, B. Huang, G. T. Dempsey, and X. Zhuang. Multicolor Super-Resolution Imaging with Photo-Switchable Fluorescent Probes. *Science*, 317(5845):1749–1753, 2007.

[32] B. Huang, W. Wang, M. Bates, and X. Zhuang. Three-Dimensional Super-Resolution Imaging by Stochastic Optical Reconstruction Microscopy. *Science*, 319(5864):810–813, 2008.

[33] E. Rittweger, K.Y. Han, S.E. Irvine, C. Eggeling, and S.W. Hell. STED Microscopy Reveals Crystal Colour Centres with Nanometric Resolution. *Nature Photonics*, 3(3):144–147, 2009.

[34] P. Michler, A. Imamoğlu, M. Mason, P. Carson, G. Strouse, and S. Buratto. Quantum Correlation Among Photons from a Single Quantum Dot at Room Temperature. *Nature*, 406(6799):968–970, 2000.

[35] D. Englund, A. Faraon, I. Fushman, N. Stoltz, P. Petroff, and J. Vučković. Controlling Cavity Reflectivity with a Single Quantum Dot. *Nature*, 450(7171):857–861, 2007.

[36] I. Fushman, D. Englund, A. Faraon, N. Stoltz, P. Petroff, and J. Vučković. Controlled Phase Shifts with a Single Quantum Dot. *Science*, 320(5877):769–772, 2008.

[37] F. Jelezko, T. Gaebel, I. Popa, A. Gruber, and J. Wrachtrup. Observation of Coherent Oscillations in a Single Electron Spin. *Physical Review Letters*, 92(7):76401, 2004.

[38] G. Balasubramanian, P. Neumann, D. Twitchen, M. Markham, R. Kolesov, N. Mizuochi, J. Isoya, J. Achard, J. Beck, J. Tissler, et al. Ultralong Spin Coherence Time in Isotopically Engineered Diamond. *Nature Materials*, 8(5):383–387, 2009.

[39] P. C. Maurer, G. Kucsko, C. Latta, L. Jiang, N. Yao, S. D. Bennett, F. Pastawski, D. Hunger, N. Chisholm, M. Markham, et al. Room-Temperature Quantum Bit Memory Exceeding One Second. *Science*, 336(6086):1283–1286, 2012.

[40] S. Yang, Y. Wang, D.D. Rao, T. H. Tran, S. A. Momenzadeh, M. Markham, D.J. Twitchen, P. Wang, W.n Yang, R. Stöhr, et al. High fidelity transfer and storage of photon states in a single nuclear spin. *Nature Photonics*, 2016.

[41] J. M. Elzerman, R. Hanson, L. Van Beveren, B. Witkamp, L. Vandersypen, and L. P. Kouwenhoven. Single-Shot Read-Out of an Individual Electron Spin in a Quantum Dot. *Nature*, 430(6998):431–435, 2004.

[42] R. Hanson and D. D. Awschalom. Coherent Manipulation of Single Spins in Semiconductors. *Nature*, 453(7198):1043–1049, 2008.

[43] P. Neumann, J. Beck, M. Steiner, F. Rempp, H. Fedder, P. Hemmer, J. Wrachtrup, and F. Jelezko. Single-Shot Readout of a Single Nuclear Spin. *Science*, 329(5991):542–544, 2010.

[44] L. Robledo, L. Childress, H. Bernien, B. Hensen, P. Alkemade, and R. Hanson. High-Fidelity Projective Read-Out of a Solid-State Spin Quantum Register. *Nature*, 477(7366):574–578, 2011.

[45] T. van der Sar, Z. H. Wang, M. S. Blok, H. Bernien, T. H. Taminiau, D. M. Toyli, D. A. Lidar, D. D. Awschalom, R. Hanson, and V. V. Dobrovitski. Decoherence-Protected Quantum Gates for a Hybrid Solid-State Spin Register. *Nature*, 484(7392):82–86, 2012.

[46] B. Hensen, .H Bernien, A. E. Dréau, A. Reiserer, N. Kalb, M. S. Blok, J. Ruitenberg, R. Vermeulen, R. N. Schouten, .C Abellán, et al. Loophole-Free Bell Inequality Violation Using Electron Spins Separated by 1.3 Kilometres. *Nature*, 526(7575):682–686, 2015.

[47] S. A. Wolf, D. D. Awschalom, R. A. Buhrman, J. M. Daughton, S. Von Molnar, M. L. Roukes, A. Chtchelkanova, and D. M. Treger. Spintronics: a Spin-Based Electronics Vision for the Future. *Science*, 294(5546):1488–1495, 2001.

[48] I. Žutić, J. Fabian, and S. D. Sarma. Spintronics: Fundamentals and Applications. *Reviews of Modern Physics*, 76(2):323, 2004.

[49] J. Wrachtrup and F. Jelezko. Processing Quantum Information in Diamond. *Journal of Physics: Condensed Matter*, 18(21):S807, 2006.

[50] T. D. Ladd, F. Jelezko, R. Laflamme, Y. Nakamura, C. Monroe, and J. L. O'Brien. Quantum Computers. *Nature*, 464(7285):45–53, 2010.

[51] D. D. Awschalom, L. C. Bassett, A. S. Dzurak, E. L. Hu, and J. R. Petta. Quantum Spintronics: Engineering and Manipulating Atom-Like Spins in Semiconductors. *Science*, 339(6124):1174–1179, 2013.

[52] W. Gao, A. Imamoglu, H. Bernien, and R. Hanson. Coherent Manipulation, Measurement and Entanglement of Individual Solid-State Spins Using Optical Fields. *Nature Photonics*, 9(6):363–373, 2015.

[53] F. Koppens, K. Nowack, and L. Vandersypen. Spin Echo of a Single Electron Spin in a Quantum Dot. *Physical Review Letters*, 100(23):236802, 2008.

[54] Ł. Cywiński, W. M. Witzel, and S. D. Sarma. Electron Spin Dephasing due to Hyperfine Interactions with a Nuclear Spin Bath. *Physical Review Letters*, 102(5):057601, 2009.

[55] S. A. Crooker, J. Brandt, C. Sandfort, A. Greilich, D. R. Yakovlev, D. Reuter, A. D. Wieck, and M. Bayer. Spin Noise of Electrons and Holes in Self-Assembled Quantum Dots. *Physical Review Letters*, 104(3):036601, 2010.

[56] N. H. Bonadeo, J. Erland, D. Gammon, D. Park, D. S. Katzer, and D. G. Steel. Coherent Optical Control of the Quantum State of a Single Quantum Dot. *Science*, 282(5393):1473–1476, 1998.

[57] J. Meijer, B. Burchard, M. Domhan, C. Wittmann, T. Gaebel, I. Popa, F. Jelezko, and J. Wrachtrup. Generation of Single Color Centers by Focused Nitrogen Implantation. *Applied Physics Letters*, 87(26):261909, 2005.

[58] P. Siyushev, H. Pinto, M. Vörös, A. Gali, F. Jelezko, and J. Wrachtrup. Optically Controlled Switching of the Charge State of a Single Nitrogen-Vacancy Center in Diamond at Cryogenic Temperatures. *Physical Review Letters*, 110(16):167402, 2013.

[59] A.J. Freeman and R.E. Watson. Theoretical Investigation of Some Magnetic and Spectroscopic Properties of Rare-Earth Ions. *Physical Review*, 127(6):2058, 1962.

[60] L. Rippe, M.s Nilsson, S. Kröll, R. Klieber, and D. Suter. Experimental demonstration of efficient and selective population transfer and qubit distillation in a rare-earth-metal-ion-doped crystal. *Physical Review A*, 71(6):062328, 2005.

[61] R. W. Equall, Y. Sun, R. L. Cone, and R. M. Macfarlane. Ultraslow Optical Dephasing in $Eu^{3+} : Y_2SiO_5$. *Physical Review Letters*, 72(14):2179, 1994.

[62] C. W. Thiel, T. Böttger, and R. L. Cone. Rare-Rarth-Doped Materials for Applications in Quantum Information Storage and Signal Processing. *Journal of Luminescence*, 131:353–361, 2011.

[63] M. Zhong, M. P. Hedges, R. L. Ahlefeldt, J. G. Bartholomew, S. E. Beavan, S. M. Wittig, J. J. Longdell, and M. J. Sellars. Optically Addressable Nuclear Spins in a Solid with a Six-Hour Coherence Time. *Nature*, 517(7533):177–180, 2015.

[64] R. W. Equall, R. L. Cone, and R. M. Macfarlane. Homogeneous Broadening and Hyperfine Structure of Optical Transitions in $Pr^{3+} : Y_2SiO_5$. *Physical Review B*, 52(6):3963, 1995.

[65] O. L. Malta and L. D. Carlos. Intensities of $4f - 4f$ Transitions in Glass Materials. *Quimica Nova*, 26(6):889–895, 2003.

[66] M. J. Thorpe, L. Rippe, T. M. Fortier, M. S. Kirchner, and T. Rosenband. Frequency stabilization to 6 $\times 10^{-16}$ via spectral-hole burning. *Nature Photonics*, 5(11):688–693, 2011.

[67] A. Ikesue, T. Kinoshita, K. Kamata, and K. Yoshida. Fabrication and Optical Properties of High-Performance Polycrystalline Nd: YAG Ceramics for Solid-State Lasers. *Journal of the American Ceramic Society*, 78(4):1033–1040, 1995.

[68] R. C. Powell. *Physics of Solid-State Laser Materials*, volume 1. Springer Science & Business Media, 1998.

[69] W. F. Krupke. Ytterbium Solid-State Lasers. The First Decade. *Selected Topics in Quantum Electronics, IEEE Journal of*, 6(6):1287–1296, 2000.

[70] R. M. Macfarlane, A. Arcangeli, A. Ferrier, and P. Goldner. Optical measurement of the effect of electric fields on the nuclear spin coherence of rare-earth ions in solids. *Physical Review Letters*, 113(15):157603, 2014.

[71] F: Wang and X: Liu. Recent Advances in the Chemistry of Lanthanide-Doped Upconversion Nanocrystals. *Chemical Society Reviews*, 38(4):976–989, 2009.

[72] N. M. Idris, M. K. Gnanasammandhan, J. Zhang, P. C. Ho, R. Mahendran, and Y. Zhang. In Vivo Photodynamic Therapy Using Upconversion Nanoparticles as Remote-Controlled Nanotransducers. *Nature Medicine*, 18(10):1580–1585, 2012.

[73] R. Kolesov, R. Reuter, K. Xia, R. Stöhr, A. Zappe, and J. Wrachtrup. Super-Resolution Upconversion Microscopy of Praseodymium-Doped Yttrium Aluminum Garnet Nanoparticles. *Physical Review B*, 84:153413, 2011.

[74] T. Utikal, E. Eichhammer, L. Petersen, A. Renn, S. Götzinger, and V. Sandoghdar. Spectroscopic Detection and State Preparation of a Single Praseodymium Ion in a Crystal. *Nature Communications*, 5, 2014.

[75] De Riedmatten, H. and Afzelius, M. and Staudt, M. U. and Simon, C. and Gisin, N. A Solid-State Light–Matter Interface at the Single-Photon Level. *Nature*, 456(7223):773–777, 2008.

[76] C. Clausen, I. Usmani, F. Bussières, N. Sangouard, M. Afzelius, H. de Riedmatten, and N. Gisin. Quantum Storage of Photonic Entanglement in a Crystal. *Nature*, 469(7331):508–511, 2011.

[77] A. V. Turukhin, V. S. Sudarshanam, M. S. Shahriar, J. A. Musser, B. S. Ham, and P. R. Hemmer. Observation of Ultraslow and Stored Light Pulses in a Solid. *Physical Review Letters*, 88(2):023602, 2001.

[78] J. J. Longdell, E. Fraval, M. J. Sellars, and N. B. Manson. Stopped Light with Storage Times Greater than One Second Using Electromagnetically Induced Transparency in a Solid. *Physical Review Letters*, 95:063601, 2005.

[79] G. Heinze, C. Hubrich, and T. Halfmann. Stopped Light and Image Storage by Electromagnetically Induced Transparency up to the Regime of One Minute. *Physical Review Letters*, 111(3):033601, 2013.

[80] D. Schraft, M. Hain, N. Lorenz, and T. Halfmann. Stopped Light at High Storage Efficiency in a $Pr^{3+} : Y_2SiO_5$ Crystal. *Physical Review Letters*, 116(7):073602, 2016.

[81] J. H. Wesenberg, K. Mølmer, L. Rippe, and S. Kröll. Scalable Designs for Quantum Computing with Rare-Earth-Ion-Doped Crystals. *Physical Review A*, 75(1):012304, 2007.

[82] A. Walther, L. Rippe, Y. Yan, J. Karlsson, D. Serrano, A. N. Nilsson, S. Bengtsson, and S. Kröll. High-Fidelity Readout Scheme for Rare-Earth Solid-State Quantum Computing. *Physical Review A*, 92(2):022319, 2015.

[83] R. Kolesov, K. Xia, R. Reuter, R. Stöhr, A. Zappe, J. Meijer, P. R. Hemmer, and J. Wrachtrup. Optical Detection of a Single Rare-Earth Ion in a Crystal. *Nature Communications*, 3:1029, 2012.

[84] G.Liu. *Electronic Energy Level Structure*, pages 1–94. Spectroscopic Properties of Rare Earths in Optical Materials. Springer, 2005.

[85] S. Bertaina, S. Gambarelli, A. Tkachuk, I. Kurkin, B. Malkin, A. Stepanov, and B. Barbara. Rare-Earth Solid-State Qubits. *Nature Nanotechnology*, 2(1):39–42, 2007.

[86] R. Lange, W. Grill, and W. Martienssen. Observation of Single Impurity Ions in a Crystal. *Europhysics letters*, 6:499–503, 1988.

[87] R. Rodrigues-Herzog, F. Trotta, H. Bill, J. Segura, B. Hecht, and H. Güntherodt. Optical Microscopy of Single Ions and Morphological Inhomogeneities in Sm-doped CaF_2 Thin Films. *Physical Review B*, 62(16):11163, 2000.

[88] A. P. Bartko, L. A. Peyser, R. M. Dickson, A. Mehta, T. Thundat, R. Bhargava, and M.D. Barnes. Observation of Dipolar Emission Patterns from Isolated $Eu^{3+} : Y_2O_3$ doped Nanocrystals: New Evidence for Single Ion Luminescence. *Chemical Physics Letters*, 358(5):459–465, 2002.

[89] Y. V. Malyukin, A. A. Masalov, and P. N. Zhmurin. Single-ion Fluorescence Spectroscopy of a $Y_2SiO_5 : Pr^{3+}$ Nanocluster. *Physics Letters A*, 316(1):147–152, 2003.

[90] B. M. Walsh, N. P. Barnes, and B. Di Bartolo. Branching Ratios, Cross Sections, and Radiative Lifetimes of Rare Earth Ions in Solids: Application to Tm^{3+} and Ho^{3+} Ions in $LiYF_4$. *Journal of Applied Physics*, 83(5):2772–2787, 1998.

[91] H. A. Höppe. Recent Developments in the Field of Inorganic Phosphors. *Angewandte Chemie International Edition*, 48(20):3572–3582, 2009.

[92] Y. M. Cheung and S. K. Gayen. Excited-State Absorption in $Pr^{3+} : Y_3Al_5O_{12}$. *Physical Review B*, 49(21):827–835, 1994.

[93] J. Ganem, W. M. Dennis, and W. M. Yen. One-Color Sequential Pumping of the $4f5d$ Bands in Pr-doped Yttrium Aluminum Garnet. *Journal of Luminescence*, 54:79–87, 1992.

[94] J. van der Ziel, M. Sturge, and L. Van Uitert. Optical Detection of Site Selectivity for Rare-Earth Ions in Flux-Grown Yttrium Aluminum Garnet. *Physical Review Letters*, 27(8):508–511, 1971.

[95] A. Taroni. Rare-Rarth Ion Singled Out. *Nature Materials*, 11(10):829–829, 2012.

[96] I. Nakamura, T. Yoshihiro, H. Inagawa, S. Fujiyoshi, and M. Matsushita. Spectroscopy of Single Pr^{3+} ion in LaF_3 Crystal at 1.5 K. *Scientific Reports*, 4, 2014.

[97] M. A. Kastner. The Single-Electron Transistor. *Reviews of Modern Physics*, 64(3):849, 1992.

[98] A. Morello, J. J. Pla, F. A. Zwanenburg, K. W. Chan, K. Y. Tan, H. Huebl, M. Möttönen, C. D. Nugroho, C. Yang, J. A. van Donkelaar, et al. Single-Shot Readout of an Electron Spin in Silicon. *Nature*, 467(7316):687–691, 2010.

[99] J. J. Pla, K. Y. Tan, J. P. Dehollain, W. H. Lim, J. Morton, D. N. Jamieson, A. S. Dzurak, and A. Morello. A single-Atom Electron Spin Qubit in Silicon. *Nature*, 489(7417):541–545, 2012.

[100] M Veldhorst, C. H. Yang, J. Hwang, W. Huang, J.P. Dehollain, J.T. Muhonen, S. Simmons, A. Laucht, F.E. Hudson, K. M. Itoh, et al. A Two-Qubit Logic Gate in Silicon. *Nature*, 2015.

[101] C. Yin, M. Rancic, G. G. de Boo, N. Stavrias, J. C. McCallum, M. J. Sellars, and S. Rogge. Optical Addressing of an Individual Erbium Ion in Silicon. *Nature*, 497(7447):91–94, 2013.

[102] J.C. Krupa and M. Queffelec. UV and VUV Optical Excitations in Wide Band Gap Materials Doped with Rare Earth Ions: $4f--5d$ Transitions. *Journal of alloys and compounds*, 250(1):287–292, 1997.

[103] W. P. Ambrose and W. E. Moerner. Fluorescence Spectroscopy and Spectral Diffusion of Single Impurity Molecules in a Crystal. *Nature*, 349:225–227, 1991.

[104] R.G. Neuhauser, K.T. Shimizu, W.K. Woo, S.A. Empedocles, and M.G. Bawendi. Correlation between Fluorescence Intermittency and Spectral Diffusion in Single Semiconductor Quantum Dots. *Physical Review Letters*, 85(15):3301, 2000.

[105] T. Tomiki, F. Fukudome, M. Kaminao, M. Fujisawa, Y. Tanahara, and T. Futemma. Optical Spectra of $Y_3Al_5O_{12}$(YAG) single crystals in the vacuum ultraviolet region. *Journal of the Physical Society of Japan*, 58(5):1801–1810, 1989.

[106] Y. Xu and W. Y. Ching. Electronic Structure of Yttrium Aluminum Garnet($Y_3Al_5O_{12}$). *Physical Review B*, 59(16):530–535, 1999.

[107] L. Zheng, J. Xu, and L. Su. *Growth and Characterization of Ytterbium Doped Silicate Crystals for Ultra-Fast Laser Applications*. INTECH Open Access Publisher, 2012.

[108] X. Xu, Z. Zhao, J. Xu, and P. Deng. Distribution of Ytterbium in Yb: YAG Crystals and Lattice Parameters of the Crystals. *Journal of crystal growth*, 255(3):338–341, 2003.

[109] R. C. Wheeler G. F. Koster, J. O. Dimmock and H. Statz. *Properties of the Thirty-Two Point Groups*, page 36. Cambridge, Mass, 1963.

[110] Chemistry table. https : //www.webelements.com/.

[111] Janus Hallelov Wesenberg. *Quantum Information Processing in Rare-Earth-Ion Doped Crystals*. PhD thesis, University of Arahus, Denmark, 2004.

[112] S. Hüfner. *Optical Spectra of Transparent Rare Earth Compounds, Academic Press*. 1978.

[113] M. K. Kim and R. Kachru. Hyperfine Measurements of the $^1D_2 - ^3 H_4$ Transition in Pr^{3+}: Yttrium Aluminum Garnet using Photon Echo. *Physical Review B*, 40(4):2082–2089, 1989.

[114] G. Özen, O. Forte, and B. Di Bartolo. Downconversion and Upconversion Dynamics in Pr-doped $Y_3Al_5O_{12}$ Crystals. *Journal of Applied Physics*, 97(1):013510, 2005.

[115] M. J. Weber. Nonradiatice Decay from $5d$ States of Rare Earths in Crystals. *Solid State Communications*, 12:741–744, 1973.

[116] S. K. Gayen, Bin Qing Xie, and Y. M. Cheung. Two-Photon Excitation of the Lowest $4f^2 \rightarrow 4f5d$ Near-Ultraviolet Transitions in $Pr^{3+} : Y_3Al_5O_{12}$. *Physical Review B*, 45:20–28, 1992.

[117] J. Yang and Y. Xu. A Study of the Faraday Effect in Yttrium Aluminium Garnets Doped with Cerium. *Zeitschrift für Physik B Condensed Matter*, 101(1):23–28, 1996.

[118] P. A. Tanner, L. Fu, L. Ning, B. Cheng, and M. G. Brik. Soft Synthesis and Vacuum Ultraviolet Spectra of YAG: Ce^{3+} Nanocrystals: Reassignment of Ce^{3+} Energy Levels. *Journal of Physics: Condensed Matter*, 19(21):216213, 2007.

[119] R. R Jacobs, W. F. Krupke, and M. J. Weber. Measurement of Excited-State-Absorption Loss for Ce^{3+} in $Y_3Al_5O_{12}$ and Implications for Tunable 5 $d \rightarrow 4f$ Rare-Earth Lasers. *Applied Physics Letters*, 33(5):410–412, 1978.

[120] V. Bachmann, C. Ronda, and A. Meijerink. Temperature Quenching of Yellow Ce^{3+} Luminescence in YAG: Ce. *Chemistry of Materials*, 21(10):2077–2084, 2009.

[121] W. J. Miniscalco, J. M. Pellegrino, and W. M. Yen. Measurements of Excited-State Absorption in Ce^{3+}: YAG. *Journal of Applied Physics*, 49(12):6109–6111, 1978.

[122] L. Lyu and D.S. Hamilton. Radiative and Nonradiative Relaxation Measurements in Ce^{3+} Doped Crystals. *Journal of luminescence*, 48:251–254, 1991.

[123] Ying Yan. *Towards Single Ce Ion Detection in a Bulk Crystal for the Development of a Single-Ion Qubit Readout Scheme*. PhD thesis, Lund University, 2013.

[124] Jenny Karlsson. *Cerium as a Quantum State Probe for Rare-Earth Qubits in a Crystal*. PhD thesis, Lund University, 2015.

[125] J. Zhong, H. Liang, S. Qiang, J. Zhou, and J. Wang. Spectroscopic Properties of Vacancies and Trap Levels in $Lu_3Al_5O_{12}$: Ce^{3+} crystals. *Transactions of Nonferrous Metals Society of China*, 19(6):1628–1633, 2009.

[126] K. Blazek, A. Krasnikov, K. Nejezchleb, M. Nikl, T. Savikhina, and S. Zazubovich. Luminescence and Defects Creation in Ce^{3+}-Doped $Lu_3Al_5O_{12}$ Crystals. *physica status solidi (b)*, 241(5):1134–1140, 2004.

[127] J. J. Longdell, M. J. Sellars, and N. B. Manson. Demonstration of conditional quantum phase shift between ions in a solid. *Physical Review Letters*, 93(13):130503, 2004.

[128] J. Wen, C. Duan, L. Ning, Y. Huang, S. Zhan, J. Zhang, and M. Yin. Spectroscopic Distinctions Between Two Types of Ce^{3+} ions in X2-Y_2SiO_5: A Theoretical Investigation. *The Journal of Physical Chemistry A*, 118(27):4988–4994, 2014.

[129] J. Lin, Q. Su, H. Zhang, and S. Wang. Crystal Structure Dependence of the Luminescence of Rare Earth Ions (Ce $^{3+}$, Tb $^{3+}$, Sm $^{3+}$) in Y_2SiO_5. *Materials Research Bulletin*, 31(2):189–196, 1996.

[130] W. Drozdowski, A. J. Wojtowicz, D. Wiśniewski, P. Szupryczyński, S. Janus, J. Lefaucheur, and Z. Gou. VUV Spectroscopy and Low Temperature Thermoluminescence of LSO: Ce and YSO: Ce. *Journal of alloys and compounds*, 380(1):146–150, 2004.

[131] D. W. Cooke, J. K. Lee, B. L. Bennett, J. R. Groves, L. G. Jacobsohn, E. A. McKigney, R. E. Muenchausen, M. Nastasi, K. E. Sickafus, M. Tang, et al. Luminescent Properties and Reduced Dimensional Behavior of Hydrothermally Prepared Y_2SiO_5: Ce nanophosphors. *Applied physics letters*, 88(10):103108–103108, 2006.

[132] R. Kolesov, K. Xia, R. Reuter, M. Jamali, R. Stöhr, T. Inal, P. Siyushev, and J. Wrachtrup. Mapping Spin Coherence of a Single Rare-Earth Ion in a Crystal onto a Single Photon Polarization State. *Physical Review Letters*, 111(12):120502, 2013.

[133] R. Kolesov. Dynamics of Laser-Induced Magnetization in Ce-Doped Yttrium Aluminum Garnet. *Physical Review A*, 76(4):043831, 2007.

[134] R. Orbach. Spin-Lattice Relaxation in Rare-Earth Salts. In *Proceedings of the Royal Society of London A: Mathematical, Physical and Engineering Sciences*, volume 264, pages 458–484. The Royal Society, 1961.

[135] J. Bylander, S. Gustavsson, F. Yan, F. Yoshihara, K. Harrabi, G. Fitch, D. G. Cory, Y. Nakamura, J. Tsai, and W. D. Oliver. Noise Spectroscopy Through Dynamical Decoupling with a Superconducting Flux Qubit. *Nature Physics*, 7(7):565–570, 2011.

[136] E. L. Hahn. Spin Echoes. *Physical Review*, 80(4):580, 1950.

[137] N. A. Kurnit, I. D. Abella, and S. R. Hartmann. Observation of a photon echo. *Physical Review Letters*, 13(19):567, 1964.

[138] J. Du, X. Rong, N. Zhao, Y. Wang, J. Yang, and R. Liu. Preserving Electron Spin Coherence in Solids by Optimal Dynamical Decoupling. *Nature*, 461(7268):1265–1268, 2009.

[139] M. J. Biercuk, H. Uys, A. P. VanDevender, N. Shiga, W. M. Itano, and J. J. Bollinger. Optimized Dynamical Decoupling in a Model Quantum Memory. *Nature*, 458(7241):996–1000, 2009.

[140] G. de Lange, Z. H. Wang, D. Riste, V. V. Dobrovitski, and R. Hanson. Universal Dynamical Decoupling of a Single Solid-State Spin from a Spin Bath. *Science*, 330(6000):60–63, 2010.

[141] B. Naydenov, F. Dolde, L. T. Hall, C. Shin, H. Fedder, L. Hollenberg, F. Jelezko, and J. Wrachtrup. Dynamical Decoupling of a Single-Electron Spin at Room Temperature. *Physical Review B*, 83(8):081201, 2011.

[142] H. Y. Carr and E. M. Purcell. Effects of Diffusion on Free Precession in Nuclear Magnetic Resonance Experiments. *Physical Review*, 94(3):630, 1954.

[143] S. Meiboom and D. Gill. Modified Spin-Echo Method for Measuring Nuclear Relaxation Times. *Review of scientific instruments*, 29(8):688–691, 1958.

[144] C. A. Ryan, J. S. Hodges, and D. G. Cory. Robust Decoupling Techniques to Extend Quantum Coherence in Diamond. *Physical Review Letters*, 105(20):200402, 2010.

[145] P Siyushev, K Xia, R Reuter, M Jamali, N Zhao, N Yang, C Duan, N Kukharchyk, AD Wieck, R Kolesov, et al. Coherent Properties of Single Rare-Earth Spin Qubits. *Nature Communications*, 5, 2014.

[146] M. S. Dietz, D. Haße, D. M. Ferraris, A. Göhler, H. Niemann, and M. Heilemann. Single-Molecule Photobleaching Reveals Increased MET Receptor Dimerization upon Ligand Binding in Intact Cells. *BMC Biophysics*, 6(1):6, 2013.

[147] M. Pelton, G. Smith, N. F. Scherer, and R. A. Marcus. Evidence for a Diffusion-Controlled Mechanism for Fluorescence Blinking of Colloidal Quantum Dots. *Proceedings of the National Academy of Sciences*, 104(36):14249–14254, 2007.

[148] N. Aslam, G. Waldherr, P. Neumann, F. Jelezko, and J. Wrachtrup. Photo-Induced Ionization Dynamics of the Nitrogen Vacancy Defect in Diamond Investigated by Single-Shot Charge State Detection. *New Journal of Physics*, 15(1):013064, 2013.

[149] J. S. Stroud. Photoionization of Ce^{3+} in Glass. *The Journal of Chemical Physics*, 35(3):844–850, 1961.

[150] C. Pedrini, F. Rogemond, and D. S. McClure. Photoionization Thresholds of Rare-Earth Impurity Ions. Eu^{2+} : CaF_2, Ce^{3+} : YAG, and Sm^{2+} : CaF_2. *Journal of Applied Physics*, 59(4):1196–1201, 1986.

[151] J. Ueda, S. Tanabe, and T. Nakanishi. Analysis of Ce^{3+} Luminescence Quenching in Solid Solutions Between $Y_3Al_5O_{12}$ and $Y_3Ga_5O_{12}$ by Temperature Dependence of Photoconductivity Measurement. *Journal of Applied Physics*, 110(5):053102, 2011.

[152] C. R. Varney, D. T. Mackay, S. M. Reda, and F. A. Selim. On the Optical Properties of Undoped and Rare-Earth-Doped Yttrium Aluminium Garnet Single Crystals. *Journal of Physics D: Applied Physics*, 45(1):015103, 2012.

[153] E. Van der Kolk, J. De Haas, A. Bos, C. Van Eijk, and P. Dorenbos. Luminescence Quenching by Photoionization and Electron Transport in a $LaAlO_3$: Ce^{3+} crystal. *Journal of Applied Physics*, 101(8), 2007.

[154] D. T. Mackay, C. R. Varney, J. Buscher, and F. A. Selim. Study of Exciton Dynamics in Garnets by Low Temperature Thermo-Luminescence. *Journal of Applied Physics*, 112(2):023522, 2012.

[155] B. Dalton, R. McDuff, and P. Knight. Coherent Population Trapping. *Journal of Modern Optics*, 32(1):61–70, 1985.

[156] S. Harris, J. Field, and A. Imamoğlu. Nonlinear Optical Processes using Electromagnetically Induced Transparency. *Physical Review Letters*, 64(10):1107, 1990.

[157] K. J. Boller, A. Imamolu, and S. E. Harris. Observation of Electromagnetically Induced Transparency. *Physical Review Letters*, 66:2593–2596, 1991.

[158] D. Phillips, A. Fleischhauer, A. Mair, R. Walsworth, and M. Lukin. Storage of Light in Atomic Vapor. *Physical Review Letters*, 86(5):783, 2001.

[159] M. Scully, S. Zhu, and A. Gavrielides. Degenerate Quantum-Beat Laser: Lasing without Inversion and Inversion without Lasing. *Physical Review Letters*, 62(24):2813, 1989.

[160] M. Fleischhauer, A. Imamoglu, and J. P. Marangos. Electromagnetically induced transparency: Optics in coherent media. *Reviews of modern physics*, 77(2):633, 2005.

[161] C. Santori, P. Tamarat, P. Neumann, J. Wrachtrup, D. Fattal, R. G. Beausoleil, J. Rabeau, P. Olivero, A. D. Greentree, S. Prawer, et al. Coherent Population Trapping of Single Spins in Diamond under Optical Excitation. *Physical Review Letters*, 97(24):247401, 2006.

[162] X. Xu, B. Sun, P. R. Berman, D. G. Steel, A. S. Bracker, D. Gammon, and L. J. Sham. Coherent Population Trapping of an Electron Spin in a Single Negatively Charged Quantum Dot. *Nature Physics*, 4(9):692–695, 2008.

[163] E. Togan, Y. Chu, A. Imamoglu, and M. D. Lukin. Laser cooling and real-time measurement of the nuclear spin environment of a solid-state qubit. *Nature*, 478(7370):497–501, 2011.

[164] B. Pingault, J. N. Becker, C. H. Schulte, C. Arend, C. Hepp, T. Godde, A. I. Tartakovskii, M. Markham, C. Becher, and M. Atatüre. All-Optical Formation of Coherent Dark States of Silicon-Vacancy Spins in Diamond. *Physical Review Letters*, 113(26):263601, 2014.

[165] L. J. Rogers, K. D. Jahnke, M. H. Metsch, A. Sipahigil, J. M. Binder, T. Teraji, H. Sumiya, J. Isoya, M. D. Lukin, P. Hemmer, et al. All-Optical Initialization, Readout, and Coherent Preparation of Single Silicon-Vacancy Spins in Diamond. *Physical Review Letters*, 113(26):263602, 2014.

[166] K. De Greve, P. L. McMahon, D. Press, T. D. Ladd, D. Bisping, C. Schneider, M. Kamp, L. Worschech, S. Höfling, A. Forchel, et al. Ultrafast Coherent Control and Suppressed Nuclear Feedback of a Single Quantum Dot Hole Qubit. *Nature Physics*, 7(11):872–878, 2011.

[167] A. Golter and H. Wang. Optically Driven Rabi Oscillations and Adiabatic Passage of Single Electron Spins in Diamond. *Physical Review Letters*, 112(11):116403, 2014.

[168] L. Childress, M. Gurudev Dutt, J. Taylor, A. Zibrov, F. Jelezko, J. Wrachtrup, P. Hemmer, and M. Lukin. Coherent Dynamics of Coupled Electron and Nuclear Spin Qubits in Diamond. *Science*, 314(5797):281–285, 2006.

[169] G. Dutt, L. Childress, L. Jiang, E. Togan, J. Maze, F. Jelezko, A. Zibrov, P. Hemmer, and M. Lukin. Quantum Register Based on Individual Electronic and Nuclear Spin Qubits in Diamond. *Science*, 316(5829):1312–1316, 2007.

[170] John B. Gruber, Marian E. Hills, Roger M. Macfarlane, Clyde A. Morrison, and Gregory A. Turner. Symmetry, Selection Rules, and Energy Levels of $Pr^{3+} : Y_3Al_5O_{12}$. *Chemical Physics*, 134:241–257, 1989.

[171] M. K. Kim and R. Kachru. Hyperfine Structures of Praseodymium Ions in Solids Using Stimulated-Photon-Echo Modulation. *Physical Review B*, 44(18):9826–9832, 1991.

[172] M. Jamali, I. Gerhardt, M. Rezai, K. Frenner, H. Fedder, and J. Wrachtrup. Microscopic Diamond Solid-Immersion-Lenses Fabricated around Single Defect Centers by Focused Ion Beam Milling. *Review of Scientific Instruments*, 85(12):123703, 2014.

[173] P. Siyushev, F. Kaiser, V. Jacques, I. Gerhardt, S. Bischof, H. Fedder, J. Dodson, M. Markham, D. Twitchen, F. Jelezko, and J. Wrachtrup. Monolithic Diamond Optics for Single Photon Detection. *Applied Physics Letters*, 97(24):241902, 2010.

[174] E. Eichhammer, T. Utikal, S. Götzinger, and V. Sandoghdar. Spectroscopic Detection of Single Pr^{3+} Ions on the $^3H_4 -^1 D_2$ Transition. *New Journal of Physics*, 17(8):083018, 2015.

[175] X. Li, Y. Wu, D. Steel, D. Gammon, T. Stievater, D. Katzer, D. Park, C. Piermarocchi, and L. Sham. An All-Optical Quantum Gate in a Semiconductor Quantum Dot. *Science*, 301(5634):809–811, 2003.

[176] D. Press, T. Ladd, B. Zhang, and Y. Yamamoto. Complete Quantum Control of a Single Quantum Dot Spin Using Ultrafast Optical Pulses. *Nature*, 456(7219):218–221, 2008.

[177] J. F. Gibbons. Ion Implantation in Semiconductors—Part I: Range Distribution Theory and Experiments. *Proceedings of the IEEE*, 56(3):295–319, 1968.

[178] J. F. Gibbons. Ion Implantation in Semiconductors—Part II: Damage Production and Annealing. *Proceedings of the IEEE*, 60(9):1062–1096, 1972.

[179] J. Meijer, S. Pezzagna, T. Vogel, B. Burchard, H. Bukow, I. Rangelow, Y. Sarov, H. Wiggers, I. Plümel, F. Jelezko, et al. Towards the Implanting of Ions and Positioning of Nanoparticles with nm Spatial Resolution. *Applied Physics A*, 91(4):567–571, 2008.

[180] B. Naydenov, R. Kolesov, J. Batalov, A .and Meijer, S. Pezzagna, D. Rogalla, F. Jelezko, and J. Wrachtrup. Engineering Single Photon Emitters by Ion Implantation in Diamond. *Applied Physics Letters*, 95(18):181109, 2009.

[181] B. Naydenov, V. Richter, J. Beck, M. Steiner, P. Neumann, G. Balasubramanian, J. Achard, F. Jelezko, J. Wrachtrup, and R. Kalish. Enhanced Generation of Single Optically Active Spins in Diamond by Ion Implantation. *Applied Physics Letters*, 96(16):163108, 2010.

[182] B. Hausmann, T. Babinec, J. Choy, J. Hodges, S. Hong, I. Bulu, A. Yacoby, M. Lukin, and M. Lončar. Single-Color Centers Implanted in Diamond Nanostructures. *New Journal of Physics*, 13(4):045004, 2011.

[183] R. Evans, A. Sipahigil, D. Sukachev, A. Zibrov, and M. Lukin. Narrow-Linewidth Homogeneous Optical Emitters in Diamond Nanostructures via Silicon Ion Implantation. *Physical Review Applied*, 5(4):044010, 2016.

[184] Y. Tang, K. Heasman, W. Gillin, and B. Sealy. Characteristics of Rare-Earth Element Erbium Implanted in Silicon. *Applied Physics Letters*, 55(5):432–433, 1989.

[185] F. Widdershoven and J. Naus. Donor Formation in Silicon Owing to Ion Implantation of the Rare Earth Metal Erbium. *Materials Science and Engineering: B*, 4(1):71–74, 1989.

[186] N. Kukharchyk, S. Shvarkov, S. Probst, K. Xia, H. Becker, S. Pal, S. Markmann, R. Kolesov, P. Siyushev, J. Wrachtrup, et al. Nanoscale Nonlinear Effects in Erbium-Implanted Yttrium Orthosilicate. *Journal of Luminescence*, 177:266–274, 2016.

[187] T. Kornher, K. Xia, R. Kolesov, N. Kukharchyk, R. Reuter, P. Siyushev, R. Stöhr, M. Schreck, H. Becker, B. Villa, et al. Production Yield of Rare-Earth Ions Implanted into an Optical Crystal. *Applied Physics Letters*, 108(5):053108, 2016.

[188] F. Dolde, I. Jakobi, B. Naydenov, N. Zhao, S. Pezzagna, C. Trautmann, J. Meijer, P. Neumann, F. Jelezko, and J. Wrachtrup. Room-Temperature Entanglement between Single Defect Spins in Diamond. *Nature Physics*, 9(3):139–143, 2013.

[189] B. Ofori-Okai, S. Pezzagna, K. Chang, M. Loretz, R. Schirhagl, Y. Tao, B. Moores, K. Groot-Berning, J. Meijer, and C. Degen. Spin Properties of very Shallow Nitrogen Vacancy Defects in Diamond. *Physical Review B*, 86(8):081406, 2012.

[190] Y. Chu, N. De Leon, B. Shields, B. Hausmann, R. Evans, E. Togan, M. Burek, M. Markham, A. Stacey, A. Zibrov, et al. Coherent Optical Transitions in Implanted Nitrogen Vacancy Centers. *Nano Letters*, 14(4):1982–1986, 2014.

[191] C. Dujardin, C. Pedrini, J. Gâcon, A. Petrosyan, A. Belsky, and A. Vasil'ev. Luminescence Poperties and Scintillation Mechanisms of Cerium-and Praseodymium-doped Lutetium Orthoaluminate. *Journal of Physics: Condensed Matter*, 9(24):5229, 1997.

[192] H. Jang, W. Im, D. Lee, D. Jeon, and S. Kim. Enhancement of Red Spectral Emission Intensity of $Y_3Al_5O_{12}$: Ce Phosphor via Pr Co-Doping and Tb Substitution for the Application to White LEDs. *Journal of Luminescence*, 126(2):371–377, 2007.

[193] L. Zhang, C. Pedrini, C. Madej, C. Dujardin, J. Gacaron con, B. Moine, I. Kamenskikh, A. Belsky, D. Shaw, M. MacDonald, et al. Fast Fluorescence and Scintillation Properties of Cerium and Praseodymium Doped Lutetium Orthoborates. *Radiation Effects and Defects in Solids*, 150(1-4):47–52, 1999.

[194] H. Yang and Y. Kim. Energy Transfer-Based Spectral Properties of Tb-, Pr-, or Sm-codoped YAG: Ce Nanocrystalline Phosphors. *Journal of Luminescence*, 128(10):1570–1576, 2008.

[195] Interionic Energy Transfer in $Y_3Al_5O_{12} : Ce^{3+}, Pr^{3+}$ Phosphor, author=Wang, L. and Zhang, X. and Hao, Z. and Luo, Y. and Zhang, J. and Wang, X. *Journal of Applied Physics*, 108(9), 2010.

[196] J. Karlsson, L. Rippe, and S. Kröll. A Confocal Optical Microscope for Detection of Single Impurities in a Bulk Crystal at Cryogenic Temperatures. *Review of Scientific Instruments*, 87(3):033701, 2016.

[197] H. Walther, B. Varcoe, B. Englert, and T. Becker. Cavity Quantum Electrodynamics. *Reports on Progress in Physics*, 69(5):1325, 2006.

[198] J. Majer, J. Chow, J. Gambetta, J. Koch, B. Johnson, J. Schreier, L. Frunzio, D. Schuster, A. Houck, A. Wallraff, et al. Coupling Superconducting Qubits via a Cavity Bus. *Nature*, 449(7161):443–447, 2007.

[199] J. McKeever, A. Boca, D. Boozer, J. Buck, and J. Kimble. Experimental Realization of a One-Atom Laser in the Regime of Strong Coupling. *Nature*, 425(6955):268–271, 2003.

[200] J. McKeever, A. Boca, A. Boozer, R. Miller, J. Buck, A. Kuzmich, and J. Kimble. Deterministic Generation of Single Photons from One Atom Trapped in a Cavity. *Science*, 303(5666):1992–1994, 2004.

[201] S. Ritter, C. Nölleke, C. Hahn, A. Reiserer, A. Neuzner, M. Uphoff, M. Mücke, E. Figueroa, J. Bochmann, and G. Rempe. An Elementary Quantum Network of Single Atoms in Optical Cavities. *Nature*, 484(7393):195–200, 2012.

[202] A. Faraon, P. Barclay, C. Santori, K. Fu, and R. Beausoleil. Resonant Enhancement of the Zero-Phonon Emission from a Colour Centre in a Diamond Cavity. *Nature Photonics*, 5(5):301–305, 2011.

[203] D. Ding, L. Pereira, J. Bauters, M. Heck, G. Welker, A. Vantomme, J. Bowers, M. de Dood, and D. Bouwmeester. Multidimensional Purcell Effect in an Ytterbium-Doped Ring Resonator. *Nature Photonics*, 10(6):385–388, 2016.

[204] M. Eichenfield, J. Chan, R. Camacho, K. Vahala, and O. Painter. Optomechanical Crystals. *Nature*, 462(7269):78–82, 2009.

[205] Y. Vlasov, M. O'Boyle, H. Hamann, and S. McNab. Active Control of Slow Light on a Chip with Photonic Crystal Waveguides. *Nature*, 438(7064):65–69, 2005.

[206] K. Xia, R. Kolesov, Y. Wang, P. Siyushev, R. Reuter, T. Kornher, N. Kukharchyk, A. D. Wieck, B. Villa, S. Yang, and J. Wrachtrup. All-Optical Preparation of Coherent Dark States of a Single Rare Earth Ion Spin in a Crystal. *Physical Review Letters*, 115(9):093602, 2015.

[207] P Siyushev*, K Xia*, R Reuter, M Jamali, N Zhao, N Yang, C Duan, N Kukharchyk, AD Wieck, R Kolesov, et al. Coherent Properties of Single Rare-Earth Spin Qubits. *Nature Communications*, 5, 2014. (*contributed equally to this work).

[208] R. J. Stöhr, R. Kolesov, K. Xia, and J. Wrachtrup. All-Optical High-Resolution Nanopatterning and 3D Suspending of Graphene. *ACS Nano*, 5(6):5141–5150, 2011.

[209] R. J. Stöhr, R. Kolesov, K. Xia, R. Reuter, J. Meijer, G. Logvenov, and J. Wrachtrup. Super-Resolution Fluorescence Quenching Microscopy of Graphene. *ACS Nano*, 2012.

[210] K. Xia, Y. Wang, R. Kolesov, P. Siyushev, T. Kornher, S. Yang, and J. Wrachtrup. Coherent Addressing of Single Rare Eeath Nuclear Spins in Solids. In Preparation, 2016.

List of publications

1. N. Kukharchyk, S. Shvarkov, S. Probst, K. Xia, H. Becker, S. Pal, S. Markmann, R. Kolesov, P. Siyushev, J. Wrachtrup, et al. Nanoscale Nonlinear Effects in Erbium-Implanted Yttrium Orthosilicate. *Journal of Luminescence*, 177:266–274, 2016

2. T. Kornher, K. Xia, R. Kolesov, N. Kukharchyk, R. Reuter, P. Siyushev, R. Stöhr, M. Schreck, H. Becker, B. Villa, et al. Production Yield of Rare-Earth Ions Implanted into an Optical Crystal. *Applied Physics Letters*, 108(5):053108, 2016

3. K. Xia, R. Kolesov, Y. Wang, P. Siyushev, R. Reuter, T. Kornher, N. Kukharchyk, A. D. Wieck, B. Villa, S. Yang, and J. Wrachtrup. All-Optical Preparation of Coherent Dark States of a Single Rare Earth Ion Spin in a Crystal. *Physical Review Letters*, 115(9):093602, 2015

4. P Siyushev*, K Xia*, R Reuter, M Jamali, N Zhao, N Yang, C Duan, N Kukharchyk, AD Wieck, R Kolesov, et al. Coherent Properties of Single Rare-Earth Spin Qubits. *Nature Communications*, 5, 2014. (*contributed equally to this work)

5. R. Kolesov, K. Xia, R. Reuter, M. Jamali, R. Stöhr, T. Inal, P. Siyushev, and J. Wrachtrup. Mapping Spin Coherence of a Single Rare-Earth Ion in a Crystal onto a Single Photon Polarization State. *Physical Review Letters*, 111(12):120502, 2013

6. R. Kolesov, K. Xia, R. Reuter, R. Stöhr, A. Zappe, J. Meijer, P. R. Hemmer, and J. Wrachtrup. Optical Detection of a Single Rare-Earth Ion in a Crystal. *Nature Communications*, 3:1029, 2012

7. R. Kolesov, R. Reuter, K. Xia, R. Stöhr, A. Zappe, and J. Wrachtrup. Super-Resolution Upconversion Microscopy of Praseodymium-Doped Yttrium Aluminum Garnet Nanoparticles. *Physical Review B*, 84:153413, 2011

8. R. J. Stöhr, R. Kolesov, K. Xia, and J. Wrachtrup. All-Optical High-Resolution Nanopatterning and 3D Suspending of Graphene. *ACS Nano*, 5(6):5141–5150, 2011

9. R. J. Stöhr, R. Kolesov, K. Xia, R. Reuter, J. Meijer, G. Logvenov, and J. Wrachtrup. Super-Resolution Fluorescence Quenching Microscopy of Graphene. *ACS Nano*, 2012

10. K. Xia, Y. Wang, R. Kolesov, P. Siyushev, T. Kornher, S. Yang, and J. Wrachtrup. Coherent Addressing of Single Rare Eeath Nuclear Spins in Solids. In Preparation, 2016

Acknowledgments

The past over six years as a master and a Ph.D. student in the 3. Physikalisches Institut at University of Stuttgart has been a great pleasure. I would like to take this opportunity to thank my colleagues, friends, and family. This dissertation would not be possible without their support and help.

I would like to express my sincerest gratitude to my supervisor **Prof. Dr. Jörg Wrachtrup** for giving me the opportunity to pursue my study in this world pioneer research institute with such fascinating topic in the past. I acknowledge his excellent support, inspiration and guidance throughout my Ph.D. studies. His knowledge in many fields always broadens my horizon. I would like to give my deepest gratitude to my group leader **Dr. Roman Kolesov** for his valuable guidance continuous availability and countless hours of discussion. The joy and enthusiasm he has for research were contagious and motivational for me. I am grateful to both of them for their great patient, encouragement and all kinds of help both in research and life. Their earnest endeavors have always motivated me and I am incredibly proud of having worked under their guidance. Their enthusiasm and integral view and taste on research have made a deep impression on me. Their advice was and will forever be invaluable for me.

I would like to thank **Prof. Dr. Peter Michler** for agreeing to be co-advisor on this dissertation, and giving the second referee report of this dissertation with a short notice. I want to thank **Prof. Dr. Günter Wunner** for acceptance to be the chairman of the examination committee. I would like to mention the invention from **Prof. Dr. Fedor Jelezko** in 2009. This invention helps me to start this incredible journey in Germany.

I want to deeply thank **Dr. Rolf Reuter** for his great support of the best rare earth ions in YAG nanocrystal. Great thanks to **Dr. Petr Siyushev**. I appreciate him providing me with valuable guidance and knowledge of cryogenic temperature physics study. The time we were studying the coherent properties of single Ce ions in YAG crystal together, was the happiest time during my Ph.D. studying. I owe special thanks to him for dedicating long time of fruitful discussion and inspiring. My deep gratitude goes to **Dr. Rainer Stöhr**, he has walked me through all the stages of my master study. Without his consistent and illuminating instruction in the earlier state, my Ph.D. study would not have been possible. I feel so grateful of his constant support, encouragement and help in varies ways.

I want to thank **Dr. Nan Zhao**. The calculations and simulations provided by him, have not only acted as to confirm our experimental results, but also helped me to understand the limit and interpret experimental data.

Many thanks to **Thomas Kornher**. He joined the group at the later stage of my Ph.D.. He is always the first to offer his help in the lab. I also want to send the greeting to **Bruno Villa**, **Dr. Genxu Chen**, and **Tugrul Inal**. All of them spent one year in our group and provide a lot of support during the experiments. I would also like to send my greeting to **Dr. Andrea Zappe** for the biology experiments.

I would like to express my gratitude towards **Dr. Ya Wang** for the supporting of the theory part and read this dissertation from the begin till the end. I am also very grateful to **Dr. Sen Yang**, for his help of the SILs fabrication and intensive discussion. They emotionally support me for the entire Ph.D. time.

I also want to thank **Prof. Dr. Andreas Wieck** and **Dr. Nadezhda Kukharchyk** for providing us the ion implanted samples.

Many thanks would go to **Dr. Philippe Goldner**, **Prof. Dr. Alban Ferrier**. They offer many high quality crystals to us.

Monika Ubl, **Dr. Mario Hentschel**, **Ramon Walter** and **Nikolai Strohfeldt** from microstructure lab are acknowledged for helping me to prepare the samples in MSL. I would also thank **Prof. Dr.Jürgen Weis** and **Dr. Ulrike Waizmann** in nanostructure lab in MPI-FKF for offer me the opportunity and help me to use the instruments. I would also thank **Dr. Amit Finkler** for his help of e-beam lithography at the beginning stage.

Many thanks to my colleagues **Dr. Bernard Grotz**, **Thai Hien Tran**, **Stefan Lasse**, **Ali Momenzadeh**, **Torsten Rendler**, **Matthias Widmann**, **Matthias Niethammer**, **Sina Burk**, **Thomas Häberle**, **Dominik Schmid-Lorch** for many joy and "dark working" time together. Great thanks to **Dr. Andrej Denisenko**, **Dr. Philipp Neumann**, **Stephan Hirschmann**, **Ingmar Jakobi**, **Dr. Sang-Yun Lee**, **Julia Michl**, **Farida Shagieva**, and **Sebastian Zaiser**. It is nice to work in such friendly atmosphere.

I also want to mention the great contribution from institute secretary **Ms. Claudia Unger** for organizing a lot of paper work. Many thanks to **Ms. Ivanka Spajic** for the delicious dinner service at the beginning and helping to clean the office and lab. I also want to mention the support given by the mechanical workshop, the low temperature workshop, the electronics workshop, and the glass work shop.

My time in Germany was made enjoyable in large part due to some friends. My deep gratitude goes to **Junjie Luo**, and **Yi Lu** for always filling my memories with strong impressions of joy and fun. Thanks to all my friends indeed for their affection and for helping me with their character and their personality to become who I am.

I am grateful to other institute members whom are not mentioned so far but helped me throughout the past six years.

Finally, I would like to mention my deepest gratitude to my family in China for their long standing support, encouragement and love. I would like to extend my deepest gratitude to my beloved wife **Jia** for sharing with me joys, disappointments, adventures and discoveries, for every up and down moment of my life. Without her constant love and support, I would not have come this far.